Al-Mukhtar Journal of Basic Sciences

Voulme 22
Issue 3
DEC 2024

EISSN :3006 - 8649

PUBLISHED BY OMU

Al-Mukhtar Journal of Basic Sciences

Peer-reviewed scientific journal, Volume Twenty-Two, Issue Three, 2024

Published by Omar Al-Mukhtar University, Al-Bayda, Libya

A peer-reviewed journal published by Omar Al-Mukhtar University,

Al Bayda, Libya

Peer-reviewed scientific journal, Volume Twenty-Two, Issue Three, 2024

Email: ljbs.sci@omu.edu.ly

EDITORS & STAFF

Al-Mukhtar Journal of Basic Sciences 22: (3), 2024

Al-Mukhtar Journal of Basic Sciences 22 (3): 159-165, 2024
Doi: https://doi.org/10.54172/tr3mwd31

Research Article **Open Access**

Chemical composition of *Ocimum sanctum* by GC-MS Analysis

Ahmed A. Mustafa[*], Mubarak S. Hamad[1], Haifa A. Awad[2] and Hatil El-kamali[3]

Corresponding Author: ahmad.ali11526@uofg.edu.sd, Department of Botany and Microbiology, Faculty of Science, University of Gezira, Wad-madani, Sudan.

[1]Department of Taxonomy and Phytochemistry, Medicinal, Aromatic and Tradition Medicine,Research Institute, National Center for Research, Khartoum, Sudan.

[2]Department of Botany, Faculty of Science, Sudan University of Science and Technology, Khartoum, Sudan.

[3]Department of Botany Faculty of Science and Technology , Omdurman Islamic University, Omdurman, Sudan.

Received:
30 November 2023

Accepted:
10 October 2024

Publish online:
31 December 2024

Abstract

The chemical composition of the n-hexane extract from the aerial parts of *Ocimum sanctum.*, was investigated using gas chromatography-mass spectrometry (GC/MS), identifying 46 different compounds. Terpenoids were the most abundant, with monoterpenes representing 21.82% of the extract. The primary components identified were methyl eugenol (27.24%), squalene (11.84%) α-bergamotene (9.83%), linalool (8.42%), and fenchyl acetate (7.56%). These results indicate that *O. sanctum* could serve as a valuable source of food and medicinal agents.

Keywords: *Ocimum sanctum.*, GC

INTRODUCTION

Medicinal plants are well-known for their diverse range of bioactive compounds, which have long been used to treat chronic and infectious diseases (Periyasamy Ashokkumar et al., 2010). Natural products derived from plant extracts/fractions are potent therapeutic agents for various infectious as well as degenerative diseases. In herbal medicines, various parts of the plant (root, stem, flower, fruit, twig exudates and modified plant organs) are used having diverse therapeutic properties. To utilize these plants, they are collected on the minute scale by local communities and folk healers, while to trade for herbal industries numerous other plants are collected in large amounts as a raw material (Sahreen et al., 2015). In recent years for the management and protection against pathogens, a large number of plants have been examined for their antimicrobial characteristics as an integrative system of medicine (Hosseinzadeh et al., 2015).

For centuries, plant extracts and oils have served various medicinal and practical purposes (EL-

Kamali & EL-Amir, 2010). The genus *Ocimum*, which includes 160 species, is distributed across tropical and subtropical regions, showing considerable morphological variability from herbs to sub-shrubs (Mustafa & El-kamali, 2019). The morphology of *Ocimum* varies from herb to sub-shrubs with large variations in leaf shape, size, glands, hairs and many more morphological peculiarities. Each species produces essential oils with antimicrobial, antioxidant, antifungal, and anti-inflammatory properties, although their taxonomy remains somewhat unclear (Nahak et al., 2011).

Ocimum sanctum., is widely recognized in traditional and modern medicine across Africa, Asia, Europe, and South America (Mustafa & El-kamali, 2020). This study aims to identify the chemical composition of the n-hexane extract from the aerial parts of *O. sanctum*.

MATERIALS AND METHODS

Plant Material

The aerial parts of *Ocimum sanctum.*, were collected from Sinnar State in April, 2018 and identified by Prof. Maha Kordofani from the University of Khartoum, Botany Department, Sudan.

Extraction

Twenty grams (20g) of dried aerial parts were macerated in n-hexane for 72 hours. After filtration, the extract was concentrated, yielding 80 mg of dried material (Omer et al., 2024).

GC-MS Analysis

GC/MS analysis was performed on a Shimadzu GC/MS-QP2010A system in ET mode (70ev) equipped with at a split /splitters injector (250ºC), at split ratio of 5/50 using DB-5MSColumn (30m x 0.25mm id, film thickness: 0002E25 miss J and W scientific, fulsome, CA,WA). Injection volume was 1misarlitre and electronic pressure programming was used to maintain a constant flame (0.67ml/mins) of the Helium carrier gas. The oven temperature was programmed from 150ºC (4mins) to 320ºC at a rate of 2c/mins and held at that temperature 200ºC and interface temperature 250ºC. The relative approach percentage of each compound was determined by area. Components identification was carried out using the NIST 147 and NIST 27 libraries (Mustafa & El-kamali, 2019).

RESULTSAND DISCUSSION

GC-MS analysis of the n-hexane extract from *O. sanctum.*, aerial parts revealed 46 chemical constituents (Table1) The major compound was methyl eugenol (27.24%), followed by squalene (11.84%), α-bergamotene (9.83%), linalool (8.42%), and fenchyl acetate (7.56%). Sesquiterpenes (48.33%) and monoterpenes (21.25%) were the dominant compound groups, with other identified components including triterpenol hydrocarbons, esters, ketones, fatty acids, and alcohols.

The results can be justified by the already reported work (Khair-ul-Bariyah, 2013). The work has been reported regarding the chemical constituents of *O. sanctum* (Mondello et al., 2002). Similarly, linalool of up to 71.4% in essential oil from Bulgaria has been reported (Jirovetz et al., 2001). From China, Croatia, Israel, the Republic of Guinea, Nigeria, Egypt, Pakistan and Malaysia, (z)cinnamic acid methyl ester, linalool, eugenol, estragol, bergamotene, 1,8-cineol, α-cadinol, methyl cinnamate and limonene has been listed as major components of the essential oil. Forty seven components comprising 97.99% of total oil have been reported (Hassanpouraghdam et al., 2010).

Generally, the work has been reported monoterpenoids comprise the major fraction of the oil (77.8%) followed by sesquiterpenoids (12.8%). Oxygenated monoterpenes are 75.3% present with estragole (21.5%), menthone (33.1%), menthol (6.1%), isoneomenthol (7.5%) and pulegone (3.7%) being the main compounds. The only monoterpene hydrocarbon is limonene (1.5%). Menthyl acetate was found in trace amounts (5.6%) (Khair-ul-Bariyah, 2013). The presence of bioactive compounds supports the traditional use of *O. sanctum* for medicinal purposes, and it was classified as a methyl eugenol chemotype.

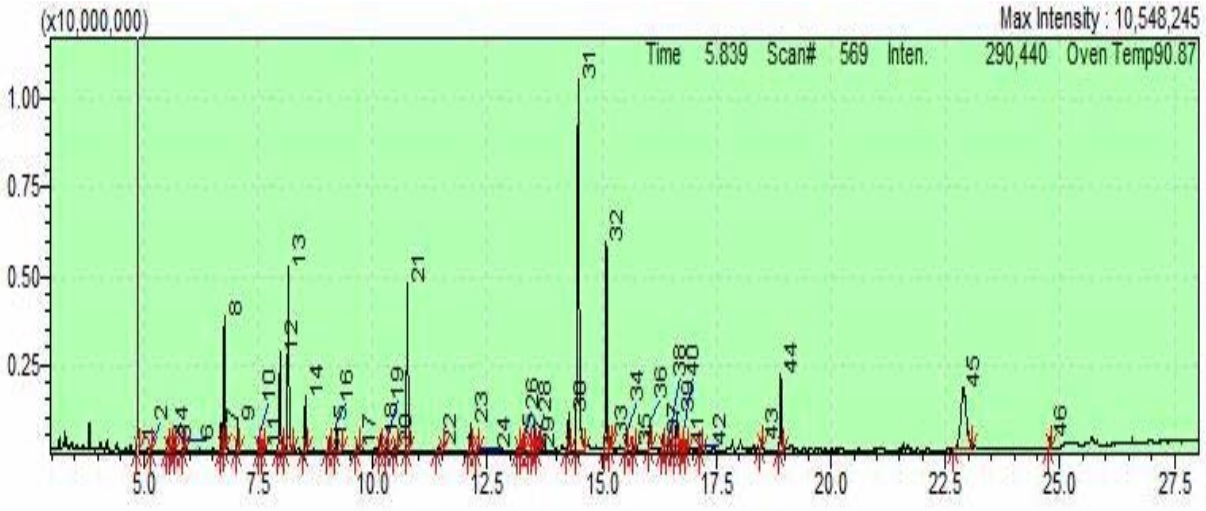

Figure (1). GC/MC chromatogram of *Ocimum sanctum.*, n-hexan extract

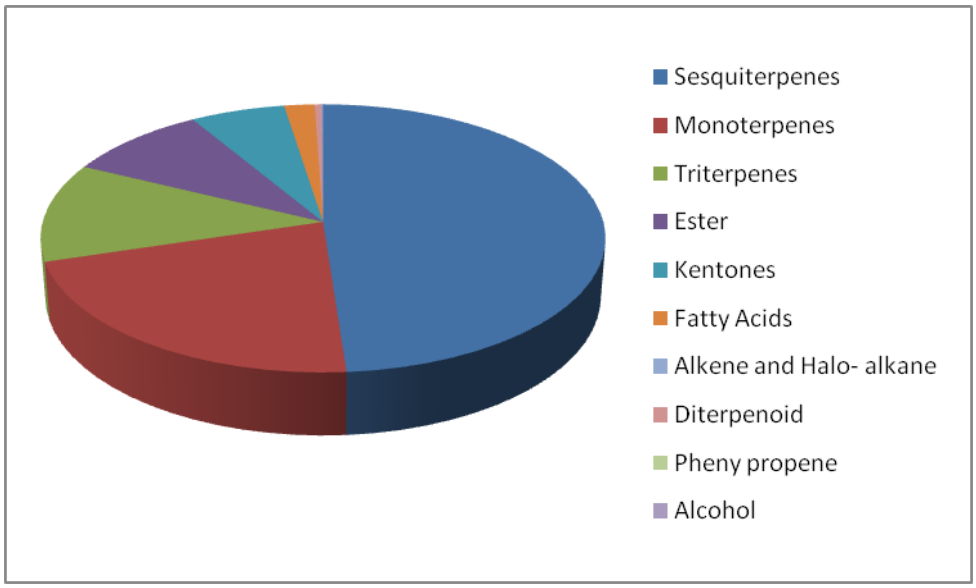

Figure (2). Percentage of compounds

Table(1). Chemical composition of n-hexane extract of aerial parts of *Ocimum sanctum.,:*

NO	Compounds	R.T	%	Formula	Class type
1	α –pinene	4.866	0.38	$C_{10}H_{16}$	MH
2	Camphene	5.152	0.13	$C_{10}H_{16}$	MH
3	Hexen-2-one	5.523	0.42	$C_6H_{10}O$	OH
4	β – phellandrene	5.598	0.20	$C_{10}H_{16}$	MH
5	β- (-)pinene	5.680	0.40	$C_{10}H_{16}$	MH
6	β – myrcene	5.888	0.41	$C_{10}H_{16}$	MH
7	D- Linanene	6.689	1.06	$C_{10}H_{16}$	MH
8	Eucalyptol	6.762	5.25	$C_{10}H_{18}O$	OM
9	B- Ocimene	7.048	1.09	$C_{10}H_{16}$	MH
10	Cyclohexanol,1-methyl-4-(1-methylethenyl	7.516	0.41	$C_{10}H_{18}O$	OM
11	α-methyl-alpha-(4-mehyl-3pentenyl)	7.609	0.17	$C_{10}H_{18}O_2$	FA
12	L-fenchone	7.976	4.48	$C_{10}H_{16}O$	Ketone
13	Linalool	8.159	8.42	$C_{10}H_{18}O$	OM
14	Bicyclo (2.2.1) hepta-2-ol ,1,3,3-trimethyl-	8.530	2.16	$C_{10}H_{18}O$	OM
15	3-cyclohexene-1-methanol	9.047	0.59	$C_7H_{12}O$	Alkene
16	(+)-2-bornanone	9.207	1.14	$C_{10}H_{16}O$	Ketone
17	L-α- terpineol	9.667	0.29	$C_{10}H_{18}O$	OM
18	α – terpineol	10.167	0.67	$C_{10}H_{18}O$	OM
19	Estragole	10.308	0.33	$C_{10}H_{12}O$	OM
20	Octyl acetate	10.480	0.25	$C_{10}H_{20}O_2$	FA
21	Fenchyl acetate	10.755	7.56	$C_{12}H_{20}O_2$	FA
22	Geraniol	11.440	0.38	$C_{10}H_{18}O$	OM
23	Bornyl acetate	12.136	1.18	$C_{12}H_{20}O_2$	FA
24	Hexadecane,1-chloro	12.280	0.12	$C_{16}H_{33}CL$	Halo-alkane
25	-β elemene	13.181	0.28	$C_{15}H_{24}$	SH
26	2-hydroxycineol	13.253	0.14	$C_{12}H_{20}O_3$	Ether
27	α – culenene	13.423	0.04	$C_{15}H_{24}$	SH
28	6-isopropenyl-3-(methoxy meth-oxy)-3-methyl	13.528	0.07	$C_{12}H_{20}O_2$	FA
29	Hydroxycineol	13.586	0.13	$C_{10}H_{18}O_2$	FA
30	Elemene	14.275	1.64	$C_{11}H_{14}O_2$	FA
31	Methyl eugenol	14.491	27.24	$C_{15}H_{24}$	SH
32	α- Bergamotenol	15.096	9.83	$C_{15}H_{24}$	SH
33	α- Guaiene	15.188	0.45	$C_{15}H_{24}$	SH
34	Humulene	15.537	0.64	$C_{15}H_{24}$	SH
35	β- cubebene	15.700	0.25	$C_{15}H_{24}$	SH
36	β -Ylangene	16.047	1.50	$C_{15}H_{24}$	SH
37	Germcrene B	16.338	0.63	$C_{15}H_{24}$	SH
38	α-bulnesene	16.477	0.71	$C_{15}H_{24}$	SH
39	γ-maurolene	16.636	1.76	$C_{15}H_{24}$	SH
40	β-Sesquiphella-ndrene	16.737	0.34	$C_{15}H_{24}$	SH
41	2-α-trans-bergamolol	16.832	0.20	$C_{15}H_{24}O$	OS
42	Trans –α-begamotol	17.156	0.30	$C_{15}H_{24}O$	OS
43	Cubenol	18.476	0.38	$C_{15}H_{26}O$	OS
44	Cadinol	18.903	3.78	$C_{15}H_{26}O$	OS
45	Squalene	22.884	11.84	$C_{30}H_{50}$	Triterpenoids
46	Phytol	24.788	0.38	$C_{20}H_{40}O$	Diterpene

MH=monoterpene hydrocarbon; OM=oxygenated monoterpene ; FA=fatty acid;
SH=sesquiterpene hydrocarbon; OS=oxygenated sesquiterpene; OH: Oxgenated hydrocarbon.

Table (2). The high compounds in *Ocimum sanctum.,* with biological activity:

Compounds	%	Medicinal uses and biological activity	References
Methyl eugenol	27.24	anti-inflammatory, Nematodes, Antifeedant and Insects.	(Desai et al., 1996; Park et al., 2007)
Squalene	11.42	Antioxidant and Antitumor activities.	(Saint-Leger et al., 1986; Yano, 1987)
α-bergamotene	9.83	Antiepileptic and anti-inflammatory activity.	(Kohno et al., 1995)
Linalool	8.42	Antibacterial, antifungal and Anti-inflammatory.	(Desai et al., 1996)
Fenchyl acetate	7.56	Food flavour (chewing gum, toothpaste).	(Sabogal-Guáqueta et al., 2016)
Eucalyptol	5.25	Insecticidal, flavorings, fragrances, and cosmetics.	(Sfara et al., 2009)

CONCLUSIONS

A higher percentage of sesquiterpenes was found in the *O. sanctum* n-hexane extract which might be used in the pharmaceutic industry, some compounds found in *O. sanctum.*, aerial parts are toxic such as phytol, which requires caution. To establish therapeutic uses of *O. sanctum* in modern medicine, scientists and researchers must study the pharmacological effects of different extracts on different body systems.

Duality of interest: The authors declare that they have no duality of interest associated with this manuscript.

Author contributions : Contribution is equal between authors.

Funding: No specific funding was received for this work.

REERENCES

Desai, K., Wei, H., & Lamartiniere, C. (1996). The preventive and therapeutic potential of the squalene-containing compound, Roidex, on tumor promotion and regression. *Cancer letters, 101*(1), 93-96.

EL-Kamali, H. H., & EL-Amir, M. Y. (2010). Antibacterial activity and phytochemical screening of ethanolic extracts obtained from selected Sudanese medicinal plants. *Current Research Journal of Biological Sciences, 2*(2), 143-146.

Hassanpouraghdam, M. B., Hassani, A., & Shalamzari, M. S. (2010). Menthone-and estragole-rich essential oil of cultivated Ocimum basilicum L. from Northwest Iran. *Chemija, 21*(1), 59-62.

Hosseinzadeh, S., Jafarikukhdan, A., Hosseini, A., & Armand, R. (2015). The application of medicinal plants in traditional and modern medicine: a review of Thymus vulgaris. *International Journal of Clinical Medicine, 6*(9), 635-642.

Jirovetz, L., Buchbauer, G., Stoyanova, A., & Balinova, A. (2001). Analysis, chemotype and quality control of the essential oil of a new cultivated basil (Ocimum basilicum L.) plant from Bulgaria. *Scientia Pharmaceutica, 69*(1), 85-89.

Khair-ul-Bariyah, S. (2013). Comparison of the Physical Characteristics and GC/MS of the Essential Oils of Ocimum basilicum and Ocimum sanctum. *International Journal of Scientific Research in Knowledge, 1*(9), 363.

Kohno, Y., Egawa, Y., Itoh, S., Nagaoka, S.-i., Takahashi, M., & Mukai, K. (1995). Kinetic study of quenching reaction of singlet oxygen and scavenging reaction of free radical by squalene in n-butanol. *Biochimica et Biophysica Acta (BBA)-Lipids and Lipid Metabolism, 1256*(1), 52-56.

Mondello, L., Zappia, G., Cotroneo, A., Bonaccorsi, I., Chowdhury, J. U., Yusuf, M., & Dugo, G. (2002). Studies on the essential oil ‐ bearing plants of Bangladesh. Part VIII. Composition of some Ocimum oils O. basilicum L. var. purpurascens; O. sanctum L. green; O. sanctum L. purple; O. americanum L., citral type; O. americanum L., camphor type. *Flavour and fragrance journal, 17*(5), 335-340.

Mustafa, A. A., & El-kamali, H. H. (2019). Chemical composition of Ocimum americanum in Sudan. *Res. Pharm. Health Sci, 5*(3), 172-178.

Mustafa, A. A., & El-kamali, H. H. (2020). Proximate and phytochemical constituents of in Sudan Ocimum sanctum.

Nahak, G., Mishra, R., & Sahu, R. (2011). Taxonomic distribution, medicinal properties and drug development potentiality of Ocimum (Tulsi). *Drug Invention Today, 3*(6).

Omer, H. A., Mustafa, A. A., Kabbashi, A. S., & Taher, A. R. (2024). Antimicrobial, Antioxidant Activities and total phenolics contents of Portulaca oleracea., crude extracts, Sudan.

Park, I.-K., Kim, J., Lee, S.-G., & Shin, S.-C. (2007). Nematicidal activity of plant essential oils and components from ajowan (Trachyspermum ammi), allspice (Pimenta dioica) and litsea (Litsea cubeba) essential oils against pine wood nematode (Bursaphelenchus xylophilus). *Journal of nematology, 39*(3), 275.

Periyasamy Ashokkumar, P. A., Rajkumar, R., & Mahalingam Kanimozhi, M. K. (2010). Phytochemical screening and antimicrobial activity from five Indian medicinal plants against human pathogens.

Sabogal-Guáqueta, A. M., Osorio, E., & Cardona-Gómez, G. P. (2016). Linalool reverses neuropathological and behavioral impairments in old triple transgenic Alzheimer's mice. *Neuropharmacology, 102*, 111-120.

Sahreen, S., Khan, M. R., Khan, R. A., & Hadda, T. B. (2015). Evaluation of phytochemical content, antimicrobial, cytotoxic and antitumor activities of extract from Rumex hastatus D. Don roots. *BMC complementary and alternative medicine, 15*, 1-6.

Saint-Leger, S., Bague, A., Cohen, E., & Chivot, M. (1986). A possible role for squalene in the pathogenesis of acne. I. In vitro study of squalene oxidation. II. In vivo study of squalene oxides in skin surface and intra-comedonal lipids of acne patients.

Sfara, V., Zerba, E., & Alzogaray, R. A. (2009). Fumigant insecticidal activity and repellent effect of five essential oils and seven monoterpenes on first-instar nymphs of Rhodnius prolixus. *Journal of medical entomology*, *46*(3), 511-515.

Yano, K. (1987). Minor components from growing buds of Artemisia capillaris that act as insect antifeedants. *Journal of Agricultural and Food Chemistry*, *35*(6), 889-891.

Al-Mukhtar Journal of Basic Sciences 22 (3): 166-182, 2024
Doi: https://doi.org/10.54172/9f44gj91

Research Article

Open Access

Dynamic Simulation Model for Smart Irrigation Using IOT and MCU Technologies

Abdalla M. Elsheikhi[1], Mohammed S. Saleh[2]* and Nadir S. Nabous[3]

[1] Department of Information Technology, Benghazi University, Al- Marj Branch, Libya.

[2]***Corresponding author:** Mohammed.saad@omu.edu.ly
Department of Computer Sciences, Omar Al-Mukhtar University, Libya.

[3] National research center for Tropical and Transboundary diseases, Qasr Bin Ghasher, Libya.

Received:
14 July 2024

Accepted:
14 October 2024

Publish online:
31 December 2024

Abstract
The efforts and projects of countries around the sector are coming together with the intention of growing the productivity of agriculture and productivity rates by combining numerous new technologies to enhance and develop the tactics utilized in agriculture. The top priority that requires attention is improving irrigation efficiency in agriculture, because of its unparalleled importance in maintaining sustainable agricultural production. This study suggests a novel approach to lower the amount of water used for soil irrigation, i.e., preserve water and manage water resources as well, which has the potential to effectively increase agricultural sustainability and ensure food security. In fact, the study embraces the concept of 'Smart Agricultural' and the integration of advancing agricultural technologies. Genuinely, the proposed system is built on embedded cutting-edge tools; including the 'Internet of Things' (IoT) and the 'Micro-Controller Unit' (MCU). It is worth mentioning that the working mechanism of the aforesaid developed system, which operates automatically through the embedded MCU or remotely via IoT, is based on the idea that the sprinklers activate when the water level falls below (5) cm meanwhile is cut off when it surpasses (25.0) cm. additionally, the developed system can determine and approve whether the networked devices, IoT components, and MCU can function properly.

Keywords: Smart Agriculture, Smart irrigation System, Internet of Things (IoT), Micro-Controller Unit (MCU), Water Security, Water conservation.

INTRODUCTION

The growing worldwide population and water scarcity, according to (Pathmudi, et al., 2023), make water management in agriculture a crucial concern. Although they have been around for a while, traditional irrigation methods are frequently wasteful and inefficient. in the same vein, (Vadivu, et al. 2023) indicated that crop irrigation can be done more effectively and efficiently using smart irrigation systems, which make use of the newest technological advancements. This literature review's objective is to investigate the body of knowledge regarding intelligent irrigation systems and how they affect the agriculture industry. The significance of water management in agriculture is covered in the introduction of the review. From there, topics include the creation of smart irrigation methods, their elements, advantages, and effects on the atmosphere and the farming industry. In addition to being one of the most important resources for producing food, agriculture contributes significantly to the Gross Domestic Product, which powers any country's economy. However, there are a

number of problems with traditional agricultural practices, including significant water waste during field irrigation, reliance on non-renewable energy sources, and resource constraints in terms of time, money, and labor. Today, everything is smart, thus for the country to prosper, the agriculture industry needs to be developed strategically (Kumar, Kumar & Sharma, 2017).

In the same manner, (Vadivu, et al. 2023) said: “The agricultural sector plays a significant role in the economy of many countries, and irrigation is a critical component of successful agriculture. However, traditional irrigation methods can be time-consuming and labor-intensive, and often result in the over or under-watering of crops, which can negatively impact crop yields. To overcome these challenges, smart irrigation systems have been developed to assist farmers in managing their crops and increasing their yield” (Vadivu, et al., 2023: p. 196).

In compliance with (Cui,. 2021), a smart irrigation system is composed of numerous components, such as sensors, controllers, communication gadgets, and client interfacing. Soil dampness sensors are among the foremost vital components of clever water system frameworks. These sensors evaluate the dampness level of the soil and offer information that helps in deciding how much water the plants require. Sensors for sun oriented radiation, temperature, and stickiness are additional components that may be consolidated into brilliantly water system frameworks. Pursuant to (Barriga, et al., 2022), the controller, which modifies the system in response to data collected by the sensors, is another important component of smart watering systems. Data from sensors, controllers, and user interfaces are transmitted over wireless networks or cellular devices. The user interface is the component of the system that enables users to view, interact with, and change system settings as needed. Water, with accordance to (Chamara, et al., 2022) is a resource that crops require to flourish, and managing water resources well is key to getting the best crop yields. More food must be produced with less water due to the world's expanding population. As reported by (Fernando, et al., 2017), According to the Food and Agriculture Organization (FAO), agriculture consumes around 70% of all water consumed globally, and this figure is expected to rise as the world's population grows. As a result, agriculture's efficient use of water is critical to guaranteeing food security and meeting the rising population's food needs.

Besides, food security is highly reliant on agricultural activity to drive the world economy. However, this activity is in great danger due to climatic changes and improper use of irrigation techniques. Consequently, the lives of numerous individuals worldwide are in jeopardy. In light, this paper proposes a smart irrigation system based on the integration of new technologies.

Actually, compared to conventional irrigation systems, smart irrigation systems provide a more effective and efficient means of irrigating crops. In order to maximize irrigation schedules, these systems gather and analyze data from a variety of sensors using cutting-edge technologies, including the Internet of Things. Increased agricultural yields, lower labor costs, less water waste, and better water efficiency are just a few advantages of using smart irrigation systems. Preserving water supplies through The deployment of smart irrigation systems will improve crop quality, benefiting the agricultural business. As a result, smart irrigation systems have the potential to revolutionize how we irrigate crops and provide food security for the expanding global population (Junior, et al., 2023; Delpiazzo, et al., 2023).

The development of smart irrigation systems, as emphasized by (Zamani, et al., 2022; Mahbub, et al., 2021), has been fueled by technological advancements, mainly in the field of IoT (Internet of Things). Data from a range of sensors can be gathered and analyzed by IoT-based systems to optimize irrigation systems. Soil-based and weather-based smart irrigation systems are the two main

categories. Weather-based systems employ weather forecasts to change irrigation schedules, whereas soil-based systems use soil moisture sensors to determine when and how much water to use.

Smart irrigation systems offer numerous benefits over traditional irrigation systems, including reduced labor costs, decreased water waste, and increased agricultural output. They consume less water as well. Smart irrigation systems use less water by only delivering water when needed since they have sensors that detect the soil's moisture content. Agricultural harvests are also increased when plants obtain the proper sum of water for growth (Ashlock, 2022).

(Zamani, et al., 2022; Mahbub, et al., 2021) announced that Smart Irrigation Systems (SIS) can save labor expenses because they require less maintenance and monitoring than traditional systems. Intelligent irrigation systems have the ability to benefit both the environment and the agricultural economy. Smart irrigation systems can assist conserve water resources by decreasing water wastage, which is especially important in places with limited water supplies. Furthermore, (Chinasho et al., 2023) noted that by reducing the amount of nutrients and chemicals that leak from the soil, smart irrigation systems can reduce the requirement for fertilizers and pesticides since they allow for precise water distribution. Into the bargain, (Sangaiah, et al., 2023) pronounced that water sources like rivers and lakes may be maintained clean by doing this. The agriculture industry can increase crop yields with the usage of smart irrigation systems, which is significant for assembly the food requirements of the assembling population.

Intelligent irrigation systems, as emphasized by (Katimbo, et al. 2023), can improve crop quality by providing the appropriate quantity of water and nutrients, which can consequence in food that tastes better and is higher in nutrients. This can also raise the quality of the food produced. Higher farm earnings and a more sustainable agriculture sector overall could arise from this.

In this paper, the significance of simulation tools within the context of smart irrigation systems is investigated. It also explored their role in dataset generation, model testing, and validation. As resulting the paper provides a description of a proposed model for simulating a smart irrigation management system using the most recent release of Cisco Packet Tracer. The simulation setup allows for the activation of devices based on certain conditions. It also suggests future uses for the simulation model, such as testing and evaluating a range of agricultural applications. Numerous research works address the advantages of intelligent irrigation systems. These systems optimize water utilization in agriculture through the use of sensors and Internet of Things technology, improving crop quality and quantity. In order to increase irrigation efficiency in smart agriculture, (Gamal, et al. 2023) conducted a review of intelligent irrigation control and monitoring systems. The scheduling and control of irrigation through monitoring techniques have been the foundation of this study. Additionally, a discussion about prospective pathways for future research based on study gaps has been scheduled. It is suggested in this context that open fields be investigated in conjunction with a discrete forecasting control system that uses a combination of soil-based, weather-based, and plant-based monitoring techniques. Open-area agricultural irrigation systems, as opposed to environmentally controlled agriculture research, have unknowns that must be investigated. (Gamal et al. 2023) stated that future research would focus on the development of process dynamics approaches for irrigation systems, as well as the implications of intelligent management and monitoring tactics on irrigation output in open field agricultural systems. In order to address the issues surrounding the design and construction of an Internet of Things (IoT) - based autonomous irrigation system that will greatly reduce the amount of time and money farmers must spend; (Kumar et al,. 2023) conducted a study. There will be less human interaction in the fields. Soil moisture sensors monitor variations in soil moisture, and Internet of Things technology is used to automate irrigation. Be-

cause it is so affordable, the suggested technique is best suited for developing nations. The sensor identifies and notifies the node MCU, which turns on the motor, based on the moisture content of the soil. The motor turns off by itself when the plants get enough water. Through his mobile device, the user will receive an alert on the moisture satisfied of the soil. Kumar and colleagues (2023) concluded that their campus has adopted the suggested smart irrigation system, which uses less water and energy. In the same vein, and in order to avoid wasting water resources, (Das et al., 2023) carried out a study with the goal of automating the entire irrigation system in terms of the crop's water requirements by monitoring the soil's moisture content and climate.

The article also discusses how IoT technology allows for remote control of the irrigation system from home. As a result, the system will offer easy access to it and shield the farmer from intense heat and cold. In fact, Das, et al's study sought to improve a Smart Irrigation System using IoT (Internet of Things) technology. According to Das et al., agriculture is one of the most essential resources for producing food and, because it contributes to GDP, is essential to maintaining the stability of any country's economy. However, there are a number of problems with traditional agricultural practices, including significant water waste during field irrigation and reliance on non-renewable resources like petroleum coal, time, money, and human resources, among others. With the rising need for non-renewable energy sources, automation, and digitization, SMART agriculture is seen as the nation's most promising industry for food production (ibid).

In order to avoid wasting water resources, Kumar, (Kumar, and Sharma's, 2017) study focused on creating a Smart Irrigation System using IoT technology. The goal was to automate the entire irrigation system and provide crops with the necessary amount of water by monitoring soil moisture and climate conditions. According to Kumar, Kumar, and Sharma, farmers will benefit greatly from the new irrigation system as well. It will get easier and more pleasant to irrigate distant areas from home. Furthermore, it will reduce the farmer's time traveling to and from the field in addition to shielding them from the intense heat and cold.

MATERIALS AND METHODS

Simulation Framework: Packet Tracer 7.3, a Cisco Systems tool, is used for modeling smart irrigation systems. It supports network creation, configuration, and troubleshooting. Its user-friendly interface encourages users to learn its functionalities using help documents. It offers a virtual lab for network building practice, network visualization, and cabling skills enhancement. It also ropes IoT device integration for creating smart home networks (Official Packet Tracer Tutorials, 2024). The services provided by the current design include managing the water supply, monitoring field conditions, and making necessary decisions for the virtual agricultural field based on data analysis. The system allows for manual and remote operation via tablet/PC or Smartphone, potentially improving water usage and energy savings. It outlines the steps taken to design and implement the smart irrigation management simulation model. These steps include the selection of smart devices (sensors and actuators), configuration of the microcontroller MCU, gateway, interconnecting devices, and the development of the web interface.

Network Topology: Figure 1 depicts the system design, which consists of three levels. Misra (2021) distinguishes three layers: sensing and actuating, distant processing and service, and application. The functionalities of the various levels of this system are as follows:

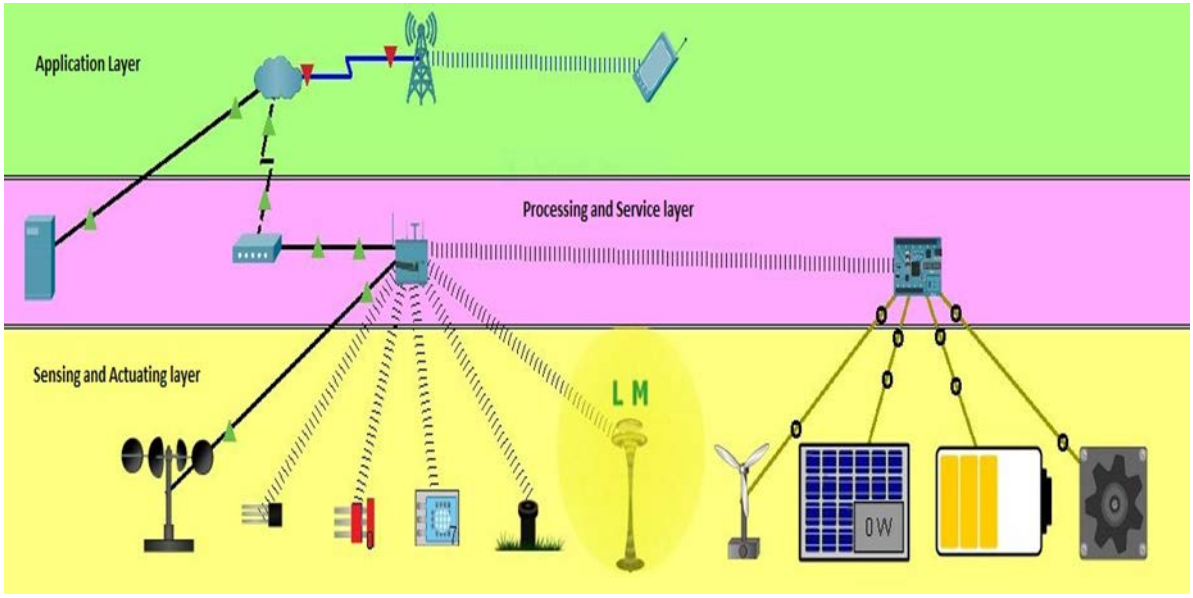

Figure (1). The system design consists three layers

At the sensing and actuating level: various sensor nodes are arranged in the field to measure soil moisture and water levels. Actuators, such as lawn sprinklers and solenoid valves, are installed at this level. Wi-Fi communication modules are used for data collection and irrigation activation as needed.

Processing and Service Layer: Serves as an intermediary, storing and providing access to processed data for future use and remote access by authorized users.

Application Layer: Allows operators to display and control irrigation through cell phones, and an IoT monitor application.

The interconnection of these devices is facilitated by an application programming interface (API), a computing interface that outlines interactions between many software mediators. It provides a platform for the devices to operate and integrates them, fetching information through the cloud (WAN) (Official Packet Tracer Tutorials, 2024). The APIs employed in our work are designed to enhance the functionality of the devices.

The figure 1 illustrates a system consisting of IoT components and interconnecting devices, all connected to the internet. A smartphone is employed for real-time monitoring of field devices. Wireless devices, such as a Home Gateway and IoT devices equipped with wireless modules, are utilized to implement the Wireless Sensor Network (WSN). Table (1) below includes IoT components that are utilized in the proposed network.

These components of IoT can be managed remotely through the Registration Server. Sensors or actuators are registered with the Home Gateway, which provides wireless connectivity. By connecting to the Home Gateway using a web browser application on a PC, devices can be controlled locally. For remote monitoring, configuration, or programming, devices could be connected to a remote IoE Registration Server located on a server. The IoT Registration Service is activated by default via the Services tab on the IoE page of the server device.

Table (1). IoT's components used in WSN

Component	Use
Humidity Monitor	Checks environment values to find the humidity. Registration Server Compatible.
Water Sensor	Senses water level in the soil
Temperature Monitor	Detects and displays the temperature Displays result in a registration server.
Water Level Monitor	Water level detection Registration Server Compatible
Lawn Sprinkler	Raises the water level Registration Server Compatible
Solar Panel	Detects and views the amount of power being generated.
Wind Turbine	Generates electric power
Battery	Shows the percentage of charge left in the battery Registration Server Compatible
DLC100 Home Gateway	Enables wireless interconnecting, Allows end users to monitor, protect and manage their homes using a smartphone, tablet or PC.
Microcontroller (MCU-PT)	Connects and controls things such as sensors and actuators
Motor	Increase or decrease the power controls the engine speed.

Operation of IoT Devices using MCU: The Microcontroller Unit (MCU) is a board used for interconnecting smart things like sensors and actuators. It provides a programming environment to manage the things connected to it. This is crucial for the operation of the hardware as shown in Fig.2. The primary function of this MCU is to activate the system, specify actions, display the water level on the LCD, activate sprinklers, and support detection to achieve specific goals.

The programming for IoT devices, including the water level monitor and lawn sprinklers, was done by Integrated Development Environments (IDEs) specific to each device. Writing code and uploading it to the board were straightforward tasks.

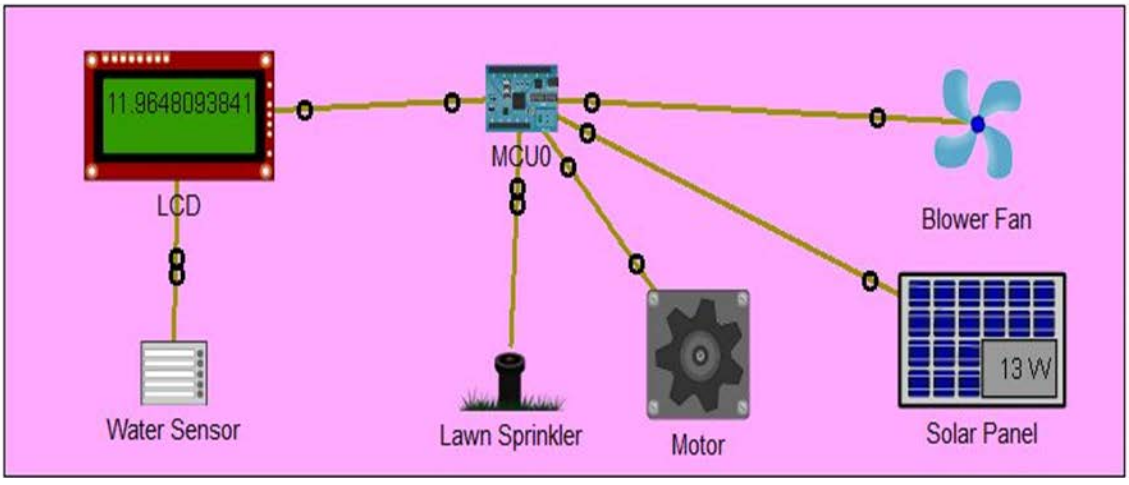

Figure (2). Integrated Development Environments

RESULTS

The proposed architecture on which the simulation is applied, stands for an agricultural field that is divided into subfields as seen in (Figure 3)

Figure (3). An agricultural field that is divided into subfields

The IoT irrigation method is reasonably segmented into three zones: the agricultural field sensors and actuators, Internet service provider servers' central office server and IoT Registration Server, and end-user devices, as illustrated in Figure 4. Upper-side sprinklers, water level monitor, humidity monitor, temperature monitor and solar panel are wirelessly connected to the home gateway.
The home gateway uses a DSL connection to send data to the cloud. This data is stored on servers and can be accessed by end-user devices via cell towers and wireless networks. The home gateway's internet settings include the wireless Service Set Identifier (SSID) and password. All wireless devices utilize the same SSID, password, and DHCP default settings.

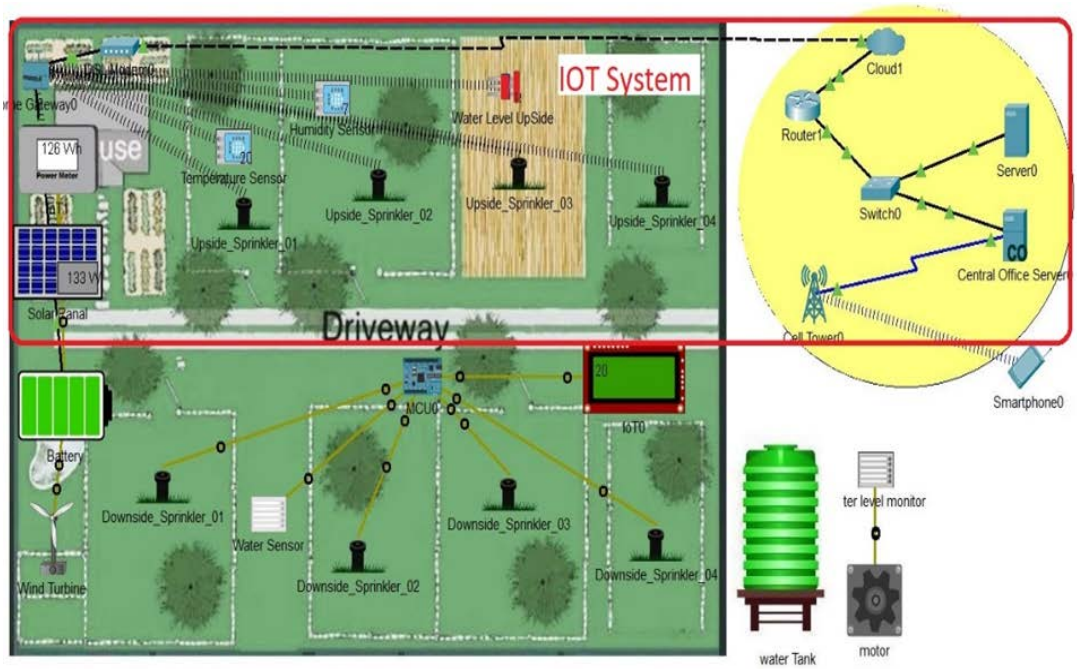

Figure (4). An agricultural field sensors and actuators, Internet service provider servers' central office server and IoT Registration Server, and end-user devices.

IoT devices are remotely connected to the IoT registering server. This connection allows operators to check the position of the IoT devices from an IoT browser site as shows in (Figure 5).

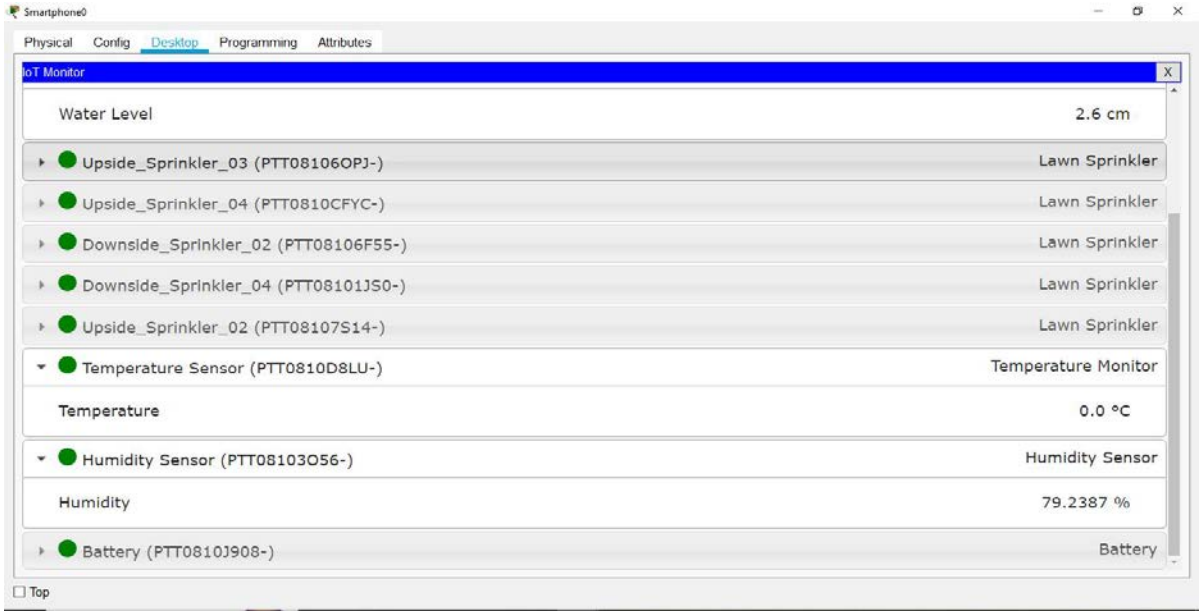

Figure (5). Checking the status interface of the IoT devices

For setting irrigation water level rules, the researchers used Python programming. Figure 6 shows the flawed chart of irrigation water level processing. This processing is includes 4 steps as following:

Initially, the sensors detect their particular parameters based on pre-set conditions.
The sensed values which are analog such as water Level (A0) are then digitized (x).
The current analog water level A0 from sensor, which gives values from 0 to 255, which will be mapped to 0 to 20 cm using the Interpolation formula (where X means original water level):

$$x = 0 + \frac{(A0 - 0) * (20 - 0)}{(255 - 0)}$$

$$x = \frac{20 * A0}{255}$$

These formatted values are subsequently supplied to the actuators. The actuators are triggered based on the input received, adhering to predefined situations, as depicted in Figure 4 below. In an irrigation system, the sprinklers are activated once the water level falls below 5 cm and turn off when the water level exceeds 25.0 cm.

The homepage shows a list of smart gadgets, displays their status, and allows for remote interaction with them. Logical interactions between smart devices can be set up while connected to the main IoT portal. These interactions are based on predetermined conditions, such as activating the sprinkler when the water level in a specific region drops, or lowering the water level in the tank that powers the solenoid valve, as seen in figure 7 below.

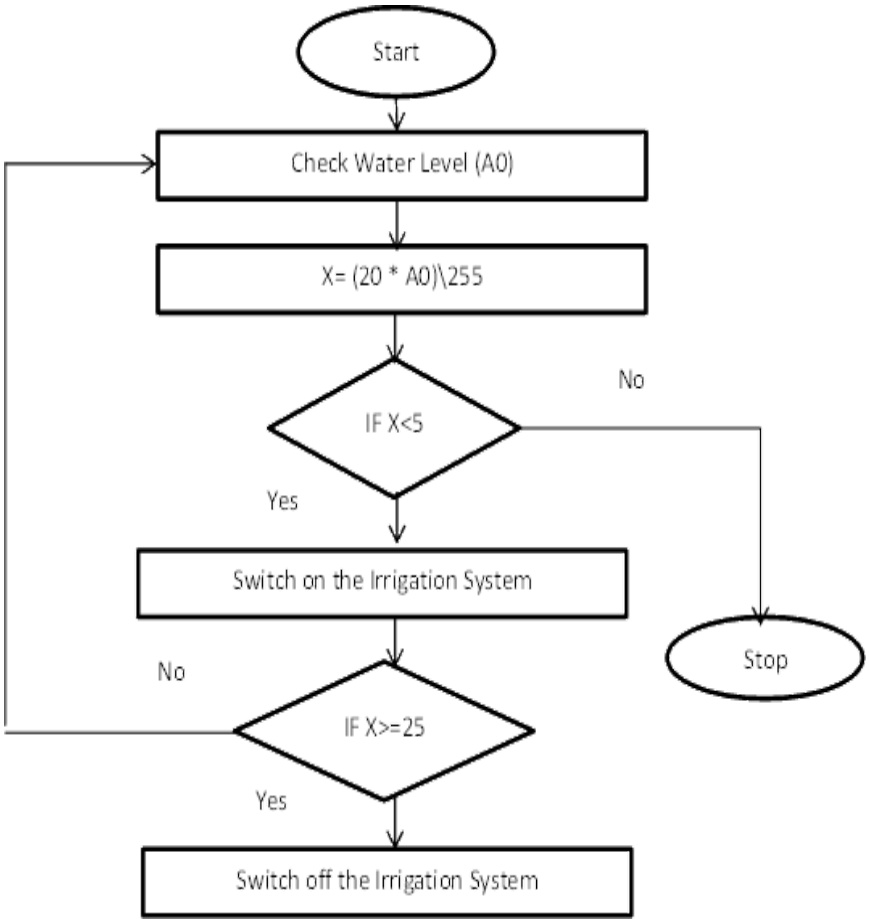

Figure (6). Flaw chart of the flaw chart of irrigation water level processing

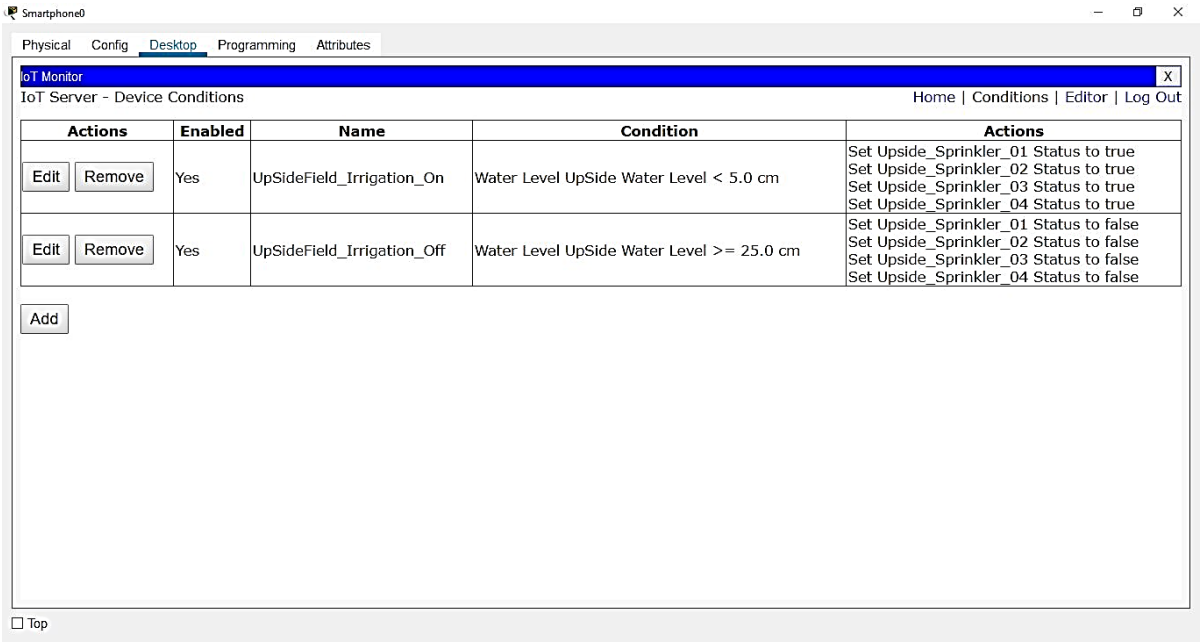

Figure (7). The rules base interface for water level in the tank

Network Interconnection: The network Gateway serves as a central hub for all devices within the system, establishing wireless network links. It enables the interconnection between a Local Area Network (LAN) and a Wide Area Network (WAN), using a DSL modem. This is the point of convergence for all devices and Internet of Things (IoT) components as indicated. In this configuration, a single Home Network Gateway was set up. The assigned IPv4 address is 192.168.25.1, which is typically the default IP address for the home gateway, and the subnet mask is set to 255.255.255.0. The authentication process is stopped while the Service Set Identifier (SSID) is renamed to "Farm-Gateway", aligning with the server's username as depicted in (Figure 8).

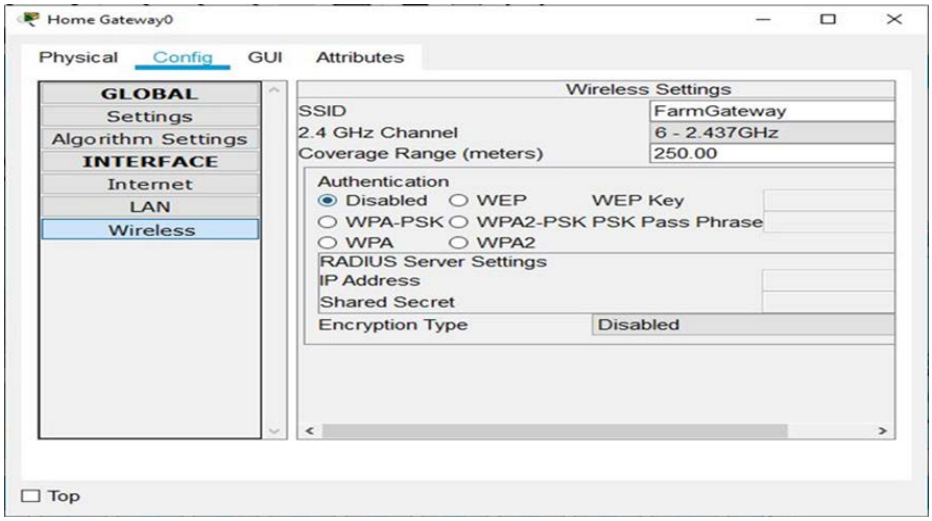

Figure (8). The Farm gateway interface

In this project, all IoT devices are connected to the home gateway with the server-generated username and password. The IoT server is given a static IP address that remains consistent, removing the need to reconfigure devices with new IoT server IP addresses, as shown in figure 9. It offers DHCP services, IoT, and DNS functionality. These features enhance the IoT simulation's backend intelligence and make it easier to host the IoT webpage, from which end users may connect and interact with the smart irrigation system. The DNS service transforms the IoT homepage URL into the IoT server IP address.

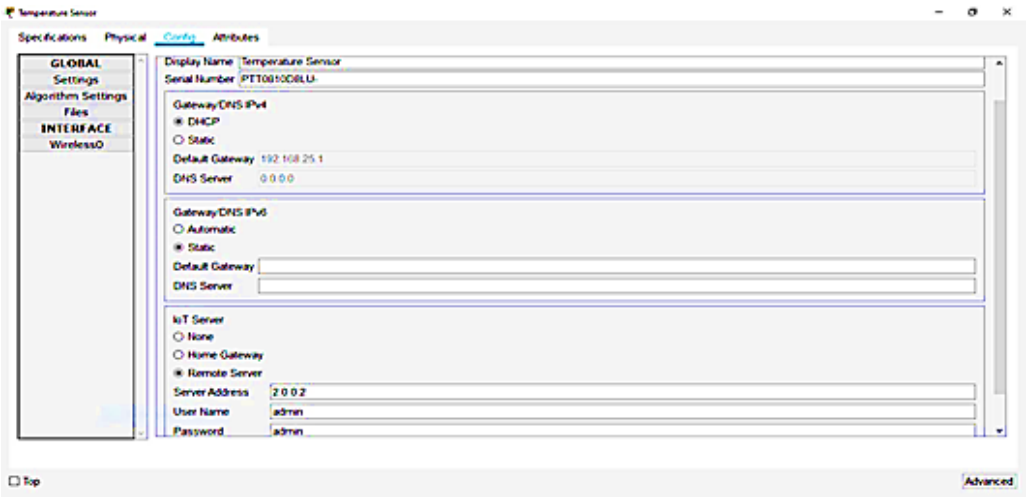

Figure (9). DHCP, IoT and DNS services interface

IoT is also used in smart irrigation systems which can enhance agricultural productivity while conserving water resources. By leveraging data-driven perceptions, these systems contribute to sustainable and efficient farming practices. Smart irrigation management systems use wireless sensor networks (WSN) and the Internet of Things (IoT) to optimize water use efficiency in the agricultural sector (Difallah, 2018**;** Misra, 2021). The systems rely on sensors to provide simultaneous information on environmental situations such as temperature and soil moisture levels, allowing for the optimization of irrigation schedules and well-organized use of water resources. The integration of wireless sensor networks (WSN) and the Internet of Things (IoT) can address these challenges by providing continuous real-time information on soil moisture, temperature, weather conditions, and other parameters to optimize irrigation schedules. This allows for efficient water use and can also reduce labor and energy costs for farmers. Moreover, it can help to prevent over-irrigation and water waste and reduce the negative ecological impact of traditional irrigation on soil fertility and groundwater depletion. Additionally, these technologies can also help to enhance crop yield and the quality of crops grown (Khan, 2013). Simulation tools are essential for testing and evaluating system performance during the development of smart home systems (Dogman, 2020). According to (Sadek, 2023), simulation tools like Cisco Packet Tracer can be used to test and assess a range of smart home applications, including energy management, health monitoring, and home security (Gwangwava, 2021) discusses an industrial use case for an IoT-based smart stimulant manufacturing vegetable that was implemented using Cisco Packet Tracer. Notably, simulation tools have emerged as valuable assets in this domain. They allow researchers to create synthetic environments for testing and assessing a wide range of smart home applications, including energy management, health monitoring, and home security. Various implementations of smart irrigation systems are discussed, such as automated drip irrigation systems, remote monitoring systems, and intelligent irrigation management systems.

Traditional irrigation practices face countless challenges such as water waste due to over-irrigation, lack of real-time monitoring and control of water usage, and inefficient water management. It is a labor-intensive (Khan, 2013). Furthermore, the data on soil moisture, weather conditions, and other factors relevant to irrigation can create more challenges. This can lead to lower crop yields and higher costs for farmers (Suba, 2015).

In this paper, the significance of simulation tools within the context of smart irrigation systems is investigated. It also explored their role in dataset generation, model testing, and validation. As resulting the paper provides a description of a proposed model for simulating a smart irrigation management system using the most recent release of Cisco Packet Tracer. The simulation setup allows for the activation of devices based on certain conditions. It also suggests future uses for the simulation model, such as testing and evaluating a range of agricultural applications.

DISCUSSION

Figure 10 illustrates how Cisco Packet Tracer features move between real-time and simulation modes. The real-time mode enables the establishment of the underlying network, the connecting of IoT devices, and the construction of IoT backend logic. However, only the simulation mode allows for validation of the network communication layer between devices. This mode simulates packet traffic between nodes and devices to verify connection, routing protocols, and other network logic. It aids in the physical visualization and debugging of any network, such as configuring pings or more complicated packets between nodes.

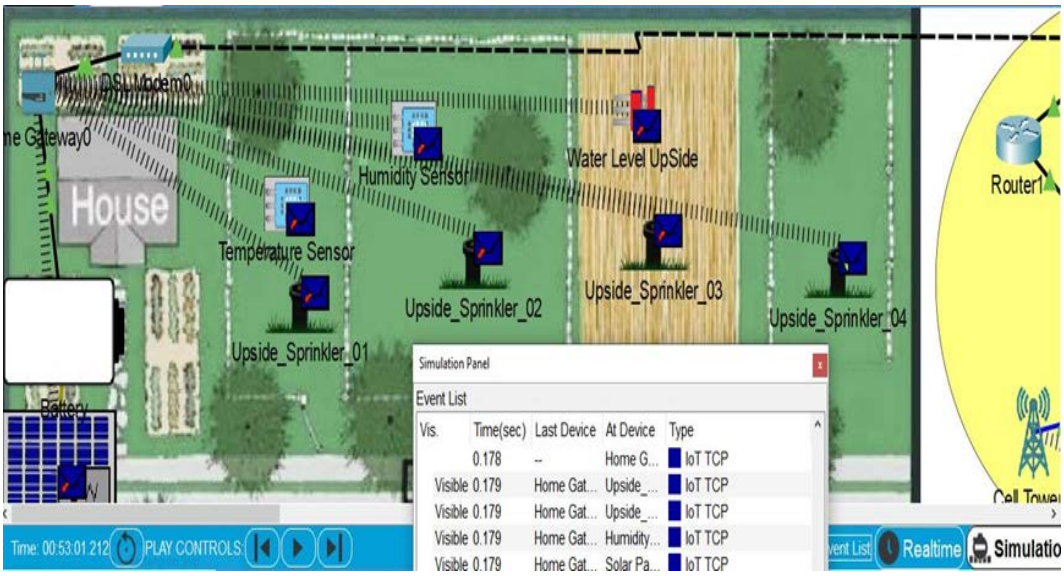

Figure (10). Run real-time and simulation modes**.**

Network Echo Test : This examination is conducted to confirm if the interconnected devices and IoT components are part of the same WSN/internet, demonstrating their ability to interact. As per the above Network Echo Test, all IoT devices and other network elements are connected and work well. It is also possible to control the sprinklers and water valve locally through the digital and analog ports using a microcontroller. The microcontroller is wired to the lower-side sensors, LCD and water Level sensor. The MCU sends an on or off command to the sprinklers, depending on the water level. Additionally, it's probably to control the lower-side sprinklers locally through the digital ports, as illustrated in the figure below.

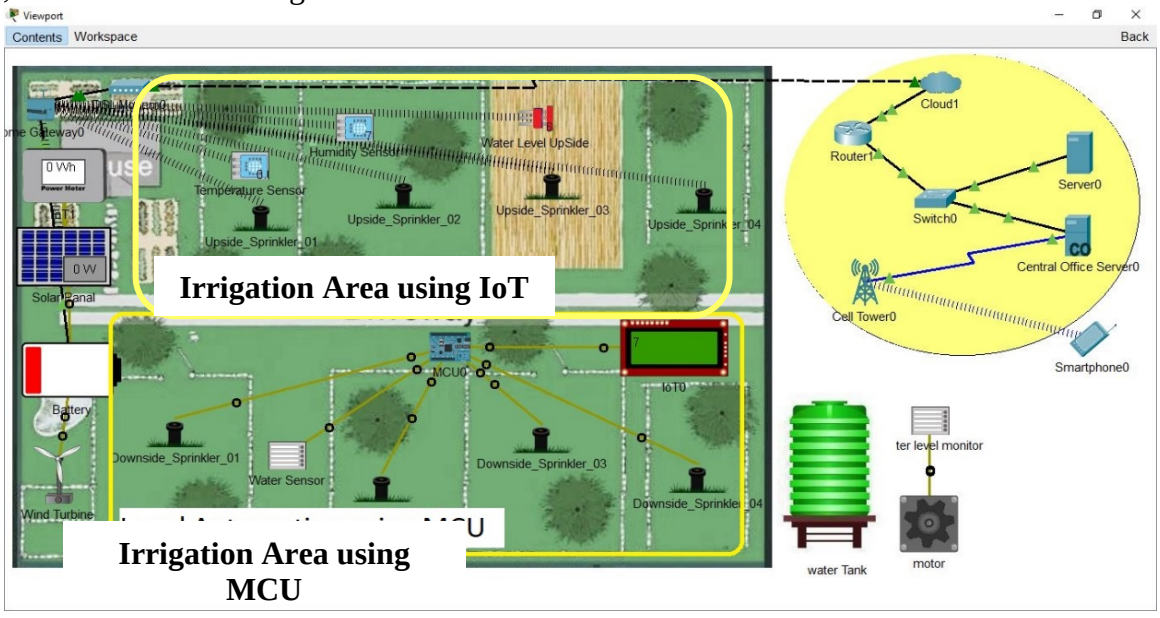

Figure (11). The developed system for smart irrigation farm

The developed simulation of the smart irrigation system has been tested and worked successfully. This system can be used now for real-time monitoring and control of the actuators, ensuring quality, safety, and efficiency. As a result, all devices within the system are monitored through a

smartphone as IoT or MCU systems. Both developed systems show a significant outcome as seen in the following results:

Water Level Monitoring: The sprinklers are activated when the water level falls below 5 cm and are turned off when the water level exceeds 25.0 cm.

Renewable Power Energy System: This system is linked to the cloud through the home gateway. The solar panel converts sunlight, and the wind turbine converts wind energy into electricity. This electricity is stored in a battery connected to all devices. The end user can monitor the percentage of power.

Water Level in Water Tank System: A water level sensor activates a motor that pumps water into the tank in an efficient way. As seen both developed systems have been worked efficiently. However, regarding start time speed we have seen the MCU always starts first by few seconds before IoT.

CONCLUSION

The present study suggested a novel approach to lower the amount of water used for soil irrigation, i.e., preserve water and manage water resources as well, which has the potential to effectively increase agricultural sustainability and ensure food security. In fact, the study embraces the concept of 'Smart Agricultural' and the integration of advancing agricultural technologies. In light of the foregoing, the study introduced a 'Smart Irrigation System' that was developed by the researchers. Genuinely, the proposed system is built on embedded cutting-edge technologies; including the 'Internet of Things' (IoT) and the 'Micro-Controller Unit' (MCU). It is worth mentioning that the working mechanism of the aforesaid developed system, which operates automatically through the embedded MCU or remotely via IoT, is based on the idea that the sprinklers activate when the water level falls below (5) cm meanwhile is cut off when it surpasses (25.0) cm. additionally, the developed system can determine and approve whether the networked devices, IoT components, and MCU can function properly. In conclusion, our research has effectively proven the establishment of a smart irrigation system using IoT technology. The technology is made to use less water, give corps the best irrigation possible, and enable remote operation and monitoring. Several sensors are used in the data collecting stage to get information on the water level. After processing this data, the system moves on to the control stage, where it makes the required adjustments, such as turning on and off pumps, to guarantee ideal irrigation. The user can monitor and control the machine remotely thanks to the remote operation stage. The system's ability to reduce water consumption and provide corps with adequate watering is demonstrated by the trial results. Because of the system's ability to use less water, irrigation will cost less overall. All things considered; the research's smart irrigation system has the ability to completely change how agriculture uses irrigation. The technology is economical and effective, saving water and enabling the best possible irrigation. Furthermore, the system may be conveniently and easily monitored and controlled thanks to the remote operation capability. Farmers, landscapers, and other industries that depend on irrigation stand to gain a great deal from this technology, which might ultimately lead to a more maintainable and effective usage of water resources.

Duality of interest: There is no conflict of interest.

Author contributions: A.B The authors developed the theoretical work, implemented the system, tested it, and followed the system rules to obtain the findings from simulations. C author performed the writing and structure of the manuscript.

Funding: No specific funding was received for this work.

REFERENCES

Ashlock, D. (2022). "Modeling Frameworks for Knowledge Engineering Approaches". *Journal of Computing and Natural Science, vol.2, no. (**1**), pp. 015-020, January 2022*. DOI:10.53759/181X/JCNS202202003 .

Barriga, J; Blanco-Cipollone, F; Trigo-Córdoba, E; García-Tejero, I; Clemente, P. (2022). "Crop-water assessment in Citrus (Citrus sinensis L.) based on continuous measurements of leaf-turgor pressure using machine learning and IoT". *Expert Systems with Applications, vol. 209, p. 118255, Dec. 2022*. DOI: 10.1016/j.eswa.2022.118255.

Chamara, N; Islam, D; G. Bai, G; Shi, Y; Ge, Y. (2022). "Ag-IoT for crop and environment monitoring: Past, present, and future". *Agricultural Systems, vol. 203, p. 103497, Dec. 2022*. DOI: 10.1016/j.agsy.2022.103497. Available online: https://www.sciencedirect.com/science/article/pii/S0308521X22001330

Chinasho, A; Bedadi, B; Lemma, T; Tana, T; Hordofa, T; Elias, B. (2023). "Response of maize to irrigation and blended fertilizer levels for climate smart food production in Wolaita Zone, southern Ethiopia". *Journal of Agriculture and Food Research, vol. 12, p. 100551, Jun. 2023*. DOI: 10.1016/j.jafr.2023.100551

Cui, X. (2021). "Cyber-Physical System (CPS) architecture for real-time water sustainability management in manufacturing industry". *Procedia CIRP, vol. 99, pp. 543–548, 2021*. DOI: 10.1016/j.procir.2021.03.074

Das, S; Saha, S; Podder. (2023). "Arduino Based Smart Irrigation System". *International Research Journal of Modernization in Engineering Technology and Science: Volume:05/Issue:01/January-2023*. Available online: https://www.researchgate.net/publication/367499767_ARDUINO_BASED_SMART_IRRIGATION_SYSTEM

Delpiazzo, E; Bosello, F; Dasgupta, S; Bagli, S; Broccoli, D; Mazzoli, P; Luzzi, V. (2023). "The economic value of a climate service for water irrigation. A case study for Castiglione District, Emilia-Romagna, Italy". *Climate Services, vol. 30, p. 100353, Apr. 2023*. DOI: 10.1016/j.cliser.2023.100353

Dholu, M and Ghodinde, K. (2018). "Internet of Things (IoT) for Precision Agriculture Application". *the 2nd International Conference on Trends in Electronics and Informatics ICOEI*, p. 4. DOI:10.1109/ICOEI.2018.8553720

Difallah, W; benahmed, K; Bounaama, F; Belkacem, D. (2018). "Intelligent Irrigation Management System". *International Journal of Advanced Computer Science and Applications: 9(**9**)*. DOI:10.14569/IJACSA.2018.090954

Dogman, A.m and Jewiley, M. (2020). "Design and Implement IoT Smart Home via Cisco Packet Tracer: Applications and Simulations". *Bright Star University - The Sixth International Con-*

ference - Smart Cities and State of the Map - Libya. Available Online: https://media.sotm.bsu.edu.ly/Content/Papers/G2/G2_4.pdf (*Accessed on: 20th, June, 2024*).

Fernando, E; Bandala, A; Gan Lim, L; Maglaya, A; Ledesma, N; Vicerra, R; Gonzaga, E. (2017). "Design of a fuzzy logic controller for a vent fan and growlight in a tomato growth chamber". Publisher: Institute of Electrical and Electronic Engineers **(**IEEE). *2017IEEE 9th International Conference on Humanoid, Nanotechnology, Information Technology, Communication and Control, Environment and Management (HNICEM)*, Manila, Philippines, 2017, pp. 1-5.
DOI: "https://doi.org/10.1109/HNICEM.2017.8269526"\t"_blank"10.1109/HNICEM.2017.8269526

Gamal, Y; Soltan, A.; Said, L.; Madian, H; Radwan, A. (2023). "Smart Irrigation Systems: Overview". *IEEE Access* 2023, *4*. Pp. 1-1. 10.1109. DOI: "http://dx.doi.org/10.1109/ACCESS.2023.3251655" \t "_blank" 10.1109/ACCESS.2023.3251655

Gautam, G., and Sen, B. (2015). "Design and Simulation of Wireless Sensor Network in NS2". *International Journal of Computer Applications*:113(16):14-16. DOI: "http://dx.doi.org/10.5120/19910-2018" \t "_blank" 10.5120/19910-2018

Gwangwava, N. and Mubvirwi, T. (2021). "Design and Simulation of IoT Systems Using the Cisco Packet Tracer". *Advances in Internet of Things*, ***11***, 59-76. DOI: "https://doi.org/10.4236/ait.2021.112005" \t "_blank" 10.4236/ait.2021.112005

Janitor, J., Jakab, F. and Kniewald, K. (2010). "Visual Learning Tools for Teaching/Learning Computer Networks: Cisco Networking Academy and Packet Tracer". *Sixth International Conference on Networking & Services, Cancun, 7-13 March 2010, 351-355*. Retrieved from: https://doi.org/10.1109/ICNS.2010.55

Junior, A; da Silva, T; Andrade, S. (2023). "Smart IoT lysimetry system by weighing with automatic cloud data storage". *Smart Agricultural Technology, vol. 4, p. 100177, Aug. 2023*. DOI: 10.1016/j.atech.2023.100177

Katimbo, A; Rudnick, D; Zhang, J; Ge, Y; DeJonge, K; Franz, T; Shi, Y; Liang, W; Qiao, X; Heeren, D; Kabenge, I; Nakabuye, H; Duan, J. (2023). "Evaluation of artificial intelligence algorithms with sensor data assimilation in estimating crop evapotranspiration and crop water stress index for irrigation water management". *Smart Agricultural Technology Journal, vol. 4, p. 100176, Aug. 2023*. DOI:10.1016/j.atech.2023.100176

Khan, R; Ali, I; Suryani, A; Ahmad , M; Zakarya, M. (2013). "Wireless Sensor Network Based Irrigation Management System for Container Grown Crops in Pakistan". *World Applied Sciences Journal 24* ***(8)***: 1111-1118, 2013.

Kumar, A; Kumar, A; Sharma, P. (2017). "Smart Irrigation System using IoT: SIS". *International Journal of Engineering Research and V6(06)*. DOI: "http://dx.doi.org/10.17577/IJERTV6IS060067"\t"_blank" 10.17577/IJERTV6IS060067

Kumar, S; Nagaraju, G; Rohith, D; Vasudevarao, A. (2023). “Design and Development of Smart Irrigation System Using Internet of Things (IoT) - A Case Study”. *Nature Environment and Pollution Technology Journal: 22(1):523-526*. DOI: "http://dx.doi.org/10.46488/NEPT.2023.v22i01.052" \t "_blank" 10.46488/NEPT.2023.v22i01.052

Mahbub, M; Hossain, M; Gazi, S. (2021). “Cloud-Enabled IoT-based embedded system and software for intelligent indoor lighting, ventilation, early-stage fire detection and prevention”. Computer Networks Journal: vol. 184, p. 107673, Jan. 2021. DOI: 10.1016/j.comnet.2020.107673

Misra, S; Mukherjee, A; Roy, A. (2021). "*Introduction to IoT"*. Cambridge University Press, 2021; ISBN, 110884295X, 9781108842952.

Osita, K. (2022). "IOT Based Smart Greenhouse: Using Packet Tracer Software". *Open Access Library Journal, (**9**),* 1-13. DOI: "https://doi.org/10.4236/oalib.1109535" \t "_blank" 10.4236/oalib.1109535

Pathmudi, V; Khatri, H; Kumar, S; Abdul-Qawy, A; Vyas, A. (2023). “A systematic review of IoT technologies and their constituents for smart and sustainable agriculture applications”. Scientific African Journal: vol. 19, p. e01577, Mar. 2023, DOI: 10.1016/j.sciaf.2023.e01577

Raut, S.. and Motade, S. (2021). "IOT Based Smart Irrigation System using Cisco Packet Tracer". *International Journal of Computer Sciences and Engineering: Vol. 9, Issue.2, February 2021*. DOI: https://doi.org/10.26438/ijcse/v9i2.1216. Available online at: ttps://www.ijcseonline.org/pub_paper/3-IJCSE-08461.pdf

Roy, S; Misra, S; Raghuwanshi, N; Roy, A. (2017). "A Smart Irrigation Management System using WSNs". *Indian patent granted on May 28, 2024 (Patent No. 539519) (Filed No. 201731031610, on September 6, 2017)*. RAetrieved from: https://ipindiaservices.gov.in/publicsearch

Sadek, R., & Khalifa, A. (2022). "IoT-Network Automation System Design and Implementation Simulation for Smart Home application". *Journal of Communication Sciences and Information Technology (JCSIT): VOLUME XX, 2022*. Retrieved from: https://jcsit.journals.ekb.eg/article_328556_47c49a85b831b227ef60bdff8c8b6034.pdf

Sangaiah, A; Rezaei, S; Javadpour, A; Zhang, W. (2023). “Explainable AI in big data intelligence of community detection for digitalization e-healthcare services”. *Applied Soft Computing, vol. 136, p. 110119, Mar. 2023*. DOI:10.1016/j.asoc.2023.110119

Sinaga, D; Tampubolon, G; Ndruru, I. (2024). "Implementation of a Smart Home Based on Internet of Things using CISCO Packet Tracer". *Journal Of Computer Networks, Architecture and High-Performance Computing: Vol. 6 (1)*. DOI: https://doi.org/10.47709/cnahpc.v6i1.3518"10.47709/cnahpc.v6i1.3518 .

Vadivu, S; Reddy, P; Rane, K; Kumar, N; Karthikayen, A; Behare, N. (2023). “An IoT-Based System for Managing and Monitoring Smart Irrigation through Mobile Integration”. *Journal of*

Machine and Computing 3(3). DOI: http://dx.doi.org/10.53759/7669/jmc202303018"\t"blank"10.53759/7669/jmc202303018

Varsha, T; Shrihari; Nagaraja, G.S. (2023). "IoT based a Smart Home Automation System Using Packet Tracer". *International Journal for Research in Applied Science& Engineering Technology (IJRASET): Volume 11, (1),* page. 7. DOI: https://doi.org/10.22214/ijraset.2023.48514.

Zamani, A; Anand, L; Rane, K; Prabhu,P; Buttar,A; Pallathadka,H; Raghuvanshi,A; Dugbakie, B. (2022). “Performance of Machine Learning and Image Processing in Plant Leaf Disease Detection”. Journal of Food Quality: Volume 2022, Article ID 1598796, 7 pages. Available Online: https://doi.org/10.1155/2022/1598796

Al-Mukhtar Journal of Basic Sciences 22 (3): 183-194, 2024
Doi: https://doi.org/10.54172/4y131d82

Research Article **Open Access**

A computational study to compare some plastic polymers with potassium bromide using density functional theory and UV-Visible spectroscopy

Boubaker M. Hosouna[1*], Omar Bay [2], Altayeb Alhoudairy [2]

[1,2] Department of Chemistry, Faculty of Science, Sebha University, Libya.

***Corresponding author:** bou.hosouna@sebhau.edu.ly
Department of Chemistry, Faculty of Science, Sebha University, Libya.

Received:
28 July 2024

Accepted:
05 December 2024

Publish online:
31 December 2024

Abstract
This study presents the value of computer simulation in a comparative analysis of some of the most common polymers (polyamide, polyethylene, and polycarbonate) used in the plastics industry. The introduction of density functional theory (DFT) has greatly facilitated the application of computational science to these materials, in addition to the calculation of UV-visible spectra. The objective of this study was to ascertain the potential of these calculations to elucidate and compare polymers when mixed with a potassium bromide promoter. The most favorable result was observed for polyethylene, where the highest internal energy was 3812.125698 Hartree and the lowest polar moment was 8.417560 Debye. This resulted in a reduction of the total charge between the potassium bromide complex and polyethylene. Additionally, the highest UV absorbance was 800.00 nm, thus making it the safest of the remaining polymers. This provides assurance that when used as a carrier for any baked goods where potassium bromide has been used as a strengthening agent, it is the optimal choice.

Keywords: Polyamide, Polyethylene and Polycarbonate, Potassium bromide, DFT, UV-visible.

INTRODUCTION

The history of plastic production can be traced back to the mid-19th century. However, the modern era of plastics manufacturing did not begin until the early 20th century, with the development of Bakelite, the first fully synthetic plastic. Subsequently, significant developments in polymer chemistry have resulted in the creation of an extensive range of plastics, which have had a transformative impact on sectors such as packaging, transportation, construction, and healthcare (Carwile et al., 2011).

A multitude of plastic polymers are utilized in food packaging. The plastic polymers employed in food packaging can be categorized according to their chemical composition and properties. The most prevalent polymer employed is polyamide (PA) in figure 1, which is a polymer comprising imide groups and is categorized as a high-performance plastic. Polyamides possess exceptional heat resistance, rendering them suitable for a multitude of applications in contexts where durable organic materials are required, including high-temperature fuel cells, displays, and various military applications.(Braun et al., 2013), Furthermore, polyamide resin is employed as an insulating layer in the fabrication of integrated circuits and microelectromechanical system chips. Polyamide films

demonstrate optimal mechanical elongation and rigidity, which is beneficial for grip between polyamide layers or between a polyamide film and a stored metal layer. (Krakuer, 2006) The minimal interaction between the gold foil and the polyamide film, coupled with the high temperature stability of the polyamide film, results in a robust framework that provides reliable protection when subjected to diverse forms of natural stress. Furthermore, polyamide is employed as a substrate for mobile phone radio wires (Ono & Erhard, 2011).

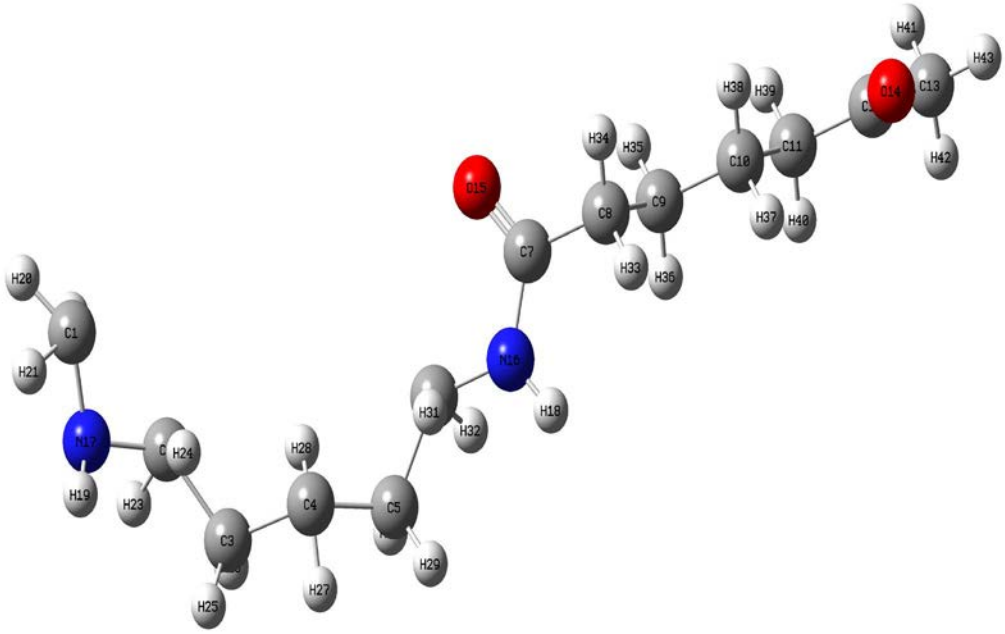

Figure: (1). The spatial structure of the polyamide composite

Polyethylene is a material that is widely employed in the packaging of foodstuffs due to its low cost, versatility, and ability to protect against moisture and synthetic chemicals Figure 2. The most commonly utilized forms of polyethylene in packaging applications are high-thickness polyethylene (HDPE) and low-thickness polyethylene (LDPE). They are the most widely manufactured plastic. HDPE is a polymer that is employed primarily for packaging purposes, including plastic sacks, plastic films, geofilms, and containers such as bottles. (Whiteley et al., 2000) Beginning in 2017, the production of polyethylene tars reached 100 million tons per year, accounting for 34% of the global plastics market.(Geyer et al., 2017), Plastics Europe.

Archived from the original on 4 February 2018] The polyethylene family encompasses a number of known types, the synthetic recipe of which is $(C_2H_4)_n$. Polyethylene is typically a blend of undifferentiated polymers of ethylene, exhibiting a range of advantageous properties. It can be classified as either low-density or high-density or alternatively, as one of the numerous transitional varieties.(Yao et al., 2022) Additionally, the material's properties can be modified through cross-linking or copolymerization. All structures are non-toxic and possess compound adaptability, which contributes to polyethylene's prominence as a flexible plastic. Furthermore, polyethylene's chemical versatility renders it resistant to degradation and corrosion when improperly discarded. As a hydrocarbon, polyethylene is characterized by a lack of impurities and coloring agents and is combustible. (Sepe, 2024).

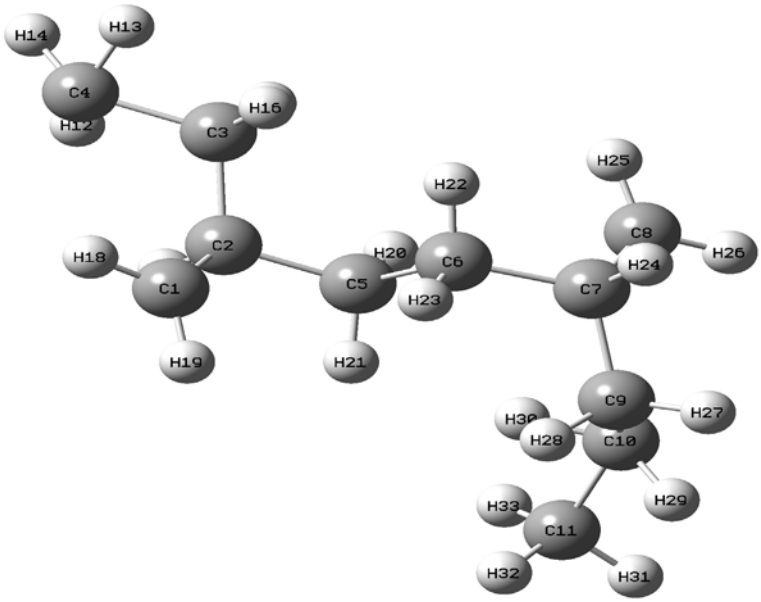

Figure:(2). The spatial structure of the polyethylene composite

Polycarbonate (PC) is a thermoplastic polymer comprising carbonate groups within its intrinsic structure Figure 3. The polycarbonates employed in the construction of various products are distinguished by their strength and versatility, with specific grades additionally exhibiting optical transparency. The aforementioned materials can be readily manipulated through processes such as shaping and thermoforming. As a consequence of these characteristics, polycarbonate is employed in a multitude of applications. Polycarbonate does not possess a unique serial number identification code (RIC).(Lexan sheet technical manual, 2015), The extensive deployment of polycarbonate in electronic applications contributes to the overall security profile of these devices. It functions as an efficacious electrical insulator, exhibiting both high-voltage and heat resistance properties. Consequently, it is utilized in the mechanical assembly of power organizations and broadcast communication equipment. It can be utilized as an electrical insulator in high-strength capacitors. (Serini, 2000).

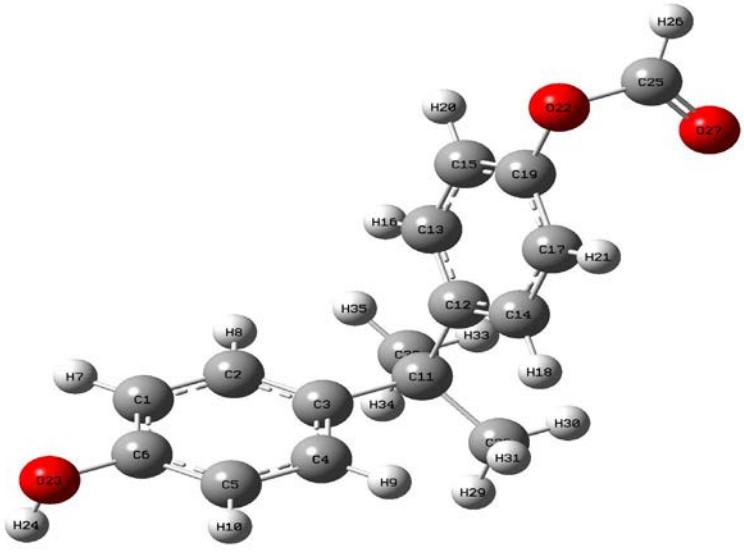

Figure: (3). The spatial structure of the polycarbonate composite

The use of plastic polymers has become ubiquitous in contemporary culture, assuming a pivotal role in numerous facets of daily life. The flexibility, durability, and cost-effectiveness of these materials have facilitated their extensive utilization across a diverse range of industries, including food and beverage packaging, medical services, electronics, and automotive manufacturing. (Kubwabo et al., 2009), Although plastic polymers offer a number of advantages, their unavoidable use has also given rise to concerns about the potential for contamination of natural materials, particularly in light of the potential risks associated with the presence of added substances and impurities. One such risk is the potential for substance migration, whereby plastic materials may transfer harmful synthetics into foodstuffs via an interaction known as migration. The rate and degree of compound movement can be influenced by a number of factors, including temperature, contact time, and the corrosiveness of the food in question. Furthermore, the movement of substances from plastic packaging to food occurs via various pathways that may be influenced by temperature.

The process of dispersion refers to the movement of particles from an area of higher concentration to an area of lower concentration. The transfer of synthetic compounds from plastic packaging to foodstuffs can occur via the process of diffusion. (González-Sálamo et al., 2018), As atoms move from areas of high fixation (e.g., plastic) to areas of low focus (e.g., food), the rate of dispersion can be significantly accelerated by elevated temperatures, thereby expediting the relocation of designed materials into food. In order to address these difficulties, a number of measures have been implemented. These include improvements to biodegradable plastics, which form the basis of reuse programs, and the implementation of administrative measures with the specific aim of monitoring plastic waste and promoting the use of financial packaging arrangements.(Rhim & Ng, 2007).

A variety of contextual analyses conducted in authentic settings have identified the potential risks associated with the relocation of synthetic compounds from plastic bundling materials utilized for food storage and organization. For example, a review published in Ecological Well-Being Perspectives found that plastic containers designed for microwave warming delivery may leach BPA and phthalates into food, potentially exposing consumers to harmful synthetic compounds. Furthermore, studies examining the transfer of synthetic compounds from plastic baby bottles and food containers have highlighted potential health concerns regarding the use of these items, particularly for infants and young children., There has been a notable increase in consumer awareness and concerns about the safety of plastic food packaging in recent years. This is driven by a combination of growing scientific evidence and media coverage that has highlighted the potential health risks associated with the use of plastics in food packaging.

These risks are attributed to the cost-effectiveness and versatility of plastics, which have become ubiquitous in food packaging. Plastic materials, which are pervasive in food packaging due to their cost-effectiveness and versatility, have been subjected to intensifying scrutiny regarding their capacity to leach potentially harmful chemicals into food, particularly under conditions of heat or acidity.(Geyer et al., 2017), An additional creative methodology entails the integration of dynamic fixings into plastic bundling materials, with the objective of extending the usability period of transient food sources and reducing food waste. For example, antimicrobial additives can be incorporated into packaging materials to inhibit microbial growth and extend the shelf life of packaged food products. Similarly, the use of oxygen scavengers and moisture scavengers can prevent oxidation and decay, thereby maintaining the quality and safety of packaged items. (Thompson et al., 2009), Nevertheless, the extensive adoption of novel packaging technologies gives rise to a number of challenges and constraints. A significant challenge is to guarantee that new packaging materials and additives comply with the relevant regulatory requirements and safety standards. It is incumbent upon regulatory agencies to subject new packaging solutions to exhaustive testing and evaluation in

order to ascertain their safety with respect to food contact and environmental impact. Furthermore, the expansion of production operations for novel packaging technologies may necessitate substantial investments in equipment and infrastructure, in addition to a meticulous examination of supply chain logistics and associated costs (Ragaert et al., 2017).

Despite these challenges, continued technological advances hold the promise of enhancing the safety, sustainability, and performance of plastic packaging. By employing innovative materials, coatings, and manufacturing processes, the industry can address consumer concerns regarding chemical migration while simultaneously reducing its environmental impact and enhancing food security (Kefeni et al., 2011). Moreover, the current analytical techniques employed for the detection and quantification of migrating chemicals in food samples may lack the requisite sensitivity or specificity for some compounds, particularly those of an emerging nature or degradation products of plastic polymers. It is imperative that methodological advances be made in order to improve the accuracy, precision, and throughput of analytical techniques, thereby allowing for more comprehensive screening of a wider range of chemicals at trace levels (Groh et al., 2017).

In order to address these complex research questions, it will be essential to engage in interdisciplinary collaboration between food scientists, materials engineers, toxicologists, and analytical chemists. An interdisciplinary approach that integrates experimental studies, computational modeling, and risk assessment frameworks can facilitate a comprehensive understanding of the factors that influence chemical migration and their potential health effects (Muncke, 2009), Although significant progress has been made in understanding the effects of plastic polymers on hot food, there are still knowledge gaps and research methodologies that require further investigation. By addressing these gaps and adopting a multidisciplinary approach, researchers can advance their understanding of this complex issue and develop evidence-based strategies to mitigate potential risks to human health and food safety (Wagner & Oehlmann, 2011).

One of the most well-known additives that has significantly influenced its incorporation into polymer plastic molecules is potassium bromide. Modern salt was extensively employed as an anticonvulsant and narcotic throughout the late nineteenth and mid-twentieth centuries, with over-the-counter use becoming prevalent in the United States by 1975. The pharmacological action of this substance is attributed to the bromide ion, and sodium bromide has a similar effect. Potassium bromide Figure 4 is employed in the treatment of epilepsy in canines as a veterinary pharmaceutical.
The white crystalline powder that constitutes potassium bromide is its typical physical form under standard conditions. The problematic substance is insoluble in acetonitrile; however, water has the capacity to dissolve it. In a diluted aqueous solution, potassium bromide has been described as having a sweet flavor. However, at higher concentrations, the substance is perceived as bitter, and at even higher concentrations, it is perceived as salty. The characteristics of the potassium ion are the primary cause of these effects. The perception of sodium bromide as salty remains constant regardless of the concentration. At elevated concentrations, it has been demonstrated that potassium bromide is a significant irritant to the gastric mucosa, resulting in symptoms such as nausea and vomiting. This phenomenon is not exclusive to potassium bromide, as it is a common occurrence in soluble potassium salts (ChemIDplus, 2014).

Until 1975, bromide was present in a number of over-the-counter medications in the United States. This was due to the fact that bromide compounds, particularly sodium bromide, were outlawed from such products due to their chronic toxicity. Such products included the original formulation of Bromo-Seltzer. The long half-life of bromide in the body presented a challenge in determining the appropriate dosage without adverse effects. As a consequence of the advent of a plethora of superi-

or sedatives with shorter durations of action, bromide was no longer employed for medical purposes in the United States at this juncture (Adams, 1907).

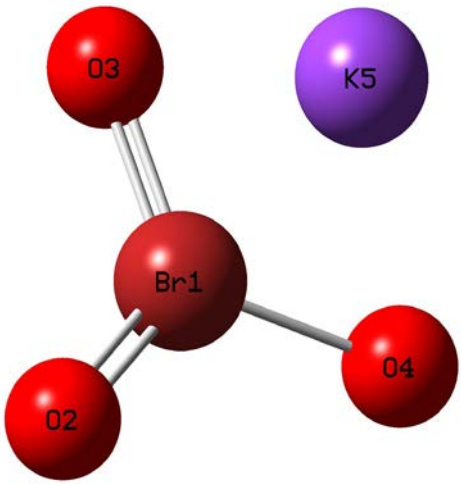

Figure: (4). The spatial structure of the potassium bromide complex

The objective of this study is to quantify the migration of chemicals from plastic polymers to heated foods, which represents a significant hazard to human health. The objective of this study is to ascertain which types of plastic are the most stable and prevent the interaction of plastic particles with potassium bromide on baked foods, and to determine their ability to withstand the surrounding conditions. This will be achieved by simulating their interaction with potassium bromide, a food improver used to improve the specifications of bread and baking.

MATERIALS & METHODS

The study of electron behavior through mathematical approximations concerns the examination of the properties of matter. Consequently, the equations of quantum mechanics were initially employed solely for single-electron systems. Over time, a plethora of mathematical techniques have been devised to approximate solutions for many electron systems through computational means (Esposito et al., 2004).

The significance of quantum computing emerged from the inability of classical physics to elucidate certain phenomena, including the blackbody effect, the photoelectric effect, the Kempton effect, and other such occurrences. (Rai-Choudhury, 1997) The geometric structures of the complexes were constructed on the foundation of the structures derived from the crystal parameters furnished by Cambridge Structural and were subsequently optimized through the utilization of the Density Functional Theory (DFT) method, employing the Gaussian 09 software package. The initial geometries of the compact complexes were constructed using HyperChem version 8.0, developed by Hypercube, Gainesville, FL, USA.

The objective of the geometry optimization process is to ascertain the position of the stable point at which the molecule is most stable. The stable point may be identified as the minimum energy configuration, which is indicative of the molecular system being most stable at low energies (Natelson et al., 2000)

The process of optimizing the input structure in order to reach the transition state structure commences with a structure that exhibits a lower energy state. The calculation of vibrational frequencies is frequently undertaken subsequent to the identification of the stable point through the process

of geometry optimization (Tsuji, 2015). The DFT method is a frequently employed technique for calculating electron density in a diverse array of compounds. It is employed in the treatment of large molecules in computational chemistry, where it is particularly advantageous. A quantum chemistry approach based on the Schrödinger equation is the DFT method.(Natelson et al., 2000). B3LYP is a widely employed methodology in the field of chemical systems, primarily due to its high degree of accuracy in determining the final geometry, approximate structural formula, final energy, and bond lengths. It is also crucial to consider the internal bond lengths and angles (Tsuji, 2015).

RESULTS & DISCUSSION

The results and discussion demonstrate the significance of examining the total energy and the spectrum of absorbed ultraviolet rays, in addition to the polar moment, which encapsulates the strength of the activity of the physically interfering compounds between the polymers used with potassium bromide. As illustrated in Table 1, the lowest polar moment was observed for polyethylene, which exhibited the highest absorption and a relatively high energy level among the other polymers. Conversely, there is a marked increase in the polar moment of potassium bromide and a notable reduction in energy, which renders it highly stable. However, this increased stability may pose a risk if the permitted limit is exceeded in the bread and baking industry. Accordingly, the utilization of a specific type of plastic for polymers with a low polar moment was imperative to circumvent interference and absorption within the ultraviolet spectrum. This phenomenon was observed in the case of the polymer (polyethylene) in its individual state. However, to gain a comprehensive understanding of the interplay between the components and to ascertain the most optimal configuration, computational integration is essential. This will facilitate the identification of the lowest polar moment, which will ultimately determine the most active component and the most suitable integration strategy. This is a provisional measure.

Table 1: Energy of the polymers polyamide, polyethylene, polycarbonate and potassium bromide individually.

Structure	EN, hartree	Dipole moment, Debye	UV-Vis, nm
PA	- 769.644140	7.642117	750.00
PE	- 431.592646	1.641764	786.00
PC	- 844.570386	2.410575	265.03
KBr	-3382.703071	10.748100	760.00

As evidenced in Table 2, there is a notable discrepancy in the total internal energy values of the polymer complexes with potassium bromide. Among the polymers, polyethylene exhibits the most favorable interaction with bromide, characterized by a low polar moment and high absorption. While the energy remains relatively high for the other polymers, it has decreased significantly from its single-case value.

Table 2: Energy of complexes formed between polymers and potassium bromide.

	KBr		
	EN, hartree	Dipole moment, Debye	UV-Vis, nm
PA	- 4166.32120	23.207191	760.00
PE	-3812.125698	8.417560	800.00
PC	-4241.374936	16.330985	680.00

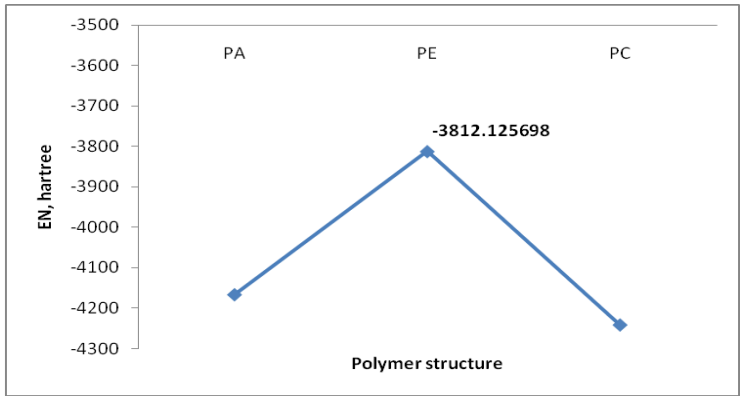

Figure: (5). Energy of complexes combined between polymers and potassium bromide

The energy of the polymer complexes combined with potassium bromide exhibits a discernible distinction in figure 5. In this regard, polyethylene displays the most notable energy profile, imparting heightened activity without undue interference over an extended duration. This distinguishes it from the other polymers, which exhibit less pronounced energy profiles.

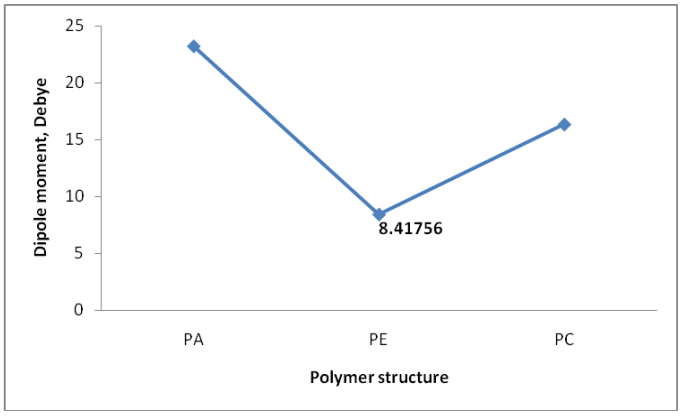

Figure: (6). Polar moment values for the complexes combined between polymers and potassium bromide

Figure 6 illustrates a reduction in the polar moment value for the polyethylene-potassium bromide mixture, which lends further support to the use of polyethylene plastic as a safe carrier. This is due to the decrease in bromide activity, which is reduced to a lower degree among the other polymers used.

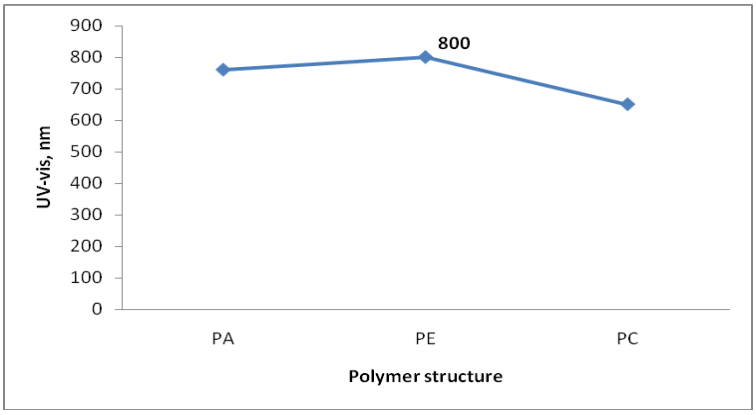

Figure: (7). UV spectrum curve of the complexes combined between polymers and potassium bromide

The UV absorption spectrum of polyethylene complex with potassium bromide, as illustrated in Figure 7, exhibits the highest absorption rate of polymers under consideration. This result corroborates the suitability of polyethylene as a safe carrier in the presence of bromide. The subsequent figures (8, 9, 10, 11, 12, and 13) illustrate the integrated complexes and simulated UV absorption spectrum of samples of polymers, namely polyamide, polyethylene, and polycarbonate with potassium bromide. It is notable that there is a discernible difference in the absorption curves.

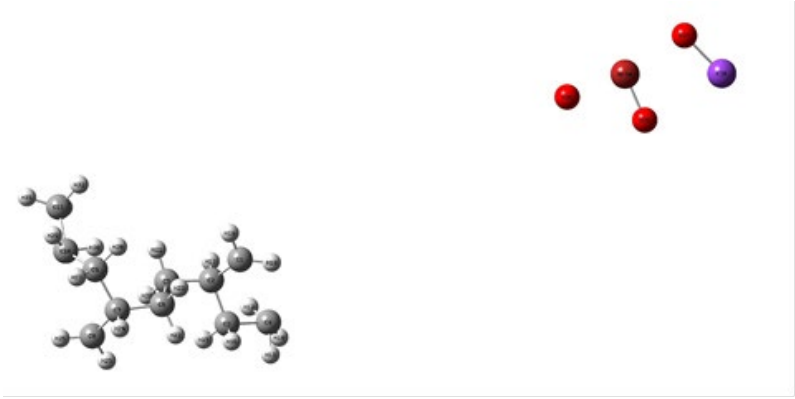

Figure 8: (9). Polyamide integrated with potassium bromide

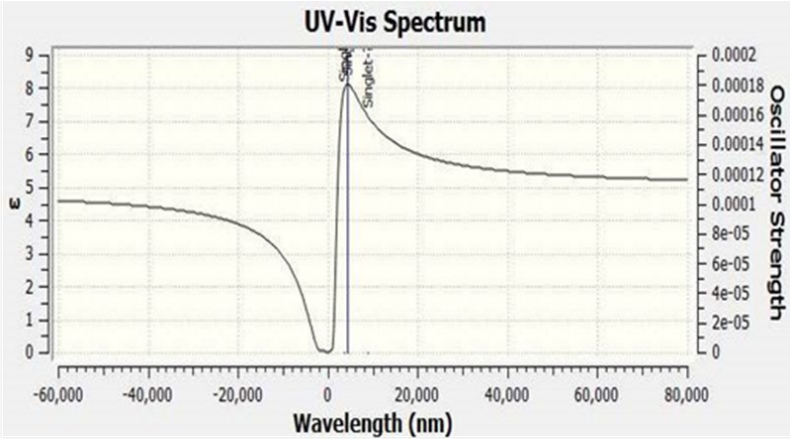

Figure : (9). UV spectrum curve of polyamide complex with potassium bromide

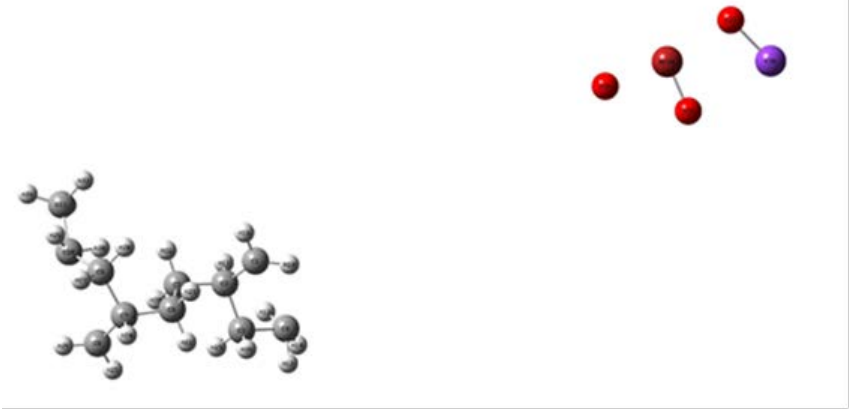

Figure: (10). Polyethylene combined with potassium bromide

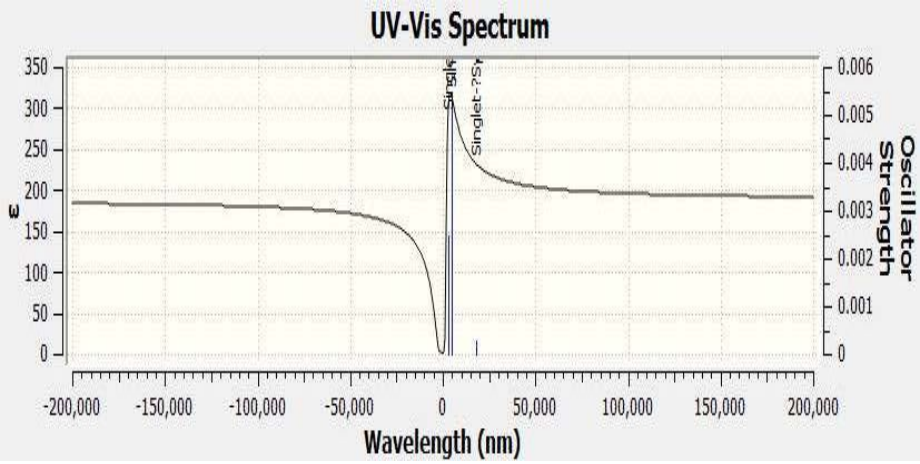

Figure: (11). UV spectrum curve of polyethylene complex with potassium bromide

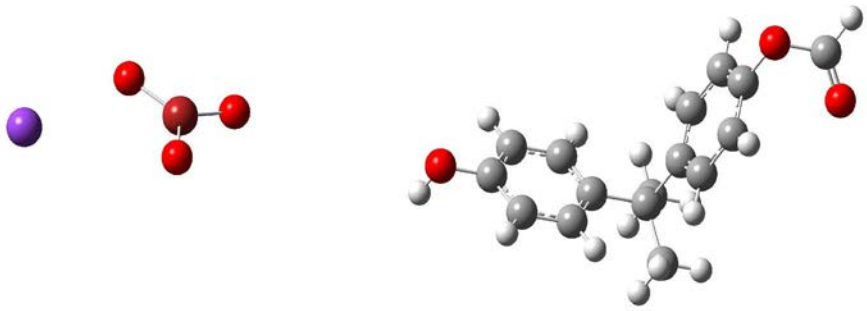

Figure: (12). Polycarbonate combined with potassium bromide

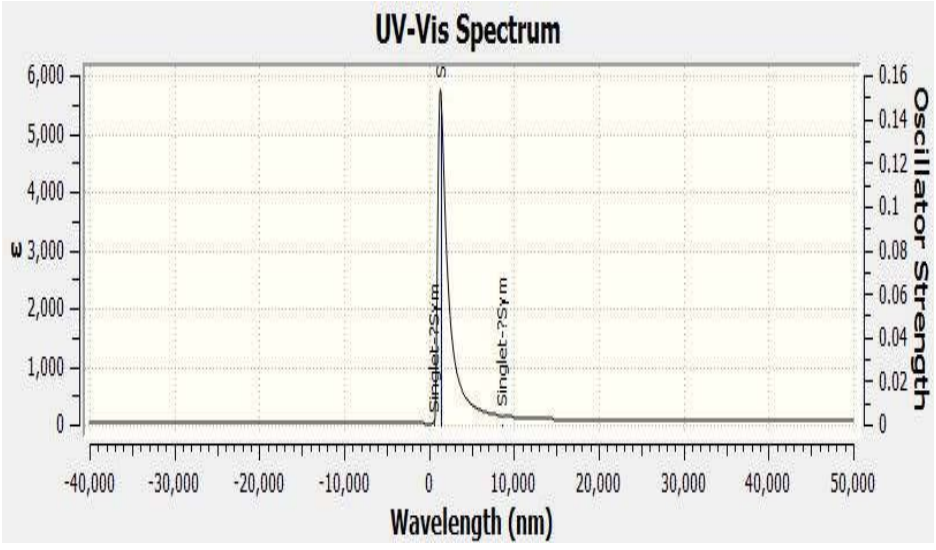

Figure: (13). UV spectrum curve of polycarbonate complex with potassium bromide

CONCLUSION

The findings of this study indicate that there are significant differences in the energy of the integrated complexes, polar moment, and UV absorption spectrum of the polymers under examination. It is evident that polyethylene is the optimal choice, as it exhibits the greatest degree of non-interference, providing a high degree of assurance when employed as a carrier for baked foods in which potassium bromide was utilized as an improving material.

RECOMMENDATIONS

It is imperative that this line of research be continued, and that the quality of plastic be enhanced. This can be achieved through collaboration between researchers in this field and stakeholders in the baked food industry. By doing so, we can guarantee the safety of baked foods and ensure that packaging meets the scientific specifications set forth in this study and other studies in this field.

Duality of interest: The authors declare that they have no duality of interest associated with this manuscript.

Author contributions: Contribution is equal between authors.

Funding: No specific funding was received for this work.

REFERENCES

Adams, S. H. (1907). *The Great American fraud*. PF Collier & Son.

Braun, J. M., Sathyanarayana, S., & Hauser, R. (2013). Phthalate exposure and children's health. *Current opinion in pediatrics, 25*(2), 247-254.

Carwile, J. L., Ye, X., Zhou, X., Calafat, A. M., & Michels, K. B. (2011). Canned soup consumption and urinary bisphenol A: a randomized crossover trial. *JAMA, 306*(20), 2218-2220.

ChemIDplus, U. (2014). National Library of Medicine.

Esposito, G., Marmo, G., & Sudarshan, G. (2004). *From classical to quantum mechanics: an introduction to the formalism, foundations and applications*. Cambridge University Press.

Geyer, R., Jambeck, J. R., & Law, K. L. (2017). Production, use, and fate of all plastics ever made. *Science advances, 3*(7), e1700782.

González-Sálamo, J., Socas-Rodríguez, B., & Hernández-Borges, J. (2018). Analytical methods for the determination of phthalates in food. *Current Opinion in Food Science, 22*, 122-136.

Groh, K. J., Geueke, B., & Muncke, J. (2017). Food contact materials and gut health: Implications for toxicity assessment and relevance of high molecular weight migrants. *Food and Chemical Toxicology, 109*, 1-18.

Kefeni, K. K., Okonkwo, J. O., Olukunle, O. I., & Botha, B. M. (2011). Brominated flame retardants: sources, distribution, exposure pathways, and toxicity. *Environmental Reviews, 19*(NA), 238-253.

Krakuer, D. (2006). Digital isolation offers compact, low-cost solutions to challenging design problems. *Analog Dialogue, 40*.

Kubwabo, C., Kosarac, I., Stewart, B., Gauthier, B., Lalonde, K., & Lalonde, P. (2009). Migration of bisphenol A from plastic baby bottles, baby bottle liners and reusable polycarbonate drinking bottles. *Food Additives and Contaminants, 26*(6), 928-937.

Lexan sheet technical manual, S. (2015). Retrieved 2015-07-18 from https://film-sheet-products.com/

Muncke, J. (2009). Exposure to endocrine disrupting compounds via the food chain: Is packaging a relevant source? *Science of the total environment, 407*(16), 4549-4559.

Natelson, D., Willett, R., West, K., & Pfeiffer, L. (2000). Fabrication of extremely narrow metal wires. *Applied Physics Letters, 77*(13), 1991-1993.

Ono, K., & Erhard, A. (2011). Nondestructive Testing, 3. Ultrasonics. *Ullmann's Encyclopedia of Industrial Chemistry*.

Ragaert, K., Delva, L., & Van Geem, K. (2017). Mechanical and chemical recycling of solid plastic waste. *Waste management, 69*, 24-58.

Rai-Choudhury, P. (1997). *Handbook of microlithography, micromachining, and microfabrication: microlithography* (Vol. 39). SPIE press.

Rhim, J.-W., & Ng, P. K. (2007). Natural biopolymer-based nanocomposite films for packaging applications. *Critical reviews in food science and nutrition, 47*(4), 411-433.

Sepe, M. (2024). *Understanding the 'Science' of Color*. Retrieved 25 April 2024 from https://www.ptonline.com/articles/understanding-the-science-of-color

Serini, V. (2000). Polycarbonates. *Ullmann's Encyclopedia of Industrial Chemistry*.

Thompson, R. C., Moore, C. J., Vom Saal, F. S., & Swan, S. H. (2009). Plastics, the environment and human health: current consensus and future trends. *Philosophical transactions of the royal society B: biological sciences, 364*(1526), 2153-2166.

Tsuji, M. (2015). Docking Study with HyperChem, Revision G1. *Institute of Molecular Function, Saitama, Japan*.

Wagner, M., & Oehlmann, J. (2011). Endocrine disruptors in bottled mineral water: estrogenic activity in the E-Screen. *The Journal of steroid biochemistry and molecular biology, 127*(1-2), 128-135.

Whiteley, K. S., Heggs, T. G., Koch, H., Mawer, R. L., & Immel, W. (2000). Polyolefins. *Ullmann's Encyclopedia of Industrial Chemistry*.

Yao, Z., Seong, H. J., & Jang, Y.-S. (2022). Environmental toxicity and decomposition of polyethylene. *Ecotoxicology and Environmental Safety, 242*, 113933.

Al-Mukhtar Journal of Basic Sciences 22 (3): 196-206, 2024
Doi: https://doi.org/10.54172/m05etc53

Research Article

Open Access

Homotopy Perturbation Method for Solving Mathematical Model of Brain Tumor Growth

Suhaylah S. Abreesh[1*]

*Corresponding author: s.abreesh@zu.edu.ly, Department of Mathematics, Faculty of Education, University of Zawia, , Libya.

Received:
14 August 2024

Accepted:
09 December 2024

Publish online:
31 December 2024

Abstract

The tumor growth models are vital and efficient tools for treating and diagnosing the disease. Therefore, we will find in this paper an approximate solution to the brain tumor growth model for a variable killing rate under medical treatment by applying the homotopy perturbation method (HPM). This method is both effective and simple, as it doesn't require the development of any iterative scheme to find a solution to the given equations. We will apply a new homotopy perturbation method (NHPM), which shortens the steps used in HPM by utilizing the first approximate solution to get the exact solution. The efficiency and reliability of the presented methods will be tested using some examples. Additionally, we will calculate the norm errors L_2, L_∞, and absolute error. Furthermore, we will conduct numerical simulations and generate graphics for this model using the Wolfram Mathematica 13.2 code.

Keywords: Brain tumor growth; Burgess equation; Homotopy perturbation method.

INTRODUCTION

Cancer cells grow and multiply very quickly, and most cancer treatments only rarely kill active-stage cells, this has prompted scientists to develop models of the growth of these tumors to develop effective treatment strategies and improve diagnostic and prevention methods. These models help improve patient care and also work to simulate the effects of different treatments on growth tumors and achieve the best results with the least side effects. In our study, we will study the growth model of a glioma brain tumor, which is commonly found in humans and can be managed with chemotherapy, radiotherapy, and surgery.in (Burgess et al., 1997) presented the initial formula for studying the glioma model, where they proposed a three-dimensional model for the growth of glioma that is devoid of any medical treatment and can grow without restrictions. This model was developed by many physicists, mathematicians, biologists, and medicines by incorporating cancer-killing substances into treatment. It was done by utilizing differential or integral equations, combining ideas derived from these sciences (Cruywagen et al., 1995; González-Gaxiola & Bernal-Jaquez, 2017; Wein & Koplow, 1999). In our research, we will study how to apply the homotopy perturbation method (HPM) and the modified homotopy perturbation method (NHPM) to a developed model of the Burgess equation, as this method was studied for the first time in (He, 1999) to solve nonlinear differential and integral equations. We will compare the approximate solution obtained from this

method with the exact solution provided in the examples. This will be done using the absolute error and the norm errors L_2, L_∞. To calculate the results, we will use the Wolfram Mathematica 13.2 software.

Mathematical model of the Brain tumor growth (BTG):

Several scholars have discussed the Mathematical model describing brain tumor growth (Ganji et al., 2021; Tracqui et al., 1995).

The equation that expresses the tumor rate is (González-Gaxiola & Bernal-Jaquez, 2017; Nayied et al., 2023):

$$\frac{\partial n(x,\tau)}{\partial \tau} = D\nabla^2 n(x,\tau) + \rho(\tau)n(x,\tau)$$
$$= D\frac{1}{x^2}\frac{\partial}{\partial x}\left(x^2\frac{\partial n(x,\tau)}{\partial x}\right) + \rho(\tau)n(x,\tau) \quad (1)$$

Where $n(x,\tau)$ is the tumor cell concentration at the time t, $\nabla^2$is the Laplacian operator, D the diffusion coefficient, and $\rho(\tau)$ is the growth rate of the tumor. The equation (1) is known as the Burgess equation, but this model has been modified by adding the killing rate $k(\tau)$ to equation (1) by (Wein & Koplow, 1999) so the Burgess equation was obtained in the form:

$$\frac{\partial n(x,\tau)}{\partial \tau} = D\frac{1}{x^2}\frac{\partial}{\partial x}\left(x^2\frac{\partial n(x,\tau)}{\partial x}\right) + \rho(\tau)n(x,\tau) - k(\tau)n(x,\tau) \quad (2)$$

Equation (2) can be rewritten as

$$\begin{cases} \frac{\partial n(x,\tau)}{\partial \tau} = D\frac{1}{x^2}\frac{\partial}{\partial x}\left(x^2\frac{\partial n(x,\tau)}{\partial x}\right) + \rho(\tau)n(x,\tau) - k(\tau)n(x,\tau) \\ n(x_0,\tau_0) = n_0 \end{cases} \quad (3)$$

Following (Andriopoulos & Leach, 2006; Singha & Nahak, 2022), we propose the change of variables $t = 2D\tau, u(x,t) = x\,n(x,\tau), and\ w(x,t) = \frac{\rho-k}{2D}u(x,t)$ in equation (3), we get

$$\begin{cases} \frac{\partial u(x,t)}{\partial t} = \frac{1}{2}\frac{\partial^2 u(x,t)}{\partial x} + w(x,t) \\ u(x,0) = f(x) \end{cases} \quad (4)$$

Where $w(x,t)$ represents the source term.

MATERIAL AND METHODS

The iterative methods employed in this paper to find the approximate solution of the glioma brain tumor model will be introduced in this section (Kashkari & Saleh, 2017; Pal et al., 2023; Sobamowo, 2023).

Homotopy perturbation method (HPM)

Consider examining the nonlinear differential equation that follows

$$A(u) - f(r) = 0, r \in \delta \quad (5)$$

With the conditions

$$B\left(u, \frac{\partial u}{\partial n}\right) = 0, r \in \Gamma \quad (6)$$

Where $A,\ B, \mathrm{r}, f(r), \Gamma$ respectively, are a general differential operator, a boundary operator, a coordinate, a known function, and the boundary of the domain δ. Operator A can be split into two separate operators, L (linear operator) and N (nonlinear operator). Consequently, equation (5) can be rewritten as follows:

$$L(u) + N(u) - f(r) = 0 \quad (7)$$

Using the homotopy technique, we can create a homotopy denoted as $v(r,p): \delta \times [0,1] \to \Re$. Which meets the following conditions:

$$H(v,p) = (1-p)[L(v) - L(u_0)] + p[A(v) - f(r)] = 0, \qquad p\epsilon[0,1],\ r\epsilon\delta \quad (8)$$

Where u_0 is an initial approximation of Eq. (5). Using the homotopy technique, we can assume that the solution of equation (8) is as follows:

$v = v_0 + pv_1 + p^2v_2 + \cdots\cdots\cdots$

By setting $p = 1$, we obtain the solution of the equation (5)

$u = \lim_{p\to 1} v = v_0 + v_1 + v_2 + \cdots\cdots$

New homotopy perturbation method

The idea of this method is similar to HPM. First, we consider the Eqs. (5), (6), (7). Using NHPM we construct the following homotopy:

$$H(v,p) = (1-p)[L(v) - u_0] + p[A(v) - f(r)] = 0 \quad (9)$$

Where u_0, is as in Eq. (8) . By using the homotopy technique and assuming that the solution of equation (9) can be expressed as:

$$v = v_0 + pv_1 + p^2v_2 + \cdots\cdots\cdots \quad (10)$$

By setting the initial approximation of Eq. (5) in the form

$$u_0 = \sum_{i=0}^{\infty} c_i(x)R_i(x)\ , R_i(x) = t^i \quad (11)$$

Where, $c_i(x)$ are unknown coefficients and $R_i(x)$ are known functions. By substituting (10) and (11) into (9) and comparing the coefficients of p to the same powers, we assume $u_1(x,t) = 0$. Therefore the exact solution can be obtained as:

$$w(x,t) = f(x) + \sum_{i=0}^{\infty} c_i(x)\frac{R_{i+1}(x)}{i+1} \quad (12)$$

Where $R_i(x) = t^i, c_i(x), i = 0,1,\cdots$ unidentified quantities that would be evaluated

Application of Iterative Methods in the Brain Tumor Growth Model

Application of Homotopy Perturbation Method in the Brain Tumor Growth Model

This part is dedicated to the analysis of the BTG model (4) by using HPM, where

$$L[u(x,t)] = u_t(x,t)\ , N[u(x,t)] = -\left(\frac{1}{2}u_{xx}(x,t) + w(x,t)\right), f(x,t) = 0$$

i.e. $A\big(u(x,t)\big) = u_t(x,t) - \frac{1}{2}u_{xx}(x,t) - w(x,t)$

Where $w(x,t) = \frac{\rho-k}{2D}u(x,t)$

By employing the homotopy technique, we obtain

$$H(u,p) = u_t - v_{0t} + p\left(v_{0t} - \frac{1}{2}u_{xx} - w(x,t)\right) \quad (13)$$

Substituting the initial condition and $u = \sum_{i=0}^{\infty} p^i u_i$ in the above equation

In the first case, if $w(x,t) = au(x,t), a\ is\ constant$, then

$$\frac{\partial u_0}{\partial t} + p\frac{\partial u_1}{\partial t} + p^2\frac{\partial u_2}{\partial t} + \cdots - v_{0t} + p\left(v_{0t} - \frac{1}{2}\left(\frac{\partial^2 u_0}{\partial x^2} + p\frac{\partial^2 u_1}{\partial x^2} + p^2\frac{\partial^2 u_2}{\partial x^2} + \cdots\right) - a(u_0 + pu_1 + p^2u_2 + \cdots)\right) = 0$$

By comparing the coefficient of terms with identical power of p, we get

$$p^0: u_{0t} - v_{0t} = 0 \Rightarrow u_0 = u(x,0)$$

$$p^1: u_{1t} = au_0 + \frac{1}{2}u_{0xx} - v_{0t}\ , u_1(x,0) = 0$$

$$p^2: u_{2t} = au_1 + \frac{1}{2}u_{1xx}, u_2(x,0) = 0 \quad (14)$$

$$p^3: u_{3t} = au_2 + \frac{1}{2}u_{2xx}, u_3(x,0) = 0$$

$$\vdots$$

$p^n: u_{nt} = au_{(n-1)} + \frac{1}{2}u_{(n-1)xx}, u_n(x,0) = 0$

By integrating both sides of the above equations for t, we get the required solution.

In the second case, if $w(x,t) = g\big(u(x,t)\big), i.e. w(x,t)$ is a nonlinear function of $u(x,t)$.

Using the same steps as in the first case, but setting $w(x,t) = g(u_0 + pu_1 + p^2u_2 + \cdots)$ and using Taylor's series in Eq. (13).

Application of New Homotopy Perturbation Methods in the Brain Tumor Growth Model

For solving Eq.4 by NHPM we construct the following homotopy:

$$u_t = v_0 - p\left(v_0 - \frac{1}{2}u_{xx} - w(x,t)\right) \quad (15)$$

Integrate both sides of the above equation for t

$$u(x,t) = u(x,0) + \int_0^t v_0 dt - p\int_0^t \left(v_0 - \frac{1}{2}u_{xx} - w(x,t)\right)dt \quad (16)$$

Where $u = \sum_{i=0}^{\infty} p^i u_i, v_0 = \sum_{i=0}^{\infty} c_i(x)R_i(t), R_i(t) = t^i$ in the eq. (16) and equating the coefficients of p with the same power leads to

In the first case, if $w(x,t) = au(x,t), a$ is a constant:

$$p^0: u_0 = u(x,0) + \int_0^t (c_0 + c_1 t + c_2 t^2 + \cdots)dt$$

$$p^1: u_1 = -\int_0^t \left((c_0 + c_1 t + c_2 t^2 + \cdots) - \frac{1}{2}u_{0xx} - au_0\right)dt \quad (17)$$

$$p^2: u_2 = -\int_0^t \left(-\frac{1}{2}u_{1xx} - au_1\right)dt$$

$$p^3: u_3 = -\int_0^t \left(-\frac{1}{2}u_{2xx} - au_2\right)dt$$

$\vdots$

And, so on

If we solve eq.'s (17) in a manner that

$$u_1 = -\int_0^t \left((c_0 + c_1 t + c_2 t^2 + \cdots) - \frac{1}{2}u_{0xx} - au_0\right)dt = 0$$

Then, the equations (17) get the yield to

$u_m = 0, m = 2,3,4,\cdots$

Thus, the exact solution can be obtained as follows:

$u(x,t) = f(x) + \sum_{i=0}^{\infty} c_i \frac{R_{i+1}}{i+1}, \quad R_i = t^i$

In the second case, if $w(x,t) = g\big(u(x,t)\big), i.e. w(x,t)$ is a nonlinear function of $u(x,t)$.

Using the same steps as in the first case, but setting $w(x,t) = g(u_0 + pu_1 + p^2u_2 + \cdots)$ and using Taylor's series in Eq. (16).

Numerical simulation

In this section, we will employ our methods to obtain an approximate solution of the BTG model (4) to verify the efficiency of the methods used in this paper. The given examples have been chosen from (González-Gaxiola & Bernal-Jaquez, 2017; Nayied et al., 2023).

The numerical simulation for the examples was performed using the Wolfram Mathematica code. To determine the quality of the results obtained, the following error norms L_2 *and* L_∞ are calculated

$$L_2 = \|u - u_{exact}\|_2 = \sqrt{\Delta x \Delta t \sum_{i=0}^{N}\sum_{j=0}^{M}\left(u(x_i,t_j) - u_{exact}(x_i,t_j)\right)^2}, \Delta x = \frac{1}{N-1}, \Delta t = \frac{1}{M-1}$$

$$L_\infty = \|u - u_n\|_\infty = \max_{i,j}|u - u_{exact}| \, , \, abs.error = |u - u_{exact}|$$

Example 4.1

We consider the following Burgess equation

$$u_t(x,t) = \frac{1}{2}u_{xx}(x,t) + w(x,t) \quad (18)$$

With the initial condition

$$u(x,0) = e^x \quad (19)$$

Where $w(x,t) = \frac{1}{2}u(x,t)$ and the exact solution $u(x,t) = e^{x+t}$

To find a solution of eq. (18) by HPM, we will follow the same steps used in part (3.1), we obtain the following:

$$\begin{aligned} &p^0: u_0 = e^x \\ &p^1: u_1 = te^x \\ &p^2: u_2 = \frac{t^2}{2}e^x \\ &p^3: u_3 = \frac{t^3}{6}e^x \\ &\vdots \end{aligned} \quad (20)$$

Gives the series solution as:

$$u(x,t) = \sum_{n=0}^{\infty} u_n = \left(1 + t + \frac{t^2}{2!} + \frac{t^3}{3!} + \cdots\right)e^x = e^{x+t}$$

Now, we will use NHPM to find the solution to equation (18) by following the same steps as in part (3.2).

$$\begin{aligned} &p^0: u_0 = e^x + \int_0^t (c_0 + c_1 t + c_2 t^2 + \cdots)dt \\ &p^1: u_1 = -\int_0^t \left((c_0 + c_1 t + c_2 t^2 + \cdots) - \frac{1}{2}u_{0xx} - \frac{1}{2}u_0\right)dt \\ &p^2: u_2 = -\int_0^t \left(-\frac{1}{2}u_{1xx} - \frac{1}{2}u_1\right)dt \\ &p^3: u_3 = -\int_0^t \left(-\frac{1}{2}u_{2xx} - \frac{1}{2}u_2\right)dt \\ &\vdots \end{aligned} \quad (21)$$

And, so on

Now we will get the value of $u_1(x,t)$ such that the values $u_2, u_3, \ldots u_n$ will vanish.

$$-\int_0^t \left((c_0 + c_1 t + c_2 t^2 + \cdots) - \frac{1}{2}u_{0xx} - au_0\right)dt = 0 \quad (22)$$

Now putting the coefficients of t equal to zero in eq.(22), which gives

$$c_0 = e^x, c_1 = \frac{1}{2}(c_0 + c_0^{"}) = e^x, c_2 = \frac{1}{4}(c_1 + c_1^{"}) = \frac{1}{4}e^x, c_3 = \frac{1}{6}(c_2 + c_2^{"}) = \frac{1}{6}e^x \text{ and so on}$$

$$c_n = \frac{1}{n!}e^x$$

So, the solution of eq. (18) is as follows:

$$\begin{aligned} u(x,t) &= u_0(x,t) + \sum_{i=0}^{\infty} c_i \frac{R_{i+1}}{i+1}, R_i = t^i \\ &= e^x + e^x t + e^x \frac{t^2}{2} + \frac{1}{2}e^x \frac{t^3}{3} + \frac{1}{6}e^x \frac{t^4}{4} + \cdots \end{aligned}$$

$$= e^{x}\left(1 + t + \frac{t^2}{2!} + \frac{t^3}{3!} + \frac{t^4}{4!} + \cdots\right)$$

So, we get

$u(x,t) = e^{x+t}$

Which is an exact solution.

The numerical results of this example are displayed in Table 1 and Figures 1, 2, and 3. Table 1 compares the error norms L_2, L_∞ for $N = 100$ at different time levels $t \leq 1$. Figure 1 displays the graphical behavior of the numerical solution at various time levels $t \leq 1$ and $i = 10$. Figure 2 compares HPM and NHM with the exact solution at $t = 0.5$. Moreover, Fig. 3 shows the absolute error between the solutions obtained by HPM and NHM and the exact solution for $x \in [0,1], t = 0.5, i = 10$. Based on Tables 1 and 2, as well as Figures 1, 2, and 3, it is clear that we obtained good results.

Table: (1). Comparison of the error norm L_2, L_∞ at various times of ex.1

	Error	$t = 0.1$	$t = 0.3$	$t = 0.5$	$t = 0.7$	$t = 0.9$
HPM		3.4542×10^{-16}	4.7468×10^{-16}	4.6524×10^{-16}	8.6455×10^{-16}	1.0117×10^{-15}
NHPM	L_2	3.4542×10^{-16}	4.7468×10^{-16}	4.6524×10^{-16}	8.6455×10^{-16}	1.0117×10^{-15}
HPM		$8,8818\times 10^{-16}$	1.3323×10^{-15}	8.8818×10^{-16}	2.6645×10^{-15}	3.5527×10^{-15}
NHPM	L_∞	$8,8818\times 10^{-16}$	1.3323×10^{-15}	8.8818×10^{-16}	2.6645×10^{-15}	3.5527×10^{-15}

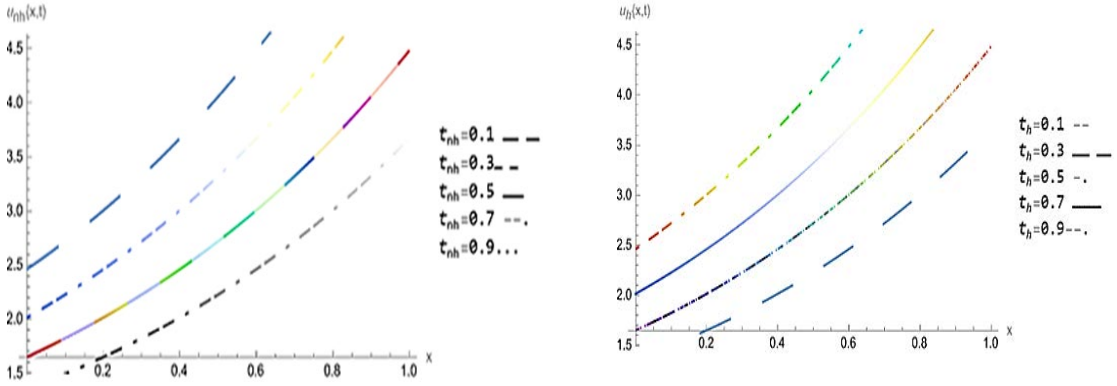

Figure: (1). Comparison of HPM versus NHM at different t of ex.1

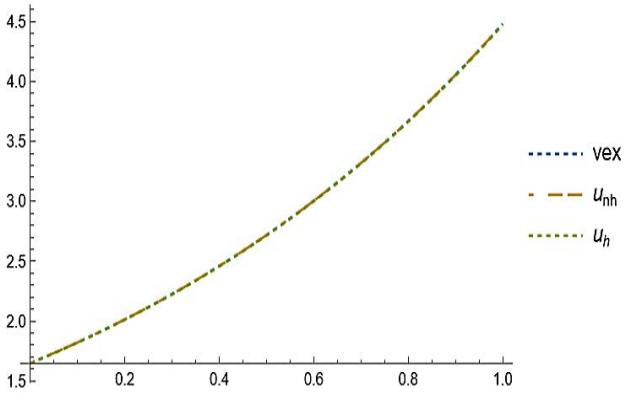

Figure: (2). Solution of HPM and NHM with exact solution at $x \in [0,1], t = 0.5$ of ex.1

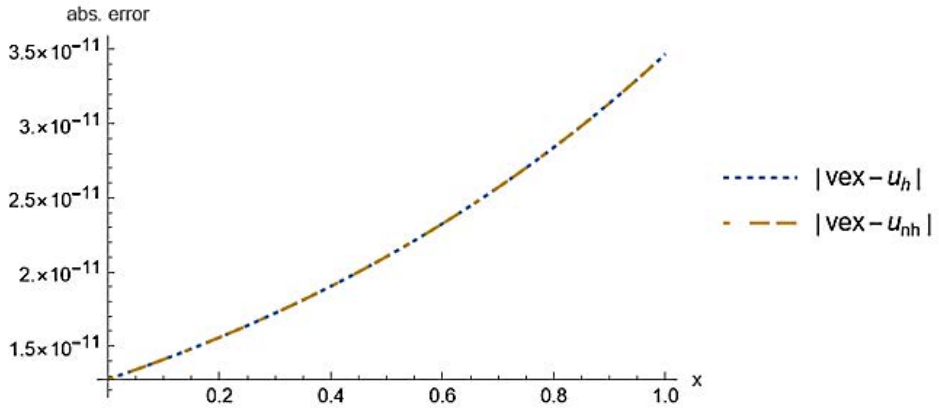

Figure: (3). Absolute error between solutions obtained by HPM and NHM for $x \in [0,1], t = 0.5, i = 10$ of ex.1

Example 4.2

Consider the nonlinear Burgess equation

$$u_t(x,t) = \frac{1}{2}u_{xx}(x,t) + w(x,t) \tag{23}$$

Subject to the initial condition

$$u(x,0) = \ln(x+2) \tag{24}$$

Where $w(x,t) = e^{-u(x,t)} + \frac{1}{2}e^{-2u(x,t)}$ and the exact solution $u(x,t) = \ln(x+t+2)$

In the first case, we will solve eq. 23 using the HPM by following the steps used in part (3.1) when $w(x,t)$ is a nonlinear function as follows:

$$\frac{\partial u_0}{\partial t} + p\frac{\partial u_1}{\partial t} + p^2\frac{\partial u_2}{\partial t} + \cdots - v_{0t} + p\left(v_{0t} - \frac{1}{2}\left(\frac{\partial^2 u_0}{\partial x^2} + p\frac{\partial^2 u_1}{\partial x^2} + p^2\frac{\partial^2 u_2}{\partial x^2} + \cdots\right) - e^{-(u_0+pu_1+p^2u_2+\cdots)} - \frac{1}{2}e^{-2(u_0+pu_1+p^2u_2+\cdots)}\right) = 0$$

By simplification of the above equation, we get

$$\frac{\partial u_0}{\partial t} + p\frac{\partial u_1}{\partial t} + p^2\frac{\partial u_2}{\partial t} + \cdots - v_{0t} + pv_{0t} - \frac{1}{2}p\frac{\partial^2 u_0}{\partial x^2} - \frac{1}{2}p^2\frac{\partial^2 u_1}{\partial x^2} - \frac{1}{2}p^3\frac{\partial^2 u_2}{\partial x^2} - \cdots$$
$$-pe^{-u_0}e^{-(pu_1+p^2u_2+\cdots)} - \frac{1}{2}pe^{-2u_0}e^{-2(pu_1+p^2u_2+\cdots)} = 0$$

By using the Taylor series to expand the previous expression, we obtain

$$\frac{\partial u_0}{\partial t} + p\frac{\partial u_1}{\partial t} + p^2\frac{\partial u_2}{\partial t} + \cdots - v_{0t} + pv_{0t} - \frac{1}{2}p\frac{\partial^2 u_0}{\partial x^2} - \frac{1}{2}p^2\frac{\partial^2 u_1}{\partial x^2} - \frac{1}{2}p^3\frac{\partial^2 u_2}{\partial x^2} - \cdots$$

$$-p\left(e^{-u_0}\left(1 - (pu_1 + p^2u_2 + \cdots) + \frac{(pu_1 + p^2u_2 + \cdots)^2}{2!} - \cdots\right)\right) - \frac{1}{2}p\left(e^{-2u_0}\left(1 - 2(pu_1 + p^2u_2 + \cdots) + \frac{4(pu_1 + p^2u_2 + \cdots)^2}{2!} - \cdots\right)\right) = 0$$

Comparing the coefficients of equal powers of p

$p^0: u_0 = \ln(x+2)$

$p^1: u_1 = \frac{t}{2+x}$ (25)

$p^2: u_2 = -\frac{t^2}{2(2+x)^2}$

$p^3: u_3 = \frac{t^3}{3(2+x)^3}$

⋮

Gives the solution as

$$u(x,t) = \ln(x+2) + \frac{t}{2+x} - \frac{t^2}{2(2+x)^2} + \frac{t^3}{3(2+x)^3} + \cdots$$

That gives the exact solution

$u(x,t) = \ln(x+t+2)$

In the second case, we will solve eq.23 using the NHPM. By following the steps in part (3.2), we get

$$u(x,t) = \ln(x+2) + \int_0^t v_0 dt - p\int_0^t \left(v_0 - \frac{1}{2}\left(\frac{\partial^2 u_0}{\partial x^2} + p\frac{\partial^2 u_1}{\partial x^2} + p^2\frac{\partial^2 u_2}{\partial x^2} + \cdots\right) - e^{-(u_0 - pu_1 + p^2u_2 + \cdots)} - \frac{1}{2}e^{-2(u_0 - pu_1 + p^2u_2 + \cdots)}\right)$$

Solving the above equation by using the homotopy technique, we get

$$p^0: u_0 = \ln(x+2) + \int_0^t v_0 dt$$

$$p^1: u_1 = -\int_0^t \left(v_0 - \frac{1}{2}u_{0xx} - e^{-u_0} - \frac{1}{2}e^{-2u_0}\right) dt \qquad (26)$$

$$p^2: u_2 = -\int_0^t \left(-\frac{1}{2}u_{1xx} + u_1 e^{-u_0} + u_1 e^{-2u_0}\right) dt$$

$$p^3: u_3 = -\int_0^t \left(-\frac{1}{2}u_{2xx} + u_2 e^{-u_0} + u_2 e^{-2u_0} - \frac{1}{2}u_1^2 e^{-u_0} - u_1^2 e^{-2u_0}\right) dt$$

⋮

By assuming $v_0 = \sum_{i=0}^{\infty} c_i(x)R_i(t), R_i(t) = t^i$, and solving the equation $u_1(x,t) = 0$, we get

$$c_0 = \frac{1}{2+x}, c_1 = -\frac{1}{(2+x)^2}, c_2 = \frac{1}{(2+x)^3}, c_3 = \frac{1}{(2+x)^4} \cdots, c_n = (-1)^n \frac{1}{(2+x)^{n+1}}$$

Moreover, we have

$$u(x,t) = u_0(x,t) + \sum_{i=0}^{\infty} c_i \frac{R_{i+1}}{i+1}, R_i = t^i$$

$$= \ln(x+2) + \frac{t}{2+x} - \frac{t^2}{2(2+x)^2} + \frac{t^3}{3(2+x)^3} - \frac{t^4}{4(2+x)^4} + \cdots$$

Thus,

$u(x,t) = \ln(x+t+2)$

Which is an exact solution.

Both the exact solution and the approximate solutions of ex.2 are compared in Fig. 4, table 3, and Table 4, where we notice that the solutions are almost identical, but through the absolute error, we notice that there is a small difference between the exact solution and the approximate solutions. Table 2 submits a comparison of the error norm L_2 for $(x,t) \in (0.1] \times [0,1], i = 10$ and different values of N, M.

Table: (2). The error norm L_2 on $(x,t) \in (0.1] \times [0,1]$of ex.2

	Error	$N = 10, M = 10$	$M = N = 100$	*M=4,N=8*
HPM	L_2	3.8586×10^{-6}	2.1628×10^{-6}	6.1596×10^{-6}
NHPM		1.7073×10^{6}	9.1124×10^{-7}	2.7615×10^{-6}
HPM	L_∞	3.046×10^{-5}	3.046×10^{-5}	3.046×10^{-5}
NHPM		1.3929×10^{-5}	1.3929×10^{-5}	1.3929×10^{-5}

Table: (3). Comparison between solutions obtained via HPM, NHM, and exact solution on $(x,t) \in (0.1] \times [0,1]$ of ex.2

	t=0.1			t=0.5			t=0.9		
x	PHM	NHM	exact	PHM	NHM	exact	PHM	NHM	exact
0	0.74194	0.74194	0.74194	0.91629	0.91629	0.91629	1.06470	1.06471	1.06471
0.1	0.78846	0.78846	0.78846	0.95551	0.95551	0.95551	1.09861	1.09861	1.09861
0.2	0.83291	0.83291	0.83291	0.99325	0.99325	0.99325	1.13140	1.13140	1.13140
0.3	0.87547	0.87547	0.87547	1.02962	1.02962	1.02962	1.16315	1.16315	1.16315
0.4	0.91629	0.91629	0.91629	1.06471	1.06471	1.06471	1.19392	1.19392	1.19392
0.5	0.95551	0.95551	0.95551	1.09861	1.09861	1.09861	1.22377	1.22378	1.22378
0.6	0.99325	0.99325	0.99325	1.13140	1.13140	1.13140	1.25276	1.25276	1.25276
0.7	1.02962	1.02962	1.02962	1.16315	1.16315	1.16315	1.28093	1.28093	1.28093
0.8	1.06471	1.06471	1.06471	1.19392	1.19392	1.19392	1.30833	1.30833	1.30833
0.9	1.09861	1.09861	1.09861	1.22378	1.22378	1.22378	1.33500	1.33500	1.33500
1	1.13140	1.13140	1.13140	1.25276	1.25276	1.25276	1.36098	1.36098	1.36098

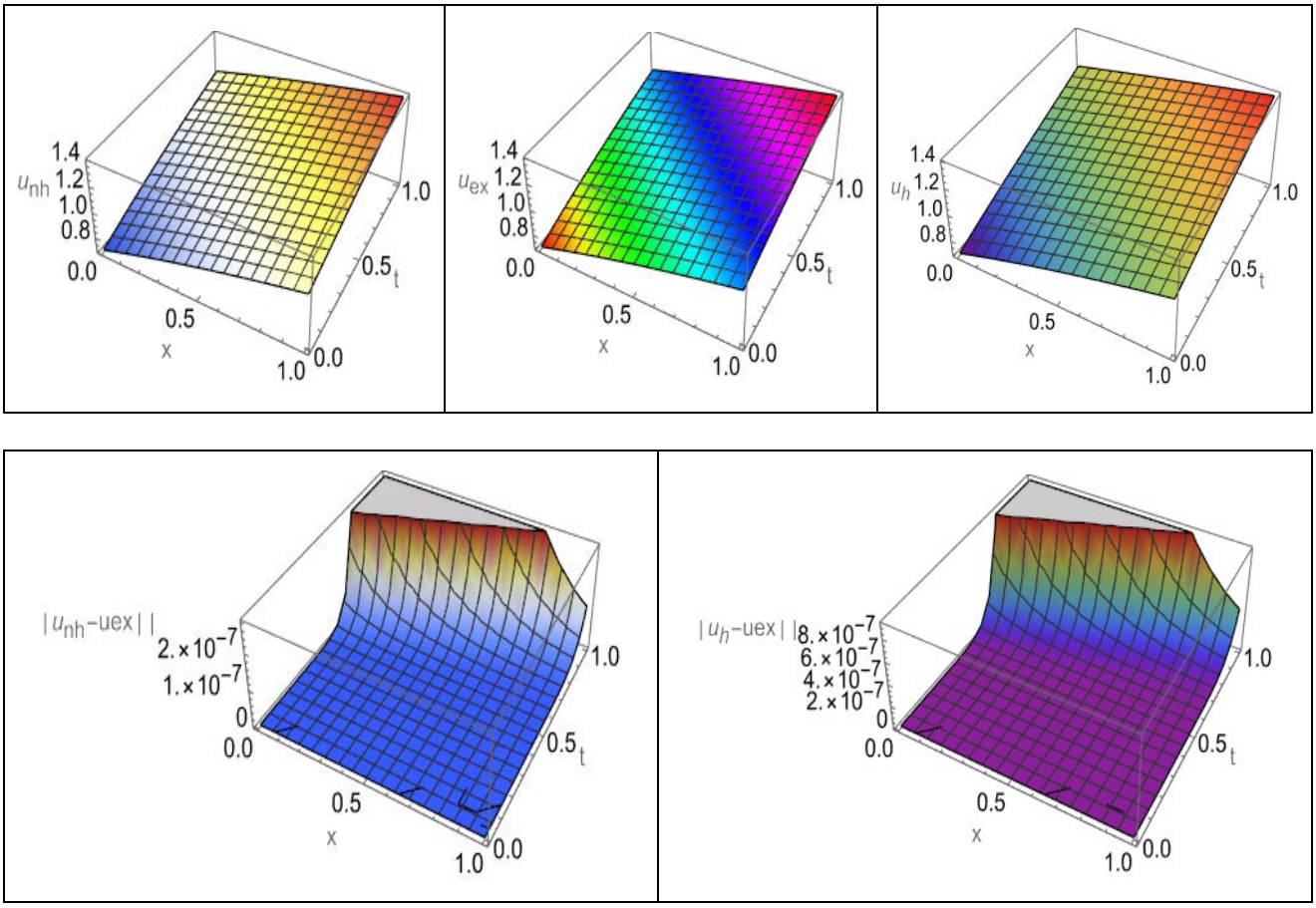

Figure: (4). Comparing between approximate solutions obtained via HPM, NHM, and exact solution on the interval $(x,t) \in (0.1] \times [0,1]$ of ex.2

Table: (4). The absolute error on $(x,t) \in (0.1] \times [0,1]$of ex.2

x	$t = 0.1$		$t = 0.5$		$t = 0.9$	
	$\|u_h - u_{ex}\|$	$\|u_{nh} - u_{ex}\|$	$\|u_h - u_{ex}\|$	$\|u_{nh} - u_{ex}\|$	$\|u_h - u_{ex}\|$	$\|u_{nh} - u_{ex}\|$
0	4.44×10^{-16}	1.11×10^{-16}	1.76×10^{-8}	4.03×10^{-9}	9.87×10^{-6}	4.06×10^{-6}
0.1	2.22×10^{-16}	1.11×10^{-16}	1.04×10^{-8}	2.26×10^{-9}	5.85×10^{-6}	2.29×10^{-6}
0.2	1.11×10^{-16}	0	6.29×10^{-9}	1.31×10^{-9}	3.55×10^{-6}	1.33×10^{-6}
0.3	3.33×10^{-16}	2.22×10^{-16}	3.89×10^{-9}	7.73×10^{-10}	2.20×10^{-6}	7.89×10^{-7}
0.4	2.22×10^{-16}	1.11×10^{-16}	2.45×10^{-9}	4.67×10^{-10}	1.40×10^{-6}	4.79×10^{-7}
0.5	0	1.11×10^{-16}	1.57×10^{-9}	2.88×10^{-10}	9.00×10^{-7}	2.96×10^{-7}
0.6	2.22×10^{-16}	0	1.03×10^{-9}	1.81×10^{-10}	5.90×10^{-7}	1.87×10^{-7}
0.7	0	2.22×10^{-16}	6.83×10^{-10}	1.16×10^{-10}	3.93×10^{-7}	1.20×10^{-7}
0.8	2.22×10^{-16}	2.22×10^{-16}	4.60×10^{-10}	1.52×10^{-11}	2.65×10^{-7}	7.82×10^{-8}
0.9	0	2.22×10^{-16}	3.14×10^{-10}	4.96×10^{-11}	1.82×10^{-7}	5.17×10^{-8}
1	2.22×10^{-16}	0	2.17×10^{-10}	3.32×10^{-11}	1.26×10^{-7}	3.47×10^{-8}

CONCLUSION

In this manuscript, we used the HPM and NHPM methods to solve the brain tumor growth model. After comparing the results obtained from various examples, we have concluded that the methods proposed in this study are effective and accurate for solving this mathematical model. We calculated the error norms L_2, L_∞ , and absolute error, and the results indicated that these error norms L_2, L_∞, and absolute errors are very small. Therefore, we can assert that the methods outlined in this paper yield good and reliable results. We utilized Wolfram Mathematica 13.2 software for performing numerical computations and generating 2D and 3D graphs relevant to this study.

Duality of interest: The author declares that they have no duality of interest associated with this manuscript.

Funding: No specific funding was received for this work.

REFERENCE

Andriopoulos, K., & Leach, P. (2006). A common theme in applied mathematics: an equation connecting applications in economics, medicine and physics. *South African journal of science*, *102*(1), 66-72.

Burgess, P. K., Kulesa, P. M., Murray, J. D., & Alvord Jr, E. C. (1997). The interaction of growth rates and diffusion coefficients in a three-dimensional mathematical model of gliomas. *Journal of Neuropathology & Experimental Neurology*, *56*(6), 704-713.

Cruywagen, G. C., Woodward, D. E., Tracqui, P., Bartoo, G. T., Murray, J., & Alvord, E. C. (1995). The modelling of diffusive tumours. *Journal of Biological Systems*, *3*(04), 937-945.

Ganji, R., Jafari, H., Moshokoa, S., & Nkomo, N. (2021). A mathematical model and numerical solution for brain tumor derived using fractional operator. *Results in Physics*, *28*, 104671.

González-Gaxiola, O., & Bernal-Jaquez, R. (2017). Applying Adomian decomposition method to solve Burgess equation with a non-linear source. *International Journal of Applied and Computational Mathematics*, *3*, 213-224.

He, J.-H. (1999). Homotopy perturbation technique. *Computer methods in applied mechanics and engineering, 178*(3-4), 257-262.

Kashkari, B. S., & Saleh, S. (2017). Variational homotopy perturbation method for solving riccati type differential problems. *Applied Mathematics, 8*(7), 893-900.

Nayied, N. A., Shah, F. A., Nisar, K. S., Khanday, M. A., & Habeeb, S. (2023). Numerical assessment of the brain tumor growth model via fibonacci and haar wavelets. *Fractals, 31*(02), 2340017.

Pal, K., Gupta, V., Singh, H., & Pawar, V. (2023). Enlightenment of heat diffusion using new homotopy perturbation method. *J. Appl. Sci. Eng, 27*(3), 2213-2216.

Singha, N., & Nahak, C. (2022). Analytical and Numerical Solutions of a Fractional-Order Mathematical Model of Tumor Growth for Variable Killing Rate. *Applications & Applied Mathematics, 17*(2).

Sobamowo, M. (2023). Direct applications of homotopy perturbation method for solving nonlinear algebraic and transcendental equations. *Int J Petrochem Sci Eng, 6*(1), 10-22.

Tracqui, P., Cruywagen, G., Woodward, D., Bartoo, G., Murray, J., & Alvord Jr, E. (1995). A mathematical model of glioma growth: the effect of chemotherapy on spatio‐temporal growth. *Cell proliferation, 28*(1), 17-31.

Wein, L., & Koplow, D. (1999). Mathematical modeling of brain cancer to identify promising combination treatments. *Preprint, D Sloan School of Management, MIT*.

Al-Mukhtar Journal of Sciences 22 (3): 207-220, 2024
Doi: https://doi.org/10.54172/1c2b0m94

Research Article Open Access

The Effect of Algal Biochar in Improving Wheat *Triticum aestivum* L Performance under Salinity Stress

Hana Abohbell[1], Amal Ehtaiwesh[2*] and Fouziyah Qarimidah[3]

[1] Department of plant science, Faculty of Science, Sabratha University, Libya

*Corresponding author: a.ehtaiwesh@zu.edu.ly, Department of plant science, Faculty of Science, University of Zawia, Libya

[3] Department of plant science, Faculty of Science, University of Zawia, Libya

Received:
15 September 2024

Accepted:
05 December 2024

Publish online:
31 December 2024

Abstract

Salinity is one of the major abiotic factors in global food security. However, algal biochar (ABC) could be particularly well suited to improve plant growth under salinity stress conditions. Therefore, the present study was conducted to evaluate the effect of Algal Biochar (ABC) on the growth and yield of wheat *Triticum aestivum* L grown under salinity stress. Pots experiment with and without combinations of algal biochar (ABC) under saline and non-saline conditions (0 and 120mM NaCl) was performed. Wheat grains were sowed in plastic pots filled with four kilograms of sandy soil and mixed with 3% of algal biochar. The experiment was designed in a completely randomized design (CRD) with four replications. The study found that 3% of ABC mitigated the negative effects of salinity stress and improved wheat performance. The result indicated that the application of ABC significantly ($P< 0.05$) increased plant height by 10%, tiller number plant^{-1} by 40%, spike number plant^{-1} by 42%, spikelet number spike^{-1} by 11%, grain number plant^{-1} by 25%, plant dry weight by 8%, 1000 grain weight by 35%, harvest index by 56%, and grain yield plant^{-1} by 69%. The study suggests that the application of ABC could be an effective strategy to improve the growth and yield of wheat crops under salinity stress conditions.

Keywords: Wheat *Triticum Aestivum* L; Salinity Stress; Algal Biochar; Growth; Yield

INTRODUCTION

Wheat *Triticum aestivum* L occupies 30% of world cereal production (770 million tons) from 220 million hectares (FAOSTAT, 2021). The world population is expected to reach nine billion people in 2050; therefore, there is an urgent need to increase the production of wheat crops to feed the population (UN, 2022). However, due to climate change, global wheat production faces several challenges, including some biotic and abiotic stresses (Liu et al., 2019; Zahra et al., 2023). Heat, drought, and salinity are considered among the most important environmental stresses facing wheat production worldwide (Ehtaiwesh, 2016; Fatima et al., 2020). Globally, salinity stress in wheat is a growing concern, and its impact on crop production has been predicted to increase because of current climate changes. Salinity is a major abiotic stress that adversely affects the growth and yield of wheat crops (Ehtaiwesh, 2019; Sadak and Dawood, 2023). However, there are many efforts to develop some strategies to mitigate the negative effects of salinity on the growth and productivity of wheat crops. Examples of these strategies include the application of some compounds such as plant

hormones, humic acid, jasmonic acid, acetylsalicylic acid, and dry yeast solution which have been shown to minimize the toxic effect of salt stress (Atia et al., 2018; Ayub et al., 2020; Saidimoradi et al., 2019; Aliet al., 2022; Ehtaiwesh, 2022a; Ehtaiwesh, 2023). In addition, another strategy to mitigate salinity is by growing salt-tolerant genotypes (Mohanavelu et al., 2021; Hossain et al., 2021; Ehtaiwesh, 2022b, Ehtaiwesh et al., 2024). Moreover, biochar addition is suggested as an effective strategy to improve crop performance under saline stress (Parkash and Singh, 2020; Kul et al., 2021).

Biochar is a carbon-rich charcoal reproduced by the process of pyrolysis, which involves heating biomass in an oxygen-limited atmosphere (Weber and Quicker, 2018). The biochar is low in surface area and cation exchange capacity, and high in ash and nutrients (Wang and Wang, 2019). Many studies indicated that biochar is used as a catalyst, soil amendment, fuel cell, heavy metal ions and contaminant adsorbent, gas storage and separation, wastewater treatment, and plant growth enhancer (Xiang et al., 2020; Zhang et al., 2020; Joseph et al., 2021; Lehmann et al., 2021; Liu et al., 2022; Qian et al., 2023). Currently, there are interests in using biochar produced from algae in agricultural fields, such as improving soil properties and using algae as an organic and biofertilizer (Baweja et al., 2019; Ammar et al., 2022). Algae are considered one of the biological species that are efficient in producing biomass and phytochemicals, due to their high efficiency in photosynthesis, in addition to their high growth rate compared to terrestrial plants (Abideen et al., 2022). Some studies mentioned that the application of algal bi-char is a sustainable solution that has the potential to improve agricultural productivity by increasing crop production (Santos and Pires, 2018; Shanmugam et al., 2018). Algal biochar is considered a soil ameliorant that may significantly improve the retention of nutrients in the soil and could rebuild organic matter in the soil (Mona et al., 2021). Many studies concluded that algal biochar has a very high exchangeable nutrient content (N, P, K, Ca, Mg, and Mo) and may add essential nutrients to the soils (Joseph et al., 2021). In addition, biochar has the potential to decrease soil acidity, increase cationic exchange capacity, and optimum nutrient availability (Pshenovschi et al., 2022). Recently, some studies indicated that the use of algal biochar has contributed to improving bio characterization, growth, and productivity of many plants such as soybean (Zhang et al., 2020), stevia plant (Abd el Aal et al., 2020), maize (Ullah et al., 2020), and tomato (Kul et al., 2021). In addition, some studies have indicated the ability of biochar to mitigate some of the negative effects of some abiotic stresses such as drought (Zhang et al., 2020), salinity (Kanwal et al., 2018), high temperature (Fahad et al., 2015) and improving overall agricultural sustainability (Abideen et al., 2022). In Libya, the calcareous sandy soils suffer from poor productivity due to their low organic matter content; their low water retention, and their deficiency of nutrients elements including nitrogen, phosphorus, potassium, and other micronutrients besides to salinity of the soils and irrigation water (Nwer et al., 2021). For these reasons, and in order to increase the productivity of these soils, it is preferable to use biochar as an organic amendment element. Therefore, the aim of this work was to study and evaluate the effect of algal biochar on salinity stress mitigation in wheat (*Triticum aestivum* L.).

MATERIALS AND METHODS

The experiment was conducted during the wheat growing season of fall/ winter of 2020 in Jodaam farm, to investigate the effects of algal biochar (ABC) on the performance of wheat crops under salinity stress conditions. Bread wheat (Salambo) seeds were obtained from National Libyan GenBank (NLGB) in Tripoli.

Algae collection

Cystoseira barbata moss was collected from the beach of the Al-Muttarid area in August 2020. At the coordinates (12◦ 48.889 East, 32◦ 47.965 North) approximately 10 meters away from the beach

and from a depth of 1-1.5 meters, the algae were washed well with seawater to get rid of impurities and plankton. Algae samples were washed with fresh water three times to get rid of salinity, and then the samples were dried in the shade for 4 days.

Algal biochar preparation

Biochar was prepared from dried algae material and then via pyrolysis at a temperature of 400°C for 1hr (Ullah et al.,2020). Then, the biochar was grounded and the resulting material was passed through a sieve (2 mm). The algal biochar was subjected to some analyses to estimate some chemical and physical properties such as acidity (pH), electrical conductivity (EC), ash percentage, and determination of some elements such as nitrogen, phosphorus, and potassium (NPK).

Estimating the electrical conductivity of biochar and its pH was done (Bird et al., 2011) by preparing a solution with a ratio of 10:1 (sample: water) and placing it in the autoclave for 35 minutes at a temperature of 121°C and at atmospheric pressure (1atm). Then the solution is filtered and the EC and pH are measured using an EC and pH meter respectively.

The Ash of the biochar was also estimated by taking 5 g of biochar sample in a crucible and placed in a combustion furnace at a temperature of 800°C for 4 hours, then cooled in a glass container. The ash was estimated from the following equation:

$$Ash\ percentage = \frac{weight\ of\ ash\ sample}{weight\ of\ dry\ ash} * 100$$

The total NPK in the biochar was estimated following the method mentioned in (George et al., 2013) using a DR 3900™ Spectrophotometer at a wavelength of 410 nm. The algal biochar properties are shown in Table 1. Mixing of biochar in soil was done in a specific concentration (3% of soil) before sowing of seeds.

Table (1). Physicochemical traits of algal biochar

Parameters	Algal biochar
PH	10
EC(ds m^1)	1.9670
Ash content (%)	45
Total nitrogen (%)	1.790
Total phosphorous (%)	5.340
Total potassium (%)	1.920

Experimental details

The experiment was designed in a completely randomized design (CRD) with four replicates for each treatment. Before sowing, the soil was mixed with biochar and sieved with a 2 mm mesh. Then, plastic pots with a capacity of 5kg were filled with 3% biochar-treated and untreated soils. Untreated soil pots served as control. Ten seeds of wheat (*Triticum aestivum* L. cv. Salambo) were sown in each pot, and seedlings were allowed to germinate for 2 weeks, then seedlings were thinned to three seedlings per pot. At the booting stage, the pots in each treatment, biochar-treated soil and untreated were divided into two groups, and each group represented a salinity treatment (0mM and 120mM). Salinity stress was applied by irrigating wheat plants with tap water with electrical conductivity (EC) of 1.7ds m^{-1}, and 120mM NaCl solution with electrical conductivity (EC) of 8.5 ds m^{-1} throughout the treatment period, which lasted for 3 weeks. Irrigation was applied manually two times a week. After salinity treatment, all plants were irrigated with tap water as needed and well

managed until wheat plants reached physiological maturity. Grain maturity was visually estimated according to the complete loss of green color from grains.

Data collection

At harvesting, four plants were collected from each treatment one plant from each replicate. Wheat plants were hand-harvested by cutting them at the soil level. Data on shoot length (cm), number of tillers plant^{-1} both fertile (with spikes) and non-fertile (without spike), and number of spikes plant^{-1} were recorded, Then plants were oven dried at 60 °C for 73 h to record plant dry weight (g). Then main spikes were hand threshed to separate grains, grain number spike^{-1} was counted manually and grain yield spike^{-1}, grain yield plant^{-1} (g), 1000-grain weight (g), and harvest index were calculated.

Statistical analysis

The experiment was conducted in a completely randomized design with four replications. Biochar was the main plot factor (two levels with (+ABC) and without Biochar (-ABC)), and salinity was assigned to subplots (two levels 0mM and 120mM NaCl). Data were analyzed using the GLM procedure in statistical SPSS software for mean and standard error estimation. Separation of means was carried out using the least significant differences (LSD; $P < 0.05$).

RESULTS

The values in Table 2 represent the probability values of the effect of algal biochar (ABC) treatment, salinity stress(S), and the interaction between Algal biochar and salinity on some growth and yield traits of wheat plants. The effect of algal biochar had a very significant ($P<0.01$) effect on all growth and yield traits of wheat plants. In addition, the effect of salinity had a highly significant ($P<0.001$) effect on the growth and yield traits of wheat plants. In the same way, there was a significant ($P<0.05$) effect of the interaction of algal biochar treatment and salinity stress on the growth and yield traits of wheat plants table2.

Table (2). Probability values of the effects of biochar (ABC), salinity (S), and ABC x S interaction on various growth and yield traits of wheat.

Traits	Algal biochar (ABC)	Salinity (S)	ABC x S
Plant height (cm)	.002	<.001	0.043
Tiller number plant^{-1}	.006	<.001	0.033
Spike number plant^{-1}	.007	<.001	0.049
Spikelet number spike^{-1}	.003	<.001	0.023
Grain number plant^{-1}	<.001	<.001	0.041
Grain yield plant^{-1} (g)	<.001	<.001	0.034
1000 grain weight (g)	0.002	<.001	0.007
Dry weight plant^{-1} (g)	<.001	<.001	0.045
Harvest index (%)	<.001	<.001	0.008

Table 3 showed the main effect of algal biochar treatment on the growth and yield of wheat plants, which indicated that the addition of algal biochar to the soil had increased wheat growth and yield traits. All growth and yield traits included in this study were increased with the addition of algal biochar, and this percentage increase ranged from 4% to 18% table3.

Table (3). The main effect of algal biochar treatments on various growth and yield traits of wheat plants. Means were estimated using the GLM procedure in SPSS.

Traits	- ABC	+ ABC
Plant height (cm)	61.5	64.4(+5%)
Tiller number plant^{-1}	5.6	6.5(+16%)
Spike number plant^{-1}	4.8	5.5(+15%)
Spikelet number spike^{-1}	16.8	17.6(+5%)
Grain number plant^{-1}	209	228(+9%)
Grain yield plant^{-1} (g)	7.7	8.5(+18%)
1000 grain weight (g)	31.3	36(+15%)
Dry weight plant^{-1} (g)	21.1	22.1(+5%)
Harvest index (%)	0.31	0.37(+17%)

Values in parenthesis indicate the percent increase from the control treatment (without ABC) to the ABC treatment (with ABC).

Table 4 shows the main effect of salinity stress on the growth and yield traits of wheat. Salinity stress had a negative effect on all growth and yield traits of wheat plants. This negative effect of salinity resulted in a decrease in all the traits studied in this experiment, and this is evident from the percentage decrease in all the traits, which ranged from -24% to -70% percent reduction over the control table3.

Table (4). The main effect of salinity on various growth and yield traits of wheat plants. Means were estimated using the GLM procedure in SPSS.

Traits	0mM NaCl	120mM NaCl
Plant height (cm)	77.3	48.7(-37%)
Tiller number plant^{-1}	7.6	4.5(-41%)
Spike number plant^{-1}	6.6	3.6(-45%)
Spikelet number spike^{-1}	19.6	14.8(-24%)
Grain number plant^{-1}	314	123(-61%)
Grain yield plant^{-1} (g)	12	3.6(-70%)
1000 grain weight (g)	38.4	29(-25%)
Dry weight plant^{-1} (g)	25.5	17.7(-31%)
Harvest index (%)	0.472	0.203(-57%)

Values in parenthesis indicate the percent differences from the control treatment (0mM NaCl) to the (120mM NaCl).

The changes in the growth and yield traits of the wheat plants under the interaction of different salinity and algal bio char applications are shown in Figures 1-3. Salt treatment significantly decreased all investigated growth and yield traits. Biochar application had a positive effect on all observed traits at both salinity levels (0mM and 120mM NaCl) compared to the respective untreated ones.

Salinity stress had a significantly negative effect on wheat growth traits such as plant height. However, at both salinity levels (0mM and 120mM NaCl), algal biochar treatment had significant ($P< 0.05$) positive effect on wheat plants, which was indicated by increasing plant height in wheat plants treated with algal biochar as compared to wheat plants without algal biochar treatment (Fig.

1a). The same trend was found with other growth trait such as tiller number, the result indicated that salinity stress had significantly negative effect on tiller number (plant^{-1}). Nevertheless, when algal biochar was added to the growth media of wheat plants at both salinity levels (0mM and 120mM NaCl), the tiller number (plant^{-1}) was increased as compared to the untreated plant (Fig1 b). Similarly, salinity stress significantly reduced above ground plant dry weight trait. Though, at both salinity levels (0mM and 120mM NaCl), algal biochar treatment had significantly increased plant dry weight as compared to untreated plants (Fig1 c).

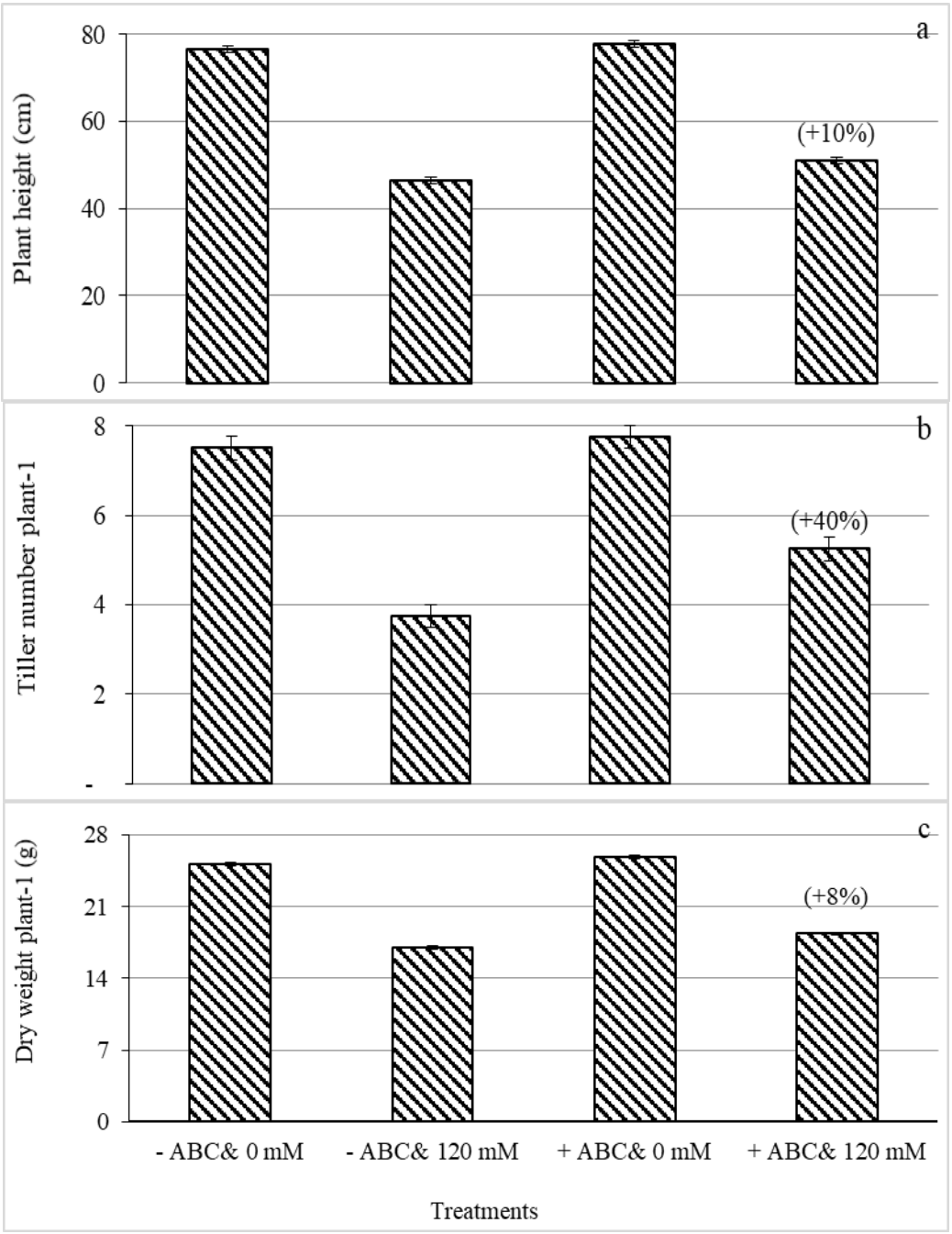

Figure (1): Effect of algal biochar and salinity treatments on (a) plant height (cm), (b) tiller number (plant $^{-1}$), and (c) total dry weight (g plant^{-1}) of wheat. Each datum indicates the mean value and vertical lines on top of bars indicate standard error of means (n = 4). Values in parenthesis indicate the percent increase from without the addition of ABC treatment to with the addition of ABC treatment under salinity stress (120mM NaCl)

The effects of algal biochar and salinity on spike number (plant^{-1}) (cm), spikelet number (spike $^{-1}$), and grain number (plant $^{-1}$) of wheat plants are shown in Fig. 2. It was found that salinity significantly (P< 0.05) decreased spike number (plant^{-1}), however when analyzed across the two salinity levels there was a tendency of increasing in spike number (plant $^{-1}$), with algal bio char addition as compared to the non-biochar treatment (Fig 2a). In addition, salinity stress significantly decreased (P< 0.05) and decreased spikelet number (spike $^{-1}$) for all wheat plants. However, this decrease was moderated by the addition of algal biochar, which resulted in a significant interactive effect of salinity and algal biochar on spikelet number (Fig. 2b). Moreover, salinity had significantly (P< 0.05) decreased grain number (plant^{-1}) of wheat plants. However, adding algal biochar had a positive effect on the number of grins (plant^{-1}), which resulted in an increase in the number of grains (plant^{-1}) compared to plants that were not treated with alga biochar (Fig. 2c).

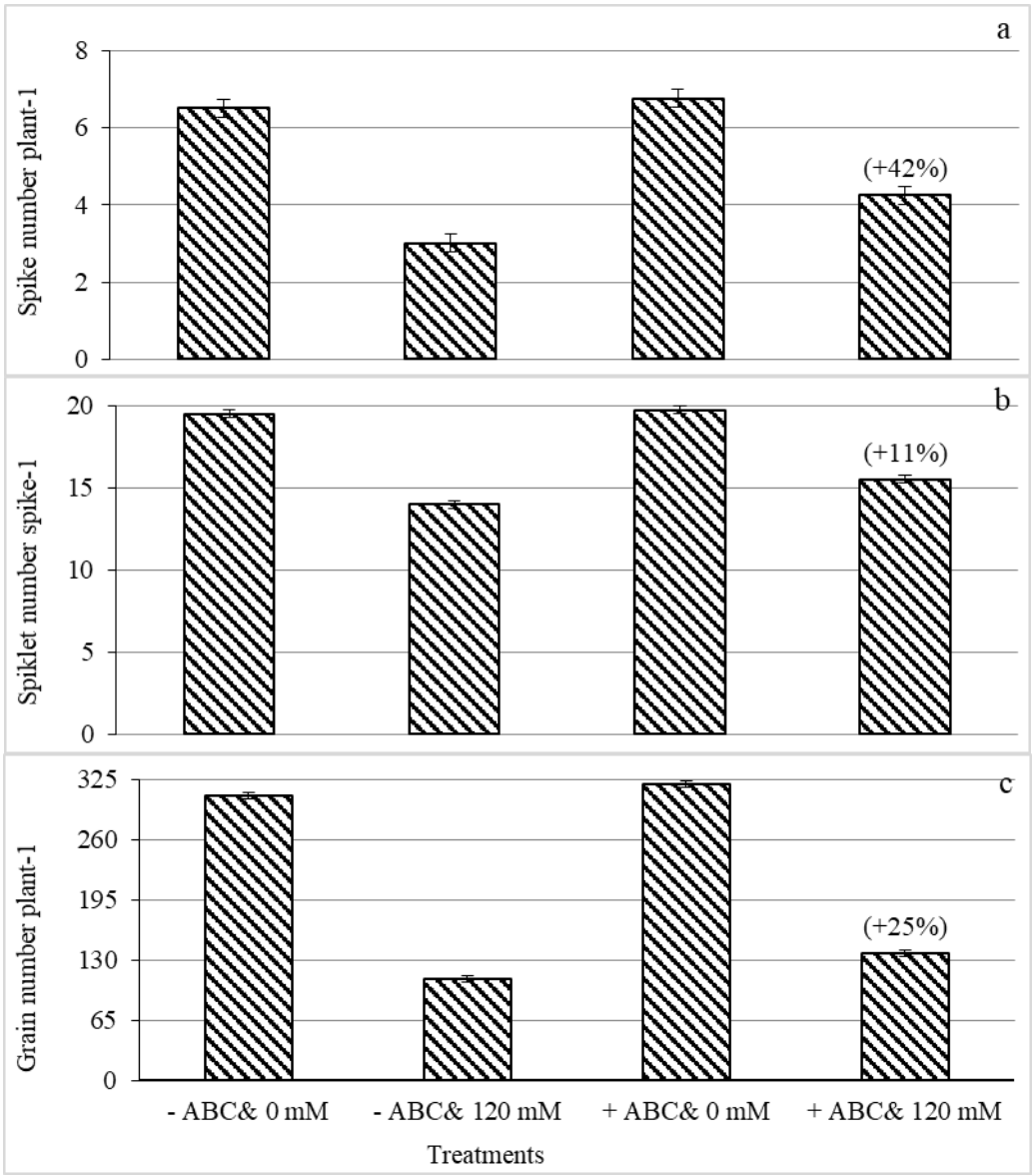

Figure (2): Effect of algal biochar and salinity treatments on (a) spike number (plant $^{-1}$), (b) spikelet number (spike $^{-1}$), and (c) grain number (plant $^{-1}$) of wheat. Each datum indicates the mean value and vertical lines on top of bars indicate standard error of means (n = 4). Values in parenthesis indicate the percent increase from without the addition of ABC treatment to with the addition of ABC treatment under salinity stress (120mM NaCl)

Both algal biochar and salinity treatments significantly ($P< 0.05$) influenced grain yield (g/plant^{1}). The result showed that salinity stress decreased grain yield (plant^{-1}) while algal biochar addition significantly increased grain yield in both salinity levels as compared to respective non-algal biochar treatment (Fig. 3a). Fig. 3b revealed that 1000 grain weight was significantly affected by salinity stress as well as algal biochar application. Under 120mM Nacl salinity level 1000 grain weight was decreased. However biochar addition alleviated the negative effect of salinity and resulted in an increased 1000 grain weight as compared to untreated plants (Fig. 3b). On one hand, the results showed that salinity stress negatively affected harvest index and resulted in decreased harvest index trait. On the other hand, the biochar addition significantly influenced harvest index traits under saline and non-saline conditions compared to respective non-biochar treatment (Fig. 3c).

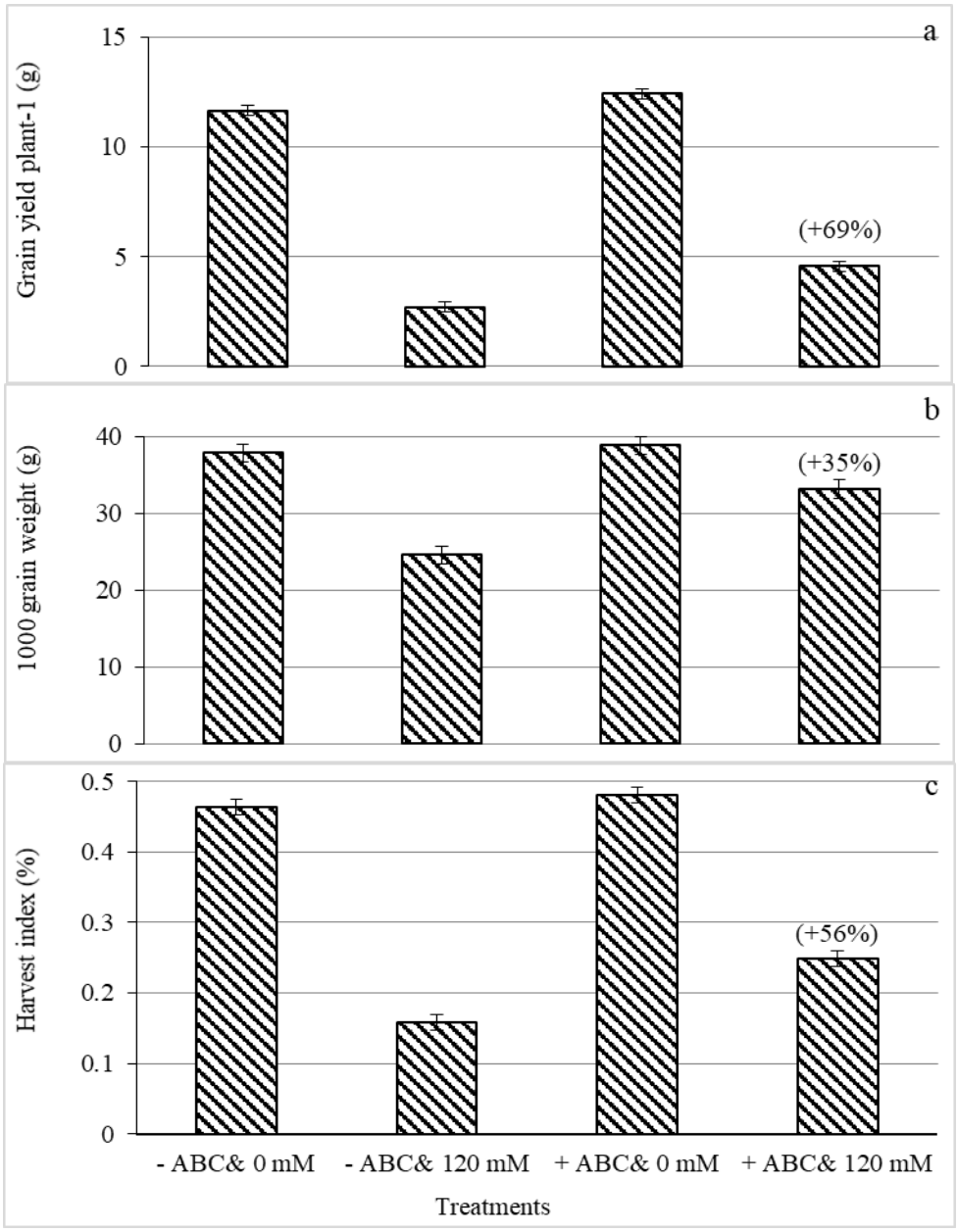

Figure (3): Effect of algal biochar and salinity treatments on (a) grain yield (g/plant^{1}) (b) 1000 grains weight (g) and (c) harvest index (%) of wheat. Each datum indicates the mean value and vertical lines on top of bars indicate standard error of means (n = 4). Values in parenthesis indicate the percent increase from without the addition of ABC treatment to with the addition of ABC treatment under salinity stress (120mM NaCl)

DISCUSSION

Salinity is considered one of the abiotic environmental stresses that limit the production of many agricultural crops, due to the huge losses it causes because of its negative impact on many morphological, physiological, and biochemical processes of the plant (Kibria and Hoque, 2019, Ehtaiwesh et al., 2024). Therefore, the development and use of modern technologies and nature-based solutions are urgently needed, it is suggested that algal biochar amendment could be an effective approach for sustaining crop production in salinity-affected soils (Mona et al., 2021; Kenneth et al., 2022). As aforementioned, the aim of the current study was to evaluate the ability of algal biochar to mitigate the negative effects of salinity on some growth and yield traits of wheat plants. The results here indicated that salinity significantly ($P< 0.001$) decreased the growth and yield traits of wheat, while the application of algal biochar mitigated the negative effects of salinity on wheat performance. This outcome agreed with previous studies, which reported that the application of biochar alleviated the negative effect of stress on crops, wheat (Akhtar et al, 2015), maize (Ullah et al., 2020; Ali et al., 2021), barley (Gul et al., 2023), rice (Chen et al., 2021), potato (Liu et al., 2017) and tomato (Almaroai and Eissa. 2020; Calcan et al., 2022). Salinity affects plant growth because it increases the osmotic pressure of the soil solution (Munns et al., 2020).

A high concentration of total salts in the soil leads to an increase in its osmotic pressure, which causes the plant to suffer when it acquires water from the soil (Zahra et al., 2020). In the present study, salinity treatment limited plant growth and yield, this reduction in growth and yield traits under salinity stress could be attributed to reduced water uptake, osmotic potential, and ions toxicity to the plants (Safdar et al., 2019; Munns et al., 2020). Soil salinity occurs when there is an accumulation of dissolved salts in the area of root growth at a concentration high enough to hinder the ideal growth of the plants. Dissolved salts in this study consist mainly of Na^+ and Cl^-, when these ions are presented in high concentrations in the root growth zone; they cause toxic effects on plant growth. It also causes an imbalance in the availability of essential nutrients, for example, the competition of Na^+ with K^+ ions. However, the application of algal biochar reduced the negative effect of salinity stress, which could be due to the adsorbing of toxic ions such as Na^+ and Cl^- from the soil solution. This finding agrees with early studies on potato plants (Akhtar et al., 2015; Ehtaiwesh, 2022c). Another possibility of the ability of biochar to minimize the negative effect of salinity stress may be due to the role of biochar in increasing the cation exchange capacity (Domingues et al, 2020; Mohamed et al., 2021; Ghassemi-Golezani and Rahimzadeh, 2024). Cation exchange capacity is a critical soil property that directly stimulates nutrient availability and plant growth (Antonangelo et al., 2024). Also, some studies have reported that adding biochar helped in nutrient and water retention, thus reducing irrigation needs, improving agricultural efficiency, and increasing crop yields (Fischer et al., 2019; Semida et al., 2019; Cui et al., 2022). In addition, many studies suggested that biochar is added to agricultural sandy and or acidic soil because it is used as a soil improver due to its unique ability to retain water and increase soil fertility, which increases agricultural production (Dai et al., 2020; Abideen et al., 2022).

CONCLUSION

Algal biochar is a sustainable and eco-friendly approach for improving plant performance under stressed conditions. The experiment was conducted to investigate the potential effects of algal biochar applied to wheat grown under saline and non-saline conditions. The study concluded that algal biochar positively enhanced wheat growth and yield indicated by better performance under both conditions. The main result overall is that algal biochar application had a major impact on the growth and yield traits of wheat compared with the controls either with, or without salinity stress. The study suggested that algal biochar could provide a significant revenue stream as a soil amelio-

rant and fertilizer under saline and non-saline conditions. However, more studies are required to explore the effect of algal biochar on both salt-tolerant and non-salt-tolerant plants in salt-affected soils.

ACKNOWLEDGEMENT

The authors are thankful to the plant science department, at Zawia University for providing equipment for the study. We are also grateful to thank Dr. Najat Owen, the director of the research and consulting office at the faculty of science at Sabratha University.

Duality of interest: The authors declare that we/ have no duality of interest associated with this manuscript.

Author contributions: Contribution is equal between authors.

Funding: The authors did not receive any funding or financial support for the work reported in this manuscript.

REFERENCES

Abd el Aal, A. A., Shehata, H. S., & Elgaml, N. M. (2020). Maximizing Utilization of Bio-Fertilizers Immobilized on Bio-Char to Improve Bio-Characterization of Stevia Plant (Honey Leaves). *Middle East J*, *9*(4), 1066-1078.

Abideen, Z., Waqif, H., Munir, N., El-Keblawy, A., Hasnain, M., Radicetti, E., ... & Haider, G. (2022). Algal-mediated nanoparticles, phycochar, and biofertilizers for mitigating abiotic stresses in plants: A review. *Agronomy*, *12*(8), 1788.

Akhtar, S. S., Andersen, M. N., & Liu, F. (2015). Biochar mitigates salinity stress in potato. *Journal of agronomy and crop science*, *201*(5), 368-378.

Ali, A. Y. A., Ibrahim, M. E. H., Zhou, G., Zhu, G., Elsiddig, A. M. I., Suliman, M. S. E., ... & Salah, E. G. I. (2022). Interactive impacts of soil salinity and jasmonic acid and humic acid on growth parameters, forage yield and photosynthesis parameters of sorghum plants. *South African Journal of Botany*, *146*, 293-303.

Ali, L., Xiukang, W., Naveed, M., Ashraf, S., Nadeem, S. M., Haider, F. U., & Mustafa, A. (2021). Impact of biochar application on germination behavior and early growth of maize seedlings: insights from a growth room experiment. *Applied Sciences*, *11*(24), 11666.

Almaroai, Y. A., & Eissa, M. A. (2020). Effect of biochar on yield and quality of tomato grown on a metal-contaminated soil. *Scientia Horticulturae*, *265*, 109210.

Ammar, E. E., Aioub, A. A., Elesawy, A. E., Karkour, A. M., Mouhamed, M. S., Amer, A. A., & El-Shershaby, N. A. (2022). Algae as Bio-fertilizers: Between current situation and future prospective. *Saudi Journal of Biological Sciences*, *29*(5), 3083-3096.

Antonangelo, J. A., Culman, S., & Zhang, H. (2024). Comparative analysis and prediction of cation exchange capacity via summation: influence of biochar type and nutrient ratios. *Frontiers in Soil Science*, *4*, 1371777.

Atia, A., Barhoumi, Z., Debez, A., Hkiri, S., Abdelly, C., Smaoui, A., ... & Gouia, H. (2018). Plant hormones: Potent targets for engineering salinity tolerance in plants. *Salinity Responses and Tolerance in Plants, Volume 1: Targeting Sensory, Transport and Signaling Mechanisms*, 159-184.

Ayub, M. A., Ahmad, H. R., Ali, M., Rizwan, M., Ali, S., ur Rehman, M. Z., & Waris, A. A. (2020). Salinity and its tolerance strategies in plants. In *Plant life under changing environment* (pp. 47-76). Academic Press.

Baweja, P., Kumar, S., & Kumar, G. (2019). Organic fertilizer from algae: a novel approach towards sustainable agriculture. *Biofertilizers for sustainable agriculture and environment*, 353-370.

Bird, M. I., Wurster, C. M., de Paula Silva, P. H., Bass, A. M., & De Nys, R. (2011). Algal biochar–production and properties. *Bioresource technology*, *102*(2), 1886-1891.

Calcan, S. I., Pârvulescu, O. C., Ion, V. A., Răducanu, C. E., Bădulescu, L., Madjar, R., ... & Jerca, I. O. (2022). Effects of biochar on soil properties and tomato growth. *Agronomy*, *12*(8), 1824.

Chen, X., Yang, S., Ding, J., Jiang, Z., & Sun, X. (2021). Effects of biochar addition on rice growth and yield under water-saving irrigation. *Water*, *13*(2), 209.

Cui, L., Liu, Y., Yan, J., Hina, K., Hussain, Q., Qiu, T., & Zhu, J. (2022). Revitalizing coastal saline-alkali soil with biochar application for improved crop growth. *Ecological Engineering*, *179*, 106594.

Dai, Y., Zheng, H., Jiang, Z., & Xing, B. (2020). Combined effects of biochar properties and soil conditions on plant growth: A meta-analysis. *Science of the total environment*, *713*, 136635.

Domingues, R. R., Sánchez-Monedero, M. A., Spokas, K. A., Melo, L. C., Trugilho, P. F., Valenciano, M. N., & Silva, C. A. (2020). Enhancing cation exchange capacity of weathered soils using biochar: feedstock, pyrolysis conditions and addition rate. *Agronomy*, *10*(6), 824.

Ehtaiwesh, Amal. (2016). Effects of salinity and high temperature stress on winter wheat genotypes. PhD diss., Kansas State University. Manhattan KS. USA.

Ehtaiwesh, A. (2019). The effect of salinity on wheat genotypes during germination stage. Al-Mukhtar Journal of Sciences. 34(1): 63-75.

Ehtaiwesh, A. (2022a). Effect of acetyl salicylic acid (aspirin) on growth and yield of faba bean (*Vicia faba* l.) under salinity stress. Azzaytuna University Journal. 42.415- 430.

Ehtaiwesh, A. F. (2022b). Evaluation of some Libyan barley *Hordeum vulgare* L genotypes for salinity tolerance at booting stage. Academy journal for Basic and Applied Sciences (AJBAS) 4(3): 1-17.

Ehtaiwesh, A. F. (2022c). The effect of salinity on nutrient availability and uptake in crop plants. Scientific *Journal of Applied Sciences of Sabratha University*. 9(2) 55-73.

Ehtaiwesh, A., Sunoj, J., Djanaguiraman, M., & Prasad, P. V. (2024). Response of winter wheat genotypes to salinity stress under controlled environments. *Frontiers in Plant Science*, *15*, 1396498.

Estefan, G., Sommer, R., and Ryan, J. (2013). Methods of Soil, Plant, and Water Analysis: A manual for the West Asia and North Africa Region: Third Edition. Beirut, Lebanon: International Center for Agricultural Research in the Dry Areas (ICARDA).

Fahad, S., Hussain, S., Saud, S., Tanveer, M., Bajwa, A. A., Hassan, S., ... & Huang, J. (2015). A biochar application protects rice pollen from high-temperature stress. *Plant Physiology and Biochemistry*, *96*, 281-287.

FAOSTAT. (2021) Wheat Production Statistics. Available online: https://www.fao.org/faostat/en/#data/QCL (accessed on 10 September 2023).

Fatima, Z., Ahmed, M., Hussain, M., Abbas, G., Ul-Allah, S., Ahmad, S., ... & Hussain, S. (2020). The fingerprints of climate warming on cereal crops phenology and adaptation options. *Scientific Reports*, *10*(1), 18013.

Fischer, B. M., Manzoni, S., Morillas, L., Garcia, M., Johnson, M. S., & Lyon, S. W. (2019). Improving agricultural water use efficiency with biochar–A synthesis of biochar effects on water storage and fluxes across scales. *Science of the Total Environment*, *657*, 853-862.

Ghassemi-Golezani, K., & Rahimzadeh, S. (2024). Biochar-based nanoparticles mitigated arsenic toxicity and improved physiological performance of basil via enhancing cation exchange capacity and ferric chelate reductase activity. *Chemosphere*, 142623.

Gul, F., Khan, I. U., Rutherford, S., Dai, Z. C., Li, G., & Du, D. L. (2023). Plant growth promoting rhizobacteria and biochar production from Parthenium hysterophorus enhance seed germination and productivity in barley under drought stress. *Frontiers in Plant Science*, *14*, 1175097.

Hossain, A., Skalicky, M., Brestic, M., Maitra, S., Ashraful Alam, M., Syed, M. A., ... & Islam, T. (2021). Consequences and mitigation strategies of abiotic stresses in wheat (Triticum aestivum L.) under the changing climate. *Agronomy*, *11*(2), 241.

Joseph, S., Cowie, A. L., Van Zwieten, L., Bolan, N., Budai, A., Buss, W., ... & Lehmann, J. (2021). How biochar works, and when it doesn't: A review of mechanisms controlling soil and plant responses to biochar. *Gcb Bioenergy*, *13*(11), 1731-1764.

Kanwal, S., Ilyas, N., Shabir, S., Saeed, M., Gul, R., Zahoor, M., ... & Mazhar, R. (2018). Application of biochar in mitigation of negative effects of salinity stress in wheat (Triticum aestivum L.). *Journal of Plant Nutrition*, *41*(4), 526-538.

Kenneth, F., Joniver, C. F., Meredith, W., & Adams, J. M. (2022). The productivity effects of macroalgal biochar from Ulva (Linnaeus) bloom species on Arabidopsis thaliana (Linnaeus) seedlings. *European Journal of Phycology*, 1-16.

Kibria, M. G., & Hoque, M. A. (2019). A review on plant responses to soil salinity and amelioration strategies. *Open Journal of Soil Science*, *9*(11), 219.

Kul, R., Arjumend, T., Ekinci, M., Yildirim, E., Turan, M., & Argin, S. (2021). Biochar as an organic soil conditioner for mitigating salinity stress in tomato. *Soil Science and Plant Nutrition*, *67*(6), 693-706.

Lehmann, J., Cowie, A., Masiello, C. A., Kammann, C., Woolf, D., Amonette, J. E., ... & Whitman, T. (2021). Biochar in climate change mitigation. *Nature Geoscience*, *14*(12), 883-892.

Liu, B., Martre, P., Ewert, F., Porter, J. R., Challinor, A. J., Müller, C., ... & Asseng, S. (2019). Global wheat production with 1.5 and 2.0° C above pre-industrial warming. *Global Change Biology*, *25*(4), 1428-1444.

Liu, C., Liu, F., Ravnskov, S., Rubæk, G. H., Sun, Z., & Andersen, M. N. (2017). Impact of wood biochar and its interactions with mycorrhizal fungi, phosphorus fertilization and irrigation strategies on potato growth. *Journal of Agronomy and Crop Science*, *203*(2), 131-145.

Liu, Z., Xu, Z., Xu, L., Buyong, F., Chay, T. C., Li, Z., ... & Wang, X. (2022). Modified biochar: synthesis and mechanism for removal of environmental heavy metals. *Carbon Research*, *1*(1), 8.

Mohanavelu, A., Naganna, S. R., & Al-Ansari, N. (2021). Irrigation induced salinity and sodicity hazards on soil and groundwater: An overview of its causes, impacts and mitigation strategies. *Agriculture*, *11*(10), 983.

Mohamed, B. A., Ellis, N., Kim, C. S., Bi, X., & Chen, W. H. (2021). Engineered biochars from catalytic microwave pyrolysis for reducing heavy metals phytotoxicity and increasing plant growth. *Chemosphere*, *271*, 129808.

Mona, S., Malyan, S. K., Saini, N., Deepak, B., Pugazhendhi, A., & Kumar, S. S. (2021). Towards sustainable agriculture with carbon sequestration, and greenhouse gas mitigation using algal biochar. *Chemosphere*, *275*, 129856.

Munns, R., Passioura, J. B., Colmer, T. D., & Byrt, C. S. (2020). Osmotic adjustment and energy limitations to plant growth in saline soil. *New Phytologist*, *225*(3), 1091-1096.

Nwer, B. A., Ben Mahmoud, K. R., Zurqani, H. A., & Elaalem, M. M. (2021). Major limiting factors affecting agricultural use and production. *The Soils of Libya*, 65-75.

Parkash, V., & Singh, S. (2020). Potential of biochar application to mitigate salinity stress in eggplant. *HortScience*, *55*(12), 1946-1955.

Pshenovschi, G., Ghimis, S., Mirt, L., & Vasilievici, G. (2022). Bio-Char Production from Algal Biomass. *Chemistry Proceedings*, *7*(1), 87.

Qian, S., Zhou, X., Fu, Y., Song, B., Yan, H., Chen, Z., ... & Lai, C. (2023). Biochar-compost as a new option for soil improvement: Application in various problem soils. *Science of The Total Environment*, *870*, 162024.

Sadak, M. S., & Dawood, M. G. (2023). Biofertilizer role in alleviating the deleterious effects of salinity on wheat growth and productivity. *Gesunde Pflanzen*, *75*(4), 1207-1219.

Saidimoradi, D., Ghaderi, N., & Javadi, T. (2019). Salinity stress mitigation by humic acid application in strawberry (Fragaria x ananassa Duch.). *Scientia Horticulturae*, *256*, 108594.

Safdar, H., Amin, A., Shafiq, Y., Ali, A., Yasin, R., Shoukat, A., ... & Sarwar, M. I. (2019). A review: Impact of salinity on plant growth. *Nat. Sci*, *17*(1), 34-40.

Santos, F. M., & Pires, J. C. (2018). Nutrient recovery from wastewaters by microalgae and its potential application as bio-char. *Bioresource Technology*, *267*, 725-731.

Semida, W. M., Beheiry, H. R., Sétamou, M., Simpson, C. R., Abd El-Mageed, T. A., Rady, M. M., & Nelson, S. D. (2019). Biochar implications for sustainable agriculture and environment: A review. *South African Journal of Botany*, *127*, 333-347.

Shanmugam, S. R., Adhikari, S., Nam, H., & Sajib, S. K. (2018). Effect of bio-char on methane generation from glucose and aqueous phase of algae liquefaction using mixed anaerobic cultures. *Biomass and Bioenergy*, *108*, 479-486.

Ullah, N., Ditta, A., Khalid, A., Mehmood, S., Rizwan, M. S., Ashraf, M., ... & Iqbal, M. M. (2020). Integrated effect of algal biochar and plant growth promoting rhizobacteria on physiology and growth of maize under deficit irrigations. *Journal of Soil Science and Plant Nutrition*, *20*, 346-356.

UN. (2022). United Nations Department of Economic and Social Affairs, Population Division (2022). World Population Prospects 2022: Summary of Results. UN DESA/POP/2022/TR/NO. 3.

Wang, J., & Wang, S. (2019). Preparation, modification and environmental application of biochar: A review. *Journal of Cleaner Production*, *227*, 1002-1022.

Weber, K., & Quicker, P. (2018). Properties of biochar. *Fuel*, 217, 240-261.

Xiang, W., Zhang, X., Chen, J., Zou, W., He, F., Hu, X., ... & Gao, B. (2020). Biochar technology in wastewater treatment: A critical review. *Chemosphere*, *252*, 126539.

Zahra, N., Raza, Z. A., & Mahmood, S. (2020). Effect of salinity stress on various growth and physiological attributes of two contrasting maize genotypes. *Brazilian Archives of Biology and Technology*, *63*.

Zahra, N., Hafeez, M. B., Wahid, A., Al Masruri, M. H., Ullah, A., Siddique, K. H., & Farooq, M. (2023). Impact of climate change on wheat grain composition and quality. *Journal of the Science of Food and Agriculture*, *103*(6), 2745-2751.

Zhang, Y., Ding, J., Wang, H., Su, L., & Zhao, C. (2020). Biochar addition alleviate the negative effects of drought and salinity stress on soybean productivity and water use efficiency. *BMC Plant Biology*, *20*, 1-11.

Al-Mukhtar Journal of Basic Sciences 22 (3): 221-232, 2024
Doi: https://doi.org/10.54172/dg3v6n81

Research Article Open Access

Existence of Local Solutions for A Chemotaxis Navier Stokes System Modeling Cellular Swimming in Fluid Drops with Logistic Source

Khayriyah Arafah[1] and Aesha Lagha[2]

***Corresponding author:** ahmedaldaly789@gmail.com, Department of Mathematics, Faculty of Education, Aljafarah University, Libya

[2]Department of Mathematics, Faculty of Science, Zawia University, Libya.

Received:
12 October 2024

Accepted:
04 December 2024

Publish online:
31 December 2024

Abstract

In this paper, we are concerned with the Cauchy problem for the three-dimensional chemotaxis system with an indirect signal production mechanism involving a diffusive partial differential equation. Which describes the motion of bacteria, Eukaryotes, in a fluid. Precisely, for the Chemotaxis-Navier–Stokes system modeling cellular swimming in fluid drops. We established the existence of local solutions to the compressible chemotaxis equation. We proved the local existence of the Cauchy problem (1.1)-(1.2) in $\mathbb{R}^3$ with the small initial data by using the energy method.

Keywords: Chemotaxis system, Energy method, nonlinear diffusion.

INTRODUCTION

Chemotaxis refers to the directional movement of organisms in response to certain chemicals in their environments, which plays an essential role in various biological processes such as wound healing, cancer invasion, and avoidance of predators (Di Francesco et al., 2010). It has attracted considerable attention due to its critical role in a wide range of biological phenomena. In 1970, (Keller & Segel, 1970) derived the following chemotaxis model

$$n_t = \nabla.(\mathrm{D}(n)\nabla n) - \nabla.(nS(n)\nabla c), \quad x \in \Omega, t > 0,$$

$$c_t = \Delta c - c + n, \qquad x \in \Omega, t > 0. \qquad (1.1)$$

Where $n(x,t) and\ c(x,t)$ represent the density of the bacteria and oxygen concentration at position x and $t > 0$, respectively. The function $\mathrm{S}(n)$ measures the chemotactic sensitivity and $D(n)$ is the diffusion function. There are a large number of results about whether the solutions for the Neumann boundary problem of (1.1) globally exist or blow up in finite time. One can refer to (Horstmann & Winkler, 2005; Winkler, 2016; Zhang & Li, 2015) to find more related results. If we consider the framework in which the chemical is produced by the cells indirectly, the corresponding chemotaxis model becomes the following Keller-Segel system with indirect signal production:

$$n_t = \nabla.(D(n)\nabla n) - \nabla.(nS(n)\nabla c), \quad x \in \Omega, t > 0,$$

$$v_t = \Delta v - v - w, \qquad x \in \Omega, t > 0,$$
$$w_t = \Delta w - w - v, \qquad x \in \Omega, t > 0. \quad (1.2)$$

In a bounded domain $\Omega \in \mathbb{R}^3$ with smooth boundary, where the variables n, v, and w represent the density of cells, the concentration of signal, and the concentration of the chemical, respectively. If $N \leq 3, D(n) \equiv 1$ and $S(n) = \chi$ with $\chi > 0$, (Fujie & Senba, 2017) proved that the homogeneous Neumann boundary problem of the system (1.2) possesses a unique and globally bounded classical solution. More recent observations show that in certain cases of chemical movement in liquid environments, the interaction between cells and liquids may be significant (see e.g. (Chae et al., 2014; Cieślak & Stinner, 2012; Shi et al., 2017) and references therein). It is also important to consider the biological situation populations of bacteria may reproduce according to a logistical plan. It can be observed experimentally that spatial patterns may arise spontaneously from initially almost homogeneous distributions of bacteria (Dombrowski et al., 2004). When bacteria of the species Bacillus subtilis are suspended in the fluid (Tuval et al., 2005). conducted a detailed experimental and theoretical study on the interaction of bacterial chemotaxis, chemical diffusion, and fluid convection. In particular, by placing a water droplet containing Bacillus subtilis in a chamber with its upper surface open to the atmosphere, they observed that bacterial cells quickly get densely packed in a relatively thin liquid layer below the water-air interface through which the oxygen diffuses into the water droplet. For such processes, a mathematical model was proposed in (Wang et al., 2018; Winkler, 2012), where it is assumed that the main responsible mechanisms are the chemical movement of bacteria towards the oxygen they consume and the effect of gravity on the movement of the fluid by heavier bacteria, and the thermal transport of both cells and oxygen through the fluid see also (Chae et al., 2012). However, in different situations, bacterial migration is greatly influenced by changes in their environment (Cieślak & Laurençot, 2010). If cells consume the chemical signal, (Tuval et al., 2005) explored the following chemotactic Navier-Stokes system:

$$n_t + u.\nabla n = \nabla.(D(n)\nabla n) - \nabla.(nS(x,n,c)\nabla c), \quad x \in \Omega, t > 0,$$
$$c_t + u.\nabla c = \Delta c - nf(c), \qquad x \in \Omega, t > 0,$$
$$u_t + \kappa(u.\nabla u)u + \nabla p = \Delta u + n\nabla\varphi, \qquad x \in \Omega, t > 0,$$
$$\nabla.u = 0\,, \qquad x \in \Omega, t > 0 \qquad (1.3)$$

in a bounded domain $\Omega \subset \mathbb{R}^3$ with a smooth boundary, where $f(c)$ measures the rate at which cells consume oxygen, and $S(x,n,c)$denotes a tensor-valued (or scalar) chemotactic sensitivity. Here $u, p, \varphi,$ and $\kappa \in$ R denote the velocity field, the associated pressure of the fluid, the potential of the gravitational field, and the strength of nonlinear fluid convection, respectively. By the chemical consumption setting and the maximum principle of the parabolic equations, one can directly deduce that c is uniformly bounded from the second equation of (1.3), which leads to it being more intensively studied than the framework with signal production by the cells.(Lorz, 2010) discussed the local existence of weak solutions to in a bounded domain in R^d, d = 2,3. In the case of homogeneous boundary conditions of Neumann type of n and c, and of Dirichlet type for u, (Winkler, 2014) showed that the global weak solutions to (1.3). For more literature about this system, one can refer to (Hillen & Painter, 2009; Winkler, 2017a) and the references therein for details. There are also more results about chemotaxis systems with nonlinear chemotaxis sensitivity functions, for which we refer to (Bellomo et al., 2015; Cieślak & Winkler, 2008, 2017; Hou & Wang, 2019; Li, 2019; Pan & Wang, 2021; Rosen, 1978; Tao & Winkler, 2012; Winkler, 2017b). (Hattori & Lagha, 2021a, 2021b) showed the global

existence and asymptotic behavior of the solutions for a chemotaxis system with chemoattractant and repellent in three dimensions. In this paper, we are concerned with the following initial value problem of the Keller-Segel-Nevier-Stokes system with nonlinear diffusion:

$$\partial_t n - \Delta n + u.\nabla n = -\chi\nabla.(\mathrm{n}\nabla c) + n(n - n_\infty)$$

$$\partial_t u - \gamma\Delta u + u.\nabla u + \nabla\pi = -n\nabla\varphi \qquad (1.4)$$

$$\partial_t c - \Delta c + u.\nabla c = -nc$$

$$\nabla.u = 0 \quad t > 0, \qquad x \in \mathbb{R}^3.$$

With initial data

$$(n,u,c)|_{t=0} = \big(n_0(x), u_0(x), c_0(x)\big),\ x \in \mathbf{R}^3, \qquad (1.5)$$

where$\big(n_0(x), u_0(x), c_0(x)\big) \to (n_\infty, 0,0)$ as $|\mathrm{x}| \to \infty$. Here $n = n(t,x), c = c(t,x), and\ u = u(t,x)$ denote the bacterial concentration, the oxygen concentration, and the fluid velocity field respectively. In addition, $\pi = \pi(t,x)$ is unknown pressure and φ is the gravitational potential function. The term $-\chi\nabla.(\mathrm{n}\nabla c)$ reflects the attractive movement of cells. While $n_0 = n_0(x)$, $u_0 = u_0(x)$, and $c_0 = c_0(x)$, are the given functions, the constants $\gamma > 0$, $\chi > 0$. Where n_∞ is a non-negative constant. A simple model case can be obtained upon the choices $\nabla\varphi = const.$, $\chi = 1$.

This paper is organized as follows, the first section is this introduction, which describes of some of the models used in chemotaxis, their rationale, and a very brief summary of the results obtained. In Section 2, we present notations and some assumptions that will be heavily used throughout the whole paper and state our main result. In Section 3, we prove the local-in-time existence of a regular solution for three-dimensional chemotaxis system with incompressible Navier-Stokes equations.

2. Main result

We first introduce some notations that we will use later in this paper. For $1 \le P \le \infty$, we denote L^p for the Lebesgue space on Ω, and the norms in the space $L^p(\boldsymbol{R}^3)$ are denoted by $\|.\|_{\mathrm{p}}$. For any integer $N \ge 0$, we use H^{N} to denote the Sobolev space $\mathrm{H}^{\mathrm{N}}(\boldsymbol{R}^3)$. Set $\mathrm{L}^2 = \mathrm{H}^0$, the norm of H^{N} is denoted by $\|.\|_{\mathrm{H}^{\mathrm{N}}}$. We set $\partial^\alpha = \partial_{x_1}^{\alpha_1}\partial_{x_2}^{\alpha_2}\partial_{x_3}^{\alpha_3}$ for a multi-index $\alpha = [\alpha_1, \alpha_2, \alpha_3]$ and length of α is $|.| = \alpha_3 + \alpha_2 + \alpha_3$. C and C_i, where $i = 1,2$, denote some positive (generally small) constant, where both C and C_i may take different values in different places. Let us denote the space

$$X(0,T) = \big\{n - n_\infty, u, c \in \mathrm{C}\big([0,\mathrm{T}];\mathrm{H}^3(\mathbf{R}^3)\big) \cap \mathrm{C}^1\big([0,\mathrm{T}];\mathrm{H}^1(\mathbf{R}^3)\big), \nabla(n - n_\infty), \nabla u, \nabla c \in \mathrm{L}^2\big([0,\mathrm{T}];\mathrm{H}^3(\mathbf{R}^3)\big)\big\}.$$

The main goal of this paper is to establish the existence of unique local solutions in three dimensions around a constant state $(n_\infty, 0, 0)$ for the above system (1.4). The main result of this paper is stated as follows:

Theorem 2.1. There exists a positive number ε_0 such that if

$$\|n_0, u_0, c_0\|_{\mathrm{H}^3} \le \varepsilon_0,$$

then the Cauchy problems (1.4)-(1.5) of the Keller-Segel-Nevier-Stokes system admits a unique local solution (n,u,c) with

$$(n - n_\infty, u, c) \in X(0,T).$$

The proof of the existence of local solutions in Theorem 2.1 by constructing a sequence of approximation functions based on iteration and some basic energy estimates. Let $U(t) = (n, u, c)$ be a smooth solution to the Cauchy problem of the Chemotaxis system (1.4) with initial data $U_0 = (n_0, u_0, c_0)$.

We set:

$$n(t,x) = n_\infty + \sigma(t,x).$$

Then, the Cauchy problem (1.4) and (1.5) are reformulated as

$$\begin{aligned}
&\partial_t\sigma - \Delta\sigma + u.\nabla\sigma + n_\infty\sigma = -\nabla.(\sigma\nabla c) - n_\infty\Delta c + \nabla\sigma^2\\
&\partial_t u - \gamma\Delta u + u.\nabla u = -\nabla\pi - (\sigma + n_\infty)\nabla\varphi\\
&\partial_t c + -\Delta c + u.\nabla c = -(\sigma + n_\infty)c\\
&\nabla.u = 0 \quad t > 0, x \in \mathbb{R}^3, \qquad (2.1)
\end{aligned}$$

with initial data

$$(\sigma, u, c)|_{t=0} = (\sigma_0, u_0, c_0) \to (0,0,0) \text{ as } |x| \to \infty, \quad (2.2)$$

where $\sigma_0 = n_0 - n_\infty$

3. Existence of local solutions

This section is devoted to the proof of Theorem 2.1. We construct the sequence $(n^j, u^j, c^j)_{j\geq 0}$ by solving iteratively the Cauchy problems on the following linear equations

$$\begin{aligned}
&\partial_t n^{j+1} + u^j.\nabla n^{j+1} = \Delta n^{j+1} - \nabla.\left(n^j\nabla c^{j+1}\right) + n^j(n^j - n_\infty)\\
&\partial_t u^{j+1} + u^j.\nabla u^{j+1} = \gamma\Delta u^{j+1} - \nabla\pi^{j+1} - n^j\nabla\varphi\\
&\partial_t c^{j+1} + u^j.\nabla c^{j+1} + \Delta c^{j+1} = -n^j c^{j+1} \qquad (3.1)\\
&\nabla.u^{j+1} = 0 \quad t > 0, \quad x \in \mathbb{R}^3,
\end{aligned}$$

with initial data

$$\left(n^{j+1}, u^{j+1}, c^{j+1}\right)\Big|_{t=0} = (n_0, u_0, c_0), \quad x \in \mathbb{R}^3, \quad (3.2)$$

for $j \geq 0$, where $(n^0, c^0, u^0)|_{t=0} = (n_\infty, 0,0)$ is set at initial step. Now, we set $n^j = \sigma^j + n_\infty$, then (3.1)-(3.2) can be rewritten as

$$\begin{cases}
\partial_t\sigma^{j+1} + u^j.\nabla\sigma^{j+1} + n_\infty\sigma^{j+1} = \Delta\sigma^{j+1} - \nabla.\left(\sigma^j\nabla c^{j+1}\right) - n_\infty\Delta c^{j+1} + \nabla\sigma^{j2}\\
\partial_t c^{j+1} + u^j.\nabla c^{j+1} + \Delta c^{j+1} = -\left(\sigma^j + n_\infty\right)c^{j+1}\\
\partial_t u^{j+1} + u^j.\nabla u^{j+1} = \gamma\Delta u^{j+1} - \nabla\pi^{j+1} - \left(\sigma^j + n_\infty\right)\nabla\varphi\\
\nabla.u^{j+1} = 0 \quad t > 0, \qquad x \in \mathbb{R}^3, \qquad (3.3)
\end{cases}$$

with initial data

$$(\sigma^{j+1}, c^{j+1}, u^{j+1})|_{t=0} = (\sigma_0, c_0, u_0) \to (0,0,0) \qquad (3.4)$$

as $|x| \to \infty$, for $j \geq 0$. In what follows, let us write $A^j = \left(\sigma^{j+1}, u^{j+1}, c^{j+1}\right)_{j\geq 0}$ and $A_0 = (\sigma_0, u_0, c_0)$, where $A^0 \equiv (0,0,0)$. Next, we prove that $(A^j)_{j\geq 0}$ is a Cauchy sequence in the Banach space $C([0,T_1];H^3)$ for $T_1 > 0$ suitable small. At last, by taking the limit and continuous argument, we prove that (σ, u, c) is a local solution to (2.1)-(2.2). Now, we can state the following result:

Theorem 3.1.

Suppose $\|A_0\|_{H^3} \leq \varepsilon_1$, for small constants $\varepsilon_1 > 0$, $T_1 > 0$, $B_1 > 0$. Then for each $j \geq 0$, $A^j \in C([0, T_1)]; H^3)$, is well defined and

$$\sup_{0\leq t\leq T_1} \left\|A^j(t)\right\|_{H^N} \leq B_1, \qquad (3.5)$$

Moreover, $(A^j)_{j\geq 0}$ is a Cauchy sequence in Banach space $C([0, T_1]; H^3)$, the corresponding limit function denoted by A belongs to $C([0, T_1]; H^3)$ with

$$\sup_{0\leq t\leq T_1} \|A(t)\|_{H^N} \leq B, \quad (3.6)$$

and $A = (\sigma, u, c)$ is a solution to the Cauchy problem (2.1)-(2.2) over $[0, T_1]$. The Cauchy problem (2.1)-(2.2) admits at most one solution $A \in C([0, T_1]; H^3)$, which satisfies (3.6).

proof .

We begin by focusing our attention on the proof of (3.5), which will be given by an inductive argument. The trivial case is $j = 0$ since $A^0 = (0,0,0)$ by the assumption at initial step. Suppose that (3.5) holds for some $j \geq 0$ where is small enough. To prove (3.5) holds for j+1, we need some energy estimates on $(\sigma^{j+1}, c^{j+1}, u^{j+1})$.

Applying ∂^α to both sides of the first equation of (3.3), multiplying by $\partial^\alpha \sigma^{j+1}$, and integrating over $\mathbb{R}^3$ with $|\alpha| \leq 3$, we obtain

$$\frac{1}{2}\frac{d}{dt}\int_{\mathbb{R}^3}\left|\partial^\alpha \sigma^{j+1}\right|^2 dx + \int_{\mathbb{R}^3} \partial^\alpha \Delta\sigma^{j+1}\, \partial^\alpha \sigma^{j+1} dx + n_\infty \int_{\mathbb{R}^3}\left|\partial^\alpha \sigma^{j+1}\right|^2 dx,$$

$$= -\int_{\mathbb{R}^3} \partial^\alpha\left(u^j . \nabla\sigma^{j+1}\right) \partial^\alpha \sigma^{j+1}\, dx - \int_{\mathbb{R}^3} \partial^\alpha \nabla .\left(\sigma^j \nabla c^{j+1}\right) \partial^\alpha \sigma^{j+1}\, dx$$

$$+ n_\infty \int_{\mathbb{R}^3} \partial^\alpha \Delta c^{j+1}\, \partial^\alpha \sigma^{j+1} dx + \int_{\mathbb{R}^3} \partial^\alpha \sigma^{j+1}\, \partial^\alpha \sigma^{j2}\, dx.$$

By using integration by parts, we have

$$\frac{1}{2}\frac{d}{dt}\int_{\mathbb{R}^3}\left|\partial^\alpha \sigma^{j+1}\right|^2 dx + \int_{\mathbb{R}^3}\left|\partial^\alpha \nabla\sigma^{j+1}\right|^2 dx + n_\infty \int_{\mathbb{R}^3}\left|\partial^\alpha \sigma^{j+1}\right|^2 dx,$$

$$= -\int_{\mathbb{R}^3} \partial^\alpha\left(u^j . \nabla\sigma^{j+1}\right) \partial^\alpha \sigma^{j+1}\, dx - \int_{\mathbb{R}^3} \partial^\alpha\left(\sigma^j \nabla c^{j+1}\right) \partial^\alpha \nabla\sigma^{j+1}\, dx$$

$$+ n_\infty \int_{\mathbb{R}^3} \partial^\alpha \nabla c^{j+1}\, \partial^\alpha \nabla\sigma^{j+1} dx + \int_{\mathbb{R}^3} \partial^\alpha \sigma^{j+1}\, \partial^\alpha \sigma^{j2}\, dx. \quad (3.7)$$

By using the Cauchy inequality the terms on the right-hand side are bounded by

$$C\|u^j\|_{H^3}\|\nabla\sigma^{j+1}\|^2_{H^3} + C\|\sigma^j\|_{H^3}\|\nabla c^{j+1}\|_{H^3}\ \|\nabla\sigma^{j+1}\|_{H^3}$$
$$+n_\infty\left(\ \|\nabla c^{j+1}\|_{H^3}\ \|\nabla\sigma^{j+1}\|_{H^3}\right) + C\|\sigma^j\|_{H^3}\ \|\nabla\sigma^{j+1}\|_{H^3} + \|\sigma^j\|^2_{H^3}. \quad (3.8)$$

Then, by taking the summation over $|\alpha| \le 3$, we have

$$\frac{1}{2}\frac{d}{dt}\|\sigma^{j+1}\|^2_{H^3} + \frac{1}{2}\|\nabla\sigma^{j+1}\|^2_{H^3} + n_\infty\|\sigma^{j+1}\|^2_{H^3}$$
$$\le C\|\nabla c^{j+1}\|^2_{H^3} + C\|(u^j,\sigma^j)\|^2_{H^3}\|\nabla(\sigma^{j+1},c^{j+1})\|^2_{H^3} + C\|\sigma^j\|^2_{H^3}. \quad (3.9)$$

By the same way, for $(3.3)_2$ on c^{j+1}, one has

$$\frac{1}{2}\frac{d}{dt}\int_{\mathbb{R}^3}|\partial^\alpha c^{j+1}|^2dx + \int_{\mathbb{R}^3}|\nabla\partial^\alpha c^{j+1}|^2dx + n_\infty\int_{\mathbb{R}^3}|\partial^\alpha c^{j+1}|^2dx$$
$$= -\int_{\mathbb{R}^3}\partial^\alpha(u^j.\nabla c^{j+1})\,\partial^\alpha c^{j+1}dx - \int_{\mathbb{R}^3}\partial^\alpha(\sigma^j c^{j+1})\,\partial^\alpha c^{j+1}dx\ .$$

The terms on the right-hand side of the previous inequality are bounded by

$$c\|u^j\|_{H^3}\|\nabla c^{j+1}\|^2_{H^3} + c\|\sigma^j\|_{H^3}\|\nabla c^{j+1}\|_{H^3}\|c^{j+1}\|_{H^3}.$$

Thus, we have

$$\frac{1}{2}\frac{d}{dt}\|c^{j+1}\|^2_{H^3} + \frac{1}{2}\|\nabla c^{j+1}\|^2_{H^3} + \frac{n_\infty}{2}\|c^{j+1}\|^2_{H^3} \le C\|(u^j,\sigma^j)\|^2_{H^3}\|\nabla c^{j+1}\|^2_{H^3}. \quad (3.10)$$

Similarly, for the $(3.3)_3$ on u^{j+1}, we get that

$$\frac{1}{2}\frac{d}{dt}\int_{\mathbb{R}^3}|\partial^\alpha u^{j+1}|^2dx + \gamma\int_{\mathbb{R}^3}|\nabla\partial^\alpha u^{j+1}|^2dx =$$
$$-\int_{\mathbb{R}^3}\partial^\alpha(u^j.\nabla u^{j+1}).\partial^\alpha u^{j+1}dx + \int_{\mathbb{R}^3}\partial^\alpha(\nabla\sigma^j\varphi).\partial^\alpha u^{j+1}dx.$$

Where the right-hand side of the previous equation is bounded by

$$C\|u^j\|_{H^3}\ \|\nabla u^{j+1}\|^2_{H^3} + C\|\sigma^j\|^2_{H^3} + \frac{1}{2}\|\nabla u^{j+1}\|^2_{H^3}.$$

Then, after taking summation over $|\alpha| \le 3$ and using the Cauchy inequality, one has

$$\frac{1}{2}\frac{d}{dt}\|u^{j+1}\|^2_{H^3} + \frac{\gamma}{2}\|\nabla u^{j+1}\|^2_{H^3} \le C\|\sigma^j\|^2_{H^3} + C\|u^j\|^2_{H^3}\|\nabla u^{j+1}\|^2_{H^3}. \quad (3.11)$$

Then the linear combination (3.9)+(3.10)× d+(3.11) leads to

$$\frac{1}{2}\frac{d}{dt}\left(\|\sigma^{j+1}\|^2_{H^3} + d\|c^{j+1}\|^2_{H^3} + \|u^{j+1}\|^2_{H^3}\right)$$

$$+C_1\left\|\nabla(\sigma^{j+1}, c^{j+1}, u^{j+1})\right\|_{H^3}^2 + C_2\left\|\sigma^{j+1}, c^{j+1}\right\|_{H^3}^2$$

$$\leq C\left\|\sigma^j\right\|_{H^3}^2 + C\left\|\sigma^j, c^j, u^j\right\|_{H^3}^2\left\|\nabla(\sigma^{j+1}, c^{j+1}, u^{j+1})\right\|_{H^3}^2, \qquad (3.12)$$

By choosing $d > 0$ large enough. Further, after Integrating (3.12) over $[0, t]$ for all $t \in [0, T_1]$, we have

$$\left\|A^{j+1}(t)\right\|_{H^3}^2 + C_1\int_0^t \left\|\nabla A^{j+1}(s)\right\|_{H^3}^2 ds + C_2\int_0^t \left\|\sigma^{j+1}, c^{j+1}\right\|_{H^3}^2$$

$$\leq C\left\|A_0\right\|_{H^3}^2 + C\int_0^t \left\|A^j(s)\right\|_{H^3}^2 ds + C\int_0^t \left\|A^j(s)\right\|_{H^3}^2 \left\|\nabla A^{j+1}(s)\right\|_{H^3}^2 ds, \quad (3.13)$$

for some positive constants C_1 *and* C_2. From the inductive assumption, the previous inequality can be re-estimated as

$$\left\|A^{j+1}(t)\right\|_{H^3}^2 + C_1\int_0^t \left\|\nabla A^{j+1}(s)\right\|_{H^3}^2 ds + C_2\int_0^t \left\|\sigma^{j+1}, c^{j+1}\right\|_{H^3}^2 ds$$

$$\leq C\varepsilon_1^2 + CB_1^2 T_1 + CB_1^2\int_0^t \left\|\nabla A^{j+1}(s)\right\|_{H^3}^2 ds, \qquad (3.14)$$

for any $0 \leq t \leq T_1$. Now, we take the small constants $\varepsilon_1 > 0$, $B_1 > 0$ and $T_1 > 0$. Then, we get

$$\left\|A^{j+1}(t)\right\|_{H^3}^2 + C_1\left\|\nabla A^{j+1}(t)\right\|_{H^3}^2 + C_2\left\|\sigma^{j+1}, c^{j+1}\right\|_{H^3}^2 \leq B_1^2, \qquad (3.15)$$

for any $0 \leq t \leq T_1$. This implies that (3.5) holds for $j + 1$, Hence (3.5) is proved for all $j \geq 0$.

Next, we define

$$E(A^{j+1}(t)) := \left\|\sigma^{j+1}\right\|_{H^3}^2 + d\left\|c^{j+1}\right\|_{H^3}^2 + \left\|u^{j+1}\right\|_{H^3}^2,$$

Where the constant $d > 0$ is given in (3.12). Similar to prove (3.12), we have

$$\left|E(A^{j+1}(t)) - E(A^{j+1}(s))\right| = \left|\int_s^t \frac{d}{d\tau} E(A^{j+1}(\tau))\, d\tau\right|$$

$$\leq C\int_s^t \left\|A^j(\tau)\right\|_{H^3}^2 d\tau + C\int_s^t (1 + \left\|A^j(\tau)\right\|_{H^3}^2)\left\|\nabla A^{j+1}(\tau)\right\|_{H^3}^2 d\tau + C_2\int_0^t \left\|\sigma^{j+1}, c^{j+1}\right\|_{H^3}^2 d\tau,$$

$$\leq CB_1^{\,2}(t - s) + C\left(1 + B_1^{\,2}\right)\int_s^t \left\|\nabla A^{j+1}(\tau)\right\|_{H^3}^2 d\tau + C_2\int_0^t \left\|\sigma^{j+1}, c^{j+1}\right\|_{H^3}^2 d\tau, \quad (3.16)$$

for any $0 \leq s \leq t \leq T_1$. Here, The time integral on the right-hand side from the above inequality is bounded by (3.15), and hence $E(A^{j+1}(t))$ is Continuous in t for each $j \geq 0$. By the same argument, we can infer that both $\left\|c^{j+1}\right\|_{H^3}^2$, and $\left\|u^{j+1}\right\|_{H^3}^2$ are continuous in t. From the continuity of $E(A^{j+1}(t))$, we can also infer the continuity of $\left\|\sigma^{j+1}\right\|_{H^3}^2$. Therefore, $\left\|A^{j+1}(t)\right\|_{H^3}^2$ is continuous in time for any $j \geq 1$.

For this step, we prove that the sequence $(A^j)_{j\geq 0}$ is a Cauchy sequence in the Banach space $C([0,T_1];H^3)$, which converges to the solution $U=(\sigma,u,c)$ of the Cauchy problem (2.1)-(2.2), and satisfies (3.6). Let us take the difference of (3.3) for $j+1$ and j so that it gives

$$\partial_t(\sigma^{j+1}-\sigma^j)-\Delta(\sigma^{j+1}-\sigma^j)+n_\infty(\sigma^{j+1}-\sigma^j)=-u^j.\nabla(\sigma^{j+1}-\sigma^j)-(u^j-u^{j-1}).\nabla\sigma^j$$
$$-\nabla.\left(\sigma^j\nabla(c^{j+1}-c^j)\right)-\nabla.\left((\sigma^j-\sigma^{j-1})\nabla c^j\right)\ -n_\infty[\Delta(c^{j+1}-c^j)]\ -(\sigma^{(j+1)2}-\sigma^{j2})$$
$$\partial_t(c^{j+1}-c^j)-\Delta(c^{j+1}-c^j)+n_\infty(c^{j+1}-c^j)$$
$$=-u^j.\nabla(c^{j+1}-c^j)-(u^j-u^{j-1}).\nabla c^j-\sigma^j(c^{j+1}-c^j)-(\sigma^j-\sigma^{j-1})c^j,$$
$$\partial_t(u^{j+1}-u^j)-\gamma\Delta(u^{j+1}-u^j)\ =\ -\nabla(\pi^{j+1}-\pi^j)-u^j.\nabla(u^{j+1}-u^j)-(u^j-u^{j-1}).\nabla u^j$$
$$\nabla.(u^{j+1}-u^j)=0,\qquad t>0,x\in\mathbb{R}^3\,.$$

By using the same energy estimates as before, we have

$$\frac{1}{2}\frac{d}{dt}\|(\sigma^{j+1}-\sigma^j)\|_{H^3}^2+\|\nabla(\sigma^{j+1}-\sigma^j)\|_{H^3}^2+n_\infty\|(\sigma^{j+1}-\sigma^j)\|_{H^3}^2$$
$$\leq C\|(u^j-u^{j-1},\sigma^j-\sigma^{j-1})\|_{H^3}^2\|\nabla(\sigma^j,c^j)\|_{H^3}^2$$
$$+C\|(\sigma^j,u^j)\|_{H^3}^2\|\nabla(\sigma^{j+1}-\sigma^j,c^{j+1}-c^j)\|_{H^3}^2+n_\infty\|\nabla(c^{j+1}-c^j)\|_{H^3}^2 \qquad (3.17)$$

$$\frac{1}{2}\frac{d}{dt}\|(c^{j+1}-c^j)\|_{H^3}^2+\frac{n_\infty}{2}\|(c^{j+1}-c^j)\|_{H^3}^2+\frac{1}{2}\|\nabla(c^{j+1}-c^j)\|_{H^3}^2\leq$$
$$C\|(\sigma^j,u^j)\|_{H^3}^2\ \|\nabla(c^{j+1}-c^j)\|_{H^3}^2+C\ \|\nabla(\sigma^j-\sigma^{j-1},u^j-u^{j-1})\|_{H^3}^2\ \|\nabla c^j\|_{H^3}^2 \qquad (3.18)$$

$$\frac{1}{2}\frac{d}{dt}\|(u^{j+1}-u^j)\|_{H^3}^2+\frac{\gamma}{2}\|\nabla(u^{j+1}-u^j)\|_{H^3}^2$$
$$\leq C\|u^j\|_{H^3}^2\ \|\nabla(u^{j+1}-u^j)\|_{H^3}^2+C\|(u^j-u^{j-1})\|_{H^3}^2\ \|\nabla u^j\|_{H^3}^2$$
$$+C\ \|\sigma^j-\sigma^{j-1}\|_{H^3}^2. \qquad (3.19)$$

We combine the equations (3.17)-(3.19) to obtain

$$\frac{1}{2}\frac{d}{dt}E(A^{j+1}-A^j)+\frac{1}{4}\|\nabla(A^{j+1}-A^j)\|_{H^3}^2+\frac{n_\infty}{2}\ \|(c^{j+1}-c^j)\|_{H^3}^2+n_\infty\|(\sigma^{j+1}-\sigma^j)\|_{H^3}^2$$
$$\leq C\|A^j-A^{j-1}\|_{H^3}^2+C\|A^j\|_{H^3}^2\|\nabla(A^{j+1}-A^j)\|_{H^3}^2+C\|A^j-A^{j-1}\|_{H^3}^2\ \|\nabla A^j\|_{H^3}^2. \qquad (3.20)$$

By integrating over $[0,t]$ for any $0\leq t\leq T_1$ from (3.20), we obtain

$$\|(A^{j+1}(t)-A^j(t)\|_{H^3}^2+C_1\int_0^t\|\nabla(A^{j+1}(s)-A^j(s))\|_{H^3}^2ds+\frac{n_\infty}{2}\int_0^t\|(c^{j+1}-c^j)\|_{H^3}^2ds$$
$$+C_2\int_0^t\|(\sigma^{j+1}-\sigma^j,c^{j+1}-c^j)\|_{H^3}^2ds$$

$$\leq C(1+B_1{}^2)T_1 \sup_{0\leq t\leq T_1} \left\|(A^j(t)-A^{j-1}(t)\right\|_{H^3} + CB_1{}^2 \int_0^t \left\|\nabla(\mathrm{A^{j+1}(s)-A^j(s)})\right\|_{\mathrm{H^3}}^2 ds,$$

which by smallness of $\mathrm{B_1}$and $\mathrm{T_1}$implies that there is a constant $C_1 < 0$, there exists a constant $\theta\epsilon(0,1)$, such that for any $\mathrm{j} \geq 1$

$$\sup_{0\leq t\leq T_1} \left\|(A^{j+1}(t)-A^j(t)\right\|_{H^3} \leq \theta \sup_{0\leq t\leq T_1} \left\|(A^j(t)-A^{j-1}(t)\right\|_{H^3},$$

which implies that $(\mathrm{A^j})_{\mathrm{J}\geq 0}$ is a Cauchy sequence in the Banach space $\mathrm{C}\big([0,\mathrm{T_1}];\mathrm{H^3}(\mathbb{R}^3)\big)$.

By the property of Banach space, we have the limit function

$$\mathrm{A} = \mathrm{A^0} + \lim_{\mathrm{i}\to\infty} \sum_{j=0}^{i} \big(\mathrm{A^{j+1}} - \mathrm{A^j}\big)$$

exists in $\mathrm{C}\big([0,\mathrm{T_1}];\mathrm{H^3}(\mathbb{R}^3)\big)$, and satisfies

$$\sup_{0\leq t\leq T_1} \|A(t)\|_{H^3} \leq \sup_{0\leq t\leq T_1} \lim_{j\to\infty} inf \left\|A^j(t)\right\|_{H^3} \leq B_1. \qquad (3.21)$$

Finally, we show that the Cauchy problem (2.1)-(2.2) admits at most one solution in $\mathrm{C}([0,\mathrm{T_1}];\mathrm{H^3}(\mathbb{R}^3))$. Suppose that there exist two solutions $A, \tilde{A}$ in $\mathrm{C}([0,\mathrm{T_1}];\mathrm{H^3}(\mathbb{R}^3))$ which satisfy (3.6). Let $\tilde{\sigma} = \sigma_1(x,t) - \sigma_2(x,t)$, $\tilde{u} = u_1(x,t) - u_2(x,t)$, and $\tilde{c} = c_1(x,t) - c_2(x,t)$ solves

$$\partial_t \tilde{\sigma} + n_\infty \tilde{\sigma} - \Delta\tilde{\sigma} = u_1.\nabla\tilde{\sigma} - \tilde{u}.\nabla\sigma_2 + \nabla.(\sigma_2\nabla\tilde{c}) - \nabla.(\tilde{\sigma}\nabla c_1) - (\sigma_1+\sigma_2)\tilde{\sigma}$$

$$\partial_t \tilde{u} + \gamma\Delta\tilde{u} = -u_2\nabla\cdot\tilde{u} - \tilde{u}\nabla\cdot u_1 - \tilde{\sigma}\nabla\varphi$$

$$\partial_t \tilde{c} - \Delta\tilde{c} + n_\infty\tilde{c} = -u_2\nabla\cdot\tilde{c} - \tilde{u}.\nabla c_1 + \tilde{\sigma}c_2 + \sigma_1\tilde{c}. \qquad (3.22)$$

Multiplying $\tilde{\sigma}$ to both sides of the first equation of (3.22) and integrating over $\mathbb{R}^3$, we have

$\int_{\mathbb{R}^3} \tilde{\sigma}\,\partial_t\tilde{\sigma}dx + n_\infty \int_{\mathbb{R}^3} \tilde{\sigma}\,\tilde{\sigma}dx - \int_{\mathbb{R}^3} \tilde{\sigma}\,\Delta\tilde{\sigma}dx = \int_{\mathbb{R}^3} \tilde{\sigma}\,\nabla.(\tilde{\sigma}\nabla c_1)dx + \int_{\mathbb{R}^3} \tilde{\sigma}\,\nabla.(\sigma_2\nabla\tilde{c})dx + \int_{\mathbb{R}^3} \tilde{\sigma}\; u_1.\nabla\tilde{\sigma}dx$
$- \int_{\mathbb{R}^3} \tilde{\sigma}\;\tilde{u}.\nabla\sigma_2 dx - \int_{\mathbb{R}^3} \tilde{\sigma}\,(\sigma_1+\sigma_2)\tilde{\sigma}dx.$

Then, after using integration by parts and the Cauchy inequality, we obtain

$$\frac{d}{2\,dt}\|\tilde{\sigma}\|_{L^2}^2 + n_\infty\|\tilde{\sigma}\|_{L^2}^2 + \|\nabla\tilde{\sigma}\|_{L^2}^2$$
$$\leq\; c\|\nabla c_1\|_{L^\infty} \int_{\mathbb{R}^3} (|\tilde{\sigma}|^2 + |\nabla\tilde{\sigma}|^2)dx$$
$$+\; c\|\sigma_2\|_{L^\infty} \int_{\mathbb{R}^3} (\,|\nabla\tilde{\sigma}|^2 + |\nabla\tilde{c}|^2)dx$$
$$+\; c\|u_1\|_{L^\infty} \int_{\mathbb{R}^3} (|\tilde{\sigma}|^2 + |\nabla\tilde{\sigma}|^2)dx \;+\; c\|\nabla\sigma_2\|_{L^\infty} \int_{\mathbb{R}^3} (\,|\tilde{\sigma}|^2 + |\tilde{u}|^2)dx$$
$$+\|(\sigma_1+\sigma_2)\|_{L^\infty} \int_{\mathbb{R}^3} |\tilde{\sigma}|^2 dx. \qquad (3.23)$$

For the estimate of $\tilde{u}$, multiplying $\tilde{u}$ to both sides of the second equation of (2.1) and taking integrations in x, we obtain

$$\int_{\mathbb{R}^3} \tilde{u}\, \partial_t \tilde{u} dx + \gamma \int_{\mathbb{R}^3} \tilde{u}\, \Delta \tilde{u} dx =$$

$$-\int_{\mathbb{R}^3} \tilde{u}\,.\,(\tilde{u}\nabla \cdot u_1) dx \; - \int_{\mathbb{R}^3} \tilde{u}\;.(u_2 \nabla \cdot \tilde{u}) dx + \int_{\mathbb{R}^3} \tilde{u}\,.\,(\tilde{\sigma}\nabla\varphi) dx.$$

By using integration by parts and the Cauchy inequality, we have

$$\frac{d}{2\,dt}\|\tilde{u}\|_{L^2}^2 + \gamma\|\nabla\tilde{u}\|_{L^2}^2 \le c\|\nabla\cdot u_1\|_{L^\infty}\|\tilde{u}\|_{L^2}^2 + \|u_2\|_{L^\infty}(\|\tilde{u}\|_{L^2}^2 + \|\nabla.\,\tilde{u}\|_{L^2}^2)$$

$$+c\|\nabla\varphi\|_{L^\infty}\left(\|\tilde{u}\|_{L^2}^2 + \|\tilde{\sigma}\|_{L^2}^2\right).$$

Since L^∞ norms of σ^i, u^i, c^i where i = 1, 2 are bounded, we have

$$\frac{d}{2\,dt}\|\tilde{u}\|_{L^2}^2 + c\|\nabla\tilde{u}\|_{L^2}^2 \le c\|\tilde{\sigma}\|_{L^2}^2 + c\|\tilde{u}\|_{L^2}^2. \qquad (3.24)$$

Similarly, as above, we estimate $\tilde{c}$ as follows:

$$\frac{d}{2\,dt}\|\tilde{c}\|_{L^2}^2 + C\|\nabla\tilde{c}\|_{L^2}^2 + n_\infty\|\tilde{c}\|_{L^2}^2 \le c\left(\|\tilde{c}\|_{L^2}^2 + \|\tilde{\sigma}\|_{L^2}^2 + \|\tilde{u}\|_{L^2}^2\right). \qquad (3.25)$$

Then, after taking the linear combination of all estimates, we obtain

$$\frac{d}{2\,dt}\left(\|\tilde{\sigma}\|_{L^2}^2 + \|\tilde{u}\|_{L^2}^2 + \|\tilde{c}\|_{L^2}^2\right) + \lambda_1\left(\left(\|\tilde{\sigma}\|_{L^2}^2 + \|\tilde{c}\|_{L^2}^2\right)\right.$$

$$\left.+\lambda_2\left(\left(\|\nabla\tilde{\sigma}\|_{L^2}^2 + \|\nabla\tilde{u}\|_{L^2}^2 + \|\nabla\tilde{c}\|_{L^2}^2\right) \le C\left(\|\tilde{\sigma}\|_{L^2}^2 + \|\tilde{u}\|_{L^2}^2 + \|\tilde{c}\|_{L^2}^2\right). \qquad (3.26)\right.$$

By applying Gronwall's inequality to the above equation, we have

$$\sup_{0\le t\le T_1}\left(\|\tilde{\sigma}\|_{L^2}^2 + \|\tilde{u}\|_{L^2}^2 + \|\tilde{c}\|_{L^2}^2\right) \le e^{cT_1}\left(\|\tilde{\sigma}(0)\|_{L^2}^2 + \|\tilde{u}(0)\|_{L^2}^2 + \|\tilde{c}(0)\|_{L^2}^2\right).$$

Since the initial data of $(\tilde{\sigma},\ \tilde{u}, \tilde{v}, \tilde{w})$ are all zero for T > 0, that implies the uniqueness of the local solution.

CONCLUSION

In this paper, we prove the existence of local solutions for Navier Stokes system modeling cellular swimming in fluid drops in three dimensions. We show the existence of local solutions by the energy method. We divided the proof into four steps, using integral by parts, Cauchy –Schwarz inequality, and Gronwall's inequality to prove these steps.

REFERENCES

Bellomo, N., Bellouquid, A., Tao, Y., & Winkler, M. (2015). Toward a mathematical theory of Keller–Segel models of pattern formation in biological tissues. *Mathematical Models and Methods in Applied Sciences, 25*(09), 1663-1763.

Chae, M., Kang, K., & Lee, J. (2012). Existence of smooth solutions to coupled chemotaxis-fluid equations. *Discrete and Continuous Dynamical Systems, 33*(6), 2271-2297.

Chae, M., Kang, K., & Lee, J. (2014). Global existence and temporal decay in Keller-Segel models coupled to fluid equations. *Communications in Partial Differential Equations, 39*(7), 1205-1235.

Cieślak, T., & Laurençot, P. (2010). Finite time blow-up for a one-dimensional quasilinear parabolic–parabolic chemotaxis system. Annales de l'Institut Henri Poincaré C, Analyse non linéaire,

Cieślak, T., & Stinner, C. (2012). Finite-time blowup and global-in-time unbounded solutions to a parabolic–parabolic quasilinear Keller–Segel system in higher dimensions. *Journal of Differential Equations, 252*(10), 5832-5851.

Cieślak, T., & Winkler, M. (2008). Finite-time blow-up in a quasilinear system of chemotaxis. *Nonlinearity, 21*(5), 1057.

Cieślak, T., & Winkler, M. (2017). Global bounded solutions in a two-dimensional quasilinear Keller–Segel system with exponentially decaying diffusivity and subcritical sensitivity. *Nonlinear Analysis: Real World Applications, 35*, 1-19.

Di Francesco, M., Lorz, A., & Markowich, P. (2010). Chemotaxis-fluid coupled model for swimming bacteria with nonlinear diffusion: global existence and asymptotic behavior. *Discrete and Continuous Dynamical Systems, 28*(4), 1437-1453.

Dombrowski, C., Cisneros, L., Chatkaew, S., Goldstein, R. E., & Kessler, J. O. (2004). Self-concentration and large-scale coherence in bacterial dynamics. *Physical review letters, 93*(9), 098103.

Fujie, K., & Senba, T. (2017). Application of an Adams type inequality to a two-chemical substances chemotaxis system. *Journal of Differential Equations, 263*(1), 88-148.

Hattori, H., & Lagha, A. (2021a). Existence of global solutions to chemotaxis fluid system with logistic source. *Electronic Journal of Qualitative Theory of Differential Equations, 2021*(53), 1-27.

Hattori, H., & Lagha, A. (2021b). Global existence and decay rates of the solutions for a chemotaxis system with Lotka-Volterra type model for chemoattractant and repellent. *Discrete & Continuous Dynamical Systems: Series A, 41*(11).

Hillen, T., & Painter, K. J. (2009). A user's guide to PDE models for chemotaxis. *Journal of mathematical biology, 58*(1), 183-217.

Horstmann, D., & Winkler, M. (2005). Boundedness vs. blow-up in a chemotaxis system. *Journal of Differential Equations, 215*(1), 52-107.

Hou, Q., & Wang, Z. (2019). Convergence of boundary layers for the Keller–Segel system with singular sensitivity in the half-plane. *Journal de Mathématiques Pures et Appliquées, 130*, 251-287.

Keller, E. F., & Segel, L. A. (1970). Initiation of slime mold aggregation viewed as an instability. *Journal of theoretical biology, 26*(3), 399-415.

Li, X. (2019). On a fully parabolic chemotaxis system with nonlinear signal secretion. *Nonlinear Analysis: Real World Applications, 49*, 24-44.

Lorz, A. (2010). Coupled chemotaxis fluid model. *Mathematical Models and Methods in Applied Sciences, 20*(06), 987-1004.

Pan, X., & Wang, L. (2021). Improvement of conditions for boundedness in a fully parabolic chemotaxis system with nonlinear signal production. *Comptes Rendus. Mathématique, 359*(2), 161-168.

Rosen, G. (1978). Steady-state distribution of bacteria chemotactic toward oxygen. *Bulletin of Mathematical Biology, 40*, 671-674.

Shi, S., Liu, Z., & Jin, H.-Y. (2017). Boundedness and Large Time Behavior of an Attraction-Repulsion Chemotaxis Model With Logistic Source. *Kinetic & Related Models, 10*(3).

Tao, Y., & Winkler, M. (2012). Boundedness in a quasilinear parabolic–parabolic Keller–Segel system with subcritical sensitivity. *Journal of Differential Equations, 252*(1), 692-715.

Tuval, I., Cisneros, L., Dombrowski, C., Wolgemuth, C. W., Kessler, J. O., & Goldstein, R. E. (2005). Bacterial swimming and oxygen transport near contact lines. *Proceedings of the National Academy of Sciences, 102*(7), 2277-2282.

Wang, Y., Winkler, M., & Xiang, Z. (2018). The small-convection limit in a two-dimensional chemotaxis-Navier–Stokes system. *Mathematische Zeitschrift, 289*, 71-108.

Winkler, M. (2012). Global large-data solutions in a chemotaxis-(Navier–) Stokes system modeling cellular swimming in fluid drops. *Communications in Partial Differential Equations, 37*(2), 319-351.

Winkler, M. (2014). Stabilization in a two-dimensional chemotaxis-Navier–Stokes system. *Archive for Rational Mechanics and Analysis, 211*, 455-487.

Winkler, M. (2016). Global weak solutions in a three-dimensional chemotaxis–Navier–Stokes system. Annales de l'Institut Henri Poincaré C, Analyse non linéaire,

Winkler, M. (2017a). Global existence and slow grow-up in a quasilinear Keller–Segel system with exponentially decaying diffusivity. *Nonlinearity, 30*(2), 735.

Winkler, M. (2017b). How far do chemotaxis-driven forces influence regularity in the Navier-Stokes system? *Transactions of the American Mathematical Society, 369*(5), 3067-3125.

Zhang, Q., & Li, Y. (2015). Convergence Rates of Solutions for a Two-Dimensional Chemotaxis-Navier-Stokes System. *Discrete & Continuous Dynamical Systems-Series B, 20*(8).

Al-Mukhtar Journal of Basic Sciences 22 (3): 233-241, 2024
Doi: https://doi.org/10.54172/sja2f058

Research Article **Open Access**

Estimation of Natural Radioactivity and Radiation Hazards Indices of Some Organic Fertilizers Used in Al-Gable Al-Akhdar, Libya

Asma M. A. Othman [1*] and Rasha Y. M. Elfallah [2]

[2] Department of Physics, Faculty of Science, Darna University, Libya.

***Corresponding author:** asma.alabrdi@omu.edu.ly
Department of Physics, Faculty of Science, Omar Al-Mukhtar University, Libya.

Received:
19 October 2024

Accepted:
27 December 2024

Publish online:
31 December 2024

Abstract

In the present work, an assessment of the following levels of natural radioactivity in 5 samples of organicafertilizers collected from the market in Al Bayda City, Libya. Sodium iodide (NaI) gamma spectroscopy was used. The activityaconcentrations ofaradionuclides in the ^{238}U and ^{232}Th natural decayachain as well as ^{40}K wereadetermined. The average activity concentrations in ^{226}Ra, ^{238}U, ^{232}Th and 40K in the samples studied were found to be (± 62.74, ± 64.42, ±63.63 and ±70.88 Bq Kg^{-1} (for samples. The results of this study have been compared with the worldarecommended values of (1550, 1500, (7-50) and (100-700)) $Bqkg^{-1}$, respectively as specified by the [UNSCEAR, 2016]. The results showed that all samples had lower levels of radioactivity than the recommended limits for ^{226}Ra, ^{238}U, ^{40}K for organic fertilizers and the activity concentrations were below the thorium (7-50 Bq kg-1) except fo1,fo4 and fo5 were higher than the recommended limits. , The a radium equivalent, absorbed dose rate in air, annual effective dose equivalent for indoor and outdoor exposure, excess lifetime cancerarisk, internal and external hazard indicators were calculated. The results ofamost samples were within theaglobal averagearecommended by [UNSCEAR,2016]. So, it is safe to consume andadoes not pose a threat to the general public.

Keywords: Organic Fertilizers; Sodium Iodide; The Activity Concentration; Exposure; Cancer Risk**.**

INTRODUCTION

Each year, the absorbed doses of radiation that humans receive varyadepending on a number of variables, aincluding climate, geologicaallocation, and the use ofaradioactive material andanuclear energy by humans, Energyamanifested as particles orawaves is called radiation. Radiation can be categorized as either ionizing or non-ionizing. Ionizing radiation, such asabeta, neutrons, and gamma radiation, has sufficientaenergy to cause electronsain their orbits to be released, forming positive ions in the atoms. Non-ionizing radiation, which includes radio waves, infrared light, and visible light, isaless energetic than ionizingaradiation and cannot produce ions. Natural radioactivity permeates the terrestrial environmentaand can be found in a variety ofageological formations, including soils, phosphate rocks, air, plants, andaanimals, Around the world, the use ofafertilizers in agriculture hasabecome crucial. In addition to improving soil qualities and nutrient deficiencies, fertilizers are crucial for raising cropayields. Different ferti-

lizers have different effects on a plant's physiology and metabolism, affecting how different elements and radionuclides are absorbed. aFertilizer application has the potential to raise radionuclide content inasoil, resulting in increasedaradionuclide uptake.(Hallenburg, 2020).More than 30 million tons ofaphosphate fertilizers areaannually consumed worldwide, which increases cropaproduction and landareclamation. However, a possibleanegative effect of fertilizers is theacontamination ofacultivated lands by asome naturallyaoccurring radioactiveamaterials the natural radionuclide of fertilizersaconsists mainly ofauranium and thorium series radioisotopes and natural ^{40}K.(KeleÅŸ & Atik, 2018).

MATERIALS AND METHODS

To assess the levels of natural radioactivity in some fertilizers, 5 samples of organic fertilizers were collectedafrom Al-Bayda city market (Libya) Theacollected samples, are locally sourced Table (1) shows the details of the collected samples. They were cleaned, ground as shown in Fig. (1), and dried inathe electric oven in the laboratory for one hour per sample to get rid of moisture in samples asashown in Fig. (2), and weighed then stored in polymer containers of 250 Cm^3 volume oraat least 30 days; toaallow radioactive equilibrium to be reached. This step isanecessary to ensure that radon gas is confinedawithin theavolume and that theadaughters will also remain inathe sample. The measurement time foraboth activity and radiologicalahazards measurement was 3600 seconds. The radionuclides activity concentrations were measured using NaI (TI) detector-based gamma spectrometric system where the digiBASE system that combines a miniaturized preamplifier and detector with a powerful digital multichannel analyzer and special features for fine time-resolution measurements. The digiBASE incorporated into the NaI (TI) detector provides a gain stabilizer to significantly reduce the sensitivity of the detector to changes in ambient temperature and magnetic fields. Three gamma-ray lines of interest were (1460, 1764 and 2615) keV (Baqir, Y.et al., 2020)

Table: (1). Description of the fertilizer samples

Samples No	Description
Fo1	Derna sheep
Fo2	AL-Bayda sheep
Fo3	AL-Bayda cows
Fo4	Derna cows
Fo5	AL hisha horses

Figure: (1). Grind some samples

Figure: (2). The electric oven device

TheoreticalaCalculations

1. Calculation the Activity Concentrations

The activity of an radioactive source is defined as the rate atawhich the isotope decays. Radioactivity may be thought of as the volumeaof radiation produced in a given amount of time. The radioactivityaconcentration of the different identified radionuclides was determined by gamma-ray spectrometry with the measured for eachapeak, and the associated activity (A) was computed by using theaformula (Al-Mousawi et al., 2020).

$$A = \frac{\text{Net area (cps)}}{I_\gamma \times \xi \, .M} \qquad (1)$$

Where **A** is the Activity concentration of the gamma spectral line in Bq/Kg, **Net area (cps)** is the net detected counts per second corresponding to the energy, ξ is the Counting system efficiency of the energy, **M** is the Mass of sample in Kg and $\mathbf{I\gamma}$ is the Intensity of the gamma spectral.

2. Radium Equivalent Activity (Bq/kg).

The concentration and distributionaof ^{226}Ra, ^{232}Th and ^{40}K in the studied a samples are not uniform. Uniformity with respect to of exposure to radiation has been defined in terms of radium equivalent Ra_{eq} in (Bq kg-1) is the most extensively used radiation danger index, to represent the activityalevels of ^{226}Ra, ^{232}Th and ^{40}K by a singleaquantity, which takes into account thearadiation hazards associated withaeach component. The radium equivalent for theasamples was calculated fromathe following relation:(Geremew, 2023; Mwalongo et al., 2023).

$$Ra_{eq} = A_{Ra} + 1.34\, A_{Th} + 0.77\, A_K \qquad (2)$$

Where A_{Ra}, A_{Th} and A_K are the activity concentrations (Bq/Kg) for ^{226}R, ^{232}Th and ^{40}K respectively. The maximum value of (Ra_{eq}) must be less than 370 $Bq.kg^{-1.}$

3. Gamma Absorbed Dose Rate (Dr).

The absorbed dose rates DR (nGy h^{-1}) due to terrestrial gamma rays at 1m above ground level can be calculated by using activity concentrations of ^{226}Ra, ^{232}Th, and ^{40}K were calculated by using the equation(AL-abrdi, 2023).

$$D_r = 0.427A_U + 0.662A_{Th} + 0.043A_K \quad (3)$$

Where A_u, A_{Th} and A_K are the activity concentrations (Bq/Kg) for ^{238}U,^{232}Th and ^{40}K respectively. (Najam et al., 2022), 0.427,0.662 and 0.043 nGy.h^{-1}/BqKg^{-1} are the conversion factors of ^{238}U,^{232}Th and ^{40}K respectively

4. Internal HazardaIndex (H_{in}).

The widely used hazard indices that reflect both internal and external exposure are called internal hazard and external hazard respectively. The internalaexposure to ^{222}Rn and its daughter products are controlled by an internal hazard index, H_{in} which is defined as (UNSCEAR, 2000).

$$H_{in} = \frac{A_{Ra}}{185} + \frac{A_{Th}}{259} + \frac{A_K}{4810} \quad (4)$$

5. External HazardaIndex (H_{ex}).

The external hazard index resulting from samples gamma-ray emissions and radiological danger was computed using the relation

$$H_{ex} = \frac{A_{Ra}}{370} + \frac{A_{Th}}{259} + \frac{A_K}{4810} \leq 1 \quad (5)$$

Where A_{Ra}, A_{Th} and A_K are the activity concentrations (Bq/Kg) for ^{226}R',^{232}Th and ^{40}K respectively (Isinkaye & Emelue, 2015).

6. Excess Lifetime Cancer Risk (ELCR).

People who are exposed to radiation for an extended period of time are thought to be at risk of developing cancer. The ELCR is the increased of acquiring cancer as a result of exposure to a radiation during a person's lifetime. It is determined using the following equation

$$ELCR = E_{out} \times DL \times RF \quad (6)$$

Where E_{out} means the annual effective dose equivalent (outdoor), DL denotes life expectancy (70 years), and RF denotes thearisk factor (Sv^{-1}), which is Sievert'safatal cancer risk (Yalcin et al., 2020).

RESULTS AND DISCUSSION

The values of activityaconcentrations for organic fertilizer samples thearecorded values of radionuclides wereavaried from (44.92 to 81.24), (43.51 to 81.79), (45.79 to 82.23) and (48.62 to 85.72) Bq kg^{-1} for ^{238}U,^{226}Ra, ^{232}Th and ^{40}Krespectively,withaaverage (64.42, 62.74, 63.63 and 70.88) Bq kg^{-1} respectively Table (2), Theaoutcomes of radioactive activity concentrations for organic fertilizerasamples, including ^{238}U,^{226}Ra, ^{232}Th, and ^{40}K The samplesaanalyzed in this investigation had activity concentrations less the allowablealevel for uranium (1500 Bq kg^{-1}) (UNSCEAR, 2017), the activity concentrations are below thearadium (1550 Bq kg^{-1}), the activity concentrations are below the thorium (7-50 Bq kg^{-1}) except forasamples (fo1,fo4 and fo5) were higher than the recommendedalimits. The activity concentration is below theapotassium suggested ranges (100–700). Figure (3) show the activity concentrations of radium, uranium, thorium, and potassium in organic fertilizers.

Table (2): The average activity concentrations (Bq kg-^{1}) of the radioactive elements (^{238}U,^{226}Ra, ^{232}Th and ^{40}K) of the investigated samples.

Samples	^{238}U	Error	^{226}Ra	Error	^{232}Th	Error	^{40}K	Error
F o1	70.98	± 2.19	65.27	± 3.90	64.65	± 2.84	76.77	± 7.55
Fo2	44.92*	± 1.32	43.51*	± 4.50	45.79*	± 3.61	48.62*	± 9.12
Fo3	47.18	± 1.19	47.86	± 4.13	45.85	± 3.00	60.13	± 8.30
Fo4	78.79	± 1.49	75.27	± 3.87	82.23**	± 2.99	85.72**	± 8.85
F05	81.24**	± 1.63	81.79**	± 4.76	79.65	± 2.76	83.17	± 9.40
Average	64.42	± 1.56	62.74	± 4.23	63.63	± 3.04	70.88	± 8.64
P.L	1500		1550		7-50		100-700	

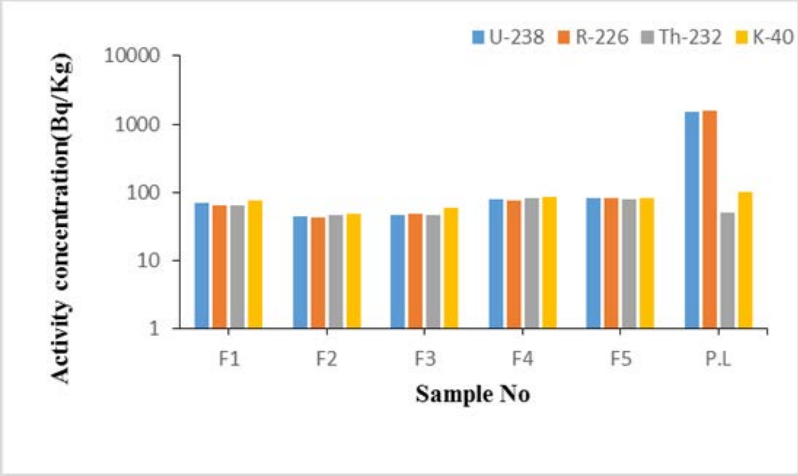

Figure: (3). The activity concentration of organic fertilizers**.**

The Radium equivalent activity (Ra_{eq}) isaa single quantity that compares the activity concentrations of ^{238}U, ^{226}Ra, ^{232}Th and ^{40}K in fertilizer samples to obtain a total activityaconcentration. The results of theacalculated (Ra_{eq}) values for organicafertilizer samples the results range from (112.74 to 202.11 Bq kg^{-1}),awith anaaverage value of 159.20 Bq/kg asashown in Fig. (4). In Table (3), the (Ra_{eq}) values for all fertilizer samples in the present study are lower than the world recommended value 370 Bq kg^{-1} . The estimated absorbed dose rate values for the investigated organic fertilizer samples range from (49.80 to 80.03 nGy h^{-1}), but theaaverage value of the absorbed dose rate for the organic fertilizer samples was 64.98 nGy h^{-1}, Fig. (5) Shows these results the studied organic fertilizer samples, they were within the recommended limits(UNSCEAR, 2017).

Table (3): The value of radium equivalent**.**

Samples code	Ra_{eq} Bq/Kg
Fo1	163.63
Fo2	112.74
Fo3	118.06
Fo4	199.47
Fo5	202.11
Average	159.20
P.L	370

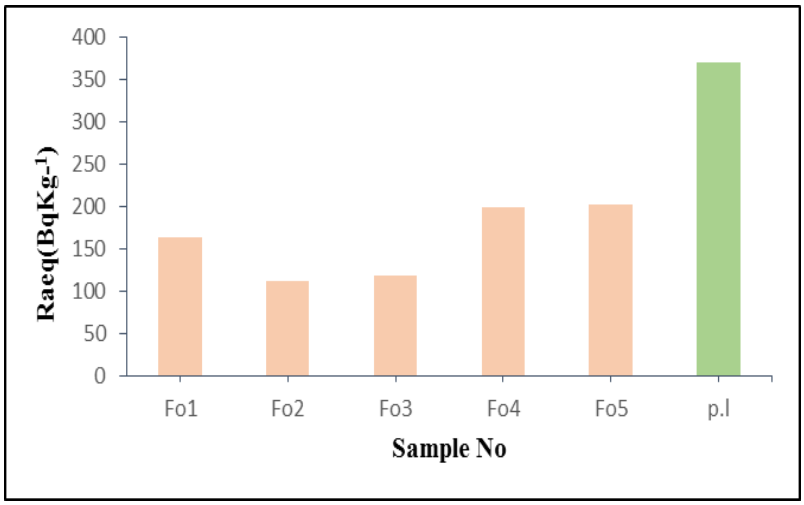

Figure: (4). Radium Equivalent of organic fertilizer samples

Table (4): The value of absorbed dose rate.

Samples code	Dose rate Dr(nGyh-$^{1)}$
Fo1	72.42
Fo2	49.80
Fo3	52.33
Fo4	70.05
Fo5	80.3
Average	64.98
P.L	84

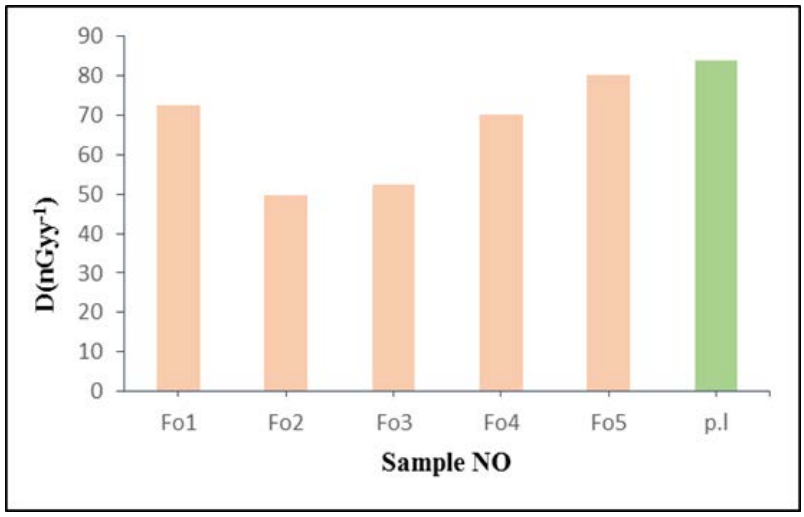

Figure: (5). The absorbed dose rate of organic fertilizer samples

The internal and externalahazard results were obtained and shownain Table (5). The results value of organicafertilizerasamples ranged from (0.42 to 0.78), with an average value 0.60, as shown in Fig. (6). in the results, all internal hazard values for the fertilizer samples under study werealower than the (UNSCEAR, 2017),arecommended values. The external hazard for organic fertilizer samples the resultsaranged from (0.30 to 0.54), with an average of 0.43, as shown in Fig. (7).

Table (5): The value of internal and external hazards

Samples code	Hin	Hex
Fo1	0.62	0.44
Fo2	0.42*	0.30*
Fo3	0.45	0.32
Fo4	0.74	0.54**
Fo5	0.78**	0.55
Average	0.60	0.43
P.L	1	1

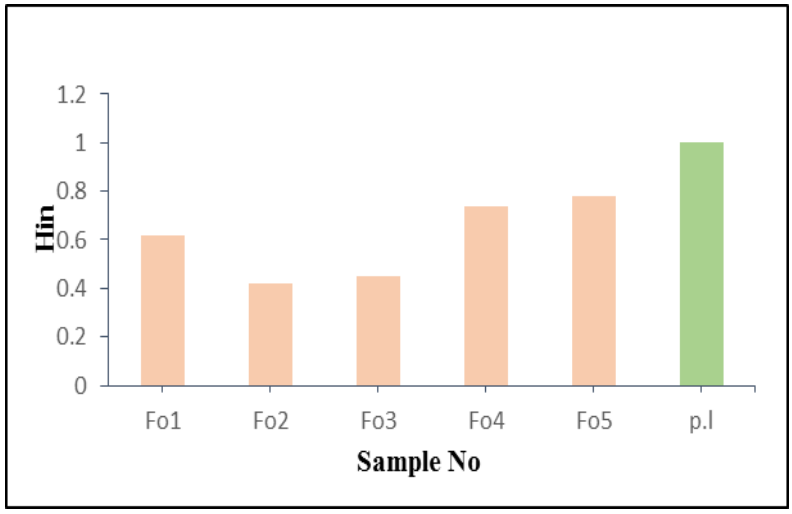

Figure: (6). Internal hazard index of organic fertilizer samples

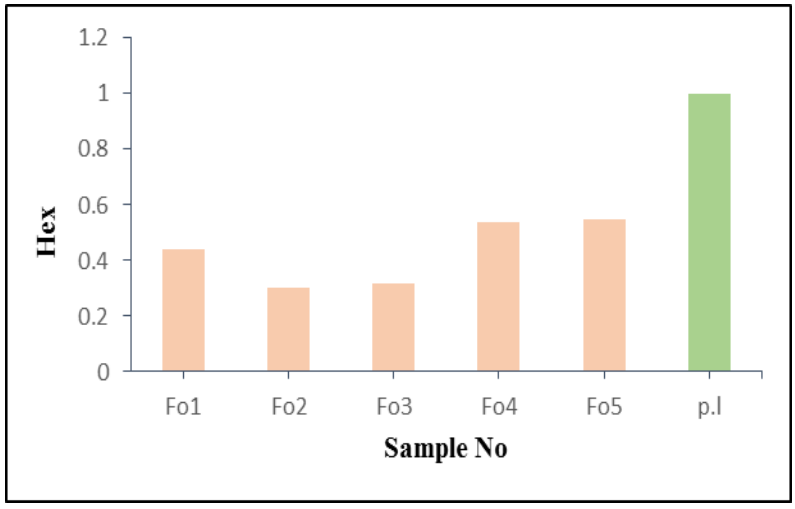

Figure: (7). External hazard index of organic fertilizer samples

Equation (6) has been calculated of ELCR where the equation dependent of life expectancy (70 years) and risk factor (0.05 sv^{-1}). Table (6) shows the excess lifetime cancer risk factor ELCR for allasamples, the recorded values of ELCR arange from (0.19 to 0.22) with an average value 0.22. The results of the ELCR values for all the organic fertilizerasamples studied were withinathe recommended limits of 0.29×10^{-3}(UNSCEAR, 2017), as shown in Fig. (8).

Table (6): The value of Excess Lifetime Cancer Risk (ELCR).

Samples code	Cancer risk factor ELCR×10^{-3}
Fo1	0.29
Fo2	0.20
Fo3	0.21
Fo4	0.19*
Fo5	0.22**
Average	0.22
P.L	0.29

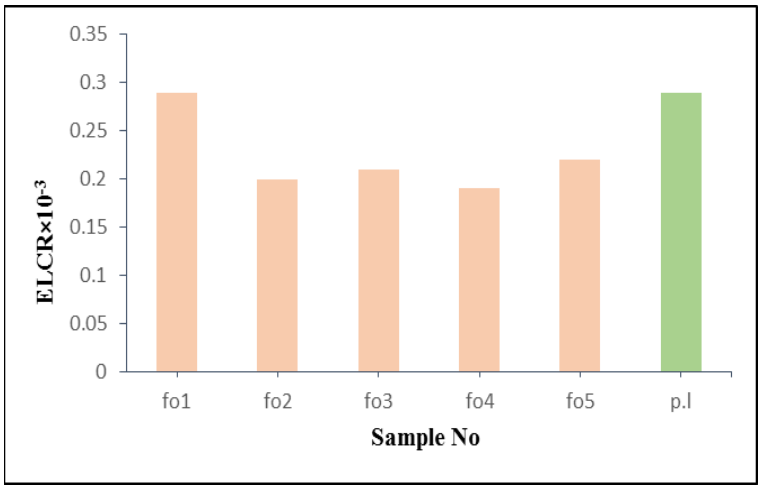

Figure: (8). The cancer risk factor of the organic fertilizer samples.

CONCLUSION

The study on natural radioactivity levels in organicafertilizers in Al-Bayda city, Libya, produced the followingaconclusions:

- Use of simple NaI gammaaspectrometer showed potential in theaassessment of radioactivity concentration.
- In this study, the activityaconcentrations of radionuclide ^{226}Ra, ^{238}U, ^{232}Th, and ^{40}K were determined to be lower than the world-recommendedavalue for all organic fertilizerasamples
- Furthermore, the activity concentrationsawere used to estimateavarious radiological features in the samples.
- The studied organic fertilizer samples hadaradium equivalent activityabelow the world recommended value of 370 Bq kg^{-1}.
- The absorbed dose rate values of theastudied samples for organic fertilizers, it was less than thearecommended limits.
- The obtained values of internal hazardaindex H_{in}, and external hazardaindex H_{ex} for all the studied sample werealower than the recommended value.
- The Excess lifetimeacancer risk (ELCR) values areafound to be much lower than the permissible level (0.29) for organic samples(UNSCEAR, 2017).

ACKNOWLEDGEMENT

We do not have any financial support or relationships that may pose conflict of interest in the cover letter submitted with the manuscript.

Duality of interest: The authors declare that they have no duality of interest associated with this manuscript.

Author contributions: A and B. developed the theoretical formalism, performed the analytic calculations and performed the numerical simulations. Both A and B. authors contributed to the final version of the manuscript. A. supervised the project.

Funding: No specific funding was received for this work.

REFERENCES

AL-abrdi, A. M. (2023). Measurements of natural radioactivity and evaluation of radiation hazard indices in Barley Samples in Libya Markets. *Libyan Journal of Basic Sciences*, *20*(2), 51-64.

Al-Mousawi, N., Mouhamad, R., & Alsaadie, N. (2020). Radiation hazards assessment of phosphate fertilizers used in Latifiyah region, Iraq. *DYSONA-Applied Science*, *1*(2), 73-80.

Geremew, H. (2023). Activity Concentration of Natural Radionuclides in Agricultural Soil, Fertilizer, their Transfer to Some Commonly Used Cereal Types, and Associated Health Hazards, Holeta, Ethiopia.

Hallenburg, J. K. (2020). *Standard methods of geophysical formation evaluation*. CRC Press.

Isinkaye, M., & Emelue, H. (2015). Natural radioactivity measurements and evaluation of radiological hazards in sediment of Oguta Lake, South East Nigeria. *Journal of Radiation Research and Applied Sciences*, *8*(3), 459-469.

KeleÅŸ, E., & Atik, D. (2018). Estimation of radioactivity caused by chemical fertilizers on Trakya sub-region soils and its potential risk on ecosystem. *European Journal of Sustainable Development*, *7*(3), 413-413.

Mwalongo, D. A., Haneklaus, N. H., Carvalho, F. P., Lisuma, J. B., Kivevele, T. T., & Mtei, K. M. (2023). Influence of phosphate fertilizers on the radioactivity of agricultural soils and tobacco plants in Kenya, Tanzania, and Uganda. *Environmental Science and Pollution Research*, *30*(34), 83004-83023.

Najam, L. A., Mahmmod, R. H., & Albanna, O. M. J. (2022). Evaluation of Natural Radionuclides in Samples of Plant Fertilizers Used in Iraq and Radiation Hazard Indicators. *Iranian Journal of Science and Technology, Transactions A: Science*, *46*(3), 979-987.

UNSCEAR, U. N. S. C. o. t. E. o. A. R. (2000). *Sources and Effects of Ionizing Radiation, United Nations Scientific Committee on the Effects of Atomic Radiation (UNSCEAR) 2000 Report, Volume I: Report to the General Assembly, with Scientific Annexes-Sources*. United Nations.

UNSCEAR, U. N. S. C. o. t. E. o. A. R. (2017). *Sources, effects and risks of ionizing radiation, united nations scientific committee on the effects of atomic radiation (UNSCEAR) 2016 report: report to the general assembly, with scientific annexes*. United Nations.

Yalcin, G. D., Danisik, N., Baygin, R. C., & Acar, A. (2020). Systems biology and experimental model systems of cancer. *Journal of Personalized Medicine*, *10*(4), 180.

Al-Mukhtar Journal of Basic Sciences 22 (3): 242-249, 2024
Doi: https://doi.org/10.54172/zbpfpp61

Research Article **Open Access**

Investigation of Impact of Antibiotics on Bacterial Strains Identified in Spring Water Located in Massa City, Libya

Abeer Hamoudah [1], Mohammed Miftah[2] and Hasna Akub[3*]

[2] Department of Botany, Faculty of Science, Omar Al-Mukhtar University, Al Bayda, Libya.

[2] Higher Institute of Medical Sciences and Technologies, Al Marj, Libya.

***Corresponding author:** hasna.akub@omu.edu.ly , Department of Microbiology, Faculty of Science, University of Omar Al-Mukhtar, Libya

Received:
02 November 2024

Accepted:
28 December 2024

Publish online:
31 December 2024

Abstract

The emergence of antibiotic-resistant bacteria in drinking water sources poses a significant public health threat. This study examines the presence of antibiotic-resistant bacteria in four springs in Massa, Libya, and explores the impact of seasonal changes on antibiotic sensitivity. Water samples were collected from each spring during the autumn and winter of 2023, and antibiotic susceptibility tests were performed using different classes of antibiotics. The results revealed the presence of antibiotic-resistant strains of *Escherichia coli*, with significant interactions between seasonal changes, bacterial species, and antibiotic types. The study highlights the complex interplay between these factors, underscoring the need for a multifaceted approach to address antibiotic resistance in drinking water sources. The findings contribute to a deeper understanding of the dynamics influencing antibiotic resistance and provide valuable insights for the development of targeted strategies to mitigate this public health challenge.

Keywords: Spring Water, Antibiotic Resistance, Bacteria, Pathogens

INTRODUCTION

The emergence of antibiotic-resistant bacteria in sources of drinking water is an escalating global issue. Research conducted by (Coleman et al., 2013) revealed that private drinking water sources in Canada were found to be contaminated with antimicrobial-resistant strains of *Escherichia coli*, which underscores the potential dangers posed by waterborne pathogens. Furthermore, a study by (Babalola et al., 2021) examined bacterial isolates from household water distribution tanks in Ado-Ekiti, specifically analyzing patterns of antibiotic resistance and the profiles of plasmids present in these isolates.

In a related investigation, (Kothari et al., 2023) assessed the interplay between antibiotics and heavy metal arsenic, focusing on the horizontal gene transfer from multidrug-resistant clinical strains to antibiotic-sensitive environmental strains. This research provides valuable insights into the mechanisms that facilitate the dissemination of antibiotic resistance. The significance of maintaining low bacterial concentrations in drinking water systems is emphasized by the US EPA's National Primary Drinking Water Regulations, which aim to safeguard water quality (US EPA, 2024). Coliform bacteria, often utilized as indicators of water quality, exhibit behaviors

akin to pathogens and are influenced by environmental conditions and treatment processes (McDonald, 2023).

The detection of multiple antibiotic-resistant bacteria in drinking water has raised significant concerns regarding their prevalence and the effectiveness of removal strategies within water systems (Sanganyado & Gwenzi, 2019). The improper use of antibiotics is a contributing factor to the rise of antibiotic-resistant bacteria, highlighting the necessity for responsible antibiotic usage and the avoidance of unnecessary prescriptions (Reitter et al., 2021). Reports of antibiotic-resistant bacteria and resistance genes in drinking water distribution systems further emphasize the urgent need for effective monitoring and mitigation strategies to address this public health challenge (Gu et al., 2022; Tiwari et al., 2022).

Recent investigations have focused on the seasonal variations in the quality of drinking water, particularly concerning bacterial populations. A study conducted by (Siedlecka et al., 2020) examined the occurrence of antibiotic-resistant bacteria (ARB) and antibiotic resistance genes (ARGs) within a drinking water distribution system (DWDS) across different seasons, specifically summer and winter. This research was carried out in Wrocław, Poland, utilizing a full-scale DWDS that received water from two distinct water treatment plants (WTPs). The findings underscored significant spatiotemporal fluctuations in both antibiotic resistance and the composition of bacterial communities present in the DWDS.

Coliform bacteria, which are typically found in the intestines of humans and animals, have been observed to thrive in drinking water reservoirs, with concentrations exceeding 10,000 per 100 ml during certain seasonal periods (Wisconsin Department of Health Services, 2024). Research by (Reitter et al., 2021) identified the genera Lelliottia and Enterobacter as key players in the seasonal variations of coliform bacteria populations. Additionally, elevated turbidity levels in drinking water have been linked to a rise in pathogenic microorganisms, including viruses, parasites, and specific bacterial strains (US EPA, 2024; McDonald, 2023).

The detection of coliform bacteria in drinking water serves as an indicator of potential contamination risks, which may include the presence of more harmful pathogens (Michigan Department of Health and Human Services, 2024; Wisconsin Department of Health Services, 2024). Understanding the effects of seasonal changes, rainfall, and other environmental influences on bacterial presence and diversity in drinking water is crucial for maintaining water quality and safeguarding public health (MacDonald, 2016). This knowledge is essential for developing effective strategies to monitor and manage drinking water systems in the face of changing environmental conditions.

The emergence of antibiotic-resistant bacteria in sources of drinking water represents a critical public health challenge. It is essential to comprehend the pathways through which antibiotic resistance disseminates, to conduct thorough assessments of water quality, and to advocate for the judicious use of antibiotics as fundamental measures to tackle this problem. There is a pressing need for additional research to investigate the occurrence of antibiotic-resistant bacteria across various water sources and to evaluate the efficacy of strategies aimed at reducing their prevalence. Moreover, further studies are required to gain insights into the factors influencing seasonal variations in water quality and to formulate effective approaches for monitoring and controlling bacterial contamination in drinking water supplies.

In the current study, we aim to explore and assess the presence of antibiotic-resistant bacteria within the environmental context of four springs located in the Massa region. This study seeks

to elucidate the impact of antibiotics on *Escherichia coli* and various other bacterial species.

MATERIALS AND METHODS

Study Area

Massa is a small city situated in eastern Libya, approximately 10 kilometers to the west of Beida. The Green Mountain region, known for its elevated terrain and forested landscapes, is located in northeastern Libya. This area is distinguished by its significant elevation compared to much of the country, as well as its notably high levels of precipitation. Furthermore, the fertile soil found in this region is conducive to agricultural activities, enhancing its value for farming endeavors.

Collecting of samples

Water samples were collected from four distinct springs, with three replicate samples gathered from each site during the autumn and winter seasons of 2023 in Massa city. In total, twelve samples were obtained and analyzed. The samples were stored in plastic containers with ice packs to maintain a cool temperature during transport, ensuring they did not freeze. Following collection, the samples were delivered to the microbiology laboratory for further analysis.

Growth media

The study employed plate count agar as the medium for culturing bacterial cells. To identify coliform bacteria present in water samples, lactose broth was utilized. For the isolation, enumeration, and differentiation of Enterobacteriaceae, Eosin Methylene Blue (EMB) agar was implemented. Additionally, Salmonella Shigella agar (SS agar) was used specifically for the isolation of S*almonella* and *Shigella* species. Finally, ECD agar served as the medium for isolating *E. coli.*

Heterotrophic plate count (HPC)

The standard plate count method, a foundational technique in microbiology for quantifying microorganisms, remains one of the most prevalent approaches utilized in the field. Another significant method for assessing the bacteriological quality of drinking water is the heterotrophic plate count (HPC) test. In this procedure, water samples are serially diluted in normal saline (8.5 g/l NaCl solution) up to 10-9 by serial dilution method. Subsequently, 0.1 ml from each dilution is spread onto nutrient agar plates, with three replicates prepared for each dilution. The plates are then incubated at 37 °C for a duration of 24 to 48 hours, after which the average number of colonies is determined and expressed as colony-forming units (CFU) per 100 µl.

Enumeration of bacteria most probable number (MPN)

The Most Probable Number (MPN) counts are regarded as statistically reliable estimates derived from the cultivation of several sample volumes, typically five, or their respective dilutions. The MPN methodology was employed to quantify coliform and fecal coliform bacteria through a series of tests. In the presumptive test phase, 10 ml, 1 ml, and 0.1 ml (from a 1:10 dilution) of water samples were inoculated into three sets of sterilized test tubes. Each set comprised five test tubes containing 9 ml of lactose broth and an inverted Durham tube, followed by incubation at 37°C for a duration of 24 to 48 hours. After the initial 24-hour incubation, the test tubes were assessed for gas production, as coliform bacteria generate gas from lactose, which becomes trapped in the inverted Durham tube. The number of positive tubes exhibiting gas production was then counted, allowing for the determination of MPN using a standard reference table.

In the confirmed test phase, 10 µl samples were taken from the positive presumptive tests and streaked onto Eosin Methylene Blue (EMB) agar plates, which were subsequently incubated at 37°C for 24 to 48 hours. For the completed test, lactose broth was inoculated with the positive con-

firmed test samples and incubated at 44.5°C for 24 to 48 hours. After this incubation period, the test tubes were again examined for gas production, and the positive tubes were counted to ascertain the MPN from the standard table. Additionally, 10 µl samples from the positive completed tests were streaked onto EMB plates and incubated at 37°C for 24 to 48 hours. To confirm the identity of the bacteria, differential staining, specifically Gram staining, was performed to verify that the isolates were gram-negative and rod-shaped.

The identification of bacterial isolates was conducted using the Phoenix TM identification panel system, which allows for species-level identification. All procedures for setting up the panels were strictly adhered to according to the manufacturer's guidelines, as outlined in the works of (Salomon et al., 1999). This systematic approach ensures accurate identification and characterization of the bacterial isolates, contributing to a better understanding of the microbial composition in the tested samples (Salomon et al., 1999).

The primary microorganisms present in drinking water samples were characterized through a series of biochemical assays. Isolates exhibiting distinct morphological colony types were carefully selected from plate count agar and subsequently subcultured. These cultures were preserved in a refrigerator at 4°C until they were required for additional testing. The biochemical assays performed included Gram staining, catalase testing, and oxidase testing (Salomon et al., 1999).

For bacterial isolation, a loopful of enriched media was inoculated onto various culture media, such as MacConkey and Eosin-Methylene Blue agar, to isolate *E. coli*, *Klebsiella, Enterobacter*, *Hafnia*, *Morganella*, and *Citrobacter*. Additionally, *Salmonella Shigella* agar was employed for the isolation of *Salmonella* and *Shigella* species, while Thiosulfate Citrate Bile Salt agar was utilized for isolating *Vibrio* species (Murray et al., 2006).

The Antibiotic susceptibility testing

Antibiotic susceptibility (AST) is performed using different classes of antibiotics: Ampicillin (30 micrograms), Amoxicillin (30 micrograms), Penicillin (30 micrograms), Colexilin (10 micrograms). Prepare the Muller Hinton agar medium, sterilize it, and pour it in sterile conditions. Leave it to solidify for 1 minute until the activity of the bacteria is stimulated, or prepare it in water 15 - Prepare a bacterial suspension on the nutrient broth tube and incubate it for 2 hours in lukewarm or saline water 0.9%. Using a cotton swab, immerse it through the tube inoculated with the bacterial suspension and wipe the entire plate clockwise. Place the tablets to be the ability of the antibiotic to inhibit bacteria on the surface of the plate is determined it is done by Measuring the distance in millimeters (mm) between the boundaries of the growing colony around the antibiotic-soaked disk.

The antibiotics are selected based on their resistance to bacterial strains. The antibiotic susceptibility of *E.coli* growth at 44.5°C will be determined by the disk diffusion method (JC & Turck, 1966). Four antibiotic susceptibility test disks will be obtained penicillin 10 units, Amoxicillin 25 µg , streptomycin 25 µg, tetracycline 50 µg. 0.1 ml of fresh culture will be spread on Muller medium plates using a sterile glass grater and then allowed to dry for 10 minutes. The four antimicrobial disks will be placed on the bacterial film (one in each quadrant of the plate). Three plates will be used for the test and a plate without any antibiotics will be used as a control. The plates will be incubated (not inverted) at 25°C overnight. The zone of inhibition for each antibiotic will be measure and the average calculated.

The data collected throughout the research was meticulously input into the R file for statistical analysis. Subsequently, the analysis of variance (ANOVA) was employed to examine the influence of different variables and their interactions on the measured inhibition zones in millimeters, which

serve as indicators of antibiotic sensitivity and facilitate the identification of the most effective antbiotic.

RESULTS

E. coli and coliform bacteria are frequently employed as indicator organisms to assess fecal contamination in water sources. Nevertheless, the mere absence of these bacteria does not guarantee that the treated water is devoid of pathogens.

The initial analysis of the comprehensive model, which encompassed all relevant factors, revealed that isolation did not emerge as a significant variable (F=0.563, p-value=0.57). Consequently, this factor was entirely excluded from the model, leading to its reconstruction without isolation.

The relationships depicted in Figure (1) are effectively illustrated through grouped box plots, which categorize the data into five distinct groups based on the types of antibiotics. Each group encompasses various bacterial species while simultaneously accounting for seasonal variations. These elements collectively exert a significant influence on antibiotic sensitivity, which is quantitatively represented by the inhibition zones measured in millimeters.

The revised model subsequently highlighted the pronounced influence of the remaining factors, which included seasonal variations (F=6.87, p-value=0.009), bacterial species (F=95.370, p-value < 2e-16), and the specific types of antibiotics administered (F=11.69, p-value=4.11e-09) that were highly significant factors in the model.

Furthermore, the analysis underscored the significant interactions between seasons coliform and fecal coliform and each bacterial species (F=24.1, p-value=1.25e-06), as well as between seasons and the types of antibiotics used (F=7.99, p-value=2.89e-06). These findings indicate that the effects of seasonal changes are not uniform across different bacterial species or antibiotic types, suggesting a complex interplay that warrants further investigation. Additionally, the interaction between bacterial species and antibiotic types also demonstrated a notable effect (F=19.11, p-value=1.02e-14), reinforcing the importance of considering these variables in tandem.

The results further illustrated the significance of interactions among all variables collectively (F=7.66, p-value=5.28e-06), indicating that the relationships between the factors are not merely additive but rather synergistic. This complexity highlights the necessity for a multifaceted approach to understanding the dynamics at play in the study. Overall, the findings emphasize the critical role of both individual factors and their interactions in shaping the outcomes of the research, thereby providing a more nuanced understanding of the underlying mechanisms involved.

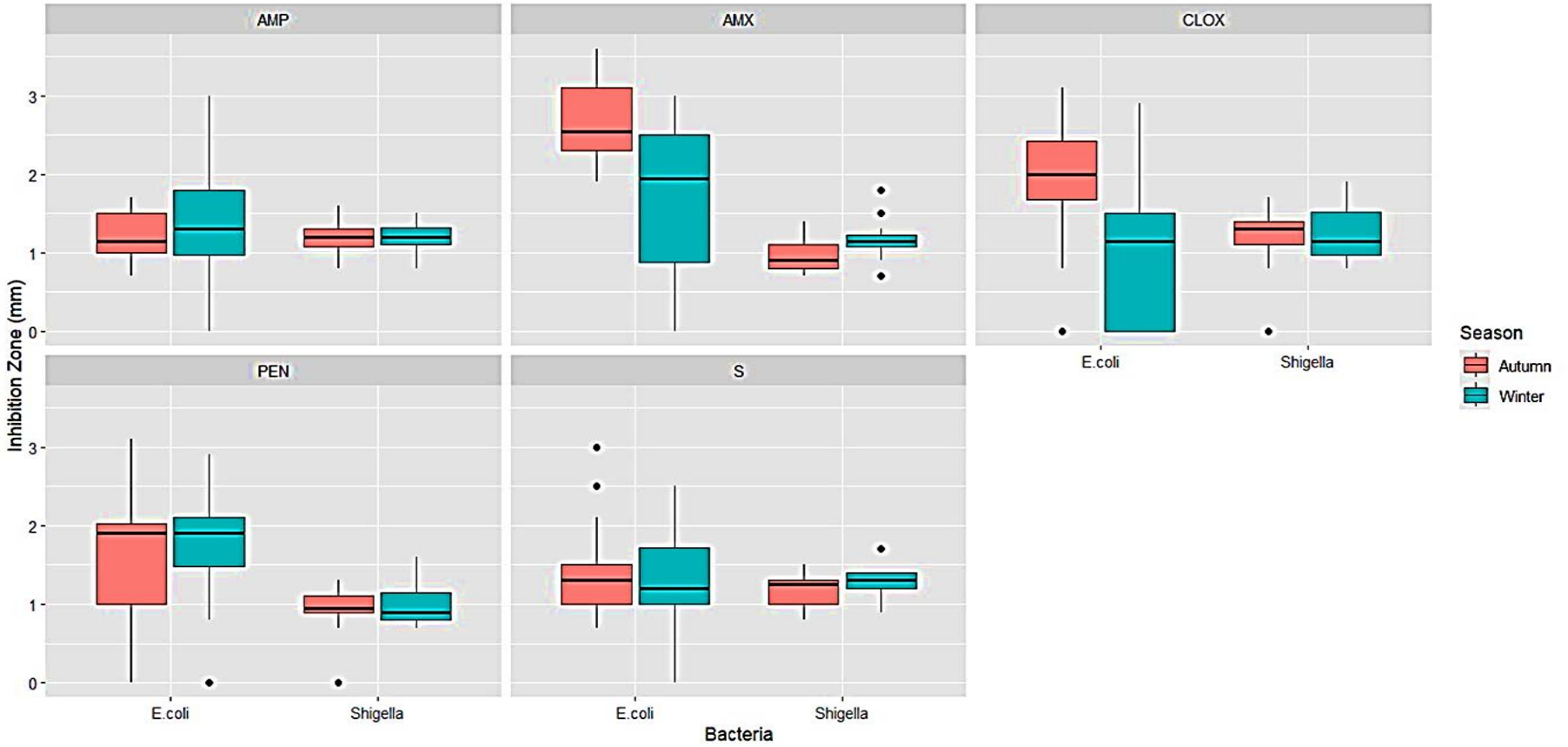

Figure (1).. Illustrates grouped box plots, which organize the data into five separate categories corresponding to different types of antibiotics. Each category includes a range of bacterial species and also considers seasonal fluctuations. Together, these factors play a crucial role in determining antibiotic sensitivity, which is quantitatively expressed through the measurement of inhibition zones in millimeters.

DISCUSSION

The extensive model examined the intricate relationships among antibiotics, various bacterial species, seasonal fluctuations, and the sensitivity of bacteria to antibiotics. The preliminary analysis indicated that isolation did not play a significant role, resulting in its removal from the model. The updated model underscored the substantial impact of seasonal changes, bacterial species, and the types of antibiotics on their sensitivity.

Noteworthy interactions were identified between the seasons and bacterial species, the seasons and antibiotic types, as well as between bacterial species and antibiotic types. These observations point to a complex interrelationship among these factors, suggesting that their influences are not merely additive but rather synergistic.

The findings of the research indicated the existence of antibiotic-resistant strains of E. coli in the drinking water sources of Massa, paralleling similar findings reported in Canada by Coleman et al. The data aligned with the observed seasonal variations in bacterial proliferation, which was notably higher during the summer months compared to winter. However, the differences in bacterial sensitivity to antibiotics across seasons were not as pronounced as those documented in the study by (Siedlecka et al., 2020)., which highlighted significant variations in antibiotic efficacy on bacteria within the drinking water distribution system (DWDS) during different seasons, particularly between summer and winter in Wrocław, Poland.

This study contributes to a deeper understanding of the complex interactions influencing antibiotic resistance, particularly in the context of environmental factors such as seasonal changes. The results underscore the necessity for a comprehensive approach to address the multifaceted nature of antibiotic sensitivity and resistance. By elucidating these dynamics, the research provides valuable insights that can inform the development of targeted strategies aimed at mitigating antibiotic resistance in various ecological contexts.

CONCLUSION

The results highlight the existence of antibiotic-resistant E. coli strains in drinking water sources, with seasonal variations in bacterial proliferation and antibiotic sensitivity. This research underscores the need for a multifaceted approach to understanding the complex dynamics of antibiotic resistance, emphasizing the importance of considering environmental factors, bacterial species, and antibiotic types in tandem. The findings provide valuable insights for the development of targeted strategies to mitigate antibiotic resistance in various ecological contexts.

ACKNOWLEDGEMENT

The source of financial support must be acknowledged. Authors must declare any financial support or relationships that may pose a conflict of interest in the cover letter submitted with the manuscript. Technical assistance may also be acknowledged.

Duality of interest: The authors declare that they have no duality of interest associated with this manuscript.

Author contributions : Contribution is equal between authors.

Funding: No specific funding was received for this work.

REFERENCES

Babalola, T., Olowomofe, T., Omodara, T., & Ogunyemi, T. (2021). Antibiotic Resistance Pattern and Plasmid Profile of Bacteria Isolates from Household Water Distribution Tanks in Ado-Ekiti. *Journal of Pure and Applied Microbiology*, *15*(3), 1697-1705.

Coleman, B. L., Louie, M., Salvadori, M. I., McEwen, S. A., Neumann, N., Sibley, K.,…Majury, A. (2013). Contamination of Canadian private drinking water sources with antimicrobial resistant Escherichia coli. *Water research*, *47*(9), 3026-3036.

Gu, Q., Sun, M., Lin, T., Zhang, Y., Wei, X., Wu, S.,…Ding, Y. (2022). Characteristics of antibiotic resistance genes and antibiotic-resistant bacteria in full-scale drinking water treatment system using metagenomics and culturing. *Frontiers in Microbiology*, *12*, 798442.

JC, B. A. K. W. S., & Turck, M. (1966). Antibiotic susceptibility testing by a standardized single disk method. *Am. J. Clin. Pathol*, *45*(4), 493.

Kothari, A., Kumar, P., Gaurav, A., Kaushal, K., Pandey, A., Yadav, S. R. M.,…Omar, B. J. (2023). Association of antibiotics and heavy metal arsenic to horizontal gene transfer from multidrug-resistant clinical strains to antibiotic-sensitive environmental strains. *Journal of Hazardous Materials*, *443*, 130260.

Murray, P., Baron, E., Jorgensen, J., Landry, M., & Pfaller, M. (2006). Manual of clinical microbiology: Volume 1.

Reitter, C., Petzoldt, H., Korth, A., Schwab, F., Stange, C., Hambsch, B.,…Hügler, M. (2021). Seasonal dynamics in the number and composition of coliform bacteria in drinking water reservoirs. *Science of the total environment*, *787*, 147539.

Salomon, J., Dunk, T., Yu, C., Pollitt, J., & Reuben, J. (1999). Rapid automated identification of gram-positive and gram-negative bacteria in the phoenix system. Abstr. 99th General Meeting ASM,

Sanganyado, E., & Gwenzi, W. (2019). Antibiotic resistance in drinking water systems: Occurrence, removal, and human health risks. *Science of the total environment*, *669*, 785-797.

Siedlecka, A., Wolf-Baca, M., & Piekarska, K. (2020). Spatiotemporal changes of antibiotic resistance and bacterial communities in drinking water distribution system in Wrocław, Poland. *Water*, *12*(9), 2601.

Tiwari, A., Gomez-Alvarez, V., Siponen, S., Sarekoski, A., Hokajärvi, A.-M., Kauppinen, A.,…Pitkänen, T. (2022). Bacterial genes encoding resistance against antibiotics and metals in well-maintained drinking water distribution systems in Finland. *Frontiers in Microbiology*, *12*, 803094.

Al-Mukhtar Journal of Basic Sciences 22 (3): 250-262, 2024
Doi: https://doi.org/10.54172/kt3kdf94

Research Article **Open Access**

Intracellular Virus Dynamics A Study of The Converting from The Deterministic Model to its Stochastic Counterpart

Asmahan M. A. Billiwa[1], Abdassalam B. H. Aldaikh[*2]

***Corresponding author:** adaikh.1962@omu.edu.ly, Department of Mathematics, Faculty of Science, University of Omar Al-Mukhtar, Libya.

[1] Department of Mathematics, Faculty of Science, University of Omar Al-Mukhtar, Libya.

Received:
09 November 2024

Accepted:
15 December 2024

Publish online:
31 December 2024

Abstract

By examining both deterministic and stochastic models, the intracellular viral movement model explores the complex dynamics of the interaction of viruses with host cells. Since such movement is not deterministic but rather random, the main goal of this study is to build a stochastic model corresponding to the deterministic one, that describes the movement of viruses and their intracellular interactions in a more realistic way. The model helps explain how viruses are produced and reproduce by analyzing the mechanisms that generate and deplete structural proteins and viral nucleic acids, and by examining the effect of the viral template, the findings may help improve methods for treating and preventing viral infections by shedding light on structural proteins and viral DNA. The deterministic and stochastic systems were solved numerically and represented using MATAB tools, to gain deeper insights.

Keywords: Intracellular Virus Movement Model, Stochastic Model, Covariance Matrix, Diffusion Matrix.

INTRODUCTION

Viruses are infectious agents that are tiny, obligate intracellular parasites that are incapable of self-replication. These are also acellular creatures, meaning that their genomes are either RNA or DNA (nucleic acid) and are encased in a protective protein coat that is encoded by the virus. Every virus can only replicate obligately in live cells. They do this by utilizing the metabolic processes and ribosomes of the host to create a collection of parts that come together to form molecules known as VIRIONS, which guard the genome and spread it to new cells (Gelderblom, 1996) https://www.uoanbar.edu.iq/eStoreImages/Bank/14736.

All living things, including bacteria, archaea, plants, and animals, are susceptible to virus infection. https://www.uoanbar.edu.iq/eStoreImages/Bank/14736.The infectious units known as viruses range in diameter from around 16 nanometers for circoviruses to over 300 nanometers for poxviruses. Because of its microscopic size, it is ultra-filterable, meaning that bacteria-resistant filters cannot hold it (Modrow et al., 2013). Humans and other species have been greatly impacted by viruses, yet until recently, little was understood about their nature. Clarifying their nature can be aided by a brief history of their discovery and identification as distinct infectious agents. Despite their ignorance of the nature of their illnesses, the ancients were aware of conditions like rabies, which are understood to have a viral cause today. Indeed, there is considerable evidence that the measles and smallpox vi-

ruses were likely responsible for the enormous epidemics that struck between 165 and 180 AD and between 251 and 266 AD., which significantly damaged the Roman Empire and contributed to its fall (Harley, 2002). Numerous discoveries in several fields of biology during the past 20 years have fundamentally altered our understanding of the viral world. The conventional understanding of viruses as passive biological entities that evolved mainly by choosing genes from their hosts and had a secondary function in evolution is contradicted by several of these findings. It is now known that viruses are extremely varied, and very old—they existed before the Last Universal Cellular Ancestor (LUCA) and that they were crucial to the evolution of life. These new findings have led to the proposal of new definitions and ideas for viruses. The idea of the viral cell, in particular, affirms that viruses are cellular entities and that they are capable of producing their own DNA (Forterre, 2017). Over millions of years, viruses have changed to fit certain creatures or their cells. Proteins make up infectious viral particles, or virions, which are encased in a fatty membrane known as the envelope in certain virus species. Only one kind of nucleic acid—either DNA or RNA—is present in the particles. Unlike bacteria, yeasts, or other cells, viruses multiply within the live cells they infect rather than by dividing (Modrow et al., 2013). Virologists study viruses, which are obviously extremely different from prokaryotic and eukaryotic microbes. Viruses are very significant and require careful consideration, even though they are simpler than biological creatures, (Harley, 2002). Although viruses may cause terrible illnesses in a variety of creatures, they are also straightforward systems that can be used for a wide range of beneficial reasons. Viruses have long been used in medicine to make vaccinations, and they are now utilized as vectors to carry chemicals that are needed to cure illnesses like cancer so that they may target certain cells. They have also been utilized to precipitate certain metals in nanotechnology and agriculture, and they have shown significant promise in the creation of nanomaterials. Additionally, they have a variety of uses in the electronics, cosmetics, pharmaceutical, and other sectors. As a result, viruses are no longer just considered adversaries (Varanda et al., 2021). We also point out that the study of viruses has made significant contributions to the science of molecular biology, as indicated by the recent appearance of AIDS and the fact that numerous viral illnesses in humans are already recognized, with new ones being identified or emerging each. Viral discoveries are the foundation of the entire discipline of genetic engineering (Harley, 2002).

The ability of viruses to infiltrate cells from bacteria, archaea, and eukaryotes is a result of their evolution. The majority of the more than 3,600 identified viruses are linked to illness, and hundreds of them have the ability to infect human cells. Animal viruses attach themselves to host cell receptors to enter the cell. Understanding how viral entry proteins interact with their host cell receptors and change conformation to allow entrance offers previously unheard-of possibilities for creating novel therapies and vaccines. The first and most crucial stage of a virus' life cycle is its entrance into the host cell. After attaching to receptors, viruses enter animal cells by either fusing with cellular membranes (enveloped viruses), penetrating through (non-enveloped viruses), or undergoing significant conformational changes to their proteins. When viral genomes are transferred into host cells, the procedure is complete (Dimitrov, 2004). Viruses are intracellular pathogens, meaning they need the metabolic machinery of their host cell to proliferate. Although there are significant differences in the reproductive life cycle of different viral kinds and classes, attachment, penetration, disassembly, replication, assembly, and virus release are the six fundamental processes required for virus reproduction. https://www.immunology.org/sites/default/files/2022-08/Virus%20replication.pdf

The public's health is still at risk from the seasonal and pandemic influenza virus (IAV). The kinetics of the immune response to IAV infection and the biological factors that significantly affect infection outcomes, however, are not well understood quantitatively. In order to tackle these prob-

lems, we statistically examine innate and adaptive immune responses to primary IAV infection using modeling techniques in conjunction with experimental data. The dynamic interactions between target (epithelial) cells, viruses like influenza virus, cytotoxic T lymphocytes (CTLs), and virus-specific IgG and IgM have been described mathematically. Simulation studies have also been conducted to determine the relative contributions of biological parameters to the clearance of IAV (Miao et al., 2010). This study provides a model of virus movement inside cells, as by adjusting the parameters according to the behaviors of different viruses, it is suitable for many viruses, including influenza virus, HIV, and others. This is to provide precise insights into how different viruses interact with cells and develop effective methods to combat viral diseases.

The basic interactions between viral components may be captured by deterministic models that are based on ordinary differential equations. On the other hand, a single viral particle can start an infection by transferring its genome — a single DNA or RNA molecule — to the host cell. A stochastic model that takes into account the natural variations in viral component levels might produce qualitatively different results in these circumstances (Srivastava et al., 2002). We have created a basic model of the intracellular dynamics of a generic virus that may be implemented either stochastically or deterministically in order to compare modeling techniques (Allen, 2010). Therefore, the proposed mathematical model is

$$\begin{cases} \frac{dT}{dt} = f_1(T,G,S) = K_1 G - K_2 T. \\ \frac{dG}{dt} = f_2(T,G,S) = K_3 T - K_1 G - K_4 GS.. \\ \frac{dS}{dt} = f_3(T,G,S) = K_5 T - K_6 S - K_4 GS. \end{cases}$$

where all constants $K_i, i = 1,2,3,4,5,6.$ are in units of day, and the variables described in Table 1.

Table: (1). Description of state variables of the proposed model

Variable	Description
T	viral template.
G	viral genome.
S	structural proteins

The model reflected the processes that produced and depleted structural proteins and viral nucleic acids. Before creating the stochastic model for the system, we will study the stability of its system at the equilibrium point (T^*, G^*, S^*) (Chou & Friedman, 2015).

1- The equilibrium points:

$$\frac{dT}{dt} = 0 \Rightarrow K_1 G - K_2 T = 0 \Rightarrow K_1 G = K_2 T \implies T^* = \frac{K_1}{K_2} G^* .$$

$$\frac{dG}{dt} = 0 \Rightarrow K_3 T - K_1 G - K_4 GS = 0 \Rightarrow S^* = \frac{K_1 K_3}{K_2 K_4} - \frac{K_1}{K_4} = \frac{K_1 (K_3 - K_2)}{K_2 K_4}.$$

$$\frac{dS}{dt} = 0 \Rightarrow K_5 T - K_6 S - K_4 GS = 0 \Rightarrow G^* = \frac{K_6 (K_3 - K_2)}{K_4 (K_5 - K_3 + K_2)}.$$

2- The Jacobian matrix:

$$J = \begin{pmatrix} \frac{\partial f_1}{\partial T} & \frac{\partial f_1}{\partial G} & \frac{\partial f_1}{\partial S} \\ \frac{\partial f_2}{\partial T} & \frac{\partial f_2}{\partial G} & \frac{\partial f_2}{\partial S} \\ \frac{\partial f_3}{\partial T} & \frac{\partial f_3}{\partial G} & \frac{\partial f_3}{\partial S} \end{pmatrix} = \begin{pmatrix} -K_2 & K_1 & 0 \\ K_3 & -K_1 - K_4 S & -K_4 G \\ K_5 & -K_4 S & -K_6 - K_4 G \end{pmatrix}.$$

$$J(T^*,G^*,S^*)=\begin{pmatrix}-K_2 & K_1 & 0\\ K_3 & -K_1-K_4S^* & -K_4G^*\\ K_5 & -K_4S^* & -K_6-K_4G^*\end{pmatrix}.$$

3- Stability study:

at (T^*,G^*,S^*):

$|J-\lambda I|=0.$

$$\left|\begin{pmatrix}-K_2 & K_1 & 0\\ K_3 & -K_1-K_4S^* & -K_4G^*\\ K_5 & -K_4S^* & -K_6-K_4G^*\end{pmatrix}-\lambda\begin{pmatrix}1&0&0\\0&1&0\\0&0&1\end{pmatrix}\right|=0.$$

$$\left|\begin{pmatrix}-K_2 & K_1 & 0\\ K_3 & -K_1-K_4S^* & -K_4G^*\\ K_5 & -K_4S^* & -K_6-K_4G^*\end{pmatrix}-\begin{pmatrix}\lambda&0&0\\0&\lambda&0\\0&0&\lambda\end{pmatrix}\right|=0.$$

$$\begin{vmatrix}-K_2-\lambda & K_1 & 0\\ K_3 & -K_1-K_4S^*-\lambda & -K_4G^*\\ K_5 & -K_4S^* & -K_6-K_4G^*-\lambda\end{vmatrix}=0.$$

$(-K_2-\lambda)[(-K_1-K_4S^*-\lambda)(-K_6-K_4G^*-\lambda)-(-K_4G^*)(-K_4S^*)]-(K_1)[K_3(-K_6-K_4G^*-\lambda)]+$
$(K_4K_5G^*)=0.$

$(-K_2-\lambda)[(K_1+K_4S^*+\lambda)(K_6+K_4G^*+\lambda)-{K_4}^2G^*S^*]-(K_1)[-K_3(K_6+K_4G^*+\lambda)]+$
$(K_4K_5G^*)=0.$

put $x=K_1+K_4S^*, y=K_6+K_4G^*, z={K_4}^2G^*S^*, h=K_4K_5G^*$.

$(-K_2-\lambda)[(x+\lambda)(y+\lambda)-z]-(K_1)[-K_3(y+\lambda)]+h=0.$

$(-K_2-\lambda)[(xy+x\lambda+y\lambda+\lambda^2)-z]+(K_1K_3y+K_1K_3\lambda-K_1h)=0.$

$(-K_2-\lambda)[(xy+(x+y)\lambda+\lambda^2)-z]+(K_1K_3(y+\lambda)-K_1h)=0.$

$-K_2xy-K_2(x+y)\lambda-K_2\lambda^2+K_2z-xy\lambda-(x+y)\lambda^2-\lambda^3+z\lambda+K_1K_3y+K_1K_3\lambda-K_1h=0.$

$-\lambda^3-((x+y)+K_2)\lambda^2-(K_2(x+y)+xy-z-K_1K_3)\lambda-(K_2xy-K_2z-K_1K_3y+K_1h)=0.$

$\lambda^3+(x+y+K_2)\lambda^2+(K_2x+K_2y+xy-z-K_1K_3)\lambda+(K_2xy-K_2z-K_1K_3y+K_1h)=0.$

$\lambda^3+((K_1+K_4S^*)+(K_6+K_4G^*)+K_2)\lambda^2+(K_2(K_1+K_4S^*)+K_2(K_6+K_4G^*)+((K_1+K_4S^*)(K_6+K_4G^*)-$
$({K_4}^2G^*S^*)-K_1K_3)\lambda+((K_2(K_1+K_4S^*)(K_6+K_4G^*)-K_2{K_4}^2G^*S^*-K_1K_3(K_6+K_4G^*)+K_1(K_4K_5G^*))=0.$

$\lambda^3+(K_1+K_4S^*+K_6+K_4G^*+K_2)\lambda^2+(K_2K_1+K_2K_4S^*+K_2K_6+K_2K_4G^*+K_1K_6+K_1K_4G^*+K_6K_4S^*+$
$K_4{}^2G^*S^*-K_4{}^2G^*S^*-K_1K_3)\lambda+(K_1K_2K_6+K_1K_2K_4G^*+K_6K_2K_4S^*+K_2K_4{}^2G^*S^*-K_2K_4{}^2G^*S^*-K_1K_3K_6-$
$K_1K_3K_4G^*+K_1K_4K_5G^*)=0.$

$\lambda^3+(K_1+K_4S^*+K_6+K_4G^*+K_2)\lambda^2+(K_2K_1+K_2K_4S^*+K_2K_6+K_2K_4G^*+K_1K_6+K_1K_4G^*+K_6K_4S^*-$
$K_1K_3)\lambda+(K_1K_2K_6+K_1K_2K_4G^*+K_6K_2K_4S^*-K_1K_3K_6-K_1K_3K_4G^*+K_1K_4K_5G^*)=0.$

$\lambda^3+(K_1+K_4(\frac{K_1(K_3-K_2)}{K_2K_4})+K_6+K_4(\frac{K_6(K_3-K_2)}{K_4(K_5-K_3+K_2)})+K_2)\lambda^2+(K_2K_1+K_2K_4(\frac{K_1(K_3-K_2)}{K_2K_4})+K_2K_6+$
$K_2K_4\left(\frac{K_6(K_3-K_2)}{K_4(K_5-K_3+K_2)}\right)+K_1K_6+K_1K_4\left(\frac{K_6(K_3-K_2)}{K_4(K_5-K_3+K_2)}\right)+K_6K_4\left(\frac{K_1(K_3-K_2)}{K_2K_4}\right)-K_1K_3)\lambda+(K_1K_2K_6+$
$K_1K_2K_4(\frac{K_6(K_3-K_2)}{K_4(K_5-K_3+K_2)})+K_6K_2K_4(\frac{K_1(K_3-K_2)}{K_2K_4})-K_1K_3K_6-K_1K_3K_4(\frac{K_6(K_3-K_2)}{K_4(K_5-K_3+K_2)})+$
$K_1K_4K_5(\frac{K_6(K_3-K_2)}{K_4(K_5-K_3+K_2)}))=0.$

$\lambda^3+(K_1+(\frac{K_1(K_3-K_2)}{K_2})+K_6+(\frac{K_6(K_3-K_2)}{(K_5-K_3+K_2)})+K_2)\lambda^2+(K_2K_1+K_1(K_3-K_2)+K_2K_6+K_2\left(\frac{K_6(K_3-K_2)}{(K_5-K_3+K_2)}\right)+$
$K_1K_6+K_1\left(\frac{K_6(K_3-K_2)}{(K_5-K_3+K_2)}\right)+K_6\left(\frac{K_1(K_3-K_2)}{K_2}\right)-K_1K_3)\lambda+(K_1K_2K_6+K_1K_2(\frac{K_6(K_3-K_2)}{(K_5-K_3+K_2)})+K_6K_1(K_3-K_2)-$
$K_1K_3K_6-K_1K_3(\frac{K_6(K_3-K_2)}{(K_5-K_3+K_2)})+K_1K_5(\frac{K_6(K_3-K_2)}{(K_5-K_3+K_2)}))=0.$

$.\lambda^3+(K_1+(\frac{K_1(K_3-K_2)}{K_2})+K_6+(\frac{K_6(K_3-K_2)}{(K_5-K_3+K_2)})+K_2)\lambda^2+(K_1K_3+K_2K_6+K_2\left(\frac{K_6(K_3-K_2)}{(K_5-K_3+K_2)}\right)+K_1K_6+$
$K_1\left(\frac{K_6(K_3-K_2)}{(K_5-K_3+K_2)}\right)+K_6\left(\frac{K_1(K_3-K_2)}{K_2}\right)-K_1K_3)\lambda+(K_1K_2K_6+K_1K_2(\frac{K_6(K_3-K_2)}{(K_5-K_3+K_2)}-K_6K_1K_2-$

$$K_1K_3\left(\frac{K_6(K_3-K_2)}{(K_5-K_3+K_2)}\right)+K_1K_5\left(\frac{K_6(K_3-K_2)}{(K_5-K_3+K_2)}\right))=0.$$

$$a_3=1>0.$$

$$a_2=K_1+\left(\frac{K_1(K_3-K_2)}{K_2}\right)+K_6+\left(\frac{K_6(K_3-K_2)}{(K_5-K_3+K_2)}\right)+K_2.$$

$$a_1=K_1K_3+K_2K_6+K_2\left(\frac{K_6(K_3-K_2)}{(K_5-K_3+K_2)}\right)+K_1K_6+K_1\left(\frac{K_6(K_3-K_2)}{(K_5-K_3+K_2)}\right)+K_6\left(\frac{K_1(K_3-K_2)}{K_2}\right)-K_1K_3.$$

$$a_0=K_1K_2K_6+K_1K_2\left(\frac{K_6(K_3-K_2)}{(K_5-K_3+K_2)}\right)-K_6K_1K_2-K_1K_3\left(\frac{K_6(K_3-K_2)}{(K_5-K_3+K_2)}\right)+K_1K_5\left(\frac{K_6(K_3-K_2)}{(K_5-K_3+K_2)}\right).$$

If $a_i>0, i=0,1,2$ *and* $a_2a_1-a_3a_0>0$

Then by the Routh-Hurwitz criterion, the system at (T^*,G^*,S^*) is stable.

Despite our continued efforts in analyzing the system, we were unable to reach a consistent result or a clear analytical solution. We faced multiple challenges that complicated the results, making it difficult to determine the system's behavior definitively. We therefore intend to resort to numerical methods as an alternative means to explore the system dynamics more precisely. By using numerical solutions, we hope to gain deeper insights into the stability of the system and its behaviors under different conditions, which may help us understand complex phenomena that we have not been able to analyze Figure 1.

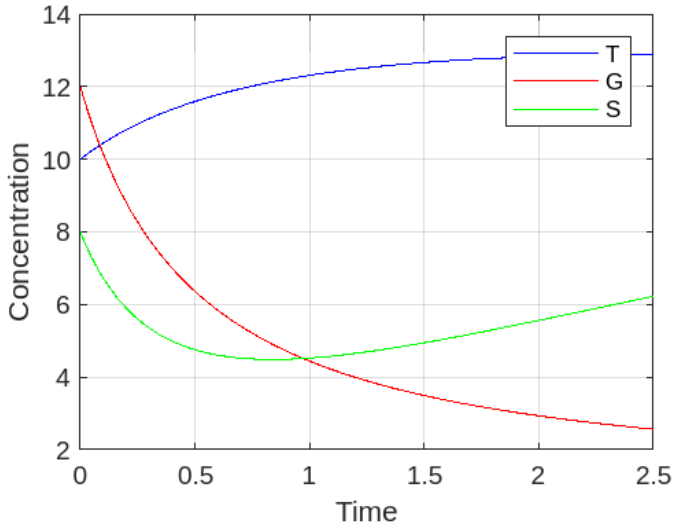

Figure: (1). intracellular viral kinetics**;** $K_1=0.5, K_2=0.1. K_3=0.3, K_4=0.2, K_5=0.1, K_6=0.4.$

Note that the viral template *T* appears concave upward, and this indicates that the amount of template increases over time, which indicates stability in growth with increasing template production. Being concave upward, this means that the increase in the amount of *T* accelerates over time, which reflects a positive dynamic in the reproduction of the virus.

As for the viral genome, it decreases over time as it is concave downwards. This decrease also indicates consumption or degradation of the viral genome. This dynamic may reflect an interaction process between the genome and the target cells. As for the amount of structural proteins, it decreases over time, and this indicates that the structural proteins are either used to build new viruses or are broken down due to cell processes. Based on the results extracted from the drawing, the system appears unstable. This is based on the data that was entered.

In fact, viruses and the host cell are exposed to random fluctuations. These fluctuations can affect the rates of interaction and reproduction. To provide a deeper understanding of how random factors

affect the movement of the virus inside cells, we can create a stochastic model that takes into account random factors and provides a better understanding of how viruses evolve and become resistant. For treatments or vaccines.

The stochastic model for the system

1- Probabilities associated with changes in the model, Table 2.

Table: (2). Probabilities associated with changes in the model

Changes, Δx_i	Probability, p_i
$(1,-1,0)^{tr}$.	$K_1 G\,\Delta t$.
$(-1,0,0)^{tr}$.	$K_2 T\,\Delta t$.
$(0,1,0)^{tr}$.	$K_3 T\,\Delta t$.
$(0,-1,-1)^{tr}$.	$K_4 GS\Delta t$.
$(0,0,1)^{tr}$.	$K_5 T\Delta t$.
$(0,0,-1)^{tr}$.	$K_6 S\Delta t$.

2- The expectation $E(\Delta x) = \sum_{i=1}^{6} p_i \Delta x_i$ is 3×1 matrix, the expectation can be expressed as follows.

$$E(\Delta x) = \sum_{i=1}^{6} p_i \Delta x_i = p_1\Delta x_1 + p_2\Delta x_2 + p_3\Delta x_3 + p_4\Delta x_4 + p_5\Delta x_5 + p_6\Delta x_6 ,$$

$$E(\Delta x) = \sum_{i=1}^{6} p_i \Delta x_i = K_1 G\begin{pmatrix}1\\-1\\0\end{pmatrix} + K_2 T\begin{pmatrix}-1\\0\\0\end{pmatrix} + K_3 T\begin{pmatrix}0\\1\\0\end{pmatrix} + K_4 GS\begin{pmatrix}0\\-1\\-1\end{pmatrix} + K_5 T\begin{pmatrix}0\\0\\1\end{pmatrix} +$$

$$K_6 S\begin{pmatrix}0\\0\\-1\end{pmatrix}.$$

$$E(\Delta x) = \begin{pmatrix}K_1 G\\-K_1 G\\0\end{pmatrix} + \begin{pmatrix}-K_2 T\\0\\0\end{pmatrix} + \begin{pmatrix}0\\K_3 T\\0\end{pmatrix} + \begin{pmatrix}0\\-K_4 GS\\-K_4 GS\end{pmatrix} + \begin{pmatrix}0\\0\\K_5 T\end{pmatrix} + \begin{pmatrix}0\\0\\-K_6 S\end{pmatrix}.$$

$$E(\Delta x) = \begin{pmatrix}K_1 G - K_2 T\\-K_1 G + K_3 T - K_4 GS\\-K_4 GS + K_5 T - K_6 S\end{pmatrix}\Delta t.$$

3- The covariance matrix, can be expressed as follows

$$E(\Delta x(\Delta x)^T) = \sum_{i=1}^{6} p_i \Delta x_i\,(\Delta x_i)^T.$$

$$= p_1\Delta x_1(\Delta x_1)^T + p_2\Delta x_2(\Delta x_2)^T + p_3\Delta x_3(\Delta x_3)^T + p_4\Delta x_4(\Delta x_4)^T +$$

$$p_5\Delta x_5(\Delta x_5)^T + p_6\Delta x_6(\Delta x_6)^T.$$

$$E(\Delta x(\Delta x)^T) = \begin{pmatrix}K_1 G\\-K_1 G\\0\end{pmatrix}(1\ -1\ \ 0) + \begin{pmatrix}-K_2 T\\0\\0\end{pmatrix}(-1\ 0\ \ 0) + \begin{pmatrix}0\\K_3 T\\0\end{pmatrix}(0\ 1\ \ 0) +$$

$$\begin{pmatrix}0\\-K_4 GS\\-K_4 GS\end{pmatrix}(0\ -1\ -1) + \begin{pmatrix}0\\0\\K_5 T\end{pmatrix}(0\ 0\ \ 1) + \begin{pmatrix}0\\0\\-K_6 S\end{pmatrix}(0\ 0\ -1)\,.$$

$$E(\Delta x(\Delta x)^T) = \begin{pmatrix}K_1 G & -K_1 G & 0\\-K_1 G & K_1 G & 0\\0 & 0 & 0\end{pmatrix} + \begin{pmatrix}K_2 T & 0 & 0\\0 & 0 & 0\\0 & 0 & 0\end{pmatrix} + \begin{pmatrix}0 & 0 & 0\\0 & K_3 T & 0\\0 & 0 & 0\end{pmatrix} +$$

$$\begin{pmatrix}0 & 0 & 0\\0 & K_4 GS & K_4 GS\\0 & K_4 GS & K_4 GS\end{pmatrix} + \begin{pmatrix}0 & 0 & 0\\0 & 0 & 0\\0 & 0 & K_5 T\end{pmatrix} + \begin{pmatrix}0 & 0 & 0\\0 & 0 & 0\\0 & 0 & K_6 S\end{pmatrix}.$$

$$E(\Delta x(\Delta x)^T) = \begin{pmatrix} K_1G + K_2T & -K_1G & 0 \\ -K_1G & K_1G + K_3T + K_4GS & K_4GS \\ 0 & K_4GS & K_4GS + K_5T + K_6S \end{pmatrix}\Delta t.$$

$$E(\Delta x(\Delta x)^T) = \begin{pmatrix} K_1G + K_2T & -K_1G & 0 \\ -K_1G & K_1G + K_3T + K_4GS & K_4GS \\ 0 & K_4GS & K_4GS + K_5T + K_6S \end{pmatrix}\Delta t = V\Delta t.$$

4- Formulate the stochastic system as

$$dX(t) = f(X(t),t)dt + h(X(t),t)dW(t).$$

where

$$dX(t) = \begin{bmatrix} dT_t \\ dG_t \\ dS_t \end{bmatrix}, f(X(t),t) = \left[\frac{E(\Delta X)}{\Delta t}\right], h(X(t),t) = \sqrt{V} \text{ and } dW(t) = \begin{bmatrix} dW_1(t) \\ dW_2(t) \\ dW_3(t) \end{bmatrix}.$$

$$\begin{pmatrix} dT_t \\ dG_t \\ dS_t \end{pmatrix} = \begin{pmatrix} K_1G - K_2T \\ -K_1G + K_3T - K_4GS \\ -K_4GS + K_5T - K_6S \end{pmatrix}dt +$$

$$\begin{pmatrix} \sqrt{(K_1G + K_2T)} & -\sqrt{K_1G} & 0 \\ -\sqrt{K_1G} & \sqrt{(K_1G + K_3T + K_4GS)} & \sqrt{K_4GS} \\ 0 & \sqrt{K_4GS} & \sqrt{(K_4GS + K_5T + K_6S)} \end{pmatrix}.\begin{pmatrix} dW_1(t) \\ dW_2(t) \\ dW_3(t) \end{pmatrix}.$$

$$\begin{cases} dT_t = (K_1G_t - K_2T_t)dt + \sqrt{(K_1G_t + K_2T_t)}\, dW_1(t) - \sqrt{K_1G_t}dW_2(t). \\ dG_t = (-K_1G_t + K_3T_t - K_4G_tS_t)dt - \sqrt{K_1G_t}dW_1(t) + \sqrt{(K_1G_t + K_3T_t + K_4G_tS_t)}dW_2(t) + \sqrt{K_4G_tS_t}dW_3(t) \\ dS_t = (-K_4G_tS_t + K_5T_t - K_6S_t)dt + \sqrt{K_4G_tS_t}\, dW_2(t) + \sqrt{(K_4G_tS_t + K_5T_t + K_6S_t)}dW_3(t). \end{cases}.$$

The equivalent system for the former system.

The diffusion matrix G of dimension 3×6 is

$$G = \begin{pmatrix} \sqrt{K_1G} & -\sqrt{K_2T} & 0 & 0 & 0 & 0 \\ -\sqrt{K_1G} & 0 & \sqrt{K_3T} & -\sqrt{K_4GS} & 0 & 0 \\ 0 & 0 & 0 & -\sqrt{K_4GS} & \sqrt{K_5T} & -\sqrt{K_6S} \end{pmatrix}.$$

$$dX(t) = f(X(t),t)dt + g(X(t),t)dW(t).$$

Where:

$$dX(t) = \begin{bmatrix} dT_t \\ dG_t \\ dS_t \end{bmatrix}, f(X(t),t) = \left[\frac{E(\Delta X)}{\Delta t}\right], g(X(t),t) = G \text{ and } dW(t) = \begin{bmatrix} dW_1(t) \\ dW_2(t) \\ dW_3(t) \\ dW_4(t) \\ dW_5(t) \\ dW_6(t) \end{bmatrix}.$$

Thus, the system takes the following form:

$$\begin{pmatrix} dT_t \\ dG_t \\ dS_t \end{pmatrix} = \begin{pmatrix} K_1G - K_2T \\ -K_1G + K_3T - K_4GS \\ -K_4GS + K_5T - K_6S \end{pmatrix}dt + \begin{pmatrix} \sqrt{K_1G} & -\sqrt{K_2T} & 0 & 0 & 0 & 0 \\ -\sqrt{K_1G} & 0 & \sqrt{K_3T} & -\sqrt{K_4GS} & 0 & 0 \\ 0 & 0 & 0 & -\sqrt{K_4GS} & \sqrt{K_5T} & -\sqrt{K_6S} \end{pmatrix}.\begin{pmatrix} dW_1(t) \\ dW_2(t) \\ dW_3(t) \\ dW_4(t) \\ dW_5(t) \\ dW_6(t) \end{pmatrix}.$$

$$\begin{cases} dT_t = (K_1G - K_2T)dt + \sqrt{K_1G}\, dW_1(t) - \sqrt{K_2T} dW_2(t) . \\ dG_t = (-K_1G + K_3T - K_4GS)dt - \sqrt{K_1G}\, dW_1(t) + \sqrt{K_3T} dW_3(t) - \sqrt{K_4GS}\, dW_4(t). \\ dS_t = (-K_4GS + K_5T - K_6S)dt - \sqrt{K_4GS}\, dW_4(t) + \sqrt{K_5T}\, dW_5(t) - \sqrt{K_6S} dW_6(t). \end{cases} .$$

A stochastic drawing shows how the viral template interacts with the genome and structural proteins in the system. While the viral template remains stable, the genome and proteins exhibit fluctuations that reflect response to random factors and changes in the cellular environment, Figure 2 and Figure3.

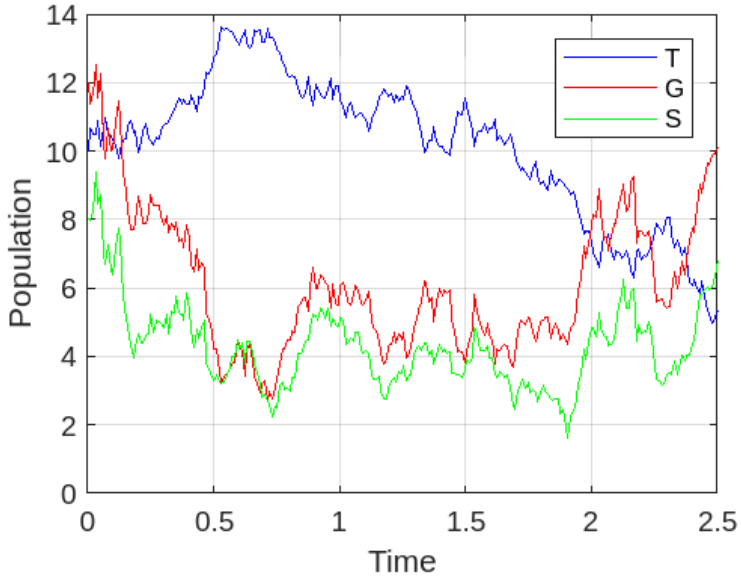

Figure: (2). intracellular viral kinetics**;** $K_1 = 0.5, K_2 = 0.1. K_3 = 0.3, K_4 = 0.2, K_5 = 0.1, K_6 = 0.4$.

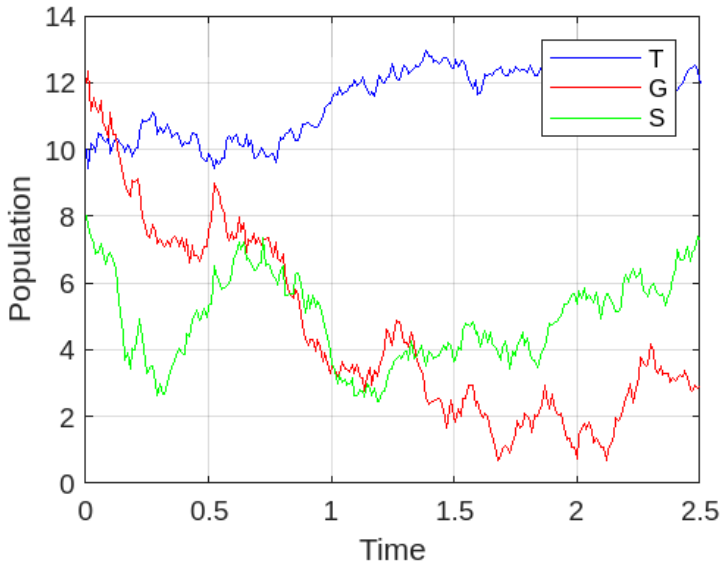

Figure: (3). intracellular viral kinetics**;** $K_1 = 0.5, K_2 = 0.1. K_3 = 0.3, K_4 = 0.2, K_5 = 0.1, K_6 = 0.4$.

Numerical Representation

The deterministic and stochastic systems solved numerically, (see the Appendix), their solutions represented using MATAB tools, and hence the following figures were obtained.

CONCLUSION

In this study, the movement of the virus inside cells was analyzed, using an advanced mathematical model, where the stability of the virus's dynamics was studied and the random model of the virus's movement inside the cells was discovered, which allowed us to better understand the dynamics of the virus and how the system works, and its influence on random factors. This study provides important insights that contribute to the development of effective treatment strategies.

The study can also be used to analyze different types of viruses, such as the immunodeficiency virus, influenza virus, coronavirus, etc., which confirms the importance of model in viral researches.

REFERENCES

Allen, L. J. (2010). *An introduction to stochastic processes with applications to biology*. CRC press.

Chou, C.-S., & Friedman, A. (2015). Introduction to Mathematical Biology.

Dimitrov, D. S. J. N. R. M. (2004). Virus entry: molecular mechanisms and biomedical applications. *2*(2), 109-122.

Forterre, P. J. O. H. U., Sem Monogr. (2017). The origin, nature and definition of viruses (and life): new concepts and controversies. *31*, 15-26.

Gelderblom, H. R. J. M. M. t. e. (1996). Structure and classification of viruses.

Harley, J. (2002). L. and Prescott, M."Laboratory Exercises in Microbiology Fifth Edition". In: McGraw-Hill Companies. New York.

Miao, H., Hollenbaugh, J. A., Zand, M. S., Holden-Wiltse, J., Mosmann, T. R., Perelson, A. S.,…Topham, D. J. J. J. o. v. (2010). Quantifying the early immune response and adaptive immune response kinetics in mice infected with influenza A virus. *84*(13), 6687-6698.

Modrow, S., Falke, D., Truyen, U., & Schätzl, H. J. M. V. (2013). Viruses: definition, structure, classification. 17.

Srivastava, R., You, L., Summers, J., & Yin, J. J. J. o. t. b. (2002). Stochastic vs. deterministic modeling of intracellular viral kinetics. *218*(3), 309-321.

Varanda, C., Félix, M. d. R., Campos, M. D., & Materatski, P. J. V. (2021). An overview of the application of viruses to biotechnology. *13*(10), 2073.

Appendix

Code of intracellular viral kinetics model (Deterministic model):

```
% Parameters
K1 = 0.5; % Parameter K1
K2 = 0.1; % Parameter K2
K3 = 0.3; % Parameter K3
K4 = 0.2; % Parameter K4
K5 = 0.4; % Parameter K5
```

```
K6 = 0.1; % Parameter K6

% ODE system
ode_system = @(t, Y) [
    K1 * Y(2) - K2 * Y(1);              % dT/dt
    K3 * Y(1) - K1 * Y(2) - K4 * Y(2) * Y(3); % dG/dt
    K5 * Y(1) - K6 * Y(3) - K4 * Y(2) * Y(3)  % dS/dt
];

% Initial conditions
T0 = 10; % Initial condition for T
G0 = 12; % Initial condition for G
S0 = 8; % Initial condition for S
Y0 = [T0; G0; S0];

% Time span
tspan = [0 2.5];

% Solve ODE
[t, Y] = ode45(ode_system, tspan, Y0);

% Plot results
figure;
plot(t, Y(:,1), '-b', 'DisplayName', 'T');
hold on;
plot(t, Y(:,2), '-r', 'DisplayName', 'G');
plot(t, Y(:,3), '-g', 'DisplayName', 'S');
xlabel('Time');
ylabel('Concentration');
legend;
grid on;
hold off;
```

Code of intracellular viral kinetics model (Stochastic model):

```
% Parameters
K1 = 0.5; % Parameter K1
K2 = 0.1; % Parameter K2
K3 = 0.3; % Parameter K3
K4 = 0.2; % Parameter K4
K5 = 0.4; % Parameter K5
K6 = 0.1; % Parameter K6

% Initial conditions
T0 = 10; % Initial condition for T
G0 = 12; % Initial condition for G
S0 = 8; % Initial condition for S
total_time = 2.5;  % Total time
dt = 0.01; % Time step
N = total_time / dt; % Number of time steps
```

```
% Preallocate arrays
T_values = zeros(1, N);
G_values = zeros(1, N);
S_values = zeros(1, N);
t = linspace(0, total_time, N);
T_values(1) = T0;
G_values(1) = G0;
S_values(1) = S0;

% Simulation using Euler-Maruyama method
for i = 1:N-1
    % Deterministic part
    dT_det = (K1 * G_values(i) - K2 * T_values(i)) * dt;
    dG_det = (-K1 * G_values(i) + K3 * T_values(i) - K4 * G_values(i) * S_values(i)) * dt;
    dS_det = (-K4 * G_values(i) * S_values(i) + K5 * T_values(i) - K6 * S_values(i)) * dt;

    % Stochastic part
    dW1 = sqrt(dt) * randn;
    dW2 = sqrt(dt) * randn;
    dW3 = sqrt(dt) * randn;

    dT_sto = sqrt(K1 * G_values(i) + K2 * T_values(i)) * dW1 - sqrt(K1 * G_values(i)) * dW2;
    dG_sto = -sqrt(K1 * G_values(i)) * dW1 + sqrt(K1 * G_values(i) + K3 * T_values(i) + K4 *
G_values(i) * S_values(i)) * dW2 + sqrt(K4 * G_values(i) * S_values(i)) * dW3;
    dS_sto = sqrt(K4 * G_values(i) * S_values(i)) * dW2 + sqrt(K4 * G_values(i) * S_values(i) + K5
* T_values(i) + K6 * S_values(i)) * dW3;

    % Update populations
    T_values(i+1) = T_values(i) + dT_det + dT_sto;
    G_values(i+1) = G_values(i) + dG_det + dG_sto;
    S_values(i+1) = S_values(i) + dS_det + dS_sto;

    % Ensure populations remain non-negative
    T_values(i+1) = max(T_values(i+1), 0);
    G_values(i+1) = max(G_values(i+1), 0);
    S_values(i+1) = max(S_values(i+1), 0);
end

% Plot results
figure;
plot(t, T_values, '-b', 'DisplayName', 'T');
hold on;
plot(t, G_values, '-r', 'DisplayName', 'G');
plot(t, S_values, '-g', 'DisplayName', 'S');
xlabel('Time');
ylabel('Population');
legend;
grid on;
```

```
hold off;
```

Code of intracellular viral kinetics model (equevelant Stochastic model):

```
% Parameters
K1 = 0.5; % Parameter K1
K2 = 0.1; % Parameter K2
K3 = 0.3; % Parameter K3
K4 = 0.2; % Parameter K4
K5 = 0.4; % Parameter K5
K6 = 0.1; % Parameter K6

% Initial conditions
T0 = 10; % Initial condition for T
G0 = 12; % Initial condition for G
S0 = 8; % Initial condition for S
total_time = 2.5;  % Total time
dt = 0.01; % Time step
N = total_time / dt; % Number of time steps

% Preallocate arrays
T_values = zeros(1, N);
G_values = zeros(1, N);
S_values = zeros(1, N);
t = linspace(0, total_time, N);
T_values(1) = T0;
G_values(1) = G0;
S_values(1) = S0;

% Simulation using Euler-Maruyama method
for i = 1:N-1
    % Deterministic part
    dT_det = (K1 * G_values(i) - K2 * T_values(i)) * dt;
    dG_det = (-K1 * G_values(i) + K3 * T_values(i) - K4 * G_values(i) * S_values(i)) * dt;
    dS_det = (-K4 * G_values(i) * S_values(i) + K5 * T_values(i) - K6 * S_values(i)) * dt;

    % Stochastic part
    dW1 = sqrt(dt) * randn;
    dW2 = sqrt(dt) * randn;
    dW3 = sqrt(dt) * randn;
    dW4 = sqrt(dt) * randn;
    dW5 = sqrt(dt) * randn;
    dW6 = sqrt(dt) * randn;

    dT_sto = sqrt(K1 * G_values(i)) * dW1 - sqrt(K2 * T_values(i)) * dW2;
    dG_sto = -sqrt(K1 * G_values(i)) * dW1 + sqrt(K3 * T_values(i)) * dW3 - sqrt(K4 * G_values(i)
* S_values(i)) * dW4;
    dS_sto = -sqrt(K4 * G_values(i) * S_values(i)) * dW4 + sqrt(K5 * T_values(i)) * dW5 - sqrt(K6
* S_values(i)) * dW6;
```

```
    % Update populations
    T_values(i+1) = T_values(i) + dT_det + dT_sto;
    G_values(i+1) = G_values(i) + dG_det + dG_sto;
    S_values(i+1) = S_values(i) + dS_det + dS_sto;

    % Ensure populations remain non-negative
    T_values(i+1) = max(T_values(i+1), 0);
    G_values(i+1) = max(G_values(i+1), 0);
    S_values(i+1) = max(S_values(i+1), 0);
end

% Plot results
figure;
plot(t, T_values, '-b', 'DisplayName', 'T');
hold on;
plot(t, G_values, '-r', 'DisplayName', 'G');
plot(t, S_values, '-g', 'DisplayName', 'S');
xlabel('Time');
ylabel('Population');
legend;
grid on;
hold off;
```

Al-Mukhtar Journal of Basic Sciences 22 (3): 263-271, 2024
Doi: https://doi.org/10.54172/fe4jrt92

Research Article **Open Access**

Foraging Behaviour of *Apis mellifera* Responses to the Position of Apple Flowers (*Malus domestica*)

Salma Y. Essa[1]*, Nesreen K. Shareef[2], Marwah Y. H. Almabrouk [3] and Ali A. Bataw[4]

***Corresponding author:** salma.yaseen@uod.edu.ly, Department of Zoology, Faculty of Science (Al guba), Derna University

[2.] Faculty of Education, Omar Al-Mukhtar University

[3].Department of Zoology, Faculty of Science and Art (Al abiar), Benghazi University.

[4.] Department of Zoology, Faculty of Science, Omar Al-Mukhtar University.

Received:
11 November 2024

Accepted:
25 December 2024

Publish online:
31 December 2024

Abstract

This study was conducted to investigate the effect of flower height on the number of worker bees, *Apis mellifera*, and its effect on the foraging behavior during its visit to the flowers of *Malus domestica*. The flowering region of the tree was divided into two equal heights, and the number of honey bee visitors and foraging behavior during the first hours of the day were monitored and calculated. The two regions showed apparent significant differences in the average number of nectar collections at 11:00 am, the highest number of visitors was recorded in the upper region 96.0 ± 6.0 workers/m^2, and the lower region of nectar with an average of 84.0±3.3 workers/m^2, and the lowest rates were recorded in the upper region of nectar, with an average of 73.3 ±63.3 workers/m^2 at 12 noon. At 9:00 am, the lower region of nectar was recorded with an average of 36.6 ± 4.6 workers/m^2. The two regions had the highest average number of pollen collectors. At 9 am, the upper region recorded 25.3 ± 0.4 workers /m^2, and the lower region recorded 13.3±0.77 workers/m^2. The lowest rates were recorded in the upper region7.00±0.9 workers/m^2 at 11:00 am. At noon, the average area recorded 3.6±0.1 workers /m^2.The result revealed no significant differences in the handling time in the two regions during the nectar collection. However, differences were recorded in the traveling time in the lower region only for nectar collectors; we conclude that the tree's height affected the behavior of the honey bee workers during the search for food and pollen collection.

Keywords: *Apis Mellifera*, The Upper And Lower Region. Foraging Behavior Apple Flower.

INTRODUCTION

The most common insect pollinator of apple is the honey bee (*Apis mellifera*); however, it is not the most efficient one; the study of the Behavior of *Apis mellifers* honey bee workers is one of the most important ancient and modern studies through which it is possible to understand the relationship between flowers and insects. They are among the most important pollinating insects found in orchards and modern agricultural systems (Morse & Calderone, 2000; Sharm et al., 2004).This indicated by (lau et al .,2019) that climatic conditions greatly affect the activity of bees while collecting pollen. as a study indicated (Silva & Dean, 2000) about concentration of sugar in the nectar ,also mentioned the climatic conditions affect the number of *A.mellifera* worker bees visiting the flowers of *M.domestica*, *P. communis*, and *P. domestic.a*. It increases with high temperature and low humidi-

ty (Essa & Bataw, 2020), as the researchers pointed out (Shareef et al., 2022) when studying it on the *Sinapisabla* plant, *Pelargonium radula*, *Stachy stournefortii*, and *Malva parviflora*. temperature factor has a direct effect on the plant , When the temperature increases, the number of honey bee workers increases, and the humidity has the opposite impact on the number of visitors to the honey bee workers. The lower the humidity, the greater the number of visitors to *A. mellifera*. As (Khanduri & Sharma,2002),indicated about the production and dispersal of pollen grains in the Himalayan sp plants, the opening of the mycelium sacs occurs periodically during the day, which is related to the temperature and relative Humidity. As indicated by (Benedek et al, 2000), the reason may be due to the quantity and quality of nectar, which has changed since its production and is affected by weather conditions. Recent studies also indicated that the variation in the time spent searching for food and foraging during the day is affected by many factors, which reflects their role in the rate of bee visitors, as it was recorded (Bataw & Sharref, 2018) that *A.mellifera* honey bee workers spent a longer handling time on the *Stachy stournefortii* plant of up to 8.6 seconds. Moreover, the least handling time on a plant that reached *Malva parviflora* was 7.2 seconds.

The reason is that the bees collect pollen and nectar simultaneously from the first plant, which takes longer, while the second collects pollen only (Gegear& Laverty, 2004). During their visit to two kinds of flowers yellow and blue flowers, the study showed that honey bees recorded high stability on one type of flower and took longer to move between flowers. In contrast, the duration of handling time on flowers did not differ much between the two types. Also, (Rust et al, 2003) noted a difference in the time of handling and traveling between the different species of bees visiting the flowers of *Ecballium* sp plant. The effect of different elevation zones on tree branches for apple blossom indicated that honey bee workers were recorded to prefer the middle zone more than the upper zone. (Joshi et al, 2010).

This study aims to identify the effect of the location of apple blossoms on the tree on the activity of the honey bee and its association with foraging behavior.

MATERIALS AND METHODS

Study area

The study was conducted in the Al-Abraq area of Al-Jabal Al-Akhdar (32° 46° 02°N 22° 00° 08°E, 677m) during the Apple bloom period of the season 2022 on a farm of 50 hectares. The study began during the peak flowering time of the apple *Malus domestica*; three days were chosen, 23-25/April. The trees were 10 –17 years old, with heights ranging from 1.5–2.5 m and an average crown size of 2.1 m × 2.0 m. Pesticides were not applied. The experiment was started when about 15-20% of the flowering took place so that bees would not forage outside the orchard on the other floral resources. The observations were made continuously for the different foraging parameters for 3 days.

The activity of honey bee workers

To assess the effect of altitude area on the number of worker honey bees visitors during their collecting nectar and pollen, the flowering area of the apple tree was divided into two equal heights, the upper and the lower region, where each region was studied separately with the recording of the surrounding climatic conditions, the number of visits of worker honey bees collecting nectar and pollen was from 9:00 am until 1:00 pm in an area. The observations were calculated for the visitors of the honey bee workers in the densely flowering branches with a length of 1 meter by following up the movements of the visiting workers of honey bees flowers, where the visiting workers of the flowers are monitored from the moment they enter the determined area and all their behaviors in collecting and pollen and how they stick to the flower and leave during the visit were recorded.

Foraging behavior

The time the worker spent collecting nectar or pollen from the flower was calculated, and the time began to be calculated until she left the flower (Handling time). Likewise, the time started to be calculated as soon as the worker stood on the flower and touched its parts. The time she moving from one flower to another (Traveling time) was calculated using the same method (Pleasant, 1981), where the period of handling and traveling time is calculated in both the upper and down regions, taking into account measurements of climatic conditions.

Weather

Temperature and relative Humidity were recorded by a psychomotor and a thermometer a every 10 minutes near the flowers of Apple flowers.

Statistical analysis

Statistical analysis of all data was carried out using the program (Minitab) version (16), analysis of variance (ANOVA), and calculation of (mean ± SE).

RESULTS

1.The foraging activity of *Apis mellifera* on flowers

a.The effect of flowers' position on the nectar collectors

The results showed significant differences in the number of visits by worker bees in each of the specific flowering regions on the apple tree during the day. In the upper region, significant differences were recorded in the number of workers who visited during the daytime (One-way ANOVA,, $F = 9.53$, $df = 3$, $P<0.0001$). The highest rate of visiting a worker was recorded at 11:00 am, where the average number of workers was 96.00± 6.0 workers/m^2. The lowest rate of female worker visits was recorded at noon, where the average number of female workers was 73.3± 2.61 female workers / m^2. The lower region, also recorded significant differences (One-way ANOVA) ($F = 25.55$, $df = 3$, $P<0.0001$) where the highest rate of a visit by a worker was recorded at 11:00 am, with an average number of 84.00± 3.3 worker/m^2. The lowest rate of female worker visits was recorded at 9:00 am, with an average number of 3.6± 0. 1 workers/m^2.(Table 1a).

Table (1a). Mean (±SE) number of honey bee's nectar collectors during day times from the two flowering height categories during the peak season (23-25 / April / 2022).

Day time	Mean No. of nectar collectors (±SE)	
	Upper region	lower region
9:00-10:00	83.3 ± 1.9 [ab]	36.6 ± 4.6 [c]
10:00-11:00	73.6± 0.8 [b]	66.6± 3.5 [b]
11:00-12:00	96.0± 6.0 [a]	84.0± 3.3 [a]
12:00 -1:00	73.3± 2.6 [b]	63.6± 3.8 [b]

Similar lowercase letters mean no significant differences in the same column.

b. The effect of flowers' position on the pollen collectors

Our results revealed a significant difference between the number of honey bee workers collecting pollen throughout the day in both flowering region (Table 1b). The upper region recorded a substantial difference in the number of bees collecting pollen through the daytime (One-way ANOVA) ($F = 159.1$, $df = 3$, $P<0.0001$). The highest rate of visiting a worker was recorded at 9:00 am, where the mean number of 25.3± 0.4 worker / m^2 was reached. while the lowest rate of a visit by a worker was recorded at noon when the average number of workers was 3.6 ± 0.4 worker/m^2. The lower region also recorded significant differences (One-way ANOVA), ($F=34.15$, $df=3$, $P<0.0001$), the highest rate of visiting a worker was recorded at 9:00 am, where the average number of workers

was 13.3± 0.77 worker/m^2. The lowest rate of a visit by a worker was recorded at noon when the average number of workers was 3.6± 0.1 worker/m^2 .

Table (1b). Mean (±SE) number of honey bee's pollen grain collectors during day times /from the two flowering height categories during the peak season. (23-25 / April / 2022).

Day time	Mean No. of pollen collectors (±SE)	
	Upper region	lower region
9:00-10:00	25.3 ± 0.4 [a]	13.3 ± 0.77 [a]
10:00-11:00	13.6 ± 0.1 [b]	11.6 ± 0.4 [a]
11:00-12:00	7.00 ± 0.9 [c]	6.3 ± 0.76 [b]
12:00 -1:00	3.6 ± 0.4 [d]	3.6 ± 0.1 [c]

Similar lowercase letters mean no significant differences between the same column.

The results showed a clear difference between the number of honey bee workers in the upper and lower regions during their visit to collect nectar and pollen during different hours of the day, where the highest preference for visiting honey bee workers during their collection of nectar was recorded in the upper region (81.6 ± 1.9) worker/m^2 the compared to the lower region. P-Value = 0.001, df = 223, T-Value = 6.05. Also, the highest preference recorded for visiting honey bee workers during pollen collection was recorded in the upper region compared to the lower region, with an average of 11.4 ± 0.8 worker/m^2, P-Value = 0.005, df = 212, T-Value = 2.85 (Table 1c). From our results, we find an apparent effect of height on the behavior of worker bees, especially in the upper region during food gathering.

Table (1c). The comparison of the mean number (±SE) of workers collecting nectar and pollen during a day time/m^2 from the two flowering height categories during the peak season (23-25 / April / 2022).

No. worker (flower/hr.)	Collecting Nectar	Collecting Pollen
Upper region	81.6 ± 1.9[a]	11.4 ± 0.8[a]
lower region	62.8 ± 2.5[b]	8.5 ± 0.5[b]

The letters different in the column are meant to find significant differences.

2. The effect of flower position on handling and traveling time

a. effect on the rate of nectar collection

The results show the handling and traveling times of honey bee workers on flowers during daylight hours in each of the two flowering regions while collecting nectar and pollen, (Table. 2a). in the upper region, we did not record significant differences during handling time for workers (df = 3, F = 1.07, P>0.363). Also, the handling time for the lower region shows no significant differences (df = 3, F = 1.06, P>0.369). The traveling time between the flowers in the upper region shows a significant difference (df=3, F=3.21, P<0.02), where the highest traveling time was recorded at 11:00 am with an average of (2.0± 0.05) sec., while the lowest traveling time between flowers was at 12 noon with an average of (1.5± 0.17) sec. in the upper region. In contrast, the traveling time between the flowers in the lower region shows no significant differences through day hours (df=3, F=0.47, P>0.701).

Table (2a). The Mean (SE±) handling and traveling time of *Apis mellifera* collecting the nectar of apple flowers *Malus domestica* during different days.

Height		Foraging times/second			
		9:00-10:00	10:00-11:00	11:00-12:00	12:00-1:00
Handling time	Upper region	1.9 ± 0.15 [a]	1.8 ± 0.8 [a]	2.2 ± 0.15[a]	1.9 ± 0.2 [a]
	lower region	1.9 ± 0.27 [a]	1.6 ± 0.1 [a]	2.12 ± 0.2[a]	2.1 ± 0.21 [a]
Traveling time	Upper region	1.7 ± 0.11 [ab]	1.7 ± 0.1[ab]	2.0 ± 0.05[a]	1.5 ± 0.17 b
	lower region	1.6 ± 0.18 [a]	1.3 ± 0.1 [a]	1.5 ± 0.07[a]	2.0 ± 0.07 [a]

Similar letters mean no significant differences between the same line.

b. Effect on the rate of pollen collection

Our results in Table (2b) show the times of foraging rate of honey bee workers on flowers during daylight hours in each region while collecting pollen, where significant differences were recorded in the upper region for the handling time (df=3, F= 9.78, P<0.0001). Where the highest handling time was recorded at 10:00 am with an average of (2.50 ± 0.3) sec. and the lowest handling time was recorded in the same area at 12 noon with an average of (0.4 ± 0.2 sec.). When recorded lower region during collection pollen significant differences (One-way ANOVA, df=3, F=8.62, P<0.0001) when was highest handling time at 10:00 am recorded with an average (2.5 ± 0.45) seconds, as well as at 12:00 noon recorded the lowest handling time was with an average of (0.3 ± 0.1) seconds, at the same time, as it was recorded in two regions traveling time, where the upper region recorded apparent significant differences (df=3, F= 31.28, P<0.0001). The highest traveling time was at 10:00 am with a mean of (1.6 ± 0.1 sec.) and recorded between 11:00 am and 12:00 noon; the lowest traveling time recorded was at 12:00 with an average of (0.2 ± 0.1) sec.. also the lower region recorded a significant difference (df=3, F=12.26, P<0.0001). The highest traveling time of a worker was at 10:00 am with an average of (1.3 ± 0.12) sec., and the lowest traveling time was at noon with an average of (0.4 ± 0.11) seconds, (Table 2b).

Table (2b). The Mean (SE±) handling and traveling time of *Apis mellifera* collecting.

Foraging Behaviour		Times(second) / day time			
		9:00-10:00	10:00-11:00	11:00-12:00	12:00-1:00
Handling time	Upper region	1.9 ± 0.15 ^{ab}	2.5 ± 0.3 a	0.8 ± 0.36^{bc}	0.4 ± 0.2 c
	Lower region	2.1 ± 0.27 ^{ab}	2.5 ± 0.45 ^{a}	1.3 ± 0.4 ^{bc}	0.3 ± 0.1 c
Traveling time	Upper region	1.1 ± 0.05 ^{b}	1.6 ± 0.11^{a}	0.4 ± 0.13^{c}	0.2 ± 0.1 c
	Lower region	1.1 ± 0.06 ^{b}	1.3 ± 0.12 ^{a}	0.7 ± 0.16bc	0.4 ± 0.11 c

Similar letters mean no significant differences between the same line.

The results revealed that no significant differences were recorded between the upper and lower regions in the handling time of honey bee workers while collecting nectar df = 229, P-Value = 0.801, T-Value = - 0.25. Also, our results did not record significant differences in the two regions for the handling time during the pollen collection, df = 232. T-Value = -0.31, P-Value = 0.753. As for the traveling time, no differences were recorded between the two regions during the nectar collection. df = 145. T-Value = 0.61, P-Value = 0.542, while the traveling time recorded significant differences between the two regions, where the pollen-collecting honey bee workers recorded the most preference for traveling. It was in the upper region with an average of (1.0 ± 0.07) seconds, df = 238. T-Value = 2.35, P-Value =0.020 (Table.2c)

Table (2c). The mean duration of the visit of *Apis mellifera* on apple flowers during the blossom season in both upper and lower regions.

Foraging region	Handling time (sec.)		Travelling time (sec.)	
	Nectar	Pollen	Nectar	Pollen
Upper region	1.92 ± 0.08 a	1.6 ± 0.1 a	1.7 ± 0.06 a	1.0 ± 0.07 a
Lower region	1.96 ± 0. 1a	1.7 ± 0.2 a	1.6 ± 0.1 a	0.7 ± 0.06 b

Similar letters mean that there are no significant differences between (in) the same column.

3. Weather conditions during the hours of the day

Temperatures recorded significant differences between the different daylight hours during the two regions (One-way ANOVA, P<0.0001 df= 3, F= 29.35), and humidity levels recorded significant differences between the different daylight hours (One-way ANOVA) F= 30.62, df=3, P < 0.0001), Where at 9:00 am the temperature was recorded at an average of 21.5°C and the average humidity

was 36.6%. Also, at 10:00 am, the temperature was recorded at an average of 23.4C°, and the average humidity was 31.0%. at 11:00 am, the average temperature was 24.5C°, and the average humidity was 26.2%. at 12:00 noon the average temperature was 27.5C°, and the average humidity was 22.1%.

DISCUSSION

The results showed apparent significant differences in the number of bee visits between day hours in the upper and lower region of the flowers during their foraging on nectar, the highest activity rates was on the upper region at 11:00 am (96.0 ± 6.0 bees / $m^{2)}$, and (84.0 ± 3.3) bees / m^2 on lower region due to the raise gradually of temperatures, which reach of 24 C°. The low rates of honey bee workers collecting nectar were recorded in the upper region at 12:00 pm, with an average of 73.3 ± 2.6 bees/ m^2, at the temperature reached of 27 C°, while at 9:00 am the lower region with an average 36.6±4.6 bees / m^2 the reason may be due to the humidity factor which reached 36.6%. The results showed apparent significant differences in collecting pollen between day hours during their visit to the upper and lower regions, the highest rates were25.3 ± 0.4 bees / m^2, in the upper regions, and 13.3 ± 0.77 bees / m^2 on the lower region at 9:00 am were the humidity was 36.6%, and this is consistent with (Essa & Bataw, 2020) who investigated the influence of higher temperatures increase the number of worker bees collecting nectar compared to decrease of humidity, and also agreed with what was indicated by (Meriti, 2003) when studying the activity of bees flowers of *Camalducnsis* sp, *Eucalyptus* sp, *Muricat*a sp, *Erica* sp. during their pollen collection. The lowest number of visiting rates of bees collecting pollen in the upper region were recorded at 11:00 am (7.00 ± 0.9 bees/m^2), as well as at 12:00 pm at lower region, when the rise in temperatures was recorded (3.6 ± 0.1 bees / m^2) and this results indicated by (Brown and Paxton, 2009) who consider the climate conditions as the important influences that play a decisive role in controlling the life and activity of insects, and changes these conditions are capable of affecting behavior, and addition to the effect of the humidity factor and its effect on the anthers of this plant, and this is consistent with what was indicated by (Malerbo et al., 2004) that honey bees collect pollen from *Citrus sinensis* in the early morning hours. The preference activity of bees was recorded the highest rates in the upper region during collect nectar (81.6 ± 1.9) worker/m^2 and pollen (11.5 ± 0.8) worker/m^2 and this is what is consistent with (Mattu,2012) that the effect of the difference in heights depends on the start of the timing of the foraging activity. The strategic positioning of flowers plays a vital role in guiding bees' approach flights and landings. By optimizing these routes, bees can conserve energy and time, which is essential for maximizing their foraging success and ensuring effective pollination by (wang et al., 2014).

Our results recorded an effect of the handling and travelling time rate on honey bee workers collecting nectar and pollen during daylight hours. No significant differences in the handling time in the upper and lower region when collecting nectar. As a result of the availability pollen and nectar, which allows bees to obtain it without fatigue and hardship, especially in the first hour of bee activity because the nature of the plant nectar changes in quantity and composition during the day (Corbet, 1978). The results recorded apparent significant differences in travelling time between flowers at the upper region during the day time, at 11:00 am, the highest rate of travelling time was recorded, with an average of (2.0 ± 0.05 sec.). and the lowest travelling time was at 12:00 noon, with an average of (1.5 ± 0.17 sec.),the high concentration and available of nectar at this time could be one of the reasons (Willmer et al, 1994 Bataw ,1996).

The handling and travelling time of the bee visit in both regions recorded the highest rates of at 10:00 am and the lowest handling and travelling time at 12 noon during collecting pollen., as result

of decrease production of new pollen grains at this time, where the apple blossoms produced pollen grains at 9:00 in the morning, and the effectiveness of the activity was high, which affected the handling time at the hour 10 am while collecting pollen at this time. and the variation in honey bee workers *A.mellifera* and *Megachile* sp continues to forage during the period of pollen release from the anthers, but *A.ceratina* forage for nectar when sugar rises and pollen decreases (Rust et al , 2003).efficient flower arrangements not only reduce handling time but also enhance the overall foraging success of bees. By minimizing the time handling on each flower, bees can visit more flowers, increasing their nectar and pollen collection, which is vital for their handlind and ecological role This strategic positioning ensures consistent pollinator movement and maximizes pollination success (Jordan et al.,2016).

The results indicated that the flower area did not affect the period of handling time in both regions during the visit of the bees to collect nectar or pollen, also the results revealed the effect of the flowers height on travelling time in the lower region during the collection of pollen. These results conclude that the behavioral activity of honey bees is determined by several factors, such as food preference or suitability of climatic conditions within the foraging flowers, which in turn reflects on the effect of tree height, and the flower position on the tree.

Duality of interest: The authors declare that they have no duality of interest associated with this manuscript.

Author contributions : Contribution is equal between authors.

Funding: No specific funding was received for this work.

REFERENCES

Bataw, A. A., & Shareef, N. K. (2018). Foraging Behaviour of Honey Bees Apis mellifera Linn. Visiting The Flowers of Some Wild Plants in Eljabal Alakhder-Libya. . *Al-Mukhtar Journal of Sciences* 33 (2): 112-118.

Bataw, A. A. (1996). *Pollination ecology of cultivated and wild raspberry (Rubus idaeus) and the behaviour of visiting insects*. University of St. Andrews (United Kingdom).

Benedek, P., Molnár, G. K., & Nyéki, J. (2000). Nectar production of pear (Pyrus communis L.) cultivars. *International Journal of Horticultural Science*, *6*(3), 67-75.

Brown, M. J., & Paxton, R. J. (2009). The conservation of bees: a global perspective. *Apidologie*, 40(3), 410-416.

Jordan, C. Y., Natta, M., & Harder, L. D. (2016). Flower orientation influences the consistency of bumblebee movement within inflorescences. *Annals of Botany*, *118*(3), 523-527. doi: 10.1093/aob/mcw132

Corbet, S. A. (1978). Bee visits and the nectar of Echium vulgare L. and Sinapis alba L. *Ecological Entomology*, *3*(1), 25-37.

Essa, S. Y., & Bataw, A. A.(2020). Foraging Behavior of *Apis mellifera* Linn. Visiting Some Plant Flowers in Aljabal Alakhder Region –Libya. Al-Mukhtar, Journal of Sciences 35 (3): 173-180.

Gegear, R. J., & Laverty, T. M. (2004). Effect of a colour dimorphism on the flower constancy of honey bees and bumble bees. *Canadian Journal of Zoology*, *82*(4), 587-593.

Joshi, N. C., & Joshi, P. C. (2010). Foraging behaviour of Apis spp. on apple flowers in a subtropical environment. *New York Science Journal*, *3*(3), 71-76.

Khanduri, V. P., & Sharma, C. M. (2002). Pollen production, microsporangium dehiscence and pollen flow in Himalayan cedar (Cedrus deodara Roxb. ex D. Don). *Annals of Botany*, *89*(5), 587-593.

Lau, P., Bryant, V., Ellis, J. D., Huang, Z. Y., Sullivan, J., Schmehl, D. R., ... & Rangel, J. (2019). Seasonal variation of pollen collected by honey bees (Apis mellifera) in developed areas across four regions in the United States. *Plos one*, *14*(6), e0217294. https://doi.org/10.1371/journal.pone.0217294

Malerbo-Souza, D. T., Nogueira-Couto, R. H., & Couto, L. A. (2004). Honey bee attractants and pollination in sweet orange, Citrus sinensis (L.) Osbeck, var. Pera-Rio. *Journal of Venomous Animals and Toxins including Tropical Diseases*, *10*, 144-153.

Mattu, V. K., Raj, H., & Thakur, M. L. (2012). Foraging behavior of honeybees on apple crop and its variation with altitude in Shimla hills of western Himalaya. *International journal of science and nature*, *3*(2), 296-301.

Merti, A. A. (2003). *Botanical Inventory and Phenology in Relation to Foraging Behaviour of the Cape Honeybees (Apis Mellifera Capensis) at a Site in the Eastern Cape, South Africa* (Doctoral dissertation, Rhodes University).

Morse, R. A., & Calderone, N. W. (2000). The value of honey bees as pollinators of US crops in 2000. *Bee culture*, *128*(3), 1-15.

Pleasants, J. M. (1981). Bumblebee response to variation in nectar availability. *Ecology*, *62*(6), 1648-1661.

Rust, R. W., Vaissière, B. E., & Westrich, P. (2003). Pollinator biodiversity and floral resource use in Ecballium elaterium (Cucurbitaceae), a Mediterranean endemic. *Apidologie*, *34*(1), 29-42.

Sharma. H.K., Gupta, J.K., & Thakur, J.R. (2004). Effect of bee pollination and polliniser proportion on apple productivity. Acta Horticulture, 662:451 - 454.

Shareef, N. K., Marwah Y. H. Almabrouk, Salma Y. Essa, & Ali A. Bataw (2022). Changes in Temperature and Humidity and their Effect on Activities of *Apis mellifera* L. Workers Visiting some Wild flowers in the Aljabal Al-Akhder. Al-Jabal Academy Journal of Pure and Applied Sciences, 1 (1): 01-09.

Silva, E. M., & Dean, B. B. (2000). Effect of nectar composition and nectar concentration on honey bee (Hymenoptera: Apidae) visitations to hybrid onion flowers. *Journal of Economic Entomology*, *93*(4), 1216-1221.

Wang, H., Tie, S., Yu, D., Guo, Y. H., & Yang, C. F. (2014). Change of floral orientation within an inflorescence affects pollinator behavior and pollination efficiency in a bee-pollinated plant, Corydalis sheareri. *PLoS One*, *9*(4), e95381. doi: 10.1371/journal.pone.0095381

Willmer, P. G., Bataw, A. A. M., & Hughes, J. P. (1994). The superiority of bumblebees to honeybees as pollinators: insect visits to raspberry flowers. *Ecological Entomology*, *19*(3), 271-284.

Al-Mukhtar Journal of Basic Sciences 22 (3): 272-288, 2024
Doi: https://doi.org/10.54172/168r0808

Research Article **Open Access**

Exploring the Impact of Pipe Material and Environmental Conditions on the Bacterial Adhesion to the Surface of the Drinking Water Distribution System

Anad M. Alshaybani [1*], Ebtesam Abdulhadi [2], Abdallah I. Abdallah [3] and Hanin Bzizi [4]

***Corresponding author:**
aafhaima2011@my.fit.edu,
Department of Chemistry, Faculty of Sciences, Sirte University, Libya.

[2] Department of Zoology, Faculty of Sciences, Sirte University, Libya.

[3] Department of Medical Microbiology, Faculty of Medicine, Sirte University, Libya.

[4] Department of Biomedical Science, Western Michigan University, Kalamazoo, MI 49008, USA.

Received:
19 November 2024

Accepted:
27 December 2024

Publish online:
31 December 2024

Abstract

Bacterial adhesion to surfaces is a complicated process influenced by several factors. Key factors are the physical properties of the materials, characteristics of the bacteria, and environmental conditions. In this study, the effects of the type of water distribution pipe material, water temperature, water flow speed, and contact time on the rate of bacterial adhesion to the pipe walls were evaluated. Two species of bacteria, gram-negative and gram-positive, were selected to study their tendency to adhere to the surfaces of two types of materials (galvanized iron and Polyvinyl Chloride (PVC)) used in the manufacture of water distribution pipes. The results showed that elevated temperature and contact time contributed to Increased adhesion of Gram positive bacteria to galvanized iron, whereas no discernible effects were observed for Gram negative bacteria. These findings also demonstrated that positively charged bacteria exhibited a higher capacity to adhere to mutually galvanized iron and PVC surfaces than Gram negative bacteria. Moreover, the rate of adhesion of Gram positive bacteria increased with increasing water flow rate, and there was no clear effect of water flow rate on the extent of adhesion of Gram negative bacteria on both surfaces. This study underscores the necessity of selecting appropriate pipe materials, factoring in operational temperatures and water flow dynamics to effectively manage bacterial biofilm development in distribution systems.

Keywords: Polyvinyl Chloride (PVC); Galvanized Iron; Bacterial Adhesion; Biofilm Formation; Water Distribution Systems; colony-forming units (CFUs).

INTRODUCTION

Biofilm growth considerably affects interactions between microbes and pipe surfaces during the initial adhesion stage. Nearly one billion people worldwide face health risks due to waterborne pathogens, predominantly facilitated by biofilm proliferation within drinking water distribution systems (DWDS) (Sharma et al., 2023; Adelodun et al., 2021; Owens et al., 2020). One of the primary avenues for these infections is through DWDS in which biofilms are frequently held within pipelines (Waqas et al., 2023; Gomez & Aggarwal, 2019; Zhang et al., 2018). Biofilms, which are resilient communities of microbes embedded within a polymer matrix, possess heightened resistance to disinfectants and environmental stressors (Rhoads et al., 2020).

The central problem revolves around understanding the influence of different pipe materials on bacterial adhesion and subsequent biofilm formation. This process is governed by physicochemical

forces between the microbes and substrates, which have been elucidated through thermodynamic principles (Bain et al., 2014; Fulaz et al., 2019). The key contributing factors include surface charge, hydrophobicity, and hydrophobicity (Oh et al., 2018; Danchik et al., 2021). Microbial appendages, such as pili, play a crucial role in overcoming repulsive forces and facilitating enduring bonds with surfaces (Costerton et al., 1995). Additionally, environmental parameters, such as water temperature, pH, disinfectant levels, and nutrients significantly influence biofilm growth (Erdei-Tombor et al., 2024; Goldberg et al., 2002; Peng et al., 2002; Stefan et al., 2023). Significantly, the material of the pipes influences the stimulation of the biofilm and the strength of adhesion (Goraj et al., 2021; Schwering et al., 2013; Zhang et al., 2022).

Commonly used distribution pipes, such as concrete, galvanized iron pipes, and Polyvinyl Chloride (PVC), may possess varying properties that effect on stimulate biofilm formation (Learbuch et al., 2021; Chen et al., 2020). However, a comprehensive comparative analysis of these different pipe types under standardized conditions is currently lacking. Addressing this issue involves rigorous exploration of the bacterial adhesion strength across various commonly used pipe materials at different temperatures. By quantifying these adhesion strengths and evaluating biofilm growth under controlled conditions, this study aims to provide actionable insights. These insights can guide the selection of pipe materials and inform strategies for managing temperature fluctuations, ultimately curbing biofilm formation, and reducing the persistence of pathogens within water distribution systems. Minimizing microbial contamination in these systems is a pivotal step toward mitigating waterborne infections globally. The primary objective of this study was to investigate the impact of pipe material, temperature variations, water flow rate, and contact time on the strength of bacterial adherence and the subsequent development of biofilms along water pipes. Through controlled experiments, this study sought to unravel the interplay between these factors and elucidate their combined influence on biofilm formation in drinking water distribution systems.

Backgraound & Related Work

Most studies have approached adhesion through a narrow lens by focusing on selected parameters (see Table 1). A deeper and more integrated understanding requires analyses that bridge the multiple domains. However, the study lacked a comprehensive explanation of the differences between various materials, leaving room for ambiguity.

(Lorenzetti et al., 2015) focused on the study of nano TiO_2 coatings and their effect on bacterial attachment. By employing a green fluorescent protein-expressing Escherichia coli strain, this study demonstrated reduced bacterial adhesion. However, the study did not establish a clear relationship with ζ potential, emphasizing the need for future studies with diverse materials to validate and generalize the findings.

(Liu and Tay, 2002) explored bacterial adhesion on different plastics, utilizing a microscopic cell counting chamber. Their findings indicate the effective role of surface hardness in bacterial adhesion. Nonetheless, the study mentioned that hydrophobicity did not influence bacterial adhesion, as shown by the complexity of the interactions involved.

(Bohinc et al., 2016) investigated the effect of surface roughness on bacterial adhesion using the crystal violet staining method.

This study indicated increased adhesion with increased surface roughness, although the absence of a study on extracellular polymeric substances (EPS) is a crucial factor that has not been explored. (Chik et al., 2018) investigated the factors affecting metallic surface adhesion using laser ablation and polishing. Their study revealed reduced adhesion after the laser treatment of metal surfaces, highlighting a potential method for deterring bacterial attachment.

Table :(1). Related Work

Author	Objective	Method	Outcome	Limitations
Yoda et al. (2014)	Investigate roughness impact on bacterial adhesion	Field emission scanning electron microscope (SEM)	Lower adhesion on hydrophobic surfaces, needs refinement	Lack of a comprehensive explanation of differences among materials.
Lorenzetti et al. (2014)	Study nano TiO_2 coatings on bacterial attachment	Green fluorescent protein expressing E. coli strain	Reduced bacterial adhesion, no relation with ζ potential	There is a need for diverse materials for validation in future studies.
Liu et al. (2023)	Explore bacterial adhesion on different plastics	Microscopic cell counting chamber	Surface hardness influential on bacterial adhesion	Hydrophobicity not dominant in bacterial adhesion
Bohinc et al. (2016)	Investigate surface roughness on bacterial adhesion	Crystal violet staining method	Increased adhesion with roughness, EPS not studied	Lack of EPS as a key factor for adhesion.
Chik et al. (2018)	Study factors affecting metallic surface adhesion	Laser ablation and polishing	Reduced adhesion after laser treatment on metal surfaces	This study primarily examined initial adhesion rates, which may not consider long-term biofilm development and stability.
Oh et al. (2018)	Analyze hydrophobicity and zeta potential effect	Scanning electron microscope (SEM) micrographs	Greater adhesion on hydrophilic substrates	Adhesion was examined only under controlled laboratory conditions.
Fink et al. (2015)	Examine liquid flow and temperature on detachment	New liquid flow chamber	Turbulent flow and higher temperature increase detachment	Further experiments are required to gain a deeper understanding.
Oder et al. (2015)	Investigate material roughness and temperature	Spectrophotometric method	Positive relation between roughness and adhesion	Ineffectiveness in detecting survivors at specific temperatures.
Zeraik & Nitschke (2012)	Assess culture media and temperature on adhesion	Crystal violet staining technique	Adhesion varied with temperature and media	Hydrophobicity is insufficient to predict bacterial adhesion.

MATERIALS AND METHODS

Bacterial Strains Isolation and identify

The bacterial strains used in this study were isolated from tap water samples collected from a local water-supply system. A mixture of 1 ml of sterile tap water and 1 ml of local tap water was incubated in nutrient broth overnight at 37°C. The following day, one colony from each freshly cultured bacterial strain was inoculated onto artificial media, specifically R2A agar (Reasoner's 2A agar). The mixture was then incubated overnight at 37°C. Finally, the isolated bacterial strains were differentiated. The distinctions among the bacterial strains were based on the shape and size of their colonies, as well as their reaction to Gram staining, categorizing them as either gram-positive or gram-negative using the Gram stain technique (Paray et al., 2023).

Preparation of Pipe Material Samples

Pipe samples were obtained from materials normally used in water distribution systems. Polyvinyl Chloride (PVC) and galvanized iron were cut into 2 × 2 cm coupons. These samples were thoroughly cleaned and sterilized using a combination of 70% ethanol and UV irradiation. For the investigational setup, every pipe coupon was strongly fixed inside a separate 150 ml beaker using metal clips as shown in fig. 1.

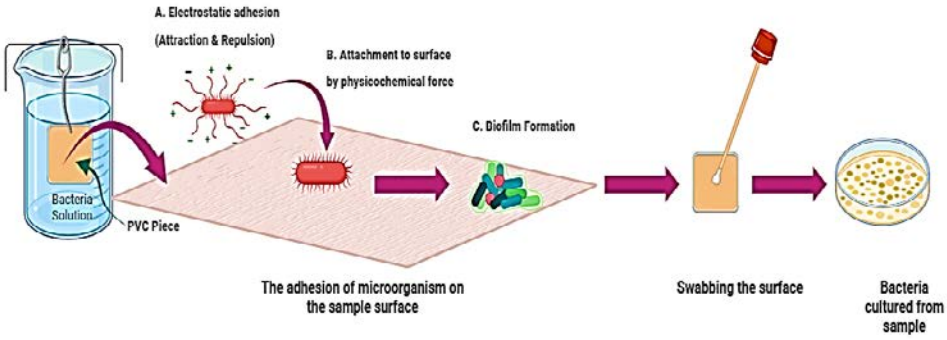

Figure: (1). The steps of experiment.

Preparation of bacterial Samples for Adhesion Assay Protocol

Approximately 10^9 colony-forming units of overnight cultured bacteria were diluted in 9 ml of sterilized tap water. One milliliter of the prepared bacterial water sample was transferred to a beaker containing 150 ml of sterilized water. Fixed polyvinyl chloride (PVC) and galvanized iron coupons were then immersed in bacterial water samples at various temperatures (5, 25, 35, and 45°C), contact times (30 and 60 min), and water flow speeds (2 and 4 rpm). After each experiment, the pipe coupon samples were gently rinsed to remove non-adherent cells.

Detachment and quantification of adhered cells on materials sample Surface

To quantify bacterial adhesion, all the bacteria that adhered to the sample coupon surface were swabbed using a swab stick. A swab stick was then immersed in 10 ml of distilled water and vortexed for 2 min to detach biofilm cells. One milliliter of each suspension was plated on R2A agar and cultured in a bacterial incubator at 37°C. After 24 h, the colony-forming units (CFUs) were counted.

Quantification of the strength of cell adhesion to PVC substrate using a centrifugation assay

The adhesion strength of the bacterial cells to the PVC coupon surfaces was evaluated using centrifugation. First, microbial cells were seeded onto the PVC coupon surfaces. The seeded PVC coupons were then transferred to a centrifuge test tube and covered with 1 ml of distilled water. The test tube was placed in a laboratory centrifuge and the bacteria were harvested by centrifugation for 2 min, applying six different dislodgement forces ranging from 0 to 3500 g. The resulting suspensions were then cultivated on R2A agar for 24 h, after which the colony-forming units (CFUs) were counted. The number of bacteria removed was plotted against the applied forces to create adhesion profile characteristics of the bacterial cells adhering to the surface.

EXPERIMENTAL DESIGN & STATISTCAL ANALYSIS

Data Description

This study applied a comprehensive dataset encapsulating various attributes related to bacterial adhesion and biofilm formation on different pipe materials under varying conditions. The data in Table 2 include categorical variables, such as pipe material, temperature, contact time, water flow speed, and bacterial type, as well as a numerical variable representing bacterial density. Each attribute plays a crucial role in analyzing the impact of environmental and experimental conditions on biofilm development.

Table :(2). Data Description

Attribute ID	Variables	Type	Description
1	Pipe material	Categorical	Two levels: Galvanized Iron and PVC
2	Temperature	Categorical	Five levels: 5°C, 15°C, 25°C, 35°C, and 45°C
3	Contact time	Categorical	Two levels: 30 minutes and 60 minutes.
4	Water flow speed	Categorical	Two levels: 2rpm and 4rpm
5	Species of bacteria	Categorical	Two Species: Gram positive and Gram negative
6	Bacteria density	Numerical	-

Experimental Design

The experimental design incorporates a set of experiments under various conditions to systematically assess the influence of pipe material, bacterial type, contact time, and temperature on bacterial adhesion. Specifically, trials used two types of pipes: galvanized iron and PVC, which represent commonly utilized distribution materials. These were tested across a range of five temperatures from 5°C to 45°C, which reflect the variable conditions in drinking water systems. Additionally, flow speeds of 2 rpm and 4 rpm were used to mimic the common water flow speeds in the pipe distribution system. Contact times of 30 min and 1 h revealed both the initial cell attachment and early biofilm development stages. By measuring adhered cell densities across these combinations of factors, the experiments enabled detailed modeling of how bacterial surface colonization depends on key physical and chemical properties. Statistical tests, such as two-way ANOVA, were performed to discern the significant main effects of each parameter and any interaction effects.

RESULTS

Assessment of bacteria adhesion

The aim of this study was to test the impact of surface type, temperature, and water flow speed on the rate of bacterial adhesion. Our results indicate that the adhesion of Gram positive bacteria onto both galvanized iron and PVC surfaces is influenced by temperature, as shown in Figure 2. We noted that a gradual increase in temperature resulted in a notable increase in bacterial adhesion, and the optimum bacterial growth temperatures were 25Cº & 45Cº for Gram positive bacteria. Our results are consistent with those of previous studies.

(Rode et al., 2007) have indicated that the rate of adhered *S. aureus* (Gram-positive bacteria) is promoted when bacteria incubate at optimal temperatures. (Da Silva-Meira et al. 2012) reported that the maximum intensity of biofilm formation on stainless steel and polypropylene was observed at 28 Cº. (Roy et al., 2021) concluded that the high temperatures (25 to 42°C) lead to increased biofilm formation on food industry surfaces. (Oder et al., 2015; Ana Eliza et al., 2012) pointed out that there is a positive correlation between temperature and the intensity of bacteria adhering to the surface, with the highest adhesion number of bacteria found at a higher temperature of 35 °C and the lowest at 4 Cº. In contrast, in our study, no significant effect was observed on the adhesion of the Gram negative bacteria to both galvanized iron and PVC surfaces.

According to (Bohinc et al., 2016) the most hydrophobic bacteria (*S. aureus ŽMJ 72 and P. aeruginosa ŽMJ 87*) adhere more to stainless steel surfaces. This effect is in agreement with the outcome of our study, which showed that the Gram positive bacteria have a greater ability to adhere to mutually galvanized iron and PVC surfaces. This can be attributed to the fact that bacteria that are more hydrophobic tend to adhere to more hydrophobic surfaces. These findings are in good agreement with those of (Doyle, 2000 ; Roosjen et al., 2006).

These studies revealed that microorganisms tend to attract more hydrophobic surfaces because of the inhibition of the formation of hydrogen-bonded water molecules. Our findings are also consistent with the common rule of bacterial adhesion that bacteria adhere to more hydrophobic surfaces (Katsikogianni and Missirlis, 2004). Additionally, the present study found that compared to PVC, the galvanized iron substratum was shown to promote the development of high-intensity adhered bacteria, as shown in Figure 2.

This result was consistent with the findings of (Niquette et al., 2000 ; Zhu et al., 2014). This difference in the number of adhered bacteria to the two types of material can be explained by the fact that microorganisms tend to adhere to rougher surface materials, as suggested by (Kerr et al., 1998).

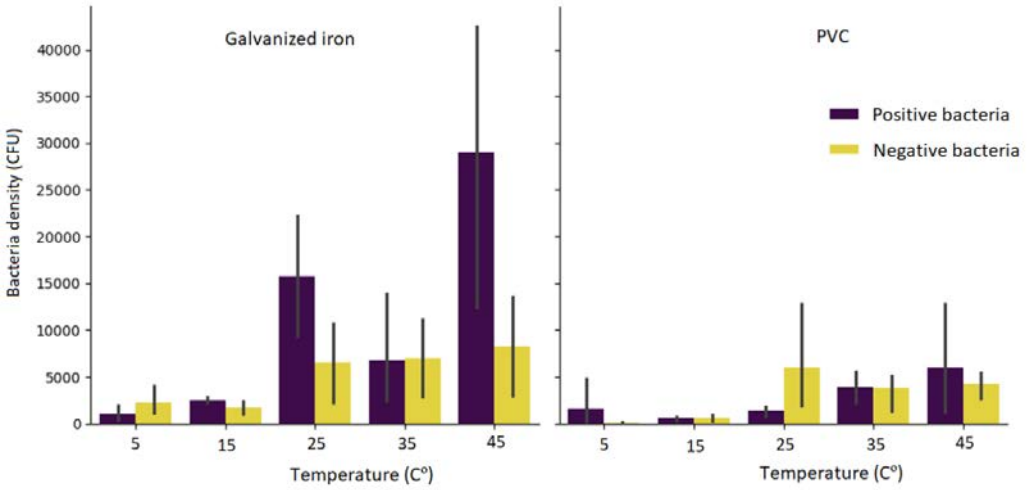

Figure (2). Adhesion assays of bacterial suspensions to galvanized iron coupon surfaces and PVC coupon surfaces at different temperatures

The impact of the water flow speed (at constant temperature and time) on bacterial adhesion to the surfaces is shown in Figure 3. The results revealed an increase in the counts of adhered- Gram positive bacteria on galvanized iron with an increased flow rate. (Liu et al. 2002; Chambless JD & Stewart PS 2007) suggested that increasing the flow of bacteria towards or parallel to the surface results in an increased rate of bacterial adhesion of microorganisms due to higher mass transport. However, the number of adhered Gram negative bacteria to galvanized iron decreased slightly with increasing flow rate because the fluid flow rate exceeded a critical value, which may prevent bacteria from having a suitable contact time to adhere and accumulate on the surface. Meanwhile, the water flow rate had no significant effect on the adhesion of bacteria to both the galvanized iron and PVC surfaces.

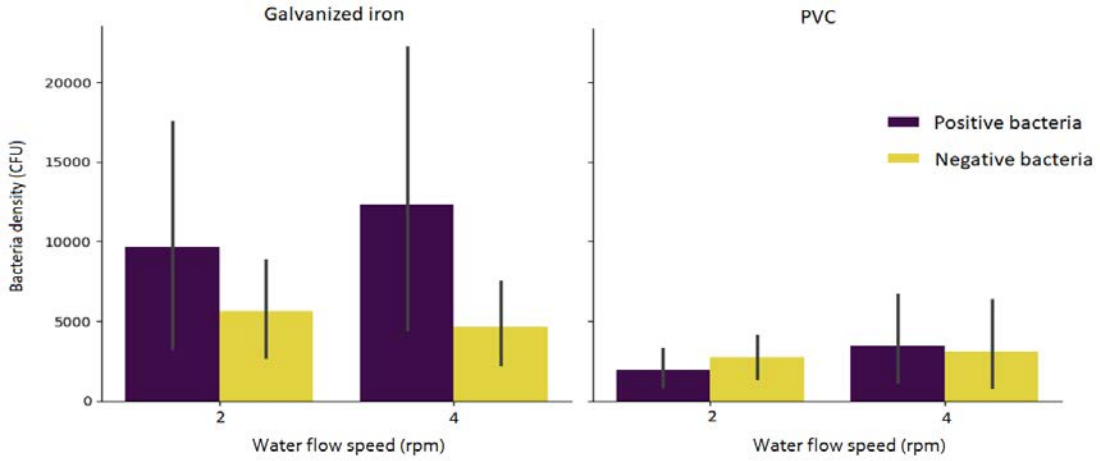

Figure: (3). Density of bacteria on galvanized iron coupon surfaces and PVC coupon surfaces at different rotational speeds (2rpm and 4rpm)

The impact of contact time on the rate of bacterial attachment to both the galvanized iron and PVC surfaces (at a constant temperature and flow rate) is shown in Figure 4. The results indicate that the number of adhered Gram positive bacteria on galvanized iron surfaces increases with increasing contact time; in contrast, there was no clear influence of contact time on the adhesion of both bacterial types to the PVC surface.

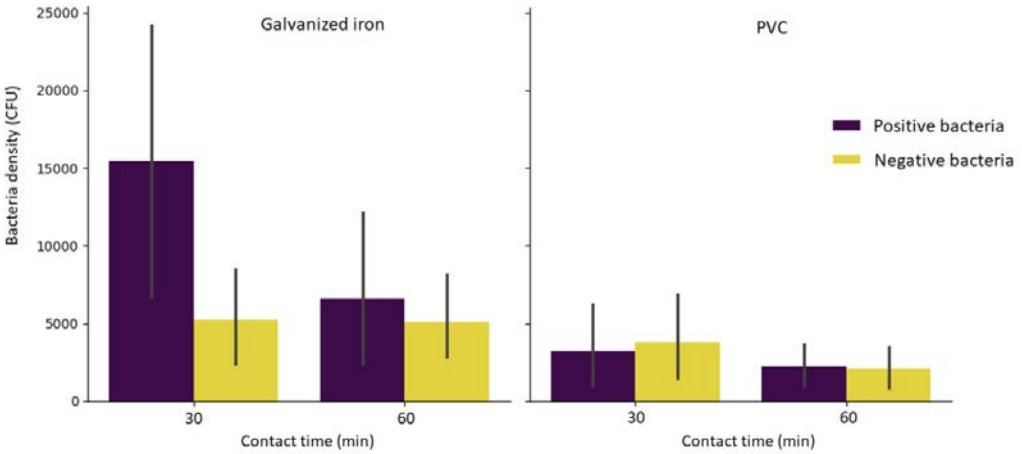

Figure (4). Density of bacteria on galvanized iron coupon surfaces and PVC coupon surfaces at different incubation times (30 min and 60 min).

To obtain further information about the interaction strength between the adhered cells and substrates, the strength of bacterial cell adhesion to the PVC substrate was evaluated using a centrifugation assay. The number of bacterial cells removed after application of the controlled force was counted.

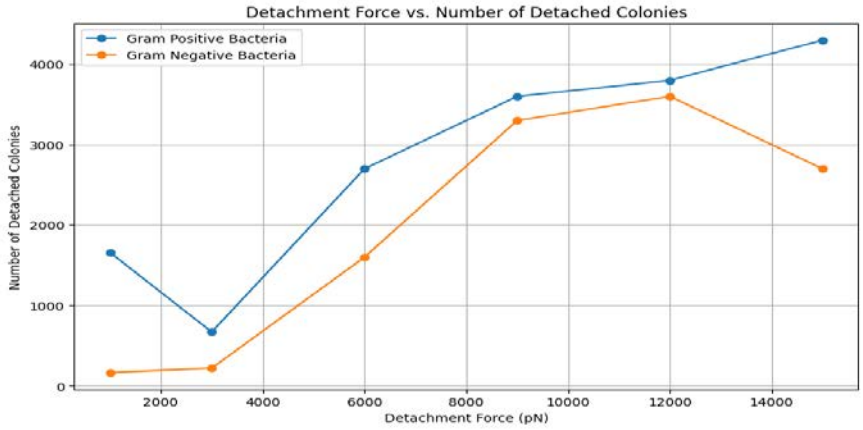

Figure (5). The relation between removal of bacteria cells and applied force.

The plot of the number of detached cells against the applied detachment force shows that the number of cells removed from the PVC surface increased exponentially as the applied force increased, as shown in Figure 5. The leftward shifts in this sigmoid curve with increasing applied force indicate that most of the bacteria were bound to the surface with a high adhesion force. This increase in the applied rupture force provided clear evidence that the bacteria adhered strongly to the surface even after short-term bacterial attachment (30 min and 60 min), which is required for the formation of biofilms on surfaces. The shape of the curve obtained is in agreement with that obtained by Reyes and García, 2003, who showed that increasing the applied force led to an increase in the number of bacteria detached from the surface.

STATISTICAL ANALYSIS

Description of Statics

A mean temperature of 20°C represents a pivotal point for bacterial behavior, as temperature is a key environmental factor influencing microbial growth and survival. A standard deviation of 11.269°C indicates substantial variability in temperature conditions. Quartile analysis showed 50% of observations below 27.5°C, with a significant portion residing in higher ranges that could exacerbate bacterial adherence and biofilm formation.

Table :(3). Description of Static Values

Factors	Mean	Standard Deviation	25%	50%	75%
Temperature	20ºC	11.269	12.50	20	27.5
Water flow speed	3rpm	1.008	2	3	4
Contact Time	45min	15.119	30	45	60
Material surface type	0.500	0.504	0	0.5	1
Bacteria Density	3627.34	5302.63	682.5	2840	4350

As shown in Table 3, a mean material value of 0.500 and a standard deviation of 0.504 demonstrated heterogeneity in the pipe properties. With 50% of the observations at or below 0.5, this underscores variations in material composition and subsequent implications for bacterial-surface interactions and water contamination. Understanding these material-specific dynamics is imperative for the development of mitigation strategies. The mean water flow speed of 3 rpm and standard deviation of 1.008 rpm indicated variability in the flow dynamics modulating bacterial transport and adherence. Distinct quartile ranges reveal nuanced spreads linking flow velocity to biofilm development. This multifaceted relationship between the key factors of temperature, pipe material, and flow rate underscores the complex interplay that governs microbial water quality.

Three-way ANOVA

In this study, the relationship between environmental factors and bacterial adherence increase was a subject of great significance. A statistical analysis, ANOVA, was performed to understand the impacts of temperature, bacterial type, and material surface type on bacterial density. The analysis was structured methodically to consider the separate and combined effects of these variables. To perform a multifactorial ANOVA that included more than two factors, we used a model that assessed the main effects of each independent variable (temperature, water flow speed, contact time, material surface type, and bacterial species) and their interactions with the dependent variable (bacterial density). Both two-way interactions (such as Temperature with Speed, Temperature with Material) and higher-order interactions (such as Temperature with Speed with Material) were applied.

Impact of Temperature, Species of Bacteria, and Material on Bacterial Density

An extensive analysis of variance (ANOVA) was performed to resolve the effects of temperature, bacterial species, and material surface on bacterial density, as shown in Table 4. Follow-up analyses revealed precise differences in bacterial adhesion to galvanized iron at 5°C and 25°C. Regression modeling based on the entire dataset predicted cell adhesion rates for novel combinations beyond those explicitly tested. The ANOVA results are presented in Table 3. The effect of temperature on the bacterial density was significant ($p < 0.000002$), indicating that temperature is a critical factor for bacterial growth in pipes. This discovery is associated with essential knowledge that bacteria are highly sensitive to their thermal environment, with their metabolic processes being regulated by temperature fluctuations.

The species of bacteria was another influential factor ($p < 0.000101$), showing the diversity that exists, including the different bacterial species. This indicates that each bacterial type possesses exclusive attributes that shape its growth patterns, displaying the changes they have undergone to survive and thrive in their respective ecological niches. The role of the material as a growth substrate was also notable ($p = 0.025257$), indicating that the physical and chemical properties of the surface can influence the density of bacterial colonies. This finding has implications in materials science, where the development of antibacterial surfaces or materials designed to promote bacterial growth is an active area of research. An interesting interaction between temperature and bacterial species was observed ($p = 0.013825$), indicating that the effect of temperature on bacterial density varies across different bacterial species. This interaction suggests that certain bacterial species may be more resilient or better adapted to specific temperature ranges than others.

Table :(4). ANOVA Summary for Temperature, Type of Bacteria, and Material

Source	Sum of Squares	df	F Value	p Value
Temperature	1.301e+09	4	10.417	0.000002
Species of Bacteria	5.417e+08	1	17.347	0.000101
Material	1.644e+08	1	5.266	0.025257
Temperature: Species of Bacteria	4.274e+08	4	3.422	0.013825
Temperature: Material	3.897e+08	4	3.120	0.021292
Species of Bacteria: Material	1.770e+08	1	5.667	0.020480
Temperature: Species of Bacteria: Material	3.590e+08	4	2.874	0.030283
Residual	1.874e+09	60	-	-

The interaction between temperature and material also proved to be significant (p = 0.021292), suggesting that the influence of the material on bacterial density is temperature dependent, as shown in Figure 6. This indicates that the properties of certain materials may change with temperature, thereby affecting bacterial adhesion and growth.

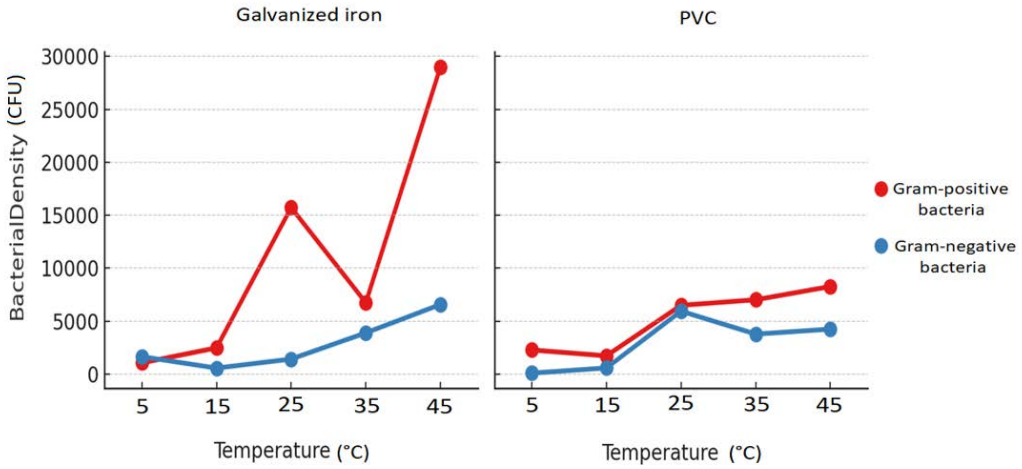

Figure (6). Interaction between temperature and type of bacteria across material levels.

The interplay between bacterial species and material was a significant factor (p = 0.020480), suggesting that certain materials may selectively favor the growth of specific bacterial species. This finding has practical implications in various fields such as medical device manufacturing and environmental biotechnology. Finally, a significant three-way interaction among temperature, bacterial species, and material was observed (p = 0.030283), highlighting the intricate nature of the microbial ecosystem, where multiple factors converge to determine bacterial density.

In this study, we explored the impact of material type, contact time, bacterial strain, temperature, and speed on bacterial adherence using galvanized iron and PVC. Our results revealed that temperature, material composition, and bacterial strain significantly influenced bacterial adherence, with distinct effects observed at different temperatures and with different materials.

Effect of Speed, Species of Bacteria, and Material on Bacterial Density

In an exploratory study examining factors influencing bacterial density, ANOVA was conducted to assess the impacts of water flow speed, species of bacteria, and material surface type, as shown in Table 5. This study aimed to elucidate the separated and interactive effects of these variables on bacterial population density.

Table :(5). ANOVA Summary for Water flow speed, Species of Bacteria, and Material

Factors	Sum of Squares	df	F Value	p Value
Water flow speed	1.288e+07	1	0.215	0.643908
Species of Bacteria	5.417e+08	1	9.063	0.003595
Material	1.644e+08	1	2.751	0.101518
Water flow speed: Species of Bacteria	8.446e+03	1	0.000141	0.990548
Water flow speed: material surface type	2.569e+07	1	0.430	0.514200
Species of Bacteria: material surface type	1.770e+08	1	2.961	0.089601
Water flow speed: Species of Bacteria: material surface type	8.971e+06	1	0.150	0.699579
Residual	4.303e+09	72	-	-

The main effect of water flow speed on bacterial density was found to be non-significant ($p = 0.644$), suggesting that variations in water flow speed within the tested range did not significantly influence the density of bacteria, as shown in Figure 7. This finding indicates that, at least within the parameters of this experiment, the bacterial density remained unaffected by changes in water flow speed. However, the species of bacteria had a significant effect on the bacterial density ($p = 0.0036$). This result indicates a distinct difference in how two species of bacteria proliferate or sustain their populations, underscoring the biological diversity between bacterial species and their unique responses to environmental conditions. Material surface type as a factor did not demonstrate a significant main effect ($p = 0.102$). However, the relatively low p-value prompts consideration of further inquiry. This indicates the possibility of material composition exerting a subtle influence on bacterial density, a hypothesis that may require additional data or a broader scope of material types for a comprehensive evaluation. The interaction between speed and type of bacteria, when explored, did not yield statistical significance ($p = 0.991$). Similarly, the interaction between the water flow speed and material also failed to show significance ($p = 0.514$).

These outcomes suggest that the interplay between these factors does not meaningfully contribute to variations in bacterial density, at least not in the context provided by the current dataset. An interesting near-significant result emerged from the interaction between the two species of bacteria of bacteria and material type ($p = 0.090$). This near-threshold finding suggests a nuanced relationship in which the material type may influence bacterial density differently depending on the two species of bacteria. This interaction warrants further investigation, as it could reveal material-specific preferences or aversions unique to each two species of bacteria.

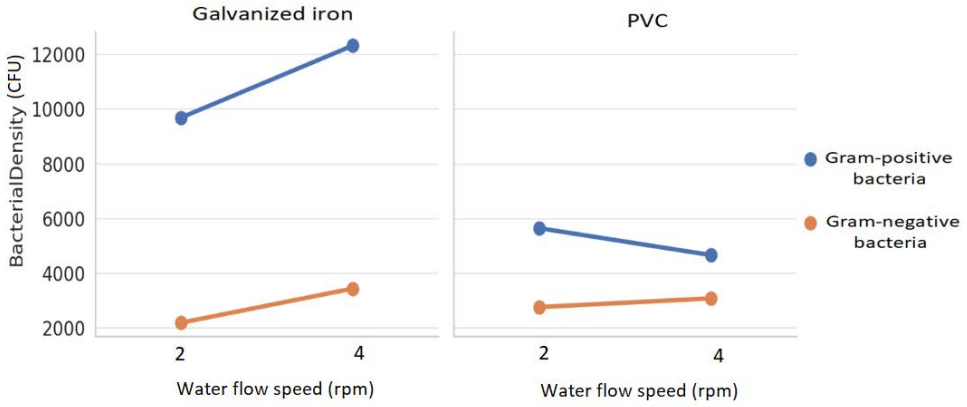

Figure (7). Interaction between speed of water and type of bacteria across material levels.

Finally, the three-way interaction between speed, species of bacteria, and material was found to be non-significant ($p = 0.700$). This indicates that the combined influences of these factors do not interact in a way that significantly deviates from their individual effects on bacterial density.

DISCUSSION

In the field of microbiology, understanding the factors that influence bacterial adherence is crucial for advancing both theoretical knowledge and practical applications. (Oh et al., 2018) analyzed the effects of hydrophobicity and zeta potential on bacterial adhesion using scanning electron microscope (SEM) micrographs. Their findings indicate greater adhesion on hydrophilic substrates, contributing to the growing understanding of the surface characteristics that influence bacterial attachment. (Fink et al., 2015) examined the influence of liquid flow and temperature on detachment by introducing a new liquid flow chamber. This study observed that turbulent flow and higher temperatures increased the detachment, signifying the need for further experiments to deepen our understanding of these dynamics. (Oder et al., 2015) investigated the relationship between material roughness, temperature, and bacterial adhesion using spectrophotometry.

Their study identified a positive correlation between roughness and adhesion, although it was noted to be ineffective in detecting survivors at specific temperatures, indicating potential limitations. (Zeraik & Nitschke 2012) assessed the impact of culture media and temperature on bacterial adhesion using the crystal violet staining technique. This study revealed that adhesion varies with temperature and media, emphasizing that hydrophobicity alone is insufficient to predict bacterial adhesion. Several limitations and gaps have been identified in studies on bacterial adhesion. First, there is a lack of comprehensive explanations for the differences observed among various materials. For instance, (Yoda et al., 2014) discovered lower adhesion on hydrophobic surfaces but failed to provide a thorough understanding of the variations in bacterial adhesion across different materials. Additionally, there are unexplored mechanisms and variations associated with different metals, as highlighted by (Chik et al., 2018).

While their study found reduced adhesion on metal surfaces after laser treatment, it did not delve into the underlying mechanisms or investigate potential variations with different metals. The incomplete understanding of how zeta potential contributes to bacterial adhesion is another notable gap identified by (Oh et al., 2018). Although they identified higher adhesion on hydrophilic substrates, a comprehensive understanding of the role of zeta potential in bacterial adhesion is lacking. Fink et al., 2014 emphasized the need for further experiments to understand the specific mechanisms under varied flow and temperature conditions. Although their study showed that turbulent flow and higher temperatures increased detachment, it underscored the necessity for additional experiments to gain a deeper understanding of the specific mechanisms involved. The ineffectiveness of detecting survivors at specific temperatures, as established by (Oder et al., 2015), reveals a positive relationship between material roughness and adhesion. However, these techniques are unable to detect survivors at certain temperatures, indicating the need for improved methods to capture the nuances of bacterial adhesion under different temperature conditions (Oder et al., 2015). Finally, the inadequacy of relying solely on hydrophobicity as a predictive factor for bacterial adhesion was highlighted by (Zeraik & Nitschke 2012). Their findings indicated that changes in temperature and media influence bacterial adhesion, emphasizing the limitations of using hydrophobicity alone as a predictive factor. Addressing these limitations and filling these gaps through further research and experimentation are crucial for developing a more comprehensive understanding of bacterial adhesion.

This study seeks to juxtapose the findings of our 2024 study with previous research, shedding light on the methodological innovations introduced, variables considered, and consequential insights derived from our investigation. Previously, research on bacterial adherence has often been segmented, with studies typically isolating single variables, such as temperature or material type, to discern their effects, as shown in Table 6. Such approaches, while foundational, offer a limited view of the multifaceted nature of bacterial behavior. In contrast, our study adopted a holistic methodology that integrates a spectrum of variables, including temperature, material type, contact time, bacterial

strain, and flow rate. This comprehensive approach not only corroborates the findings of previous studies but also unveils the complex interdependencies between these factors, thereby enriching our understanding of bacterial adherence in environments that closely mirror natural conditions.

Table :(6). Compassion for previous studies and our research.

Ref.	Temp	Time	Speed	Bacteria Type	Outcomes
da Silva et al., 2010		✓		✓	Increase in adhered Gram positive and negative bacteria on polyethylene and stainless steel at 20°C compared with lower temperatures.
Meylheuc et al., 2001	✓	✓		✓	The adhesion behavior of the bacterial cells on PTFE and AISI 304 stainless steel increased at 20 °C.
Ana & de, 2012	✓	✓		✓	The adhesion behavior was altered by temperature changes.
Fletcher, 1977	✓	✓		✓	The highest number of bacterial cells adhering to quartz was recorded at suboptimal temperatures (20°C, 25°C, and 30°C).
Morisaki, 1991	✓			✓	The adhesion behavior of the bacterial cells on polystyrene decreased with decreasing temperature.
Christersson et al., 1988		✓	✓	✓	The number of adhered bacterial cells on the titanium nanostructures decreased with increasing flow rate.
Senevirathne et al., 2022	✓		✓	✓	Sigmoidal increase in cell detachment with increased liquid velocity.
Our Research, 2024	✓	✓	✓	✓	Temperature, type of material, and type of bacteria had a greater effect on bacterial adherence to PVC and galvanized iron.

Prior investigations have consistently underscored the significant role of temperature and material type on bacterial adherence. Many studies have delineated how these factors individually affect bacterial behavior. Our research corroborates these findings but extends the inquiry to examine the synergistic effects of temperature, material type, and bacterial strains. This exploration unearthed nuanced dynamics, revealing that specific combinations of these variables can lead to markedly distinct adherence outcomes, thereby illuminating the intricate mechanisms underlying bacterial adherence. The influence of liquid velocity and flow rate on bacterial detachment and adherence has been highlighted in previous studies (Christersson et al., 1988**;** Senevirathne et al., 2022). However, these studies often limited their scope to single bacterial strains or a narrow selection of bacterial types. Building on this foundation, our study expands the scope of investigating the impact of varying flow rates across multiple bacterial strains.

This wider investigation revealed that the effect of speed on bacterial adherence is related to the bacterial type, challenging the main assumption of a uniform answer to flow rate changes and suggesting a more nuanced approach to managing bacterial adherence. While previous research has provided valuable insights into the individual factors affecting bacterial adherence, the findings have often been piecemeal. Our 2024 study synthesizes these disparate strands of knowledge and presents a unified framework that captures the complex interplay of multiple factors. The discovery of significant three-way interactions among temperature, material type, and bacterial strain not only advances our theoretical understanding, but also heralds new possibilities for targeted bacterial management strategies. Our study represents a significant leap forward in the field of microbiology by bridging the gaps left by previous research. By adopting a more integrated and comprehensive

approach, we unveiled the complex web of interactions that govern bacterial adherence. These findings not only enrich our theoretical knowledge, but also open new horizons for practical applications, from healthcare to industrial and environmental management, paving the way for innovative strategies to harness or mitigate the effects of bacteria in various contexts.

CONCLUSION

In this study, two species of materials (galvanized iron and PVC) used in the manufacturing of water distribution pipes were subjected to bacterial isolation from drinking water under various conditions of temperature, water flow speed, and contact time. The findings revealed that increasing the temperature, contact time, and flow rate led to a gradual increase in the adhesion rate of Gram positive bacteria to galvanized iron, while there was no clear effect of these factors on the Gram negative bacteria. The significant three-way interaction suggests that the influence of temperature on bacterial density cannot be fully understood without considering both the type of bacteria and material, as these factors jointly affect bacterial growth. The significant main effects and interactions observed in this study provide valuable insights for applications where bacterial density is a critical concern, such as designing antibacterial surfaces, optimizing growth conditions in bioreactors, and understanding natural bacterial colonization patterns in various environments.

ACKNOWLEDGEMENT

We sincerely thank the Chemistry and Zoology Departments, Faculty of Science, Sirte University, Libya for their essential resources and support. We also thank the Department of Medical Microbiology, Faculty of Medicine, Sirte University, Libya for their valuable collaboration and technical assistance.

Duality of interest: The authors declare no duality of interest associated with this manuscript.

Author contributions: All authors contributed to the studies conception and design. Material preparation and data collection were performed by [Anad M. Alshaybani], [Ebtesam Abdulhadi], and [Abdallah I. Abdallah], data analysis was done by [Anad M. Alshaybani] and [Hanin Bzizi], and first draft of the manuscript was written by [Anad M. Alshaybani]. All authors read and approved the final manuscript.

Funding: There are no sources of financial funding and support.

REFERENCES

Adelodun B, Ajibade FO, Ighalo JO, Odey G, Ibrahim RG, Kareem KY, Bakare HO, Tiamiyu AO, Ajibade TF, Abdulkadir TS, Adeniran KA, Choi KS (2021) Assessment of socioeconomic inequality based on virus-contaminated water usage in developing countries: A review. Environmental research 192, 110309. https://doi.org/10.1016/j.envres.2020.110309 .

Bain R, Cronk R, Wright J, Yang H, Slaymaker T, Bartram J (2014) Fecal Contamination of Drinking-Water in Low- and Middle-Income Countries: A Systematic Review and Meta-Analysis. PLoS Medicine, 11, 1–23. https://doi.org/10.1371/journal.pmed.1001644 .

Bohinc K, Jevšnik M, Nipič D, Dražić G, Abram A, Jeršek B, Kurinčič M, Raspor P (2016) Metal surface characteristics dictate bacterial adhesion capacity. International Journal of Adhesion and Adhesives, 68, 39-46–46. https://doi.org/10.1016/j.ijadhadh.2016.01.008 .

Chambless JD, Stewart PS (2007) A three-dimensional computer model analysis of three hypothetical biofilm detachment mechanisms. Biotechnology and bioengineering, 97, 1573–1584. https://doi.org/10.1002/bit.21363 .

Chen H, Wei Z, Sun G, Hu B, Lou L, Su H, Liu J, Zhou X (2020) Formation of biofilms from new pipelines at both ends of the drinking water distribution system and comparison of disinfection by-products formation potential. Environmental Research, 182, 109150. https://doi.org/10.1016/j.envres.2020.109150 .

Chik N, Wan Md Zain WS, Wan Ibrahim WH, Mohamad AJ, Sidek MZ, Reif A, Rakebrandt, JH, Pfleging W, Liu X (2018) Bacterial Adhesion on the Titanium and Stainless-Steel Surfaces Undergone Two Different Treatment Methods: Polishing and Ultrafast Laser Treatment. IOP Conference Series: Materials Science and Engineering, 358, 012034. https://doi.org/10.1088/1757-899X/358/1/012034 .

Christersson CE, Glantz PJ, Baier RE (1988) Role of temperature and shear forces on microbial detachment. European Journal of Oral Sciences, 96, 91–98. https://doi.org/10.1111/j.1600-0722.1988.tb01413.x .

Costerton JW, Lewandowski Z, Caldwell DE, Korber DR, Lappin-Scott H (1995) Microbial biofilms. Annual review of microbiology, 49, 711–745. https://doi.org/10.1146/annurev.mi.49.100195.003431 .

da Silva Malheiros P, dos Passos CT, Casarin LS, Serraglio L, Tondo EC (2010) Evaluation of growth and transfer of Staphylococcus aureus from poultry meat to surfaces of stainless steel and polyethylene and their disinfection. Food Control, 21, 298–301. https://doi.org/10.1016/j.foodcont.2009.06.008 .

Da Silva Meira QG, De Medeiros Barbosa I, Alves Aguiar Athayde AJ, De Siqueira-Júnior, JP, De Souza EL (2012) Influence of temperature and surface kind on biofilm formation by Staphylococcus aureus from food-contact surfaces and sensitivity to sanitizers. Food Control, 25, 469–475. https://doi.org/10.1016/j.foodcont.2011.11.030 .

Danchik C, Casadevall A (2021) Role of Cell Surface Hydrophobicity in the Pathogenesis of Medically-Significant Fungi. Frontiers in Cellular and Infection Microbiology, 10, 594973 https://doi.org/10.3389/fcimb.2020.594973 .

Doyle RJ (2000) Contribution of the hydrophobic effect to microbial infection. Microbes and Infection, 2, 391–400. https://doi.org/10.1016/S1286-4579(00)00328-2 .

Erdei-Tombor P, Kiskó G, Taczman-Brückner A (2024) Biofilm Formation in Water Distribution Systems. Processes, 12(2), 280. https://doi.org/10.3390/pr12020280 .

Fink R, Oder M, Rangus D, Raspor P, Bohinc K (2015) Microbial adhesion capacity. Influence of shear and temperature stress. International Journal of Environmental Health Research, 25, 656–669. https://doi.org/10.1080/09603123.2015.1007840 .

Fletcher M (1977) The effects of culture concentration and age, time, and temperature on bacterial attachment to polystyrene. Canadian Journal of Microbiology, 23, 1–6. https://doi.org/10.1139/m77-001 .

Fulaz S, Vitale S, Quinn L, Casey E (2019) Nanoparticle–Biofilm Interactions: The Role of the EPS Matrix. Trends in Microbiology, 27, 915–926. https://doi.org/10.1016/j.tim.2019.07.004 .

Goldberg J (2002) Biofilms and antibiotic resistance: a genetic linkage. TRENDS in Microbiology, 10, 264. https://doi.org/10.1016/S0966-842X(02)02381-8

Gomez CK, Aggarwal S (2019) Overview of Drinking Water Distribution System Microbiome and Water Quality. Encyclopedia of Water, 1–17. https://doi.org/10.1002/9781119300762.wsts019.

Goraj W, Pytlak A, Kowalska B, Kowalski D, Grządziel J, Szafranek-Nakonieczna A, Gałązka A, Stępniewska Z, Stępniewski W (2021) Influence of pipe material on biofilm microbial communities found in drinking water supply system. Environmental research, 196, 110433. https://doi.org/10.1016/j.envres.2020.110433 .

Katsikogianni M, Missirlis YF (2004) Concise review of mechanisms of bacterial adhesion to biomaterials and of techniques used in estimating bacteria-material interactions. European Cells & Materials, 8, 37–57.

Kerr CJ, Osborn KS, Robson GD, Handley PS (1998) The relationship between pipe material and biofilm formation in a laboratory model system. Journal of Applied Microbiology, 85, 29S. https://doi-org.portal.lib.fit.edu/10.1111/j.1365-2672.1998.tb05280.x.

Learbuch KLG, Smidt H, van der Wielen PWJJ (2021) Influence of pipe materials on the microbial community in unchlorinated drinking water and biofilm. Water Research, 194, 116922. https://doi.org/10.1016/j.watres.2021.116922.

Liu Q, Li R, Qu W, Tian X, Zhang Y, Wang W (2023) Influence of surface properties on the adhesion of bacteria onto different casings. Food Research International, 164, 112463. https://doi.org/10.1016/j.foodres.2023.112463.

Liu Y, Tay JH (2002) The essential role of hydrodynamic shear force in the formation of biofilm and granular sludge. Water research, 36, 1653–1665. https://doi.org/10.1016/s0043-1354(01)00379-7.

Lorenzetti M, Dogša I, Stošicki T, Stopar D, Kalin M, Kobe S, Novak S (2014) The Influence of Surface Modification on Bacterial Adhesion to Titanium-Based Substrates. ACS Applied Materials & Interfaces, 7, 1644–1651. https://doi.org/10.1021/am507148n.

Meylheuc T, Bellon-Fontaine MN, Van Oss CJ (2001) Adsorption of biosurfactant on solid surfaces and consequences regarding the bioadhesion of Listeria monocytogenes LO28. Journal of Applied Microbiology, 91, 822–832. https://doi.org/10.1046/j.1365-2672.2001.01455.x.

Morisaki H (1991) Measurement of the force necessary for removal of bacterial cells from a quartz plate. Journal of General Microbiology, 137, 2649–2655. https://doi.org/10.1099/00221287-137-11-2649.

Niquette P, Servais P, Savoir R (2000) Impacts of pipe materials on densities of fixed bacterial biomass in a drinking water distribution system. Water Research, 34, 1952–1956. https://doi.org/10.1016/S0043-1354(99)00307-3.

Oder M, Kompare B, Bohinc K, Torkar KG (2015) The impact of material surface roughness and temperature on the adhesion of Legionella pneumophila to contact surfaces. International Journal of Environmental Health Research, 25, 469–479. https://doi.org/10.1080/09603123.2014.963035.

Oh JK, Yegin Y, Yang F, Zhang M, Li J, Huang S, Verkhoturov SV, Schweikert, EA, Perez-Lewis K, Scholar EA, Taylor TM, Castillo A, Cisneros-Zevallos L, Min Y, Akbulut M (2018) The

influence of surface chemistry on the kinetics and thermodynamics of bacterial adhesion. Scientific Reports, 8, 17247. https://doi.org/10.1038/s41598-018-35343-1

Owens CEL, Angles ML, Cox PT, Byleveld PM, Osborne NJ, Rahman MB (2020) Implementation of quantitative microbial risk assessment (QMRA) for public drinking water supplies: Systematic review. Water research, 174, 115614. https://doi.org/10.1016/j.watres.2020.115614

Paray, A. A., Singh, M., Mir, M., & Kaur, A (2023) Gram staining: a brief review. Int J Res Rev, 10, 336–341. https://doi.org/10.52403/ijrr.20230934 .

Peng JS, Chou CC, Tsai WC (2002) Inactivation and removal of Bacillus cereus by sanitizer and detergent. International Journal of Food Microbiology, 77, 11–18. https://doi.org/10.1016/S0168-1605(02)00060-0.

Reyes CD, García AJ (2003) A centrifugation cell adhesion assay for high-throughput screening of biomaterial surfaces. Journal of Biomedical Materials Research - Part A, 67, 328–333. https://doi.org/10.1002/jbm.a.10122.

Rhoads WJ, Bradley TN, Mantha A, Buttling L, Keane T, Pruden A, Edwards MA (2020). Residential water heater cleaning and occurrence of Legionella in Flint, MI. Water Research, 171, 115439. https://doi.org/10.1016/j.watres.2019.115439.

Rode TM, Langsrud S, Holck A, Moretro T (2007) Different patterns of biofilm formation in Staphylococcus aureus under food-related stress conditions. International journal of food microbiology, 116, 372–383 .

Roosjen A, Busscher HJ, Norde W, Van der Mei HC (2006) Bacterial factors influencing adhesion of Pseudomonas aeruginosa strains to a poly(ethylene oxide) brush. Microbiology, 152, 2673–2682. https://doi.org/10.1099/mic.0.29005-0.

Roy PK, Ha AJ, Mizan MFR, Hossain MI, Ashrafudoulla M, Toushik SH, Nahar S, Kim Y K, Ha SD (2021) Effects of environmental conditions (temperature, pH, and glucose) on biofilm formation of Salmonella enterica serotype Kentucky and virulence gene expression. Poultry Science, 100, 101209. https://doi.org/10.1016/j.psj.2021.101209.

Schwering M, Song J, Turner RJ, Ceri H, Louie M (2013) Multi-species biofilms defined from drinking water microorganisms provide increased protection against chlorine disinfection. Biofouling, 29,917–928. https://doi.org/10.1080/08927014.2013.816298.

Senevirathne SWMAI, Mathew A, Toh YC, Yarlagadda PKDV (2022) Bactericidal Efficacy of Nanostructured Surfaces Increases under Flow Conditions. ACS Omega, 7, 41711–41722. https://doi.org/10.1021/acsomega.2c05828.

Sharma S, Mohler J, Mahajan SD, Schwartz SA, Bruggemann L, Aalinkeel R (2023) Microbial Biofilm: A Review on Formation, Infection, Antibiotic Resistance, Control Measures, and Innovative Treatment. Microorganisms, 11, 1614. https://doi.org/10.3390/microorganisms11061614.

Stefan DS, Bosomoiu M, Teodorescu G (2023) The Behavior of Polymeric Pipes in Drinking Water Distribution System—Comparison with Other Pipe Materials. Polymers, 15, 3872. https://doi.org/10.3390/polym15193872.

Waqas U, Farhan A, Haider A, Qumar U, Raza A (2023) Advancements in biofilm formation and control in potable water distribution systems: A comprehensive review and analysis of chloramine decay in water systems. Journal of Environmental Chemical Engineering, 11, N.PAG. https://doi.org/10.1016/j.jece.2023.111377.

Yoda I, Koseki H, Tomita M, Shida T, Horiuchi H, Sakoda H, Osaki M (2014) Effect of surface roughness of biomaterials on Staphylococcus epidermidis adhesion. BMC microbiology, 14, 234. https://doi.org/10.1186/s12866-014-0234-2 .

Zeraik AE, Nitschke M (2012) Influence of growth media and temperature on bacterial adhesion to polystyrene surfaces. Brazilian Archives of Biology and Technology 55, 569–576. https://doi.org/10.1590/S1516-89132012000400012 .

Zhang J, Li W, Chen J, Qi W, Wang F, Zhou Y (2018) Impact of biofilm formation and detachment on the transmission of bacterial antibiotic resistance in drinking water distribution systems. Chemosphere, 203, 368–380. https://doi.org/10.1016/j.chemosphere.2018.03.143 .

Zhang X, Lin T, Jiang F, Zhang X, Wang S, Zhang S (2022) Impact of pipe material and chlorination on the biofilm structure and microbial communities. Chemosphere, 289, 133218. https://doi.org/10.1016/j.chemosphere.2021.133218 .

Zhu Z, Wu C, Zhong D, Yuan Y, Shan L, Zhang J (2014) Effects of Pipe Materials on Chlorine-resistant Biofilm Formation Under Long-term High Chlorine Level. Applied Biochemistry and Biotechnology: Part A: Enzyme Engineering and Biotechnology, 173, 1564–1578. https://doi.org/10.1007/s12010-014-0935-x .

Al-Mukhtar Journal of Basic Sciences 22 (3): 289-298, 2024
Doi: https://doi.org/10.54172/t8ft5b75

Research Article **Open Access**

Life form and Chorological types spectrumof Succulent plants in Wadi Yabraq and its around, Al-Wadheia, Abyan Governorate-Yemen

Madleen A., Obel [1], Rania F. M. Ali [3*] and Mohammed A. Hussein [2]

[1] Department of Biology, Faculty of Education, Abyan University, Yemen.

***Corresponding author:** raniafarag2012m@gmail.com
Department of Botany, Faculty of Science, Omar Al-Mukhtar University, Libya.

[3] Department of Biology, Faculty of Education, Aden University, Yemen

Received:
25 November 2024

Accepted:
30 December 2024

Publish online:
31 December 2024

Abstract

The present study was based on extensive surveys and field observation of the diversity of succulent plants in Wadi Yabraq and it's around, Al-wadheea Dist. In the present investigation, it is observed about 71 Species belonging to 37genera and 21 Families were identified. Most of families of plants that contributed in the investigated area were Apocynaceae and Euphorbiaceae. Analysis of the habit shows that Shrubs are dominat with 31 species followed by herbs with 29 species, Trees with 8 species, Liana with 3 species. Investigation of life forms species shows that Chamaephytes are the most important. (49.30%), followed by Therophytes (18.30%), phanerophyte (16.90%) HemicryptophyteS (8.45%) ,Geophytes (4.22%). Among the common regions vegetative, Sudano–Zambezian, were with the highest followed by Endemic and (Sudano–Zambezian Saharo–Arabian).

Keywords: Succulents Plants, Wadi Yabraq, Families , Life Forms, Chorophytes

INTRODUCTION

Succulent plants have a global distribution and are represented in nearly all habitat types. Over 30 botanical families have succulent plant species, ranging from tiny annual plants to trees. Succulents are the camels of the plant world. They take in water and store it in their fleshy interiors, allowing them to go long periods of time without additional life giving liquid. Some of our favorite plants are succulent like aloes and most cacti (Bhalerao V. U et al., 1996).

Succulence is an adaptive response to drought, rapid drainage in rocky and sandy soil and high evaporation in windy, hot environments and in salty or alkaline habitats. There are probably more than five thousand species worldwide (Newton & Chan, 1998). Succulence is a morphological adaptation to regular drought. It is broadly defined as the presence of water storing tissue (hydrenchyma) in one or more organs. Simple parenchyma cells containing a vacuole that may occupy >95% of the cell volume are the principal site of water storage (Al-Gifri & Al-Subai, 1994; Antony et al., 2008; Gibson, 2012). Characterizing such plastic and variable traits is one of the major challenges in the study of succulent plants. Several metrics have been proposed, integrating tissue volume, mass, surface area and anatomy for quantifying water storage or water content (Gibson, 2012; Males, 2017; Ogburn et al., 2012). The objective of the study is to recognize succulent plants and

ascertain their geographical distribution within the study area, as well as to understand their adaptations to arid and semi-arid environments.

MATERIALS AND METHODS

Study area

The study area is located in the Wadi Yabraq in the district of Al-Wade'e, Abyan Governorate, Yemen and cover about 2785 square Km (figure 1), at latitude between 13.92 and 13.51 and longitude between 46.04 and 46.68, the altitude rage between 70 - 1250 meters above sea level, the southern mountain ranges in the region overlook the Gulf of Aden (figure 1).

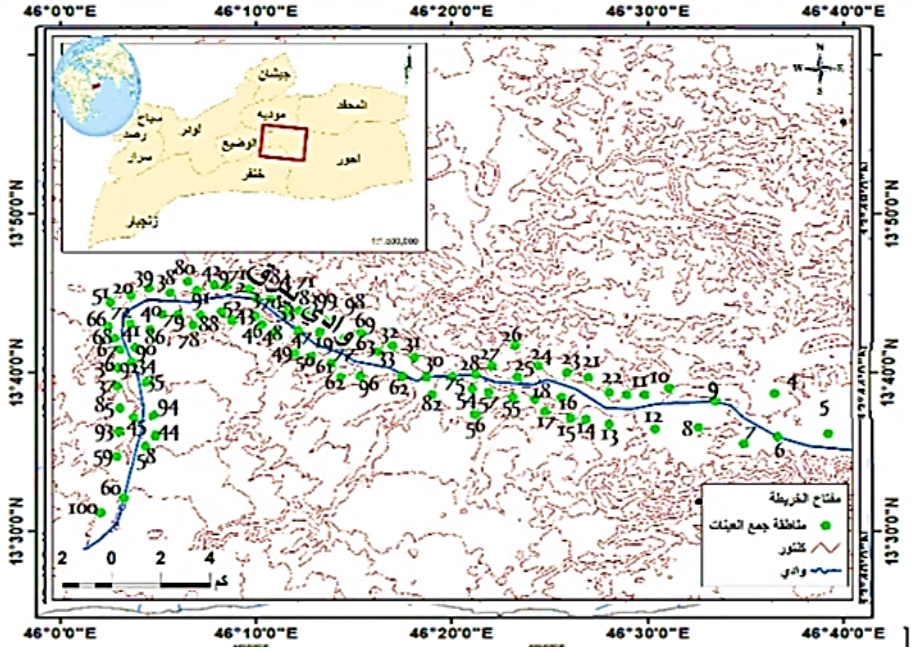

Figure: (1). Study area

The climate features of the study area are high temperature in the summer, the mean temperature was 25.5ºC in June, July and August and moderate temperature in the winter (the mean was 18ºC) in January. Rainy season mostly in the late summer (July- August and September.) with rainfall around 38.7 mm/year

The most important factors affecting the distribution of vegetation in the study area and Yemen in general are topography, the resulting presence of flat land and inclined slopes, altitude from the sea level (Al-Khulaidi & Mehdi, 1999; Al-Maisari & Hussein, 2022). A field survey was carried out through several trips from 2020 to 2022. on each trip, plant samples were collected. The plants were identified through the morphological description،the specimens were identified by (Abdullah et al., 2022; Al-Gifri & Saeed, 2017; Al-Khulaidi, 2013; Al-Gifri & Al-Subai, 1994; Giesen et al., 2007).

Identification and Nomenclature were revised for accepted names through the Plants of the (Al-Khulaidi, 2013) and world flora online Taxonomic Name Resolution Service (TNRS) Voucher specimens were deposited in the herbarium of the Biology Department, College of Sciences, Aden University. Life form categories were recognized (Al-Hawshabi et al., 2017; Al-Sodany et al., 2014; Alhood et al., 2020; Alhood & Sciences, 2024; Dahmash, 2015). Classification. Phytogeographicalcate- gories were distinguished based on World Online (POWO). The statistical analysis was performed using Microsoft Excel to create the charts and histograms.

RESULTSAND DISCUSSION

The present investigation has revealed that about 71species belong to 37genera and 2 1families have been reported from the study area (Table 1)

Habitat analysis:
Herbs and shrubs represent about 71 spp. of the total species, while the trees were represented by 8 spp. Analysis of the habit shows that shrubs are dominat with 31 species followed by herbs with 29 species, and Liana with 3 species as shown in table (2) and figure (2).

Table (2) : The contribution of various plant habits in Yabraq Valley

Life Growth	No of species	Percentage
Shrubs	31	43.66%
Herbs	29	40.84%
Trees	8	11,26%
Liana	3	4.22%

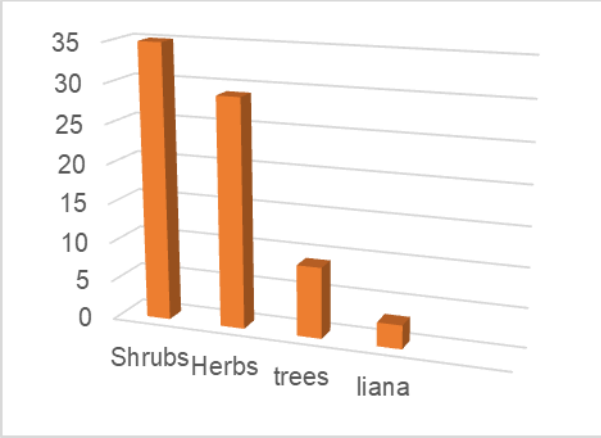

Figure (2): The Contribution of various plant habits

Table .3. and figure 3 show the biological spectrum or the life form spectrum of the given 71 species in Wadi Yabraq. The Chaemophytes have dominated the flora of the Succulent plants representing 35sp., (49.30%), followed by the therophytes 13 spp (18.30%), and Phanerophytes 12 sp. (16.90%), Hemicryptophytes 6 sp. (8.45 %) geophytes 3sp. (4.22%), parasites 2spp. (3. 27%). The life form spectra in the study area indicated that, Chamaephytes had the highest contribution. These results agree with (Al-Hawshabi et al., 2017; Alhood et al., 2020; Alhood & Sciences, 2024).

Table (3): Life forms spectrum of Yabraq Valley

N0	Life- form	Number of Taxa	Percentage (%)
1.	Chamaephyte	35	49.30%
2.	Therophyte	13	18.30%
3.	Phanerophyte	12	16.90%
4.	Hemicryptophyte	6	8.45%
5.	Geophytes	3	4.22%
6.	Parasites	2	2.81%

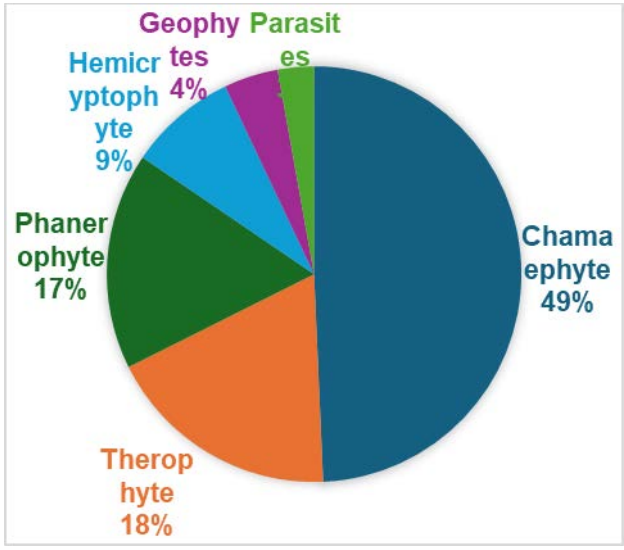

Figure (3): Different life –forms classes of WadiYabraq

In terms of chorotypes such as Sudano –Zambezian, Endemic, (Sudano –ZambezianSaharo –Arabian,) with amounts of, respectively were having in the highest and lowest levels between vegetative elements, Among the common regions vegetative, Sudano –Zambezian, were with the highest followed by Endemic, (Sudano –Zambezian, Saharo –Arabian), whereas Saharo -Arabian, Arabian, Iranian, Tropical, were with the lowest table (4) and figure. (4). the dominant Sudano -Zambenzian region confirms that the study area "as a part of Yemen" belongs to the African Horn region, and our results agree with (Alhood et al., 2020; Alhood & Sciences, 2024). Figure 5 illustrates several rare and endangered succulent plant species found within the study area.

Table (4): Chorological types spectrumof Succullent plants in Wadi Yabraq

Chorotype	Number of Species	Percentage (%)
	Mono-Regional	
TR	1	1.40%
END- N.END	16	22.53%
SA-Si	6	8.45%
Su-Za	26	36.61%
Subtotal	50	70.42%
	Bi-regional	
Su-Za,Sa-Si	9	12.67%
TR – SA-SI	1	1.40%
Su-Za , Med	3	4.22%
Su-ZA + IT	1	1.40%
Subtotal	14	19.71%
	Pluri-regional	
Su-Za, Med, Sa-Si,	1	1.40%
IT + Med. + Su - Za + Sa – Si	1	1.40%
IT + ME + Su - Za +	1	1.56%
Subtotal	3	4.22%
	Worldwide	
COSM	5	7.04%
Subtotal	4	5.63%
Total	71	100%

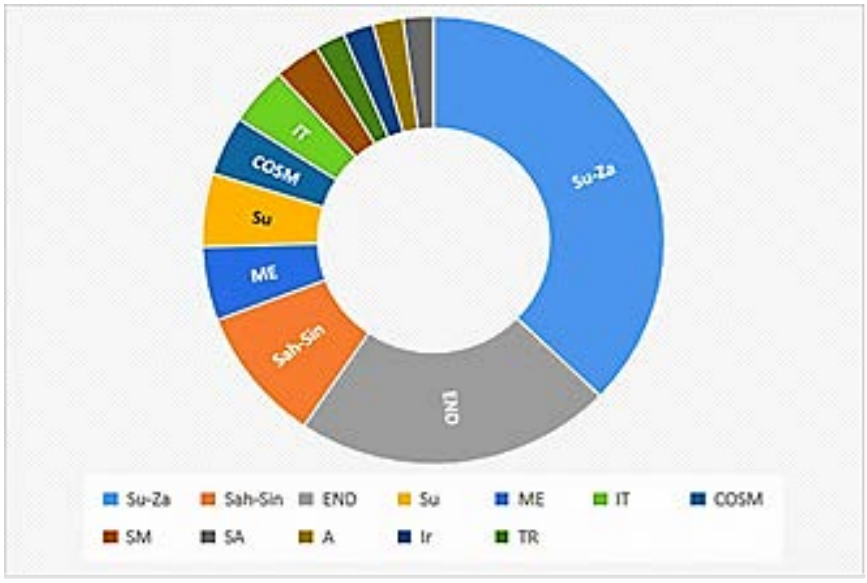

Figure (4): Chorological types spectrum of Succulent plants in WadiYabraq

Table (1):List of succulent plants species which recorded from Yabraq valley.

Family	Scientific names	Habit	Life-forms	Chorotypes
Aizoaceae	*Aizooncanarien*se L.	Herb	Th	Su-Za, Med, Sa-S,
	Trianthema crystallina (Forssk.) Vahl	Herb	Th	Su-Za
	T .portulacastrum L	Herb	Th	Su-Za
Aloeaceae	*Aloe splendens*lavranos	Shrub	Ch	END
	*A . inermis*Forssk	Shrub	Ch	N.END
	*A . vacillans*Forssk	Shrub	Ch	N.END
	A . lanata T.A.McCoy & Lavranos.	Shrub	Ch	END
Aristolochiaceae	*Aristolochiabracteolata* Lam.	Herb	Th	Su-za
Apocynaceae (Asclepiadaceae)	*Adeniumobesum* (Forssk.) Roem. &Schult	Tree	Ph	Su-Za, Sa-Si
	Caralluma adenensis (Defl.) Schum.	Herb	Ch	END
	C .awdaliana (Defl.) A. Berger	Shrub	Ch	END
	C . deflersiana (Defl.) Bergor.	Shrub	He	N.END
	C .edulis (Edgw.) Benth	Herb	He	IT + ME + Su - Za +
	*C .hexogona*lavranos	Herb	He	N.END
	C. penicillata (Defl.) N. E. Brown	Herb	Ch	Su-Za
	C .quadrangula (Forssk.) N. E. Brown	shrub	He	N.END
	Ceropegia subaphylla K. Schuhmann.	Liana	Ch	SA-SI
	C .variegata (Forssk.) Decne.	Liana	Ch	N.END
	Glossoniemavarians (Stocks) Benth. ex Hook. f.	Herb	Ch	Su-Za
	Leptadenia arborea (Forssk.) Schweinf	Shrub	Ch	Su – Za + Sa – Si.
	L .yrotechnica (Forssk.) Decne	Shrub	Ph	Sa-si.+ Ir.-Tur
	Pergulariatomentosa L.	Liana	Ch	SA-SI+SU-ZA
	*Rhytidocaulonmacrolobum*Lavranos	Shrub	Ch	Su-Za
	*Sarcostemma forskalianum*Schultes	Shrub	Ch	N.END
	S . viminale (L) R.Brown	Shrub	Ch	Su,-ZA
Asteraceae	*Kleiniaodora* (Forssk.) A. Berger.	Shrub	Ch	Su-Za
	K . semperviva (Forssk.) DC.	Shrub	Ch	Su-Za
	K .pendula (Forssk.) DC.	Shrub	Ch	Su-Za
	*Launaeahafunensis*Chiov.	Herb	G	Sa – Si.
	L .procumbens (Roxb.) Ramayya&Rajgopal.	Herb	Th	Sa – Si
	L. nudicaulis (L.) Hook. f.	Herb	Ch	Sa– Si
Buraceraceae	*Commiphoraafricana* (A.Rich.) Engl.	Tree	Ph	Su-Za
	C .kataf (Forssk.) Engl.	Tree	Ph	Su-Za
	C .myrrha(Nees) Engl.	Tree	Ph	Su-Za
	*C . schimperi (*O. Berg) Engl	Tree	Ph	Su-Za
Cactaceae	*Opuntia ficus-indica* (L.) Mill	Shrub	Ch	COSM
Capparaceae	*Cappariscartilaginea*Forssk.	Shrub	Ch	Su-Za, Sa Si.
	C .spinosa L.	Shrub	Ch	Su-Za , Sa-Si.

Family	Scientific names	Habit	Life-forms	Chorotypes
Chenopodiaceae	*Salsola forskali*Forssk.	Shrub	Ch	SA-SI, SU-ZA
	*S .spinescens*Moq	Shrub	Ch	Cosm
	Suaeda aegyptiaca (Hasselq.) Zohary	Herb	Ch	SA Si
	*S .monoica*Forssk.	Shrub	Ch	Su- Za
	*Halothamnusbottae*jaub&spack*subspniger*kathe Heinrich	Tree	Ph	N.END
Crassulaceae	*Kalanchoebentii* Hook. f. subsp. bentii	Shrub	Ch	N.END
Cynomoraceae	*Cynomoriumcoccineum*L.	Herb	P.	Su-Za,Sa-Si
Dracaenaceae	*Dracaena ombet*Kotschy&Peyr.	Tree	Ph	Su – Za
	*Sansevieriaehrenbergii*Schweinf. ex Baker	Herb	G	Su – Za
	Sansevieriaforskaoliana (Schult. f.) Hepper & J. R. I. Wood	Herb	G	Su – Za
Euphorbiaceae	*Euphorbia inarticulata*Schweinf.	Shrub	Ch	N.END
	E . balsamifera Ait. *subsp. Adenensis* (Defl.) Bally	Shrub	Ch	Su-Za
	E. cuneata Vahl subsp. cuneata	Shrub	Ch	Su – Za
	E .granulata Forssk. var. granulata	Shrub	Ch	TR
	E. greuteri N. Kilian, Kürschner& P. Hein	Herb	Ch	N END
	E .hirta L.	Herb	Th	COSM
	*E .hadramautica*E.G.Baker	Herb	Ch	END
	*E .indica*Lamk.	Herb	Th	Su-Za +Med.
	*E . larica*Boiss.	Shrub	Ph	TR – SA-SI
	*E .schimperi*Presl.	Shrub	Ch	N.END
	*E . serpens*Kunth.	Herb	Th	Su-Za ,Med.
Hydnoraceae	*Hydnorajohannis*Becc	Herb	P.	Su-Za
Lamiaceae	*Plectranthusmontanus*Benth.	Shrub	Ch	Su-Za
Molluginaceae	*Corbichoniadecumbens* (Forssk.) Exel	Herb	Th	Su-Za + IT
Polygonaceae	*Rumexvesicarius* L.	Shrub	Ph	Su-Za , Med.
Portulacaceae	*Portulaca oleracea* L. *subsp. oleracea*	Herb	Th	Cosm
	Portulacaqundrifida L.	Herb	Th	Cosm
Sterculiaceae	*Sterculiaafricana* (Lour.)Fiori	Tree	Ph	Su-Za
Vitaceae	*Cissusquadrangularis* L.	Shrub	He	Su-Za,Sa-Si
	C. rotundifolia (Forssk.)Vahl.	Shrub	He	Su-Za
Zygophllaceae	*Seetzenialanata* (willd) bull.	Herb	Th	SU
	Tetraena alba (L.F)Beier&Thulin	Herb	Ph	SA
	T. simplex (L.) Beier&Thulin	Herb	Th	IT + Med. + Su - Za + Sa– Si.

Life-form; ph = phanerophytes,Ch = chamaephytes, H = hemicryptophytes, Cr = cryptophytes, Th = therophytes, HE = hemiepiphytes, G = Geophytes, P.= Parasites.
The chorotypes are: Su-Za = Sudano –Zambezian, Sah-Sin= Saharo –Arabian, END= Endemic, N.END= Near Endemic, Su= Sudano, ME= Mediterranian, IT= Irano – Turanian, COMS= Cosmopolitan, SM Somali-anmasai, SA= Saharo-Arabian. A=Arabian, Ir= Iranian, TR= Tropical.

A. *Halothamnusbottae*jaub&spack*subspniger*kathe H
B. *GlossoniemaVarians*
C. *Dracaena ombet*
D. *Carallumaadenensis*
E. *Corbichoniadecumbens*
F. *Carallumahexogona*
G. *Euphorbia greuteri*
H. *Euphorbia Hadramautica*
I. *Hydnorajohannis*

Figure: (5). Some Succulent plants in theStudy area.

CONCLUSION

The succulent flora of Wadi Yabraq consist of 71 succulent taxa belonging to 37 genera the study area is characterized by its rich biodiversity, With 16 endemic and near-endemic species recorded. The predominant life form of the plants is Chamophyta, which is evidence of the plants tolerance to drought. Most of the plants belong to the Sudano –Zambezian, which is prevalent in dry desert areas. It was also found that most of the succulent plants are the local population utilizes these plants both as traditional remedies and as a food source. Consequently, the study suggests that further research should be undertaken on the succulent plants employed by residents for medicinal purposes.

Duality of interest: The authors declare that they have no duality of interest associated with this manuscript.

Author contributions : Contribution is equal between authors.

Funding: No specific funding was received for this work.

REFERENCES

Abdullah, M. T., Al-Dosari, M. E. J. I., & Kuwait, S. o. K. E. P. A., Gland. (2022). Vegetation of the State of Kuwait.

Al-Gifri, A. N., & Saeed, A. A. J. T. J. o. M. (2017). Phytosociology and distribution of dominant plant community types along the road from fukum khors omerah: A costal area east of Aden, Yemen. *1*(2).

Al-Hawshabi, O. S. S., Al-Meisari, M. A., & El-Naggar, S. J. C. L. S. (2017). Floristic composition, life-forms and biological spectrum of Toor Al-Baha District, Lahej Governorate, Yemen. *3*(4), 72-91.

Al-Khulaidi, A. A., & Mehdi, A. S. (1999). *Phytogeographical* (1 ed.). Dar Al-Safa for publication -Amman - Jordan (In Arabic).

Al-Khulaidi, A. J. S. N. R. M. P. I., Sana'a, Yemen. (2013). Flora of Yemen. *266*.

Al-Maisari, M. A. S., & Hussein, M. A. (2022). The Herbaceous Plants of The Plain Area, and Foothills of Tharah Mountain Range ,Lawder District, Abyan Governorate, Yemen. *University of Aden Journal of Natural and Applied Sciences, 26*(1), 71-80. https://doi.org/ https://doi.org/10.47372/uajnas.2022.n1.a07

Al-Sodany, Y., Mosallam, H., & Al-Yasi, H. J. I. J. C. L. S. (2014). Floristic diversity and plant communities associated with juniper forests in high altitudes. *4*(2), 118-133.

Al‐Gifri, A., & Al‐Subai, M. J. F. R. (1994). Vegetation between Abyan and Modia (Abyan Governorate, Yemen). *105*(3‐4), 229-234.

Alhood, F. A., Al-Hawshabi, O. S., Dahmash, A. M. J. U. o. A. J. o. N., & Sciences, A. (2020). Life-forms and Chorotypes of Succulent plants of Al-Dale'a Governorate, Yemen. *24*(1), 157-168.

Alhood, F. A. N. J. E. J. o. U. o. A. f. B., & Sciences, A. (2024). FLORISTIC COMPOSITION, LIFE-FORMS AND CHOROLOGY OF AL-MADLOOM MOUNTAIN, ADHALE DISTRICT, SOUTHERN YEMEN. *5*(1), 131-140.

Antony, E., Taybi, T., Courbot, M., Mugford, S. T., Smith, J. A. C., & Borland, A. M. J. J. o. E. B. (2008). Cloning, localization and expression analysis of vacuolar sugar transporters in the CAM plant Ananas comosus (pineapple). *59*(7), 1895-1908.

Bhalerao V. U, Arangale K. B, Shinde Y. P, Yeole A. V, & Barwant M. (1996). Survey of Succulent plants from kopergaon Tehsil of Mahrashtra. *Indian Journal of Plant Sciences, 7*(4), 1-3.

Dahmash, A. J. S. J. f. D. F. o. S. (2015). Studies on the flora of Yemen: Flora of Kharab AlMarashi, AlJawf, Republic of Yemen. *4*(1), 45-54.

Gibson, A. C. (2012). *Structure-function relations of warm desert plants*. Springer Science & Business Media.

Giesen, W., Giesen, P., Giesen, K. J. A. i. t. t. p., & vegetation types found at Lewa Wildlife Conservancy, K. A. f. t. a. (2007). Flora and vegetation of Lewa Wildlife Conservancy.

Males, J. J. J. o. E. B. (2017). Secrets of succulence. *68*(9), 2121-2134.

Newton, D. J., & Chan, J. (1998). *South Africa's trade in southern African succulent plants*. Traffic east/southern Africa.

Ogburn, R. M., Edwards, E. J. J. P., Cell, & Environment. (2012). Quantifying succulence: a rapid, physiologically meaningful metric of plant water storage. *35*(9), 1533-1542.